AN ABSTRACT OF THE THESIS OF

Jochen Braunmiller for the degree of Master of Science in Geophysics presented on July 19, 1991.

Title: Down-Dip Geometry and Depth Extent of Normal Faults in the Aegean - Evidence from Earthquakes

Abstract approved: _____ Redacted for Privacy _____

Teleseismically recorded body waves have been used to study the rupture process, geometry and rupture extent of normal faults associated with recent large earthquakes in the Aegean. The down-dip geometry was investigated for the six largest ($M_w \geq 6.2$) events (Alasehir, 1969; Gediz, 1970; Thessaloniki, 1978; and Corinth sequence, 1981) which occurred on major faults, were associated with surface ruptures, and probably ruptured the entire width of the seismogenic zone, thus providing constraints on the geometry of faulting during continental extension. The depth extent of the main shock rupture in relation to the aftershock-depth distribution was investigated for earthquakes with locally recorded and precisely located aftershocks (Thessaloniki; Corinth sequence; and Kalamata, 1986).

A three step procedure was used to investigate the fault geometry. First, the average (centroidal) description of the source was obtained by simultaneous inversion of P and SH waveforms. The presence of seismogenic slip on a detachment at the base of the brittle crust was investigated by inverting for the seismic moment release from a shallow dipping source at twice the centroid depth (step 2). Three point sources were distributed evenly along the width of the fault to determine the down-dip fault geometry (step 3). Results of models with fixed fault geometry were compared statistically to obtain bounds on possible fault curvatures. In another test the initial fault geometries were allowed to vary and the results were compared with the more constrained inversions. Short-period first motion fault plane solutions give an estimate of the fault dip at the nucleation depth and were used to provide an additional constraint on the fault geometry.

The sensitivity of the method was tested on synthetic data by comparing P, SV, and SH waveforms for planar and listric fault geometries. Fault curvature produces only a secondary azimuthally dependent effect on body wave pulses at teleseismic distances and a

good station coverage is required. Upward or downward propagating ruptures can be better resolved than bilaterally propagating ruptures. It is very important to incorporate SH waves into the analysis, since polarities and amplitudes of SH waves are more affected by changes in fault dip than P and SV waves at teleseismic distances. The centroid and the geometry were well resolved for a planar fault. For listric faults the centroid dip is not estimated correctly due to interference of direct and reflected phases which renders the excitation functions unevenly sensitive to parts of the fault at different depths. In spite of the bias, distributed source models derived from the biased centroidal solution can differentiate curved from planar geometries. Better estimates of the true curvature and fault dips are obtained when the dips at the individual subsources are allowed to vary.

Seismogenic slip on a basal detachment is not required by any of the investigated earthquakes. Observed large arrivals in later parts of the P waveforms at African stations for the Gediz and Alasehir earthquakes have been cited as evidence for low-angle normal faulting at the base of the brittle crust, however, this interpretation is not compatible with observed SH waveforms. Furthermore, three large aftershocks ($5.5 \leq M_w < 5.9$) of the Gediz event show similar arrivals, indicating that this complexity is probably related to the structure along the propagation path. Simple shear shallow faulting within the brittle crust is not supported by the results of this study.

None of the investigated earthquakes show a significant decrease of fault dip with depth, which supports models of continental extension involving high-angle planar faults. The 03/28/1970 Gediz and the 02/24/1981 Corinth earthquake ruptured on essentially planar faults. The data for the 06/20/1978 Thessaloniki and the 02/25/1981 and 03/04/1981 Corinth earthquakes are best fit by a planar fault model, but allow a small amount of fault curvature. A small amount of upward convex curvature is suggested for the 03/28/1969 Alasehir earthquake; however, a planar model is statistically indistinguishable. The small 04/19/1970 Gediz aftershock is a double event, and fault curvature is required if the two subevents ruptured along the same fault plane.

The ruptures of the Thessaloniki and the 02/24/1981 and 03/04/1981 Corinth earthquakes dynamically penetrated to depths where almost no aftershock activity occurred, whereas ruptures of the Kalamata and the 02/25/1981 Corinth earthquakes terminated at depths where the aftershock activity decreases sharply. The lack of shallow aftershock activity, the sharp boundary below which only few aftershocks occur, and the depth extent of main shock ruptures can be explained in terms of a friction-rate model of a fault zone in which earthquakes can only nucleate in a region of unstable, velocity-weakening friction, and only large earthquakes have ruptures strong enough to dynamically penetrate into regions of stable, velocity-strengthening friction.

Down-Dip Geometry and Depth Extent of Normal Faults in

the Aegean - Evidence from Earthquakes

by

Jochen Braunmiller

A THESIS

submitted to

Oregon State University

in partial fulfillment of

the requirements for the

degree of

Master of Science

Completed July 19, 1991

Commencement June 1992

APPROVED:

<u>Redacted for Privacy</u>

Major-Professor: Associate Professor of Geophysics

Redacted for Privacy

Dean of College of Oceanography

Redacted for Privacy

Dean of Graduate School

Date thesis is presented <u>July 19, 1991</u>

Typed by the author <u>Jochen Braunmiller</u>

Acknowledgements

Table of Contents

List of Figures

List of Tables

Down-Dip Geometry and Depth Extent of Normal Faults in the Aegean
-
Evidence from Earthquakes

1. Introduction

The mechanism of extension of continental crust is not well understood. The goal of this thesis is, first, to infer information about the geometry of active continental normal faults and, second, to infer the depth extent of main shock ruptures in relation to their aftershock distribution. The use of seismological data from large normal faulting earthquakes, which rupture the entire width of the seismogenic upper crust, and their aftershocks provide the opportunity to study the major structures in regions actively undergoing extension. Studying these large active faults at the time of their movements gives information about their geometry, orientation and interactions, which are difficult to deduce from the geologic record or from reflection seismic sections.

Geological mapping and reflection seismology in regions of continental extension, such as the Basin and Range region in the western United States (e.g. Wernicke and Burchfiel, 1982; Allmendinger et al., 1983; Smith and Brun, 1984; Gans et al., 1985), and passive margins, e.g., the northern Bay of Biscay (LePichon and Barbier, 1987), indicate the presence of curved, listric faults and of low-angle normal faults of large areal extent (detachment faults). The dominant structures in actively extending areas, however, seem to be arrays of steeply dipping, deep reaching, mainly planar normal faults (Jackson and McKenzie, 1983; Roberts et al., 1991), where the major fault bounded blocks are separated by a few kilometers up to about 40 km depending on the regional extensional environments (Jackson and White, 1989).

From a mechanical point of view, it is difficult to generate low-angle normal faults since the orientation of the maximum compressional axis, σ_1, is subvertical in extensional regimes, favoring the development of high angle normal faults. For a typical static rock friction coefficient of $\mu=0.75$, Sibson (1985) concludes that no frictional normal slip failure can occur on planes dipping less than 37° unless either abnormally high fluid pressures led the least principal compressional stress, σ_3, to become effectively tensile, or the stress orientations deviate significantly from horizontal (σ_3) and vertical (σ_1).

It has been suggested that detachment faults are not primary structures, but merely represent passively rotated high-angle normal faults (Jackson and McKenzie, 1983) or

ancient brittle-ductile transitions within the crust as proposed by the 'pure shear' model for continental extension (e.g. Gans et al., 1985; Gans, 1987). Furthermore, there is no compelling seismological evidence for low-angle normal faulting (Jackson, 1987; Doser and Smith, 1989; Jackson and White, 1989), but several studies indicate steep normal faults that remain planar to about 10-15 km depth (Jackson and McKenzie, 1983; Okaya and Thompson, 1985; Stein and Barrientos, 1985; Doser, 1986; Barrientos et al, 1987; Nábělek, in press). If these faults have any listric component, it has to lie beneath the seismogenic upper crust. The role of low-angle normal faults for continental extension and their relation to steep arrays of deeply biting normal faults is still enigmatic.

The nature of the brittle-ductile transition and its effect on nucleation depths and rupture extents of earthquakes will be investigated by testing a friction-rate model for faulting presented by Scholz (1988). This model predicts that earthquakes can only nucleate within the depth range where unstable velocity-weakening friction is dominant, presumably from a depth of a few km down to the onset of quartz plasticity at approximately the 300°C isotherm, and that only ruptures of large earthquakes can dynamically penetrate into the stable regions. Other investigators (e.g. Das, 1982; Eyidogan and Jackson, 1985; Strehlau, 1986; Jackson and White 1989) have also suggested that large earthquakes penetrate into the ductile portions of the crust.

The main questions posed in this thesis will be: 1) is the geometry of the fault surfaces of large normal faulting earthquakes planar or curved, e.g., does the dip decrease with depth; 2) is there evidence for detachment surfaces at the base of the aftershock zones in form of coseismic slip during large earthquakes; and 3) to what depths do ruptures of large normal faulting earthquakes extend and what is the relation between the depth extent of these ruptures, their nucleation depth, and the depth distribution of the aftershocks associated with them.

The study area will be the Aegean region, an area of pronounced continental extension situated in the back-arc of the Hellenic subduction zone. A south to southsoutheast directed extension at an average rate of 20-70 mm yr^{-1} has been inferred from the summation of moment tensors of large earthquakes (Jackson and McKenzie, 1988; Ekström and England, 1989). Possible detachment faults and metamorphic core complexes have been found on several islands in the Aegean (Lister et al., 1984). On the adjacent Turkish mainland, however, arrays of steeply dipping high-angle normal faults are exposed (e.g. Westaway, 1990) and it is interesting to investigate their interrelations.

The data set primarily used in this study consists of short- and long-period P and S wave seismograms recorded by the WWSSN (World-Wide Standardized Seismic Network) network. For the events that occurred since 1980, data from the GDSN (Global

Digital Seismic Network) network are also included. Single broadband records were produced from the digital data in multiple frequency bands. Their broader frequency content allows a more precise resolution of the rupture processes. Aftershock hypocenter depths for the Thessaloniki, Corinth, and Kalamata earthquakes are from Carver and Bollinger (1981), Soufleris et al. (1982), King et al. (1984), Lyon-Caen et al. (1988), and Papazachos et al. (1988).

P and SH waveforms were inverted for various source parameters depending on the size and complexity of the event using the inversion algorithm developed by Nábělek (1984). The approach used in this thesis is very similar to that applied to study the 1983 Borah Peak, Idaho earthquake by Nábělek (in press).

I concentrated on the largest normal faulting earthquakes in the investigated area (Alasehir, 1969; Gediz, 1970; Thessaloniki, 1978; and 1981 Corinth sequence) to study the fault geometry; these earthquakes were powerful enough to rupture the entire seismogenic width of the crust and therefore carry the information about the down-dip geometry of the major fault zones which presumably take up a significant component of extension. For earthquakes with precisely determined aftershocks (Thessaloniki, 1978; Corinth, 1981; and Kalamata, 1986), I also studied the relationship between the aftershock-depth distribution and the maximum depth to which the main shock ruptures dynamically propagate.

Models of continental extension for the brittle upper crust, the possible origin and importance of detachment faults, as well as seismological evidence for the geometry of normal faulting earthquakes from other studies will be presented in the first part of Chapter 2. The second part of Chapter 2 deals with the rheological models that are currently used to describe the nature of the brittle-ductile transitional zone in the crust. The mathematical background of the forward and inverse problem of the body wave technique is given in Chapter 3. The procedure that I followed to deduce information about the fault geometry, detachment faulting, and the depth extent of the ruptures, as well as the statistical test used to quantitatively differentiate acceptable and not acceptable fault geometries is described in the same Chapter 3. Data and data preparation are part of Chapter 4. Synthetic modeling simulating different down-dip fault geometries has been performed to investigate the sensibility of the waveforms to these differences and to estimate the capability of the employed technique to distinguish different fault geometries. Results will be shown in Chapter 5. The body wave inversion technique has been applied to thirteen earthquakes in the Aegean region, and results will be presented in Chapter 6. Fault geometry has been investigated only for the events large enough to produce surface ruptures, and depth extent of rupture was studied only for earthquakes

where high-quality aftershock locations were available. Conclusions and a summary are presented in Chapter 7.

2. Background

2.1 Models of Extension of Continental Lithosphere

2.1.1 Brittle Upper Crust

Teleseismically recorded body wave data will be used to deduce the geometry of normal faults at the time of the earthquake rupture. The two general models used to describe the deformation in the upper crust in extensional areas, involving either listric or planar faults, can then be compared with the results of this study.

Planar, 'Domino-Style' Faults

The first model involves arrays of coeval and closely spaced planar high-angle normal faults. In the process of extension, adjacent fault blocks and faults rotate in a domino like fashion (e.g. Morton and Black, 1975; Wernicke and Burchfiel, 1982; Jackson and McKenzie, 1983; Gans et al., 1985) (Fig. 2.1.1a). As the faults and blocks rotate, shear stresses in direction of the fault planes diminishes and friction increases. As extension continues, older faults with gently dipping fault planes finally lock, and new sets of steeply dipping faults develop. These new domino faults cut into older more shallow dipping inactive faults as has been observed in the upper plate of the Snake Range decollement, Nevada (Gans et al., 1985) and in the Afar region of Ethiopia (Morton and Black, 1975). The apparent space problem involved in the domino-style extension models can be reconciled by plastic deformation (Jackson et al., 1988) and/or small scale brittle internal deformation at the base of the blocks.

Listric Faults

The second model involves listric normal faults (e.g. Davis et al., 1980). Downward displacement of the upper plate on a curviplanar fault surface results either in antithetic faulting associated with minor graben formation or reverse drag flexure where the hanging wall strata adjacent to the fault rotate (Hamblin, 1965) (Fig. 2.1.1b). Successive generations of listric normal faults are proposed and new listric faults form as the older structures become unable to accommodate further movements due to geometric constraints. The hanging walls of strongly curved fault surfaces must undergo a

substantial amount of internal deformation since movements along such a surface requires each element of the adjacent hanging wall to successively change its curvature.

Syndepositional listric normal faulting has been observed within thick sedimentary sequences of passive margins, e.g., the Gulf of Mexico (Bally et al., 1981). However, flattening of the faults onto weak layers, such as overpressured shales or salt, which allow hanging wall deformation, is lithologically controlled and no basement is involved (Bally et al., 1981; Jackson et al., 1988). Bally et al. (1981) also postulate the existence of listric normal faults involving the basement during the formation of rifts in the Gulf of Biscay. However, LePichon and Barbier (1987), using a more extensive reflection data set of higher quality, interpret normal faults involving the basement in the same region as being planar.

Listric 'Master Faults'

Simultaneous operation of planar domino and listric normal faults is possible. It has been proposed (e.g. Wernicke and Burchfiel, 1982; Jackson and McKenzie, 1983) that listric normal faults are 'master faults' in extensional regions, with planar normal faults active in their hanging walls in a domino like fashion (Fig. 2.1.1c). In the model of Jackson and McKenzie (1983), normal faults, which are planar in the upper part of the crust, become slightly listric at the brittle-ductile transition due to changes in the rheological behaviour of the materials (Jackson, 1987).

In the simple domino-style model, each fault block has infinite rigidity and block rotations are achieved by rigid-body rotation against the adjacent fault. Assuming that the faults bounding extensional regions ('master faults') behave in the same rigid fashion, they must not change their shape which implies that they are listric (Wernicke and Burchfiel, 1982; Jackson and McKenzie, 1983). From investigations of the basin bounding faults within the North Sea, Roberts and Yielding (1991) deduce that these were neither rigid nor static. Incorporating the flexural-isostasy response, e.g., as described in the flexural-cantilever model of continental lithospheric extension (Kusznir et al., 1991), allows the intra-basin and basin margin faults to be modelled as planar structures (Roberts and Yielding, 1991; Kusznir et al., 1991). As pointed out by Roberts and Yielding (1991), balanced cross-sections using basin margin unconformities as pre-faulting markers may be misleading.

2.1.2 Detachment Faults

Apparent low angle normal faults are commonly refered to as detachment faults since they usually separate highly fractured upper crustal rocks from ductilely deformed rocks of middle and lower crustal origin. They were first described and extensively studied in the metamorphic core complexes of the Basin and Range region (e.g. Crittenden et al., 1980). Detachment faults are of large areal extent and appear to have formed with a gentle fault dip. For example, Planke and Smith (1991), primarily using reflection data, estimated a width of 80 to 130 km and an area of several thousand square kilometers for the Sevier Desert detachment in Utah (see also Wernicke, 1981, Allmendinger et al., 1983). The slope of the Sevier Desert detachment was found to be 10-12° (Allmendinger et al., 1983; Planke and Smith, 1991). Another example is the reported displacement of at least 40 km and the areal extent of more than 10000 km^2 for the Whipple fault in the southern Colorado River region (Lister and Davis, 1989). There exist a manifold of different interpretations for the origin of these low-angle normal faults, e.g., thrust faults, thrust faults reactivated as low-angle normal faults (Doser, 1987, for a specific case), unconformities, originally high-angle normal faults which have been rotated into low-angle normal faults (Jackson and McKenzie, 1983) or became shallower due to isostatic rebound of the unloaded footwalls (Buck et al., 1988; Buck, 1988; Wernicke and Axen, 1988), surfaces representing old brittle-ductile transition zones in the continental crust (Bally et al., 1981; Gans et al., 1985; Gans, 1987), and as normal faults with a gently dipping fault surface of their own right (Wernicke, 1981, 1985; Wernicke et al., 1985; LePichon and Barbier, 1987; Lister and Davis, 1989).

Fault plane solutions derived from body wave inversion are obtained in this study to investigate if shallow dipping detachments within or at the base of the brittle crust are seismically active. Two kinematic models for the origin of the detachments will be described next. The simple shear model views detachments as active faults, whereas the pure shear model views them as old brittle-ductile transitions. The importance of the isostatic response which is not considered in the kinematic models will also be discussed.

Simple Shear Model

The 'simple shear' model (e.g. Wernicke 1981, 1985; Davis, 1983; Lister et al., 1986; LePichon and Barbier, 1987) uses thin-skinned compressional belts as an analogue for large-scale simple-shear extension. In the original model by Wernicke (1981), the shallow (10-30°) dipping active fault represents a major through-going lithospheric

dislocation, which in its deeper parts is manifested in form of a narrow ductile shear zone. The resulting structure is asymmetric, because thinning of the upper and lower lithosphere is offset along the detachment (Fig. 2.1.2a). Cutting through the whole lithosphere requires a remarkable persistence of the detachment fault. An expected shallowing of the Moho where the shear zone enters the mantle has not been observed (Klemperer et al., 1986). Therefore later models (e.g., Wernicke et al. (1985); Lister and Davis, 1989) view detachment faults as the upper crustal part of normal-slip, shallow-dipping shear zones widening with depth. LePichon and Barbier (1987) present a similar model for the formation of passive margins, where an originally aseismic low-angle normal fault propagates upward from the lower crust into the brittle upper layers and becomes seismogenic.

Subvertical orientation of the maximum compressional stress in extensional regimes makes it difficult to generate low-angle faults (e.g., Sibson, 1985). Changes in the orientation of the principal stress directions, however, can stimulate low-angle faulting (Lister and Davis, 1989). Flexural stresses, e.g., in form of normal stresses at the base or top of crustal columns, like an isostatically uncompensated Moho bulge, may produce dipping shear stress trajectories (Spencer and Chase, 1989). Numerical modeling by Spencer and Chase (1989) indicates that a high ratio of flexural to (horizontal) extensional stress favors initiation of low-angle normal faults. The absence of currently active low-angle faulting in the Basin and Range region could be explained (Spencer and Chase, 1989) by lower flexural stresses due to flattening of the Moho (Klemperer et al., 1986).

Thermal modeling has shown that extensive magma generation as a result of adiabatic upwelling during simple shear continental rifting is very unlikely (Buck et al., 1988; Latin and White, 1990). Therefore these researchers suggest that lithospheric simple shear cannot explain observed magmatism in the actively extending Red Sea (Buck et al., 1988) and in the previously extended North Sea (Latin and White, 1990).

Pure Shear Model

In the symmetric 'pure shear' model stretching of the continental lithosphere is accompanied by a similar amount of lithospheric thinning (McKenzie, 1978a, Gans, 1987). Detachment faults are interpreted as being ancient brittle-ductile transitions within the crust (Fig. 2.1.2b), where stretching and thinning of the upper crust finally exposed these transitions. Brittle extension in the upper crust, as seen in the intensely fractured and faulted upper parts of metamorphic core complexes, has been accompanied by uniform ductile stretching of the underlying parts of the lithosphere (e.g., Gans et al.,

1985; Gans, 1987). Strong local variations in the magnitude of extension (Gans, 1987), in conjunction with an uniform Moho depth of 30-35 km (Klemperer et al., 1986) in the eastern Great Basin of the Basin and Range province, can be explained by lateral flow of lower crustal material that is decoupled from the upper crust (Gans, 1987). However, abrupt changes in metamorphic grade across the detachment and generation of mylonites prior to brittle deformation in the upper plate as has been observed in many metamorphic core complexes (e.g. Crittenden et al., 1980) is difficult to reconcile within the framework of an uniformly stretching lithosphere.

Pure Shear vs. Simple Shear

According to the 'simple shear' model, continental extension takes place primarily as the result of relative movement on low-angle normal faults and shallow dipping shear zones. This implies and requires large displacements across the detachment faults and abrupt changes of the metamorphic grade across the fault are expected. The 'pure shear' model, however, predicts small relative displacements across the 'detachment fault' and no abrupt changes in the metamorphic grade. Large displacements and abrupt changes in metamorphism in the 'pure shear' model can be expected only if the uplifted ancient brittle-ductile transition is deformed brittely.

The simultaneous operation of steep arrays of deeply biting normal faults and of gently dipping detachment faults of large areal extent seems to be impossible in a spatially limited region. Detachment faults with gentle dips prevalent over large distances of 40 km and more would be cut and made inactive by steep arrays of deeply biting ('domino-style') planar faults. On the other hand, active detachment faults preclude the simultaneous existence of steep sets of deeply biting planar faults.

Role of Isostasy

The importance of isostatic response of footwall unloading to the geometry of normal faults has been recognized only recently (e.g., Buck et al., 1988; Buck, 1988; Wernicke and Axen, 1988; Roberts et al., 1991). From numerical modeling Buck et al. (1988) and Buck (1988) find that motion along a high-angle planar fault, which cuts through the entire brittle part of the crust, causes flexural rotation of the uppermost part of the fault due to local isostatic compensation. Significant rotation results in abandonment of the upper part of the fault, which is then replaced by a new steep planar fault (Buck, 1988).

Successive extension causes further rotation of the abandoned parts until a very gently dipping inactive detachment is formed (Buck, 1988).

2.1.3 Evidence from Large Normal Faulting Earthquakes

Rocks in the upper crust can store stresses and strains until a certain threshold is reached and then they break in a brittle fashion. In deeper parts of the Earth, increase of temperature prevents rocks from breaking and they show a creeping and flowing behaviour. Earthquakes are expressions of the brittle behaviour of the upper crust and tectonic motions are usually associated with large earthquakes. Usually a large part of these motions is accommodated by faulting and a smaller part by steady state creep or other means of energy dissipation (e.g., see Jackson and McKenzie, 1988; Ekström and England, 1989). The dynamics of continental extension can therefore be investigated using data obtained from earthquakes.

Since large normal faulting earthquakes rupture through the whole brittle part of the crust, data from these earthquakes potentially contain the information about the geometry and curvature of the fault, the occurrence of detachment type faulting, and the depth extent of the ruptures in areas of continental extension. The distribution of aftershocks and the focal mechanisms of aftershocks and mainshocks argue against seismogenic detachment faulting within the brittle crust. Doser (1987) found a normal faulting earthquake in the high Andes with a relatively low-angle (30°) fault dip, but this is still too steep for a detachment type fault. Focal mechanisms of normal faulting earthquakes do not show gently-dipping nodal planes as would be required for detachment faults (e.g. Fig. 1 in Jackson and White, 1989; Fig. 4 in Doser and Smith; 1989).

Based on the dip of surface ruptures and focal mechanisms obtained from first motions, it has been deduced that faulting for the 1954-1959 Rainbow Mountain-Fairview Peak-Dixie Valley earthquake sequence, the 1978 Thessaloniki, and the 1981 Corinth main shock of February 24 occurred on approximately planar high-angle normal faults (Doser, 1985; Eyidogan and Jackson, 1985). First motion focal mechanisms contain information about fault geometry at the onset of faulting at the hypocenter, whereas focal mechanisms derived from waveform analysis of long-period seismograms describe the average geometry (centroid). For large earthquakes with finite spatial extent, hypocenter and centroid are usually not located at the same position and their fault plane solutions may differ if the faulting mechanism undergoes variations during the rupture. This difference was not recognized in many of the previous studies that used results of

centroidal models to argue about the normal fault geometry thus making their results less conclusive.

Okaya and Thompson (1985) combine seismic reflection, gravity and local seismicity data with results obtained from first motion and waveform analysis to deduce a planar steeply dipping fault geometry for the 1954 Dixie Valley earthquake in accordance with Doser (1986).

The first more extensive investigations concerning the down-dip fault geometry of a normal faulting earthquake have been done for the 1983 Borah Peak, Idaho earthquake in the Basin and Range region. Stein and Barrientos (1985) and Barrientos at al. (1987) inverted geodetic observations and concluded that the fault is planar. Inversion of teleseismic body waves was utilized by Nábělek (in press) to study the down dip geometry of the mainshock rupture. The approach of subdividing the fault along its width and inverting P and SH waves for fault dip and seismic moment release for each subdivision is very similar to the approach presented here. The results of Nábělek (in press) preclude significant listric curvature of the fault or coseismic slip on a detachment at the base of the fault.

For the Alasehir, 1969 and Gediz, 1970 earthquakes, which will be investigated in this thesis, Eyidogan and Jackson (1985), however, observed large arrivals in later parts of the P wave seismograms. They interpreted these arrivals as being due to 'slow' slip on a very low-angle detachment, deep in the semi-brittle crust. Although their model explains the P wave waveforms nicely (but not their amplitude), the SH waves, which were not incorporated in the work by Eyidogan and Jackson (1985), cannot be fit with their model (see Figure 6.1.10, and 6.1.16). To cite these late P wave arrivals as evidence for detachment faulting may therefore be wrong. As will be shown later these arrivals are most likely due to some unmodeled effects of the crustal structure (also Nábělek, 1986).

The sparse number of results obtained so far indicate that seismogenic normal faults are steeply dipping and planar across the entire brittle zone of the crust.
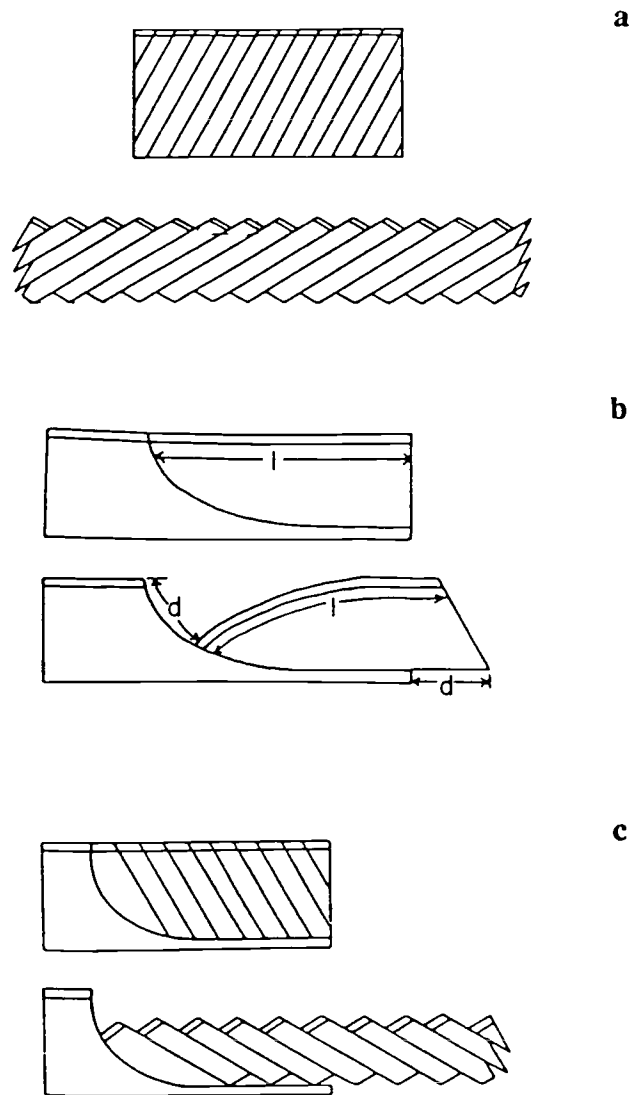
Figure 2.1.1 Models of upper crustal extension. a) coeval domino-style faulting of planar fault blocks, b) listric normal faulting with reverse drag (after Hamblin, 1965), c) listric 'master' fault bounding a family of planar fault blocks (from Wernicke and Burchfiel, 1982).

Simple Shear

Crust

Mantle Lithosphere

Asthenosphere

Pure Shear

Crust

Mantle   Lithosphere

Asthenosphere
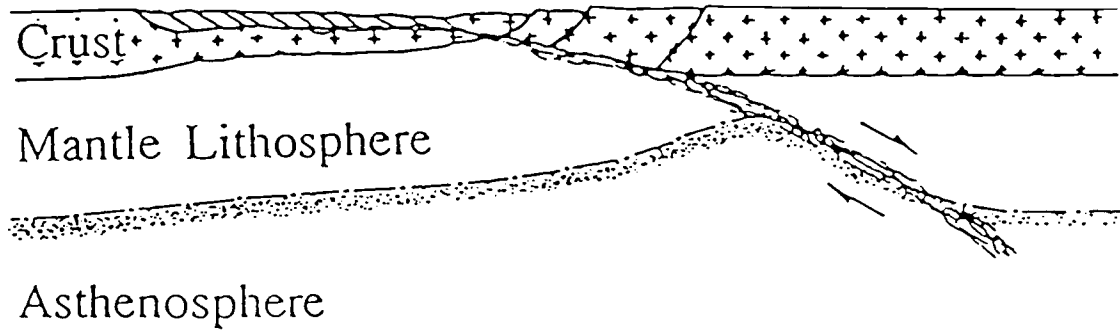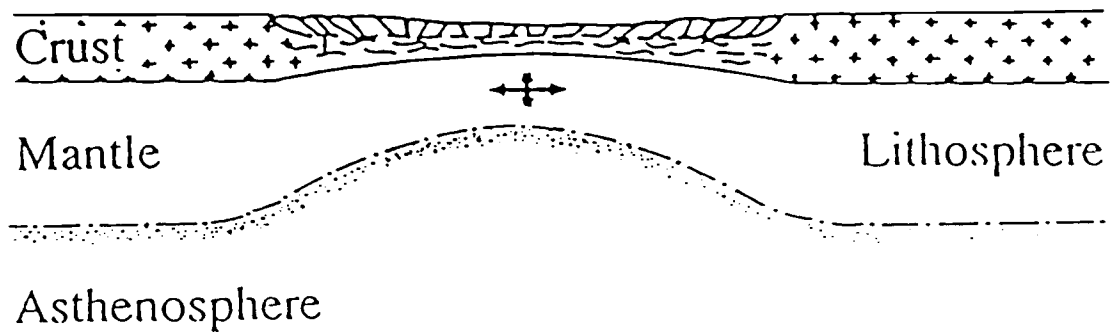
Figure 2.1.2   Two end-member models of continental extension. a) asymmetric simple shear (after Wernicke, 1985) and b) symmetric pure shear (from Buck et al., 1988).

2.2 Nature of the Brittle-Ductile Transition in Continental Crust

Rock mechanical experiments show that the strength of rocks changes with temperature and pressure (depth). Faulting takes place in an upper brittle-behaving part of the continental crust and the lower part deforms ductile (Sibson, 1982, 1984; Meissner and Strehlau, 1982; Chen and Molnar, 1983). Figure 2.2.1 shows a schematic sketch of variations of strength with depth within the crust for a simple two layer rheological model. In the brittle regime, Byerlee (1968) found that the frictional resistance to sliding is independent of rock type or displacement. Therefore a linear relationship exists between the shear stress, τ, and the effective normal stress, σ_n, at which friction is overcome on fractures. The effective normal stress, σ_n, depends on the applied stress and pore pressure. For constant pore pressure, σ_n is basically a linear function of pressure (or depth).

At greater depths, temperature effects increase and the plasticity of the rocks has to be considered. The transition from brittle to ductile behaviour occurs where the flow laws of quartzofeldspathic crust (see e.g. Brace and Kohlstedt, 1980; Sibson, 1982, 1984; Strehlau, 1986) intersect the linear brittle failure criteria. Sibson (1984) correlates the depth of ceasing microseismic activity to the onset of greenschist metamorphic conditions at about 300°C. Chen and Molnar (1983) estimate a temperature of 250-450°C at the transitional region from the depth of the deepest crustal intracontinental earthquakes. The rock strength below the transition is believed to decrease rapidly and stress levels needed to generate earthquakes in the lower crust cannot accumulate (Chen and Molnar, 1983). The depth of the transition depends on the geothermal gradient, rock composition and pressure, but pore-pressure and strain-rate also play a role (e.g. Sibson, 1984). High temperature gradients, increased quartz to feldspar ratios in crustal composition, increased pore pressures and decreased strain rates, although of different relative importance, will shift the transition to shallower depths (Brace and Kohlstedt, 1980; Sibson, 1982, 1984). Due to heterogeneity in composition of the crust, a gradual passage from dominating friction law to quasi-plastic high-temperature steady state flow can be expected (e.g. Sibson, 1984; Strehlau, 1986).

Seismological evidence of an aseismically deforming lower crust comes from depth distributions of microearthquake activity, large earthquakes and their aftershocks. Seismicity in the western United States in areas of relatively high heat flow is mainly confined to the upper 12 to 15 km of the crust (Sibson, 1982, 1984; Chen and Molnar, 1983), with exceptionally shallow activity ($\leq$ 5 km) in geothermally active areas (Sibson,

1982, 1984). Hypocenters of large earthquakes in continental crust are concentrated in the upper 12-16 km with a significant decrease in occurrence in the uppermost few kilometers and below approximately 16 km (Chen and Molnar, 1983; Jackson and White, 1989; Doser and Smith, 1989).

Based on observed nucleation depths or numerical modeling, several scholars (e.g , Sibson, 1982, 1984; Das and Scholz, 1983; Smith and Bruhn, 1984) have postulated that large earthquakes preferentially nucleate close to the brittle-ductile transition. A numerical model of crack propagation by Das and Scholz (1983), for example, shows that ruptures can only propagate (and develop into a large earthquake) when they nucleate in a region where the fault possesses high frictional strength. This can be explained within the concept of an elastic quasi-plastic rheology used to describe the strength properties of the continental crust: the shear resistance of the rocks reaches a maximum at the base of the seismogenic zone where the highest concentrations of strain energy can accumulate (Brace and Kohlstedt, 1980; Sibson, 1982). It has also been suggested, for various reasons, that large earthquakes are able to dynamically rupture into the more ductile lower layer (e.g. Das, 1982; Eyidogan and Jackson, 1985; Strehlau, 1986; Scholz, 1988; Jackson and White, 1989); e.g., suddenly increased strain-rates in otherwise ductilely deforming rocks may cause brittle failure.

Since a sharp transition from brittle to ductile behaviour cannot be expected for the heterogeneous materials comprising the Earth's crust, the concept of a simple brittle-ductile transition may not be able to explain the observed rather sharp cutoff in the hypocenter depths of earthquakes. A broad transitional field of semi-brittle behaviour between the onset of quartz plasticity at around 300°C and feldspar plasticity at around 450°C, the main constituents of the crust, is probably marked by a complex interaction of brittle cataclasis and ductile dislocation flow (Strehlau, 1986; Scholz, 1988). Based on earthquake data, experimental work (Stesky, 1978), and theoretical work on friction laws by Tse and Rice (1986), Scholz (1988) (Figure 2.2.2) proposes that earthquakes can nucleate only in a region of unstable, velocity-weakening friction, roughly in the depth range of a few km depth down to the onset of quartz plasticity. A stable, velocity-strengthening frictional behaviour prevents nucleation in the uppermost kilometers of the continental crust due to the presence of hydrous minerals and in the semi-brittle region due to increased temperature that causes some rock components to become ductile.

According to this model, it is not possible for earthquakes to nucleate in either the semi-brittle field, marked by stable frictional behaviour, or within the thin stable surface region. Large earthquakes, however, can dynamically rupture into these regions. Surface ruptures accompany many large crustal earthquakes, indicating that the upper

frictionally stable region can be easily penetrated. The evidence for ruptures penetrating into the stable region in the brittle-ductile transition is limited.

As shown by Nábělek (in press), the aftershock distribution and the rupture extent of the main shock of the Borah Peak, 1983, earthquake are consistent with the friction rate models as suggested by Tse and Rice (1986) and Scholz (1988). Aftershocks are concentrated at a depth of 4 to 12 km, whereas the mainshock rupture extended from the free surface down to at least 16 km depth.

A part of this thesis will be devoted to further investigate the validity of this friction-rate model for the Thessaloniki, 1978, the Corinth, 1981 and the Kalamata, 1986 earthquakes.
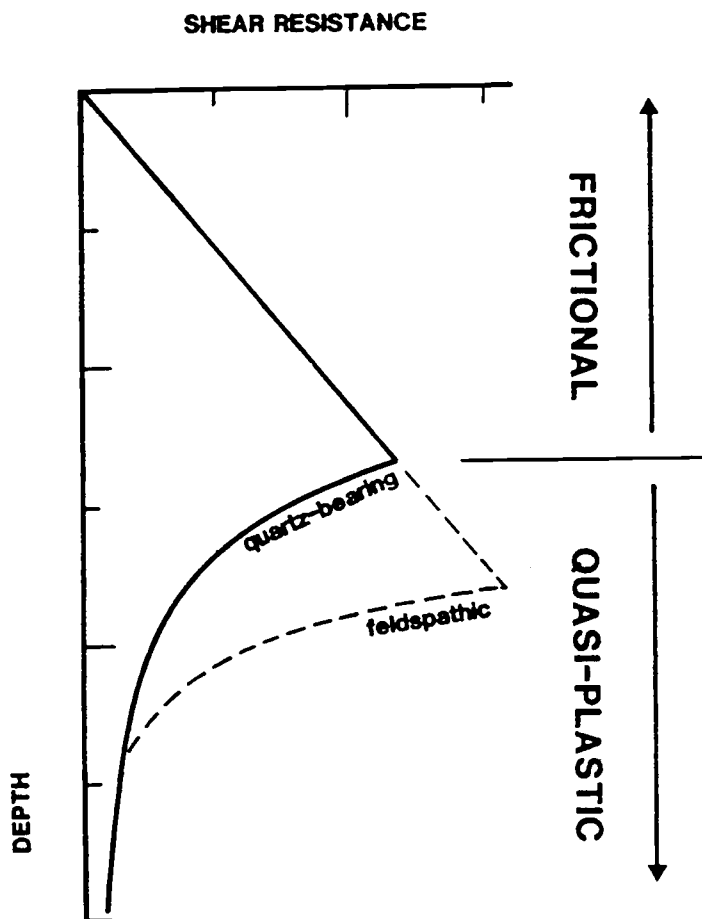
Figure 2.2.1 Simple two layer model of the variation of shear resistance (strength) with depth. Upper part undergoes brittle failure (Byerlee's law), lower part quasi-plastic flow (from Sibson, 1984).
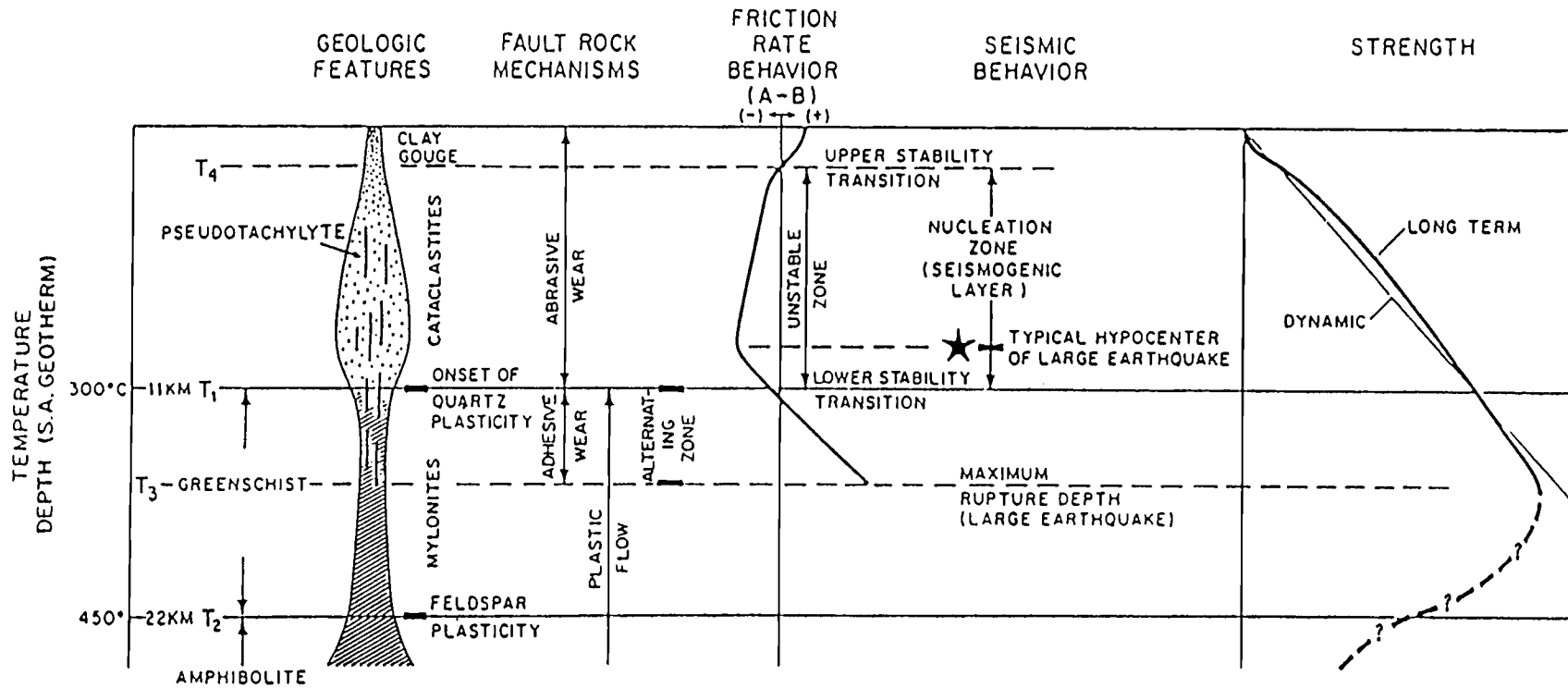
Figure 2.2.2 Fault zone model of Scholz (1988) illustrating friction-rate behaviour, seismic behaviour, strength, and other geological features as a function of temperature and depth (based on a geotherm model of San Andreas fault).

3. Body Wave Inversion Method

Body wave inversion techniques for P- and S-wave phases are now widely used (e.g. Langston, 1976; Ward, 1980; Kikuchi and Kanamori, 1982; Nábělek, 1984; Ekström, 1987) in order to obtain estimates of the focal parameters and the seismic moment, as well as to gain a better understanding about the temporal and spatial aspects of earthquake ruptures.

The body wave inversion technique used in this study and its theoretical background are described in detail by Nábělek (1984). The average (centroidal) point source parameters of the seismic source are extracted from the data by fitting waveform and amplitude information of the observed P and SH waves with synthetic seismograms in a least square sense. The source orientation is expressed in terms of a double-couple mechanism with strike, dip, rake (following the conventions by Aki and Richards, 1980), and scalar seismic moment; the centroid depth of the source, and the far-field source time function depicting the moment release rate with time are also estimated. Source finiteness effects (propagating ruptures) can be investigated using a generalized Haskell model, and earthquakes consisting of multiple events can also be modelled.

3.1 Forward Problem

3.1.1 Mathematical Description of Seismic Sources

Shallow earthquakes are caused by sudden material failure of the rocks to withstand applied tectonic stresses, resulting in a temporary breakdown of the linear stress-strain relations. Failure is usually associated with a pure shear dislocation along a relatively planar surface. The elastic rebound of the medium generates seismic waves.

The displacement, $u_n(\underline{x},t)$, at point, $\underline{x}$, and time, t, in the n-th direction, using a point source approximation, is directly proportional to the seismic moment tensor M_{pq} (e.g., see chapters 3 and 4 in Aki and Richards (1980) for derivation):

$$u_n(\underline{x},t) = \int\int_{\Sigma} m_{pq}(\underline{\xi},t)\, d\Sigma * \frac{\delta G_{np}(\underline{x},t,\underline{\xi},0)}{\delta \xi_q} = M_{pq} * G_{np,q} \qquad (3.1)$$

where '*' denotes convolution in the time domain, $G_{np}(\underline{x},t-\tau,\underline{\xi},0)$ is the elastodynamic Green's function describing the displacement in the n-th direction at $(\underline{x},t)$ due to a unit body force in the p-th direction at $(\underline{\xi},\tau)$. Σ is the fault surface. The moment tensor

density for a displacement source is given by $m_{pq}=[u_i(\xi,\tau)]c_{ijpq}v_j$, where $[u_i(\xi,\tau)]$ is the slip in the i-th direction on the fault, c_{ijpq} is the elastic tensor relating stress and strain, and v_j is the fault normal. The displacement on the fault uniquely determines the displacement everywhere. The tensor m_{pq} is symmetric because net force and net torque on the Earth vanish. For a shear dislocation, M_{pq} is a double-couple that can be expressed in terms of four independent parameters: the strike, dip, rake, and the seismic moment, depicting source orientation and strength. Only constrained double-couple solutions for M_{pq} were investigated in this thesis.

For far field observations in an elastic, homogeneous, isotropic, and infinite medium, the Green's functions take on a relatively simple form (e.g., see chapter 4.3 in Aki and Richards, 1980) and the far-field displacement becomes

$$u_n(\underline{x},t) = M_{pq} * G_{np,q} = \frac{\gamma_q}{c} \dot{M}_{pq} * G_{np} \qquad (3.2)$$

where the dot denotes the time derivative, c is either α or β depending on the wavetype under consideration, and γ_q are the direction cosines pointing from the source to the receiver. The far-field displacement is proportional to the first time derivative of the moment tensor, therefore a step like slip function at the source will result in a pulse like response at the receiver.

If all elements of M_{pq} share the same time history, $S(t)$, equation (3.2) may be rewritten as

$$u_n(\underline{x},t) = [\Omega(t) * G_{np}] M_{pq}(\underline{\xi}) \qquad (3.3)$$

where $\Omega(t) = \dot{S}(t)$ is the far-field source time function. For an axially symmetric medium, the displacement can be separated into P-SV and SH contributions (see Ward, 1980). The moment tensor components in terms of strike (ϕ_s) , rake (λ) , dip (δ) , and moment (M_o) of a double couple source are given in Aki and Richards (1980).

3.1.2 Green's Function in the Earth

At teleseismic distances ($\Delta \geq 30°$), body waves travel steeply through the inhomogeneous crustal and upper mantle parts of the Earth and most of the lateral movement is restricted to the homogeneous lower mantle. P and S waves at teleseismic distances are well separated from each other and from other seismic phases allowing

independent treatment. The Green's function is composed of several contributions (Langston and Helmberger, 1975):

$$\underline{G}(t) = \underline{C}^r(t) * M(t) * \underline{G}^s(t) \tag{3.4}$$

where $\underline{G}^s(t)$ is the displacement of the respective wave type emerging at the bottom of the crust in the source region. $\underline{C}^r(t)$ is the crustal response in the receiver region. $M(t)$ is the mantle response. Since no new phases are generated in the mantle only the effects of anelastic attenuation, geometrical spreading, and time delay are included. Uncertainties in the attenuation operator mainly affect the source duration and seismic moment and not the estimates for the orientation and depth (e.g. Nábělek, 1984; Ekström, 1987).

Travel paths for teleseismic body waves are relatively well known, and accurate estimates for the Green's function can be obtained either by the ray approximation (e.g., Langston and Helmberger, 1975) or, as used in Nábělek (1984), the reciprocity theorem (e.g., Gupta, 1967; Bouchon, 1976). The ray parameter for all direct, reflected and converted phases at teleseismic distances is approximately constant and therefore, the total crustal response function for waves emanating from a vertically stratified source region can be constructed from 4 contributions (2 in SH case) representing up- and down-going P and S waves (S waves in SH case), respectively:

$$G_{np} = G_{np}^{\uparrow P} + G_{np}^{\downarrow P} + G_{np}^{\uparrow S} + G_{np}^{\downarrow S} \tag{3.5}$$

The individual responses, G_{np}^i, entering the half-space are composed of the sum of all crustal interactions of the parent ray. In Nábělek's (1984) routine the Green's functions are calculated in the frequency domain using propagator matrices. The pseudo-reflectivity method (e.g., Bouchon, 1976) provides the contributions from all reflected and converted phases, without the need of specifying each phase explicitly as is necessary in the ray method. The free surface phases pP, sP, pS, and sS (sS in the case of SH waves), due to their delays with respect to the direct P and S phases, contain the information about the centroid depth. Synthetic seismograms can be aligned either according to general travel-time distance curves or based on observed first arrivals. When possible, I used the later method, reading the arrival times from short-period seismograms. After convergence to an intermediate solution, the seismograms were allowed to realign if a better cross-correlation could be found.

Teleseismic body wave data were used in this study because the Green's functions are well known and the frequency content of the data allows to look at the fault geometry. Strong motion and regional data are more severely affected by path related effects and a careful calibration of the travel path has to be carried out for each earthquake separately. Surface waves are also very path dependent and, moreover, lack the depth resolution for shallow earthquakes and the high frequencies necessary to investigate the fault geometry.

3.2 Procedural Steps

For all earthquakes included in this study a stable and reliable point source estimate was sought first. For the smaller events, which ruptured only a small area and did not produce surface faulting, the point source usually provided a good fit to the data. In case of additional waveform complexity, more complex source descriptions were tested; this will be described in detail for each individual earthquake. The large events (Alasehir, Gediz and Thessaloniki mainshock, and Corinth sequence), which ruptured the entire seismogenic width of the crust, were further investigated to deduce information about their fault geometries and the possibility of seismic slip along subhorizontal detachment surfaces. Depth extent of earthquake ruptures with respect to the depth distribution of the aftershock sequences was examined for events where high-quality aftershock locations from local networks were available (Thessaloniki, Corinth sequence, and Kalamata). The steps to investigate fault geometry, detachment slip, and depth extent will be described subsequently.

Point Source

The centroidal description of the seismic source in terms of its double-couple mechanism, centroid depth, seismic moment, and source time history comprises the first step (Figure 3.2.1). It is important to obtain a reliable and stable estimate of the 'true' point source solution since parameters from this estimated centroid will be used in the subsequent steps.

Detachment Faulting

In the next step, a shallow dipping source at the base of the seismogenic layer (assumed to be at twice the centroid depth) was added to the centroidal solution (Figure 3.2.1) to find indications for detachment faulting at depth. The strike derived from the point source solution was assigned to this deeper source and a pure normal faulting mechanism was assumed (rake: 270°). Dips of 0° and 10° were used to mimic a shallowly dipping detachment surface. To find possible contributions due to a detachment source at later parts of the seismogram, a long duration was a priori assigned to the source time function. The distribution and seismic moment of the detachment source were inverted for, and all other parameters for the centroid solution and the detachment source were held fixed.

Down-Dip Fault Geometry

To determine the down-dip geometry, three sources are distributed along the width of the fault, using the parameters of the average centroidal solution (Figure 3.2.1). Three sources were chosen in order to mimic a finite fault and at the same time to avoid overparameterization. Large earthquakes rupture the entire width of the seismogenic zone and the centroid depth gives an estimate of the average depth of faulting; therefore, the subsources were placed at 1/3, 3/3, and 5/3 of the point source centroid depth. The strike of the centroidal solution was assigned to each subsource. Time delays, horizontal separations and azimuths of the subsources were calculated from their depths assuming that the fault surface is planar, and has the strike and dip of the centroid. It will be shown in Chapter 5 that the exact horizontal locations are not crucial. Since the exact rupture speed and, therefore, the timing are not known, it was decided to use a fast rupture speed of $v_r = 3.1$ km/s to calculate the time delays. If the delays are too long, then arrivals from some parts of the fault may be attributed to the wrong subsource if the subsource at the appropriate depth has not been activated, and the results may be biased. On the contrary, if a subsource of the model is activated earlier than required by the data, the first elements of the source time function will be zero or small and the results are less likely to be biased.

The three subsources subdivide the point source solution and therefore the moment tensor sum of the subsources was constrained to reproduce the estimated point source moment tensor. It was assumed that the seismic moment was evenly distributed among the subsources. For a given strike and dips of the subsources, appropriate values for rake and seismic moment had to be found, in order to keep the centroidal parameters the same as found for the point source model. This was done numerically. For pure normal faulting earthquakes (rake: 270°), the rake of all three subsources will always remain at 270°; small strike-slip components (±15°) cause the rakes of the shallow and deep subsource to change by only 6° for fault curvatures of 60°, which is often within the uncertainty of the estimated centroidal rake. The effects of fault curvature on the seismic moments are more important, however, and are analogous to vector addition where the direction of the vectors influences the absolute value of the sum.

In the first set of tests, only the distribution of the seismic moment of each subsource was allowed to vary during the inversions, and all other parameters, e.g., the seismic moment and dip of each subsource, were constrained. To be able to describe differences in fault geometry for each earthquake more quantitatively, fault models with different

amounts of listricity (concave and convex upwards) were tested, and the results were later compared statistically for significance (see section 3.4). This approach leaves the least number of free parameters and allows simple statistical comparison. It was also assumed that the rupture nucleated at the bottom of the seismogenic layer and propagated upward, which is in agreement with rock mechanical models and numerical models of crack propagation (e.g. Sibson, 1982, 1984; Das and Scholz, 1983). This separates contributions from different subsources at the receivers and therefore geometrical effects should be more easily detectable than for ruptures nucleating from the center and moving upward and downward at the same time.

Ruptures propagating bilaterally upward and downward were investigated for the Gediz main shock where the width of the fault deduced from the centroid depth was relatively wide. For small widths, the sources may severely overlap and the phases which radiate from different parts arrive almost simultaneously at the receiver sites. Although this style of rupture is less likely, it can not be excluded.

The parameterization assumes even distribution of the seismic moment along the width of the fault. The strength (M_0) of the centroid is a weighted average of the seismic moment released over the finite fault and, since the large earthquakes of this study generated surface faulting, the moment release at shallow depths has to be accompanied by moment release below the centroid if the solution is not biased. In this test I simply try to determine what rupture geometry (listric or planar) most closely resembles the earthquake fault. Since all models which are compared contain the same assumption, the statistical tests should be valid.

It was not sought to find the 'best' model of the fault geometry, since solutions derived from a set of many free parameters are probably highly non-unique and parameter trade-offs may be severe. However, a second set of tests was performed where the dip, distribution and amount of the moment release for each subsource were allowed to vary. Different starting models (planar, concave and convex with 40° overall fault curvature) were used to investigate the stability of the results. The dip estimates of the shallowest subsource, representing the upper part of the fault, became in some cases unstable and inconsistent with surface observations, and the estimates for this subsource have to be disregarded. The results of these tests will not be viewed as the final answer concerning the fault geometry, but will be discussed in conjunction with other evidence.

Depth Extent of Rupture

The depth extent of the main-shock faulting was investigated in a next set of tests. Five point sources were placed at 1/3, 3/3, 5/3, 7/3, and 9/3 of the estimated centroid depth. The source orientation found from the point source was used for all subsources, therefore resembling a planar dipping fault surface. This geometry is justified by the preceding investigations of the fault geometry for the Thessaloniki and Corinth earthquakes. For the smaller Kalamata earthquake this geometry was used without precise knowledge, however, the results from the other events support this choice. The subsources were separated in space and time using the geometrical constraints of the fault plane and by assuming a fast rupture propagation speed of 3.1 km/s (≈ 0.9 v_β). It was assumed that the rupture nucleated within the brittle crust at the subsource closest to the brittle-ductile transition and propagated up- and downward bilaterally. The data were inverted for the seismic moment and time function of each subsource. To better estimate the depth below which no significant moment release can be detected, the model was 'perturbated' around the starting model by increasing or decreasing the depths of the subsources. The depth of the deepest source was varied in 450 m steps and the sources were kept equally spaced. The depth extent of the main shock rupture is then assumed to be represented by a relatively sharp drop of moment release at a certain depth with only very minor possible contributions from deeper parts.

Three Inversion Steps
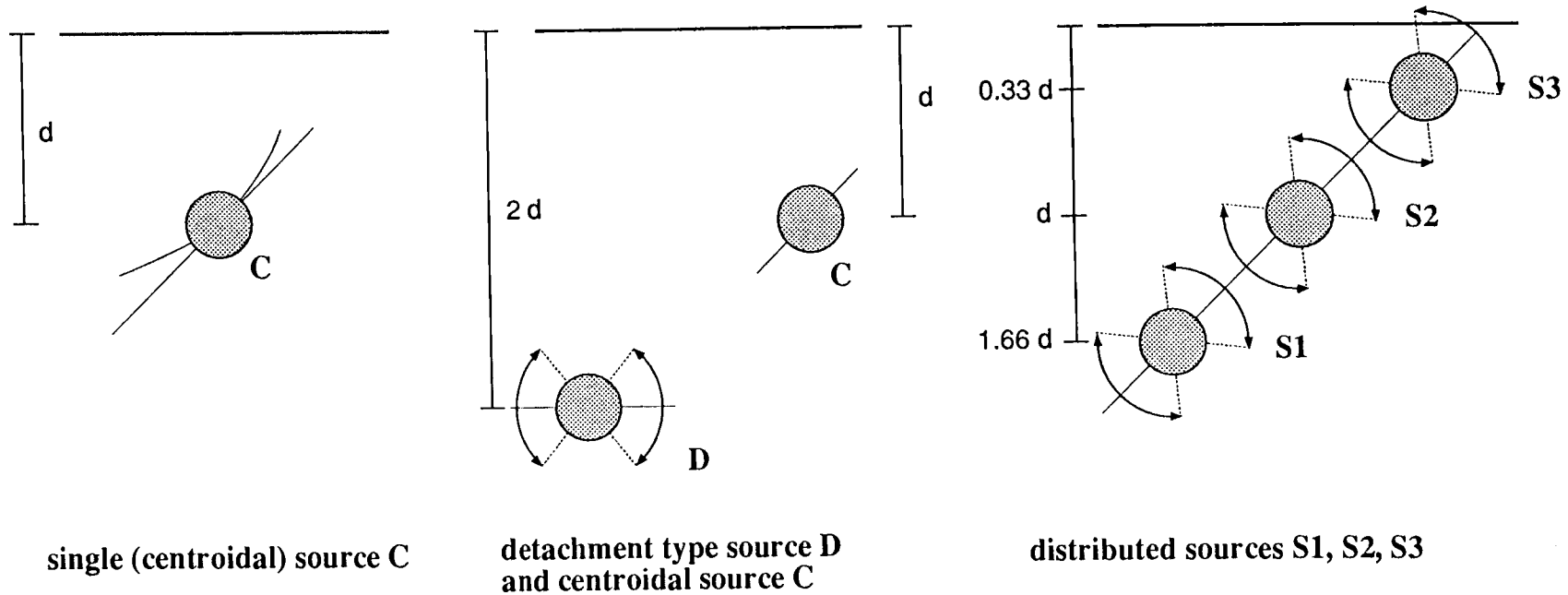
single (centroidal) source C

**detachment type source D
and centroidal source C**

distributed sources S1, S2, S3

C: all source parameters can vary

D: seismic moment, and source
time function can vary
C: parameters fixed to point
source solution

1. S1, S2, S3: source time function
can vary
2. S1, S2, S3: dip, seismic moment, and
source time function can vary

Figure 3.2.1   Schematic sketch illustrating the procedural steps used to infer the fault geometry. 1: point source solution. 2: detachment source. 3: a) dip (geometry) fixed, b) dip allowed to vary.

3.3 Inverse Problem

In section 3.1, the steps to calculate synthetic seismograms radiating from a source in a layered medium have been outlined. Information about the source parameters can be retrieved from the observed data by comparing them with synthetically calculated seismograms. In the presence of noise, uncertainties in some medium properties, and due to application of approximations, however, a perfect fit to the data is impossible. An elegant and relatively simple way to solve for the source parameters is to pose an inverse problem where the differences between the data and the synthetics are minimized; Nábělek's (1984) inversion routine minimizes the sum of the squared residuals. Since the seismograms depend in a non-linear way on the source parameters, an iterative inversion around a linearized model is used to minimize the misfit. Instabilities in the solution due to uncertainties in the model parameters or due to overparameterization can be reduced by introducing soft or hard constraints. Throughout this thesis a double-couple constraint has been applied on the moment tensor. From physical considerations, it is required that the moment release is non-negative, therefore a positivity constraint has been imposed on the elements of the source time function. In some instances, the parameters found from the best point source approximation for an earthquake were imposed on more complicated source parameterizations (e.g. propagating ruptures, multiple events) and held fixed to reduce the number of free variables and to avoid unwanted trade-offs between parameters. This should provide more stable result. If the fit is still not acceptable, some of the constraints may be released and the influence of the increased number of elements in parameter space on the match can be investigated.

The main goal of this study was to investigate the fault geometry of continental normal faulting earthquakes. To retrieve information about the down-dip behaviour of the fault I wanted to test different fault geometries but at the same time wanted to keep the number of free parameters at a minimum. Therefore, a constraint allowing only the distribution of the seismic moment to change while keeping the sum of the contributions from all source time function elements at a specified value has been added to the inversion routine.

Maximum Likelihood Inverse

For normally distributed data, $\underline{d}$ (in this case a discrete time series of seismogram amplitudes), and model (source) parameters, $\underline{p}$, the likelihood that the model, $\underline{m}(\underline{p})$,

matches the data, $\underline{d}$, and also observes a priori estimates (soft constraints) of the model parameters, $\underline{p}_o$, is proportional to $e^{-1/2X^2}$ with

$$X^2 = [\underline{d} - \underline{m}(\underline{p})]^T \underline{\underline{C}}_{d_o}^{-1} [\underline{d} - \underline{m}(\underline{p})] + [\underline{p}_o - \underline{p}]^T \underline{\underline{C}}_{p_o}^{-1} [\underline{p}_o - \underline{p}] \qquad (3.6)$$

where the uncertainties in the estimated covariance matrices of the data, $\underline{\underline{C}}_{d_o}$, and parameters, $\underline{\underline{C}}_{p_o}$, are assumed to be independent. Maximizing the likelihood that the model matches the data in the presence of some a priori constraints is equivalent with minimizing X^2 which is then equivalent to the well known least squares problem.

A general treatment of the problem involving soft constraints can be found in Nábělek (1984). The further formulations will be geared toward the problem of constraining the moment while allowing its distribution to vary freely. Therefore I will replace the general term describing a priori estimates by the 'moment constraint'

$$[M_o - M(\textstyle\sum w_i)]^T \underline{\underline{C}}_{M_o}^{-1} [M_o - M(\textstyle\sum w_i)] \qquad (3.7)$$

M_o is the a priori estimate of the seismic moment, M is the last estimate of the seismic moment (k-1th iteration step), and w_i are the weights of the i elements of the source time function, where $\sum w_i$ is equal to 1 before updating the w_i's during the kth iteration step. $\underline{\underline{C}}_{M_o}$ is a scalar and estimates the variance of M_o thus describing how precisely the seismic moment is known. The weights, $\underline{w}$, are a subset of all parameters $\underline{p}$.

Replacing the second term of equation (3.6) by expression (3.7) and minimizing equation (3.6)

$$\frac{\delta X^2}{\delta p_i} = 0 \qquad (3.8)$$

yields

$$[\underline{d} - \underline{m}(\hat{\underline{p}})]^T \underline{\underline{C}}_{d_o}^{-1} \underline{\underline{J}}(\hat{\underline{p}}) + [M_o - \hat{M}(\textstyle\sum \hat{w}_i)]^T C_{M_o}^{-1} \underline{J}(\hat{M}) = 0 \qquad (3.9)$$

$\underline{J}(\hat{\underline{p}})$ is the Jacobian with the elements $J_{ij} = \dfrac{\delta m_i}{\delta p_j}$, j being the total number of free parameters. The hat, ^, denotes the best estimate of the true parameters $\hat{\underline{p}}$. The 1 by j-matrix $\underline{J}(\hat{M})$ is given by

$$M \frac{\delta(\sum w_i)}{\delta p_j} = \begin{cases} 0 \\ M \end{cases} \tag{3.10}$$

it is 0 if p_j is not a source time function element and M if p_j is a source time function element. Since the model $\underline{m}(\hat{\underline{p}})$ is non-linearly related with the parameters $\hat{\underline{p}}$, equation (3.9) is solved iteratively for $\hat{\underline{p}}$ using a linearized form of the model [$\underline{m}(\hat{\underline{p}}) = \underline{m}(\underline{p}) + \underline{J}^T(\underline{p}) (\Delta \underline{p})$]. The improvement from the kth to the $k+1^{th}$ iteration is $\hat{\underline{p}}_{k+1} = \underline{p}_k + \Delta \underline{p}$ where $\Delta \underline{p}$ can be found from equation (3.9)

$$\Delta \underline{p} = [\underline{J}_k(\underline{p})^T \underline{\underline{C}}_{d_o}^{-1} \underline{J}_k(\underline{p}) + \underline{J}_k(M)^T C_{M_o}^{-1} \underline{J}_k(M)]^{-1}$$

$$\{ \underline{J}_k(\underline{p})^T \underline{\underline{C}}_{d_o}^{-1} [\underline{d} - \underline{m}(\underline{p}_k)] + \underline{J}_k(M)^T C_{M_o}^{-1} [M_o - M_k (\sum_i w_{ki})] \} \tag{3.11}$$

$$= (\underline{\underline{A}}_k^T \underline{\underline{A}}_k)^{-1} [\underline{\underline{A}}_k^T \underline{f}_k]$$

where

$$\underline{\underline{A}}_k^T = \{ \underline{J}_k(\underline{p})^T \underline{\underline{C}}_{d_o}^{-1/2} , \underline{J}_k(M)^T C_{M_o}^{-1/2} \}$$

and

$$\underline{f}_k^T = \{ [\underline{d} - \underline{m}(\underline{p}_k)]^T \underline{\underline{C}}_{d_o}^{-1/2} , [M_o - M_k (\sum_i w_{ki})]^T C_{M_o}^{-1/2} \}$$

Although the constraint on the moment is soft, I used small enough values of C_{M_o} to keep the moment effectively fixed to the a priori values.

3.4 T-test

To quantitatively investigate the significance of differences between two models, a statistical approach was chosen. Comparing the normalized variances of the entire data sets of two models provides a first order check. However, as argued by Huang et al. (1986), using a standard F-test to evaluate the differences of the overall variances of two models may be invalid, because individual data samples at each recording station may not be statistically independent. Instead of using residuals of each time sample, Huang et al. (1986) propose to use the mean square residuals of each individual station, which are assumed to be statistically independent. Huang et al. (1986) further note that the total number of degrees of freedom in the data will be underestimated by this procedure, which will result in a conservative estimate of the differences.

To compare two models A and B, the differences, d_i^{AB}, of the squared residuals of each of the N stations i [$(r_i^A)^2$ and $(r_i^B)^2$] are calculated:

$$d_i^{AB} = (r_i^A)^2 - (r_i^B)^2 \qquad i=1,...,\ N \qquad\qquad (3.12)$$

and used to test the null hypothesis $\mu^{AB} = 0$ by forming the statistic

$$t^{AB} = \frac{\mu^{AB} * \sqrt{N}}{\sigma^{AB}} \qquad\qquad (3.13)$$

where μ^{AB} and σ^{AB} are the mean and standard deviation of the set of d_i^{AB}, respectively. t^{AB} follows the one sided t-distribution with N-1 degrees of freedom. Huang et al. (1986) used a X^2 test to investigate the distribution of the individual station residuals $(r_i)^2$ and found that they generally follow a normal distribution as is required when applying a t-test. Another requirement is random sampling. Since station residuals are taken instead of residuals at each time increment this assumption is probably valid.

Statistical tables are then used to find the limiting values of t for which a certain confidence level, e.g., 90% or 95% confidence level, is reached. If this value is exceeded by the value t^{AB} obtained from the above statistic, the two models are classified as being significantly different. If however t^{AB} is smaller than t, than the models are assumed to be not significantly different.

Throughout this thesis this method has been used only to compare models with the same number and same kind of free parameters. Whenever applied to different sets of parameters for the same data, the results of the above statistic have to be used carefully

since it is expected that additional free parameters will generally improve the misfit. It is difficult to quantitatively predict the amount of improvement due to additional degrees of freedom, especially when very different types of parameters are involved.

4. Data and Data Preparation

The data set used in this study consists of the body wave parts of seismograms recorded mainly by the analogue WWSSN network; for the events since 1980 additional digital data from the GDSN network are available. The body wave inversion technique described earlier was applied to thirteen normal faulting earthquakes in the Aegean region with a moment magnitude of $M_w \geq 5.5$, which occurred between 1969 and 1986. The epicenter locations, origin times, depths, body wave and surface wave magnitudes of these events as reported by PDE (Preliminary Determination of Epicenters) and ISC (International Seismological Centre) are given in Table 4.1, and the locations are shown in Figure 4.1.

<u>Data Preparation for Body Wave Inversion</u>

Long-period seismograms from the WWSSN stations in the distance range of $30° \leq \Delta \leq 90°$ from the epicenter were hand-digitized. The digitized waveforms were interpolated to equal time intervals of 0.3 s and to 0.5 s for the Alasehir earthquake and the Gediz and Thessaloniki main shocks. The linear trend in the data was removed and the seismograms of the smaller events were generally high-pass filtered with a 3-pole butterworth filter with a cut-off frequency of 0.01 Hz. For a few stations higher cut-offs were applied. Internal consistency of the amplitudes and waveshapes of the data was checked. Some stations showed wrong polarities or wrong gains during certain time spans; this has been corrected. Stations which showed a low signal-to-noise ratio or anomalously looking waveshapes with respect to other nearby stations were rejected. In the figures, three letter codes (e.g., MAT) mark seismograms from analog stations.

Broadband seismograms formed from the digital data for the post 1980 events were added to the long-period analog data sets. For the P waves, the broadband seismograms were usually derived from long- and short-period records using a procedure similar to the one described by Harvey and Choy (1982), and the frequency response is flat with respect to ground displacement from the Nyquist period of 0.6 s to usually 50 s or 100 s period, depending on the signal strength. Only the long-period records are generally available for the horizontal components, therefore the S wave seismograms are broadband from 5 s to 50 s or 100 s period, also depending on the signal level. High-pass filtering of the broadband data was necessary due to instabilities of the deconvolutions at very low frequencies. The broadband data are much richer in high-frequencies than the long-

period data and should contain more information about the details of the rupture process. Digitally recording stations are marked by a four letter code (e.g., MAJO) in the figures.

Specifics of the data preparation are given for each earthquake individually. A good azimuthal coverage for all of the events could be achieved.

A half-space structure for the source and receiver crustal structures with a P- and S-wave velocity of 6.0 km/s and 3.46 km/s respectively and a rock density of 2.8 g/cm^3 were used throughout this study. Since most of the stations are located on hard rock sites, the receiver crustal response should be similar for all stations and it is expected that local effects at individual sites average out. Errors in the source crustal structure, however, will affect all synthetic seismograms in the same way and therefore inclusion of many stations will not diminish this effect. The half-space model for the source regions is certainly an oversimplification. However, tests with different crustal structures showed that the waveform inversion results are stable and generally insensitive with respect to different crustal structures. The estimate of the centroid depth is the most sensitive to velocities in the source region.

P and SH wave data were weighted so that the rms-amplitudes of the P and SH waves were approximately the same. This prevents the solution from being biased towards a result favoured by one wavetype.

Short-period vertical seismograms were used to determine the P wave arrival times. For the smaller earthquakes or earthquakes with an emergent beginning of moment release the accuracy of the readings was probably not better than 1 s. The first motions were checked for internal consistency with nearby stations.

First Motion Polarities

First motion polarities of P waves were read from short-period vertical seismograms whenever possible, since short-period records provide a picture of the onset of the rupture right at the nucleation point, whereas long-period records show the result of the more averaged faulting process.

For all lower hemisphere projections showing the first motion polarities, a P wave velocity of 6.5 km/s and a take-off angle of 53° for the P_n waves was assumed. Overlain on these data are the preferred fault plane solutions for each of the studied events obtained from the body wave inversion. Source orientations are given according to the conventions of Aki and Richards (1980).

Table 4.1   Reported Focal Parameters of Studied Earthquakes

	#	date	time	lat	lon	depth	m_b	M_s
Demirci	1	03/23/69	21:08:42	39.14	28.48	9	5.6	5.6
	2	03/25/69	13:21:34	39.18	28.37	23	5.6	5.5
Alasehir	3	03/28/69	01:48:30	38.59	28.45	9	6.0	6.4
Gediz	4	03/28/70	21:02:23	39.21	29.51	18	6.0	7.1
	5	04/16/70	10:42:22	39.02	29.91	31	5.5	
	6	04/19/70	13:29:36	39.03	29.76	18	5.5	5.6
	7	05/25/71	05:43:26	39.05	29.77	16	5.7	5.5
Thessaloniki	8	05/23/78	23:34:11	40.76	23.27	10	5.7	5.6
	9	06/20/78	20:03:21	40.74	23.23	3	6.1	6.4
Corinth	10	02/24/81	20:53:38	38.22	22.93	33	6.1	6.7
	11	02/25/81	2:35:53	38.13	23.14	33	5.7	6.4
	12	03/04/81	21:58:06	38.21	23.29	28.5	6.0	6.4
Kalamata	13	09/13/86	17:24:31	37.11	22.14	8	6.0	5.8

from ISC and PDE catalogues. Kalamata - hypocenter data from Papazachos et al. (1988). # - event number corresponing to Figure 4.1. time - origin time UTC (h:m:s). lat, lon - latitude and longitude in degree. depth - hypocenter depth in km.
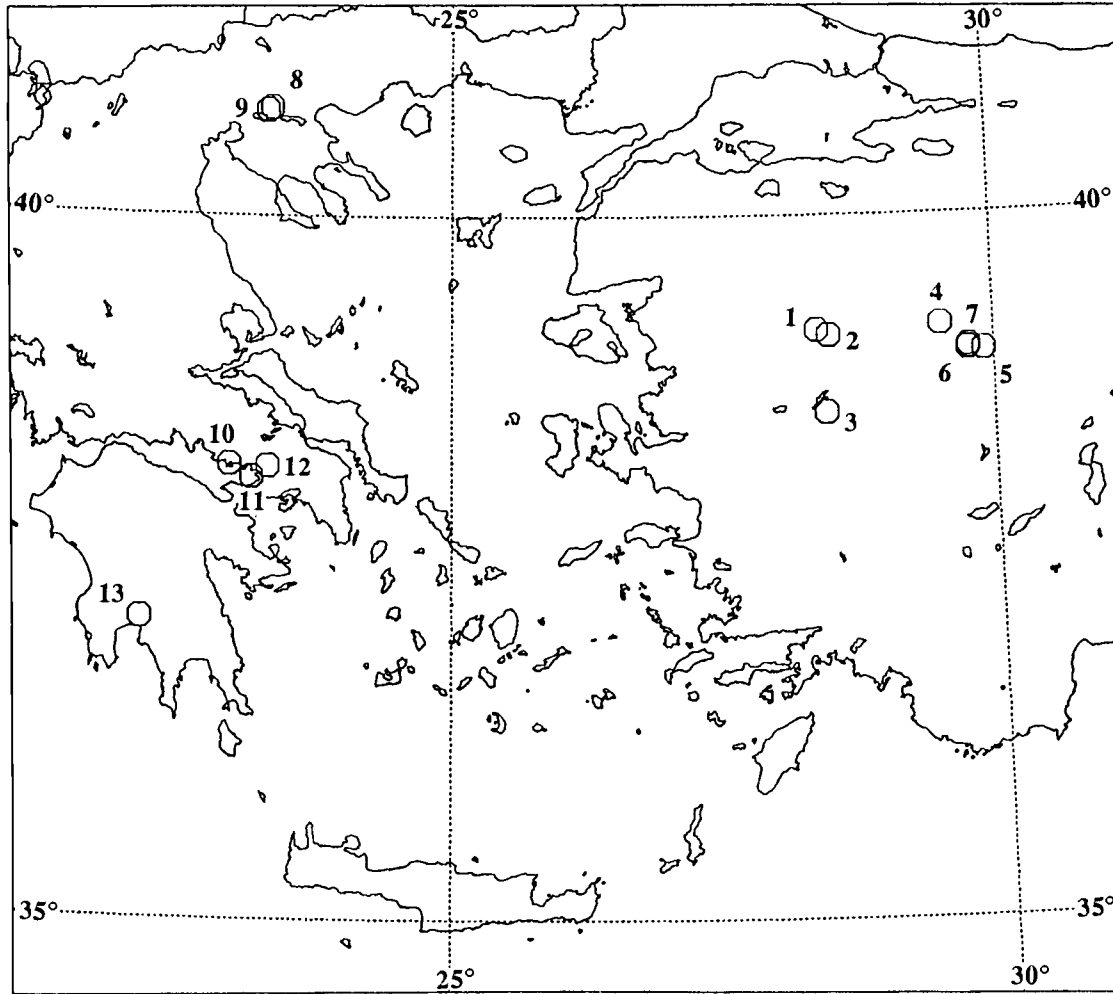
Figure 4.1   Map of the Aegean region. Octagons are epicenters of earthquakes studied in this thesis. Numbers next to the octagons refer to the earthquakes listed in Table 4.1.

5. Synthetic Modeling

Numerical modelling was performed in order to investigate the ability of the teleseismic body wave inversion method to recover correct estimates of the centroidal source parameters and the geometry of finite fault models.

Models - Synthetic Data

Two general sets of models have been used: a planar fault geometry and a listric fault geometry resembling a north-south trending pure normal fault (strike: 0°, rake: 270°) dipping towards east. In each case, the finite fault was approximated by three point sources located at 10, 6, and 2 km depth. The planar fault model consists of sources with fault dips of 45° each, whereas the listric fault model resembles an upward concave fault with dips decreasing down-dip from 65° (2 km depth) to 45° (6 km) and to 25° (10 km). For each geometry, three different sets of synthetic data were generated: one with rupture starting at the deepest source and propagating unilaterally up-dip, one where the rupture nucleates at shallow depth and propagates unilaterally downward, and a third with rupture starting in the center of the fault and the rupture front moving upward and downward simultaneously. Table 5.1 provides a list of the specific model parameters and shows the expected 'true' centroidal parameters. Tensor addition of the subsources gives the centroidal solution. In order to obtain the same centroid for the listric and planar fault models, the individual moments have to be larger for the listric than for the planar geometries. A sketch of the fault models is shown in Figure 5.1.

Noisefree broadband P, SV and SH seismograms sampled at 0.5 s time intervals were generated with Nábělek's (1984) inversion program. A simple source time history consisting of a trapezoid with 3 s rise-time, duration, and fall-time was used to calculate the synthetic seismograms for each subsource; adding these contributions provides the synthetic data of the finite faults. A half-space was used as source and receiver crustal structure for all synthetic modelling. Stations are distributed in the distance range of 30° to 90° in even azimuthal spacings of 30° on the focal sphere (Figure 5.2). The station parameters and the crustal structure used for all numerical simulations are listed in Table 5.2.

Listric and Planar Models - Effects of Curvature on Waveforms

The effects of fault curvature are expected to be secondary and it is important to find the phases and stations on the focal sphere which are most sensitive to changes in the fault geometry. In Figures 5.3, 5.4, and 5.5, the dotted lines represent the seismograms for listric fault geometries and the solid lines for the planar fault geometries for the cases of ruptures propagating unilaterally up-dip, bilaterally up- and down-dip, and down-dip, respectively. It can be seen that the waveshapes of teleseismic P and SV waves are not very sensitive and the relatively small differences are mainly restricted to the amplitudes. Correct amplitudes carry valuable information about the source strength and orientation; however, they can be more affected by the presence of noise, uncertainties in instrument magnifications, and local site characteristics and it may become difficult to recognize differences between listric and planar fault geometries solely from P and SV seismograms. Because for layered structures highly variable S_{Pl} waves contaminate the observed SV seismograms, no SV waves have been used to study the earthquake data in the following chapter. In the case of synthetic modeling, their presence or absence did not influence the solutions. Polarities and amplitudes of SH waves are more affected by changes in dip along the width of a fault, since the nodes of the SH wave radiation pattern run essentially through the center of the focal sphere and nodal stations are sensitive to variations in the fault mechanism. This can be seen in Figure 5.3 for the seismograms from the stations SH1, SH2, SH3, SH5, SH6, and SH7 where the polarity is different for the first subsource and the centroid. This shows the importance of including SH waves.

The differences between the listric and planar fault geometries are smaller for ruptures originating at the center of the fault than for models with rupture nucleation at the base or top of the fault. From a rock mechanical point of view, it is more likely that ruptures nucleate at the base of the fault, which should help my quest to determine normal fault geometries.

Simple plotting of the models on top of each other provides some important results. A good station coverage is necessary to study the fault geometry, since the small curvature effects are azimuthally dependent. It is crucial to include the SH waveforms, which are more sensitive to changes in focal mechanism than P or SV waves. For older analog WWSSN data careful hand-digitizing of the horizontal long-period components is required to obtain seismograms of high quality. Additionally, it can be expected that curvature can be best resolved for unilateral, up- or downward propagating ruptures.

Lateral Location Uncertainties

Effects of lateral mislocations of the subsources are negligible. Exact knowledge of the lateral locations of the subsources is not required, because teleseismic rays depart with a small take-off angle from the source. To illustrate this we compare model LIUP (solid lines) and the same model with all subsources placed at the same lateral position (dotted lines) (equivalent to $\Delta r = \Delta az = 0$ for model LIUP in Table 5.1) in Figure 5.6.

Model PLUP

The synthetic data are generated from a model representing a north-south trending pure normal fault of 12 km depth (Table 5.1). The time lags of the individual subsources approximate a rupture speed of 2.8 km/s, this velocity has been used for all synthetic models.

The centroidal parameters for the synthetic data were estimated from the combined set of P, SV, and SH waves using the same procedure as for the real data. Realignments of the seismograms for the best cross-correlations were allowed and the a priori duration of the source time function, which consists of a set of isoscele triangles of half-duration $\Delta \tau = 1.5$ s, was longer than for the true models.

The estimated centroidal solution is listed in Table 5.3 and is very close to the correct values of strike = 0°, dip = 45°, rake = 270°, centroid depth = 6 km, and seismic moment = 15 (Table 5.1). The error in source orientation is less than 0.5°, and the estimated moment is only 2% smaller than expected. The centroidal depth, however, is overestimated by 0.8 km. The parameter uncertainties shown in Table 5.3 are based on the noise in the data, in this case due to underparameterization; the true biases are underestimated, indicating that straight forward application of statistical methods can be misleading. Figure 5.7 shows the fit to the data.

The fault geometry has been investigated by distributing three point sources with their orientations and relative locations determined from the centroidal solution as described in Chapter 3 and only the shape of the source time function for each subsource was estimated. Since the centroidal description is very good, it is not unexpected that a model resembling a planar fault geometry with upwards propagating rupture fits the best. Applying a t-test to different solutions representing different degrees of fault curvature excludes basically any listric model; models with a small 10° change of fault dip between the shallowest and deepest subsources are inferior to the planar model at the 99.5% level of confidence.

If the data are modeled by a rupture nucleating at the center of the fault instead of a rupture which nucleates at the bottom, the misfit is only insignificantly worse (75% confidence level from t-test). This is probably caused by the small but nonetheless important misparameterizations introduced by the incorrectly estimated centroidal parameters. In the presence of noise in real data and with a smaller number of unevenly distributed stations, the centroid estimate is likely to be less accurate than for this synthetic case, and it therefore will be difficult to unambiguously resolve locations of rupture nucleation and directions of rupture propagation with the method presented here.

Planar fault geometries, either nucleating at the bottom or the center of the fault, provide a fit that is significantly better than any listric fault geometry (with some minimum curvature) for model PLUP.

Model PLBI

This model is identical to model PLUP except that the rupture nucleates at the center of the fault and propagates simultaneously up- and down-dip, the source parameters for the synthetic data as well as the expected centroidal values are given in Table 5.1. The estimated centroid (Table 5.3) almost perfectly recovers the expected values. This is no surprise, since model PLBI closely resembles a point source and finiteness effects are small.

Distributed sources resembling a planar fault geometry either nucleating at the base or the center of the fault fit significantly better than listric fault geometries with 10 and more degrees of curvature.

Model PLDO

The parameters of the model used to generate the synthetic data and its associated centroidal description are presented in Table 5.1. The estimated centroid parameters are shown in Table 5.3. The source orientation is well recovered, the seismic moment is slightly underestimated as for other planar fault geometries (PLUP, PLBI). The centroid depth is slightly biased towards the nucleation depth.

Model LIUP

The synthetic data for models resembling a listric fault with a curvature of 40° are given in Table 5.1, and a schematic sketch is showing the model in Figure 5.1. When

each subsource of the listric fault models has a strength of 5.92, the tensor sum of the subsources is equal to the centroid of the planar models PLUP, PLBI, and PLDO. The expected centroid values are: strike = 0°, dip = 45°, rake = 270°, centroid depth = 6 km, and moment of 15, with the centroid 5.3 km west and 4 km above the nucleation point at an azimuth of 270°.

Point Source

The best fitting centroid estimate is given in Table 5.3 (LIUP-bc) and shown in Figure 5.8. For comparison, Figure 5.9 shows the expected centroidal solution (with the centroid at its correct position with respect to the nucleation point). Strike and rake of the estimated centroid are correct within 0.5° and 1° respectively. The depth is slightly overestimated by 0.6 km and the moment is about 7% too large. The least resolved parameter is the dip (35° instead of 45°). The formal uncertainties given in Table 5.3 are too small and do not represent errors introduced by underparameterization of the problem.

Cause for the Incorrect Estimate of the Centroid Dip

The estimated centroid dip is severely incorrect and in the next paragraphs several possible causes will be investigated. It will be shown that the non-linear depth dependence of the excitation functions is responsible for the incorrect dip estimate.

To investigate the possible trade-off between estimated centroid depth and dip, I fixed the depth and inverted for the source orientation and seismic moment only. For all shallow point sources (1-14 km depth) the dip is always seriously underestimated ($\leq 35°$); the other parameters are best resolved and the misfit is smallest for centroid depths of 6-7 km, which is close to the true centroid depth of 6 km.

To investigate the possible bias introduced by uneven station distributions, I rotated the station distribution listed in Table 5.2 by 180°. The estimated point source parameters show the same 10°-bias in dip (LIUP-rot in Table 5.3).

Tests where a) no realignments were allowed, b) only P- and SH-wave seismograms were used, and c) all stations were placed at the same epicentral distance of 40° resulted in basically identical parameter estimates as described above.

The influence of the higher frequencies of the broadband data on the parameter estimates, especially the dip, was investigated next. Seismograms for the model LIUP were regenerated with the long-period WWSSN instrument response (most of the data for the earthquakes studied in the subsequent chapter are of this type). These data lack the

high-frequency and long period content of the broad-band data. The peak of the instrument response around 15 s smooths the waveforms and the spatial resolution of the data is somewhat reduced. This averaging, however, should stabilize the centroidal results. The estimated centroid solution is similar to the broadband estimate (LIUP-wwssn in Table 5.3); Figure 5.10 shows the fit to the waveforms. The moment is now underestimated by about 14% and the dip by 11°, the centroid depth is about 0.8 km too deep, strike and rake are within 0.3° of the expected values. Placing the source too deep may cause the underestimation of the seismic moment, but the most likely explanation is that the pass-band of the WWSSN instrument response is too narrow and lacks sufficient long-period sensitivity to properly account for the long period signal generated by the source. Forcing the centroid to a (correct) depth of 6 km does not remove the seismic moment underestimate. If the calculations are made for the long-period instrument of the SRO seismograph-system, which has its peak at about 25 s period, the seismic moment bias is removed (LIUP-sro in Table 5.3); other parameters are similar to broadband and WWSSN estimates.

Three additional models based on the model LIUP were tested: a) all three subsources were placed at the same point and nucleated without any time delay (i.e., $\Delta r = \Delta az = \Delta t = 0$ and centroid depth = 6 km for the three subsources of model LIUP in Table 5.1), b) $\Delta r = \Delta az = 0$, centroid depths at 6 km, but time delays as in Table 5.1, and c) $\Delta r = \Delta az = \Delta t = 0$, but centroid depths as in Table 5.1. Only the dip and shape of the source time function were estimated. In the first two cases the dip was correctly estimated (45°), but the estimate of the fault dip in the third case was again significantly too small (37°).

The testing so far shows that neither the azimuthal nor the spatial station distribution - as long as they are reasonably 'good' - are responsible for the incorrect estimates in fault dip. Also the instrument response and frequency content of the seismograms do not affect the point source estimates as long as the data contain sufficient long period signals below the corner frequency of the source. From the last paragraph it becomes obvious that the dip estimates become incorrect when the sources are distributed vertically at shallow depth, which could be caused either by vertical finiteness effects or by the depth dependence of the excitation functions.

To isolate the last two effects, the whole model LIUP was shifted down to a centroid depth of 100 km while all other parameters are unchanged. At this depth the P, pP, and sP (S and sS) phases are well separated, whereas at shallow depths these phases strongly interfere with each other. Now, the point source estimates are very close to the expected values (expected centroid depth = 100 km, other parameters as before) and are listed in Table 5.3, the waveform fit is shown in Figure 5.11. The strike and rake are within 0.1°,

the seismic moment estimate within 1% of the true values. The depth is underestimated by 0.8 km. The estimate of the fault dip of 44° is off by only 1°.

This is a very interesting result and shows a serious limitation of the resolving power of teleseismic body wave data for shallow sources. For deep earthquakes, a correct estimate of the centroidal dip can be obtained. At shallow depths, however, direct and reflected phases interfere strongly and the excitation functions (Green's functions) become unevenly sensitive to different depths, making the estimated centroidal dip biased towards the deeper parts of the fault. The errors in the dip estimate, however, are not aliased onto other centroidal parameters, which are well resolved.

Down-Dip Fault Geometry

In view of the bias on the estimated dip of the centroidal source parameters introduced by the shallowness of the sources, is it still possible to make any reasonable statement about the fault geometry derived from the procedure described in Chapter 3? To answer this question, I used the biased point source estimate shown in Figure 5.8 (LIUP-bc in Table 5.3) to assign source parameters to three distributed point sources and inverted only for the shape of the source time function while keeping the other parameters fixed (see Chapter 3 for details). Table 5.4 summarizes the results for ruptures propagating upwards. Model LI1 with a 10° change in fault dip between the shallow and deep source (30° and 40 ° at 11 and 2.2 km depth) provides the best overall fit. A model with a planar fault geometry (PL) is significantly worse and unacceptable based on statistical testing (99.95% level of confidence). The model LI4 with a curvature of 40°, which is the true change of the dip of the structure used to calculate the synthetic data, however, is also unacceptable at the 99.95% level of confidence. Model LI4 has the correct curvature, but incorrect individual dips, which are all too small by 10° compared to the true model, which may explain this result. The dip of the first (deepest) source of model LI2 (20° curvature) coincides with the initial dip of the true model and the fit of this model is only insignificantly worse than for model LI1. Models with rupture nucleation at the center produced similar results.

In another test I allowed the dip and seismic moment of the subsources to vary independently starting from different distributed source models (see Chapter 3). The resulting geometry is listric ('FR-' models in Table 5.4) and the estimated dips are of correct order. The estimated curvature is about 45-47° compared to the correct value of 40°. The dip for the intermediate depth source, which is slightly too deep (6.6 instead of 6 km), is always underestimated by 6-7°. The distribution of the seismic moment is also

biased towards this subsource and underestimates the source strength of the gently dipping deepest source.

From these tests we conclude that it may not be possible to retrieve quantitatively correct estimates of the fault geometry (listricity, fault dip at specific depth) if I follow the uniform procedural steps explained in Chapter 3, which assume that the centroid is faithfully estimated. However, qualitative statements can still be drawn from the results of distributed sources: the synthetic seismograms due to a listric fault geometry cannot be matched adequately by a planar fault model and some listric curvature is required to fit the seismograms best. Allowing dip and seismic moment to vary provides better estimates, since one-sided biases (e.g., all subsources having too shallow dips) are not fixed into the model and correct dip estimates may be found. However, in the presence of noise, complex source time history, and complicated Earth structure this procedure can be quite unstable. Moreover, it becomes difficult to statistically compare these models, which have added degrees of freedom, with planar models.

Model LIBI

Model LIBI is identical to model LIUP except that the rupture nucleates at the center of the fault and propagates simultaneously up- and down-dip. The best fitting centroid estimate is given in Table 5.3. Strike and rake are faithfully recovered. The centroid depth is slightly under- and the seismic moment slightly overestimated. Similar to model LIUP, the fault dip is underestimated by 8°.

Model LIDO

The parameters of the subsources used to generate the synthetic data for this downward propagating rupture are given in Table 5.1. The estimated centroid parameters (see Table 5.3) follow the pattern of the models LIUP and LIBI.

Summary

The sensitivity of the method was tested on synthetic broad-band data by comparing P, SV, and SH waveforms for planar and listric fault geometries. As expected, fault curvature has only a secondary effect on body wave pulses at teleseismic distances for typical fault widths and rupture speeds. Ruptures propagating unilaterally up-dip generate more pronounced differences between planar and listric geometries than ruptures

nucleating at the center of the fault and are easier to resolve. A good station coverage, however, is required because the curvature effects are azimuth and distance dependent. Moreover, polarities and amplitudes of SH waves are more affected by changes in dip along the width of a fault than P and SV waves, and therefore it is very important to incorporate SH waves into the analysis.

For planar fault geometries, the centroid parameters can be faithfully recovered. Only the estimated centroid depth shows a small bias towards the nucleation depth; the same has been observed for listric fault geometries. Distributed source models derived from the centroid estimate with varying amounts of fault curvature clearly favour a planar over any curved description. Therefore it should be possible to identify planar fault geometries with some confidence. However, it is not possible to unambiguously resolve the nucleation point and the mode of rupture propagation.

The point source estimates for the listric fault geometries at shallow depths showed an interesting feature: the expected fault dip was usually underestimated by about 10°, whereas all the other source parameters were reasonably well resolved. Several possible causes have been investigated. The dip was correctly estimated for listric models placed at greater depths such that the direct and reflected phases are separated sufficiently. The underestimation of the fault dip is therefore a direct result of the non-linear depth dependence of the excitation functions. For shallow sources, estimates of the fault dip are biased towards values at sub centroid depths.

Using a significantly wrong estimate of the centroidal fault dip severely affects the inferences based on distributed fault models. Correct quantitative statements about the underlying fault geometry, which the distributed source models of varying curvature are trying to match, are no longer possible. The method, where the curvature and the fault dip are prescribed based on centroidal values is not well suited for cases with significant errors in the centroidal parameters. The method, however, can distinguish between planar and listric cases, but the quantitative estimate of the curvature can be biased. Better estimates of the true curvature and dip at a specific depth may be obtained by lessening the restrictions and allowing the fault dips and seismic moment of the subsources to vary independently.

Table 5.1   Paramaters of Finite Fault Models and Expected Centroidal Parameters

	subevent	Model Parameters								Expected Centroid							
		strike deg	dip deg	rake deg	depth km	Mo	Δt s	Δr km	Δaz deg	strike deg	dip deg	rake deg	depth km	Mo	Δv km	Δh km	Δa deg
PLUP	1	0	45	270	10	5	-	-	-	0	45	270	6	15	4	4	270
	2	0	45	270	6	5	2	4	270								
	3	0	45	270	2	5	4	8	270								
PLBI	1	0	45	270	6	5	-	-	-	0	45	270	6	15	0	0	0
	2	0	45	270	2	5	2	4	270								
	3	0	45	270	10	5	2	4	90								
PLDO	1	0	45	270	2	5	-	-	-	0	45	270	6	15	-4	4	90
	2	0	45	270	6	5	2	4	90								
	3	0	45	270	10	5	4	8	90								
LIUP	1	0	25	270	10	5.9	-	-	-	0	45	270	6	15	4	5.3	270
	2	0	45	270	6	5.9	2.6	6.4	270								
	3	0	65	270	2	5.9	4.3	9.4	270								
LIBI	1	0	45	270	6	5.9	-	-	-	0	45	270	6	15	0	0	0
	2	0	65	270	2	5.9	1.7	3.0	270								
	3	0	25	270	10	5.9	2.6	6.4	90								
LIDO	1	0	65	270	2	5.9	-	-	-	0	45	270	6	15	-4	4.1	90
	2	0	45	270	6	5.9	1.7	3.0	90								
	3	0	25	270	10	5.9	4.3	9.4	90								

PL, LI - planar, and listric fault models. UP, BI, DO - rupture nucleates at bottom, center, and top respective. depth - centroidal depth. Δt, Δr, Δaz - time delay, distance and azimuth of subevent with respect to first subevent. Mo - seismic moment in arbitrary units. Δv, Δh, Δa - vertical and horizontal distance, and azimuth of centroid with respect to nucleation point, Δv: up positive.

Table 5.2   Station Parameters and Crustal Structure for Numerical Simulations

Station	Azimuth deg	Distance deg	Take-off Angle deg
P1	0	40	26.6
P2	30	50	24.2
P3	60	55	22.9
P4	90	35	27.8
P5	120	90	14.7
P6	150	65	20.7
P7	180	75	18.2
P8	210	45	25.5
P9	240	60	21.7
P10	270	80	17.0
P11	300	70	19.5
P12	330	85	15.5
SH1	0	30	29.6
SH2	30	60	23.6
SH3	60	45	26.6
SH4	90	35	28.9
SH5	120	80	19.0
SH6	150	55	24.8
SH7	180	65	22.6
SH8	210	40	27.8
SH9	240	35	28.9
SH10	270	35	28.9
SH11	300	40	27.8
SH12	330	45	26.6
SV1	0	75	20.2
SV2	30	80	19.0
SV3	60	40	27.8
SV4	90	30	29.6
SV5	120	50	25.6
SV6	150	60	23.6
SV7	180	70	21.5
SV8	210	85	17.8
SV9	240	90	16.3
SV10	270	75	20.2
SV11	300	80	19.0
SV12	330	60	23.6

Crustal Structure in Source and Receiver Regions:

v_p = 6.0 km/s v_s = 3.46 km/s   density = 2.80 g/cm^3

t^* = 1.0 s and 4.0 s for P and S waves respectively.

Table 5.3   Estimated Centroid Parameters

model	strike deg	dip deg	rake deg	depth km	Mo
PLUP	0.2±0.2	44.6±0.1	270.3±0.2	6.80±0.04	14.80±0.08
PLBI	-0.1±0.1	44.7±0.0	269.9±0.1	5.99±0.02	14.98±0.02
PLDO	-0.8±0.2	44.9±0.1	268.9±0.2	5.45±0.04	14.82±0.06
LIUP-bc	0.4±0.5	34.6±0.2	270.7±0.5	6.58±0.10	16.01±0.22
LIUP-rot	-0.6±0.5	34.7±0.2	270.7±0.5	6.07±0.10	16.24±0.20
LIUP-wwssn	-0.3±0.8	34.4±0.3	269.7±0.7	6.83±0.12	12.97±0.44
LIUP-sro	0.2±0.4	34.8±0.2	270.2±0.4	6.58±0.08	15.84±7.51
LIUP-deep	0.1±0.8	44.1±0.2	270.1±0.5	99.17±0.36	15.07±0.82
LIBI	0.4±0.3	36.6±0.1	270.5±0.2	5.71±0.06	16.00±0.10
LIDO	-0.5±0.5	35.4±0.3	269.2±0.6	5.22±0.10	16.05±0.17

Best point source estimates for the models PLUP, PLBI, PLDO, LIUP, LIBI, and LIDO. depth - estimated centroid depth. Mo - estimated seismic moment in arbitrary units.

LIUP model: bc - best centroid estimate. rot - station distribution of Table 5.2 rotated by 180°. wwssn - WWSSN instrument response. sro - SRO instrument response. deep - model shifted downward by 94 km, correct centroid depth: 100 km.

The correct centroidal values are shown in Table 5.1 (except value mentioned explicitly). The quoted uncertainties represent 2 standard deviations. See text for further explanations.

Table 5.4 Model LIUP - Test for Fault Curvature

model	depth km	dip deg	Mo	curvature deg	σ 10^{-2}	t	μ 10^{-2}	s 10^{-2}
LI4	11.0	15	6.32					
	6.6	35	6.32	-40	2.83	**3.75**	1.49	2.38
	2.2	55	6.32					
LI3	11.0	20	5.86					
	6.6	35	5.86	-30	1.80	**2.27** •	0.55	1.45
	2.2	50	5.86					
LI2	11.0	25	5.56					
	6.6	35	5.56	-20	1.40	**1.13** •	0.18	0.97
	2.2	45	5.56					
LI1	11.0	30	5.39					
	6.6	35	5.39	-10	1.20	- •	-	-
	2.2	40	5.39					
PL	11.0	35	5.34					
	6.6	35	5.34	0	2.34	**4.48**	1.04	1.39
	2.2	35	5.34					
FR-li4	11.0	24	3.85					
	6.6	38	8.18	-47	0.24			
	2.2	71	6.53					
FR-pl	11.0	24	3.78					
	6.6	39	8.43	-46	0.21			
	2.2	70	5.84					
FR-true	11.0	25	4.05					
	6.6	38	7.62	-45	0.07			
	2.2	70	6.91					

PL - planar fault model. LI - fault flattens with depth. depth, dip - centroid depth and fault dip of subsources. Mo - seismic moment (arbitrary units) for subsources. curvature - decrease (-) of fault dip with depth in degree. σ - normalized variance of residuals. t - value obtained from t-test, models compared with respect to LI1. μ,s - mean and standard deviation of differences of squared station residuals, for explanation see Chapter 3. Number of samples N=36. Value t has to exceed to be within certain confidence level: 60% - 0.26. 75% - 0.68. 90% - 1.31. 95% - 1.70. 97.5% - 2.04. 99% - 2.46. 99.5% - 2.75. 99.95 - 3.65. • - acceptable solution.

All models represent upward propagating ruptures and are derived from centroid solution LIUP-bc (see Table 5.3). Strike, rake of all subsources: 0°, 271°. Time delay, distance, and azimuth of second (third) subsource with respect to first event: 2.5 s (5.0 s), 6.4 km (12.7 km),and 270° (270°). Tensor sum of subsources identical with LIUP-bc moment tensor.

FR-li4 - dips and seismic moments allowed to vary, starting from model LI4. FR-pl - same as FR-li4, but starting from model PL. FR-true - same as FR-li4, but starting with correct values for each subsource (Table 5.1 model LIUP) except depths. The correct centroid estimates of model LIUP are listed in Table 5.1.

Input Geometry for Synthetic Modeling
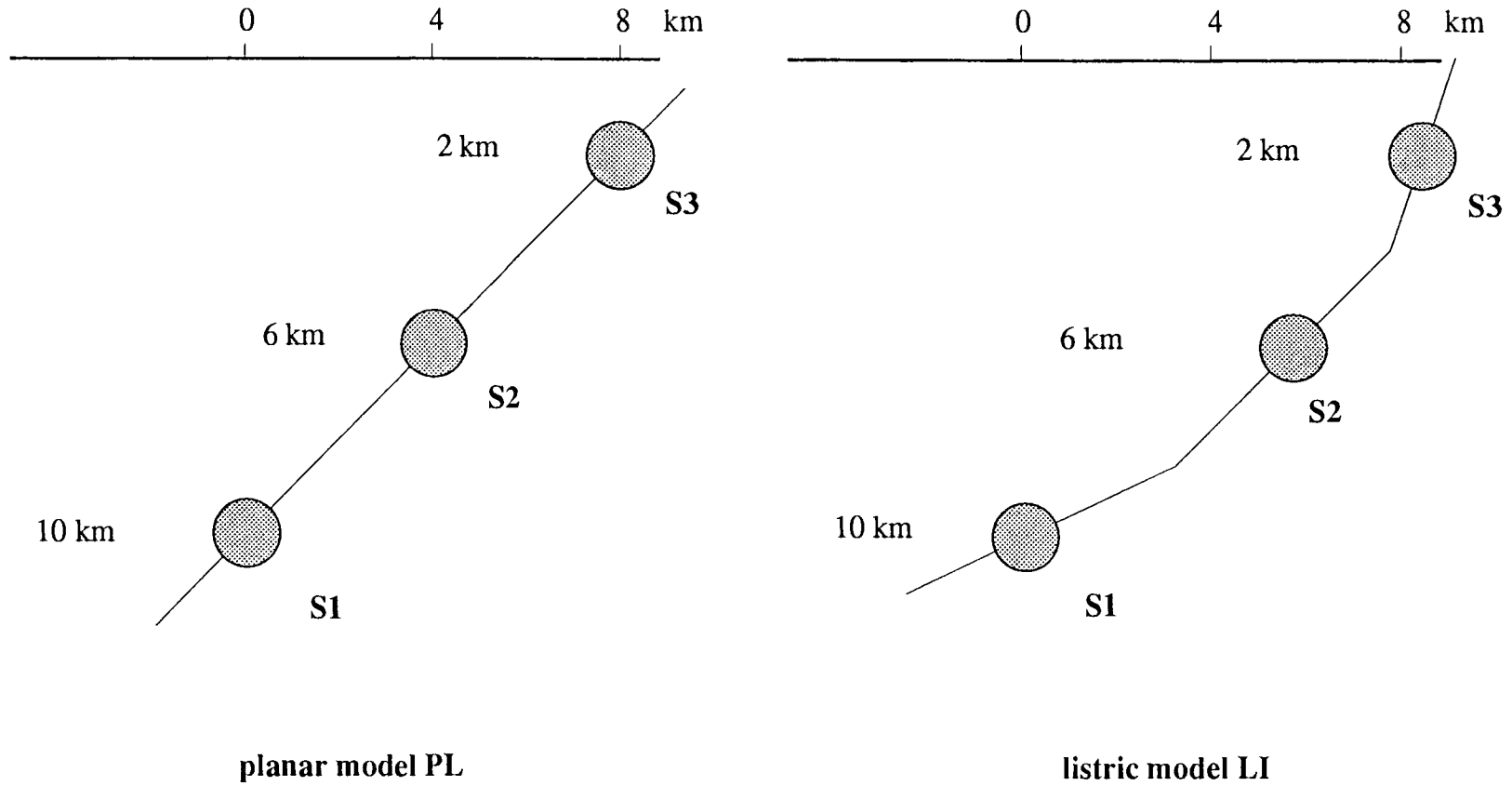
Figure 5.1   Sketch of geometries used for synthetic modeling.
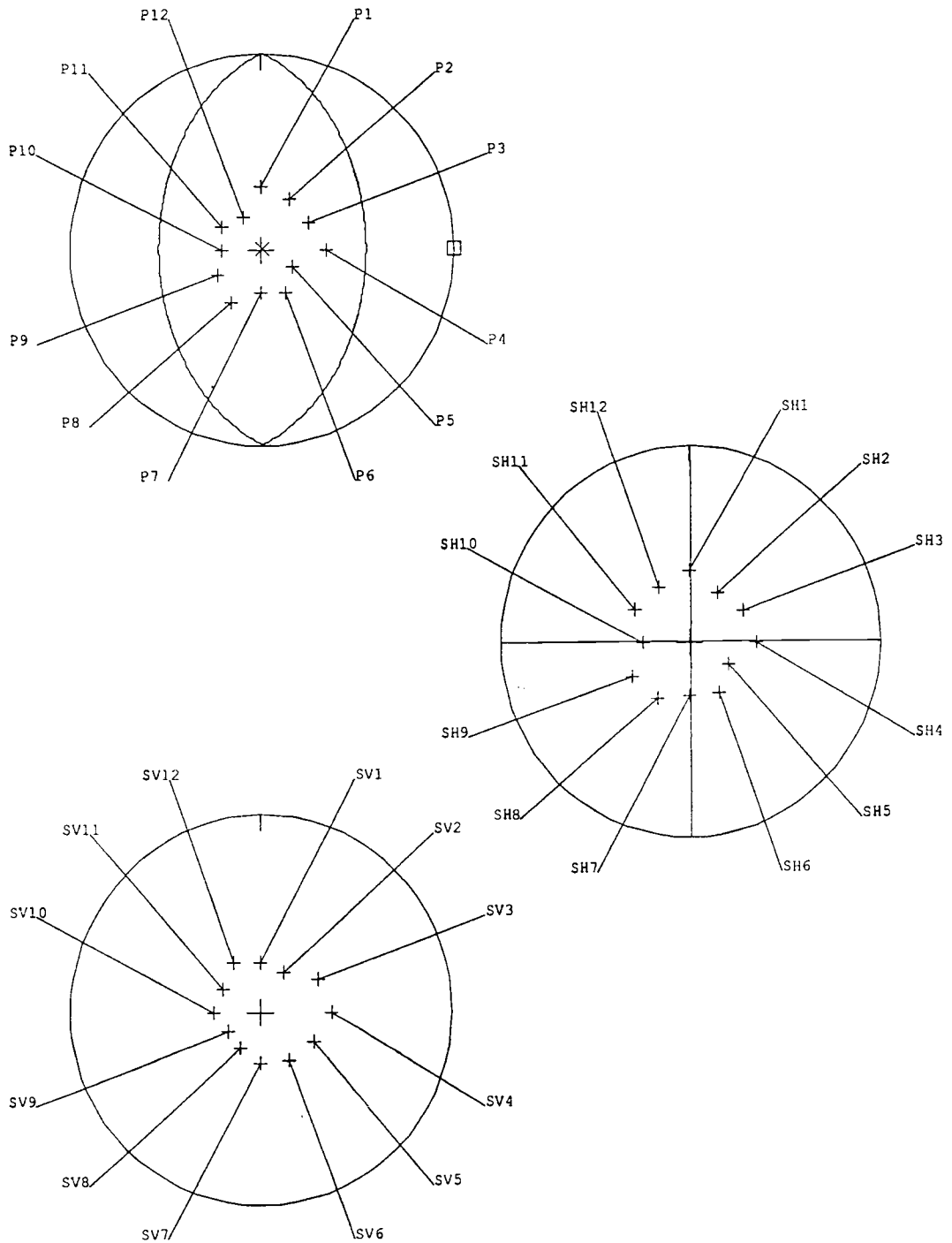
Figure 5.2 Station distribution for numerical modeling. Fault plane solution shown corresponds to correct centroidal solution of all numerical models (see Table 5.1).
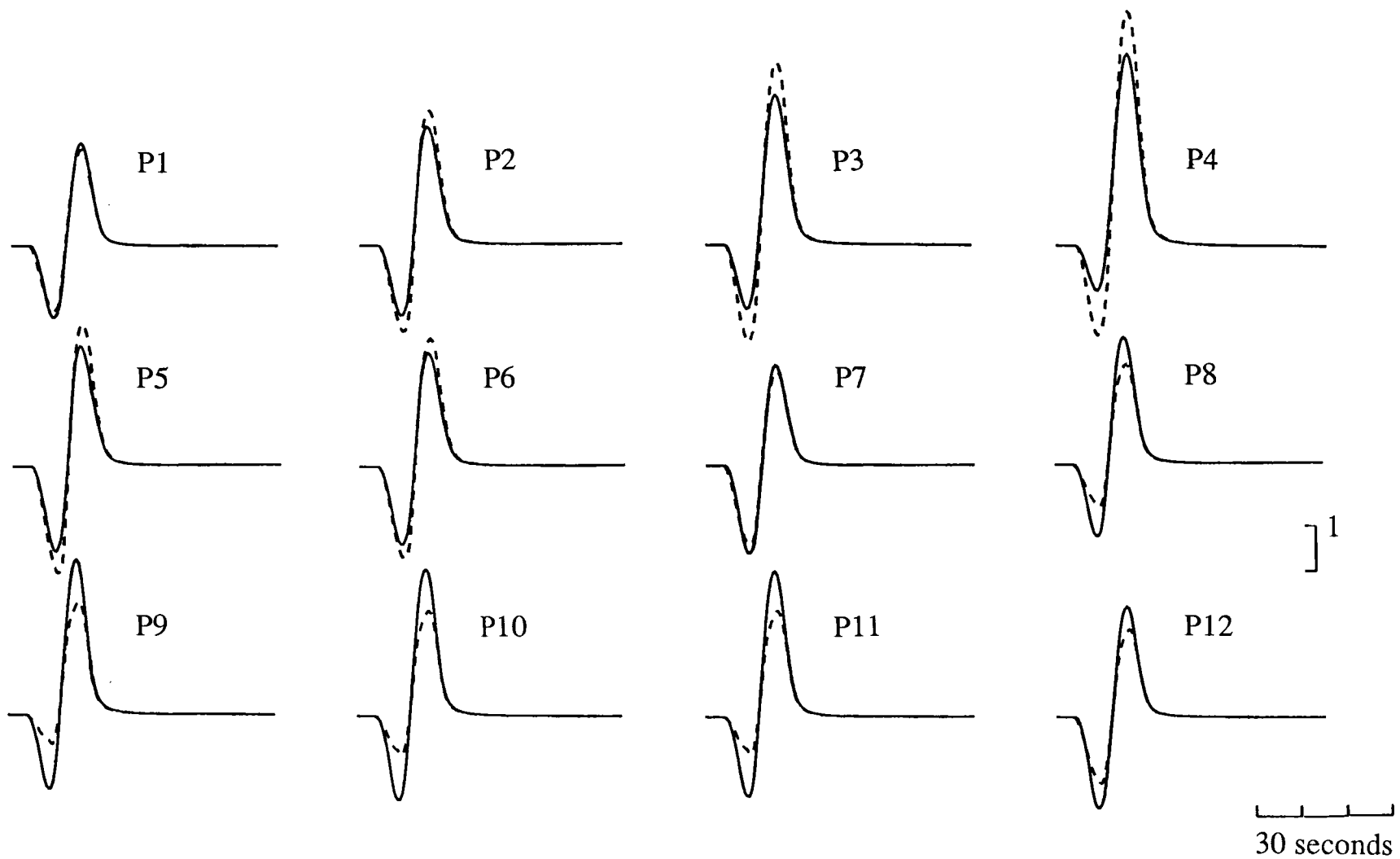
Figure 5.3   Effect of fault curvature on waveforms for upward propagating ruptures. Solid line: planar model PLUP; dotted line: listric model LIUP. P waves.
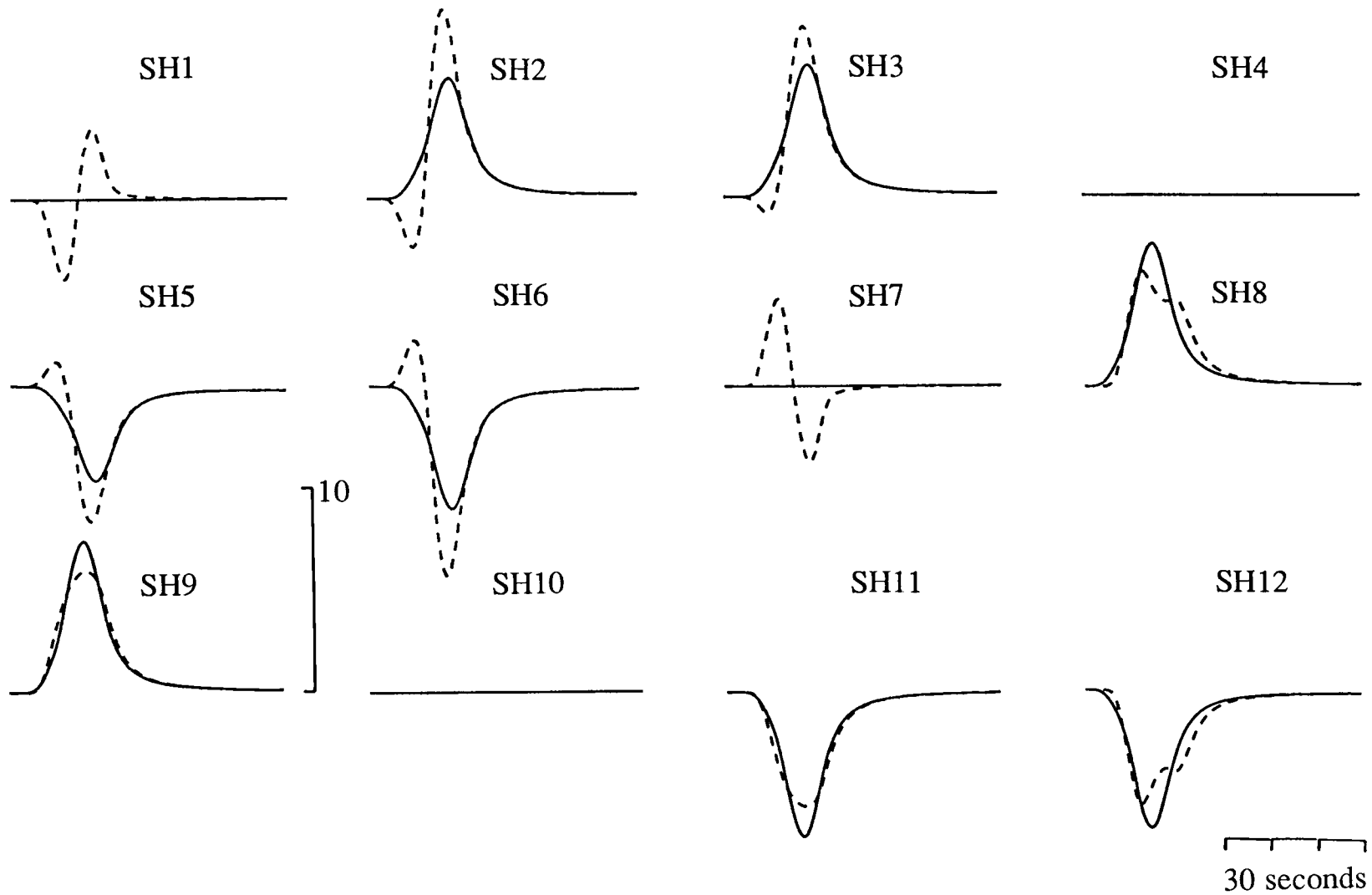
Figure 5.3   cont.   SH waves.
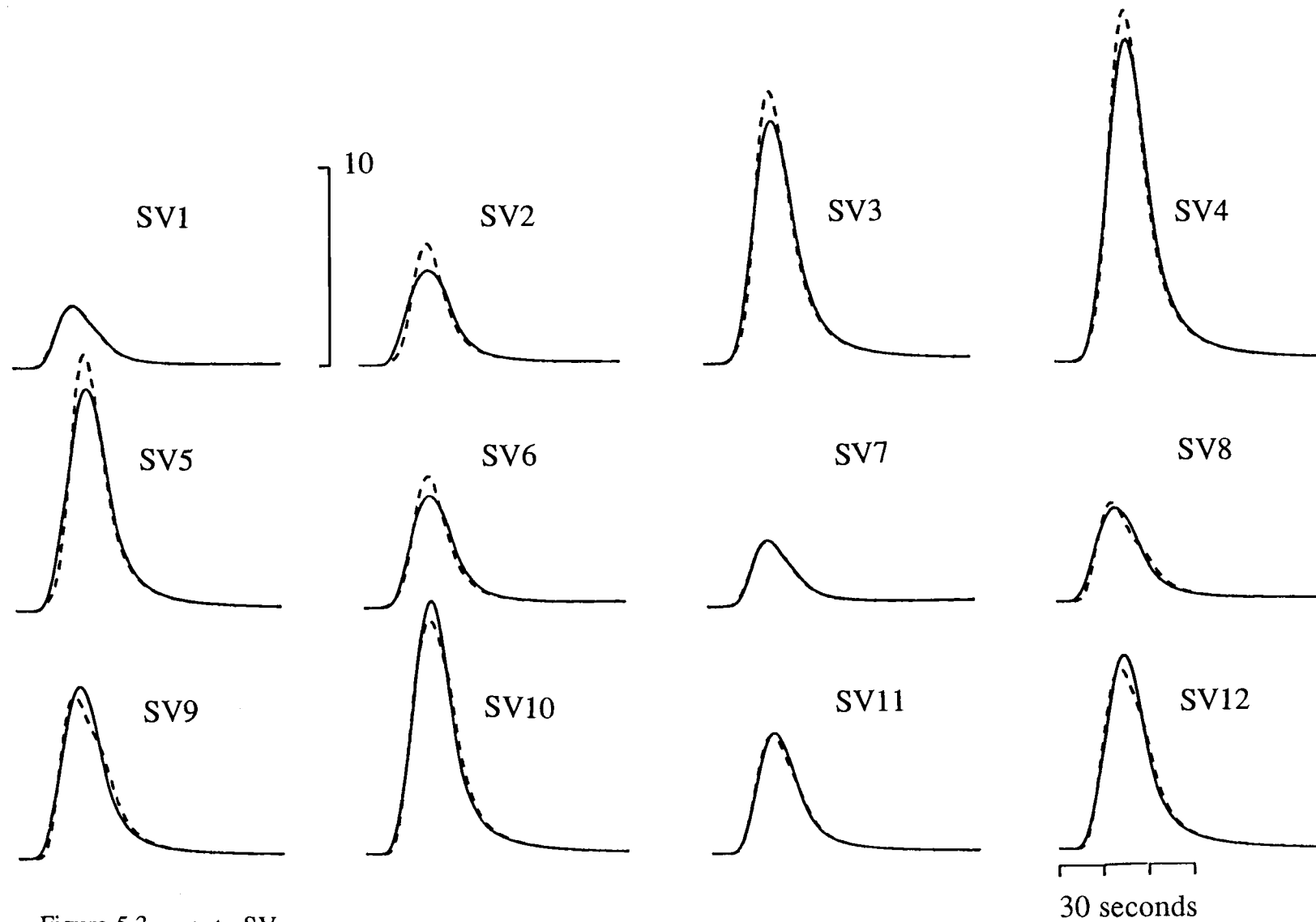
Figure 5.3   cont. SV waves.
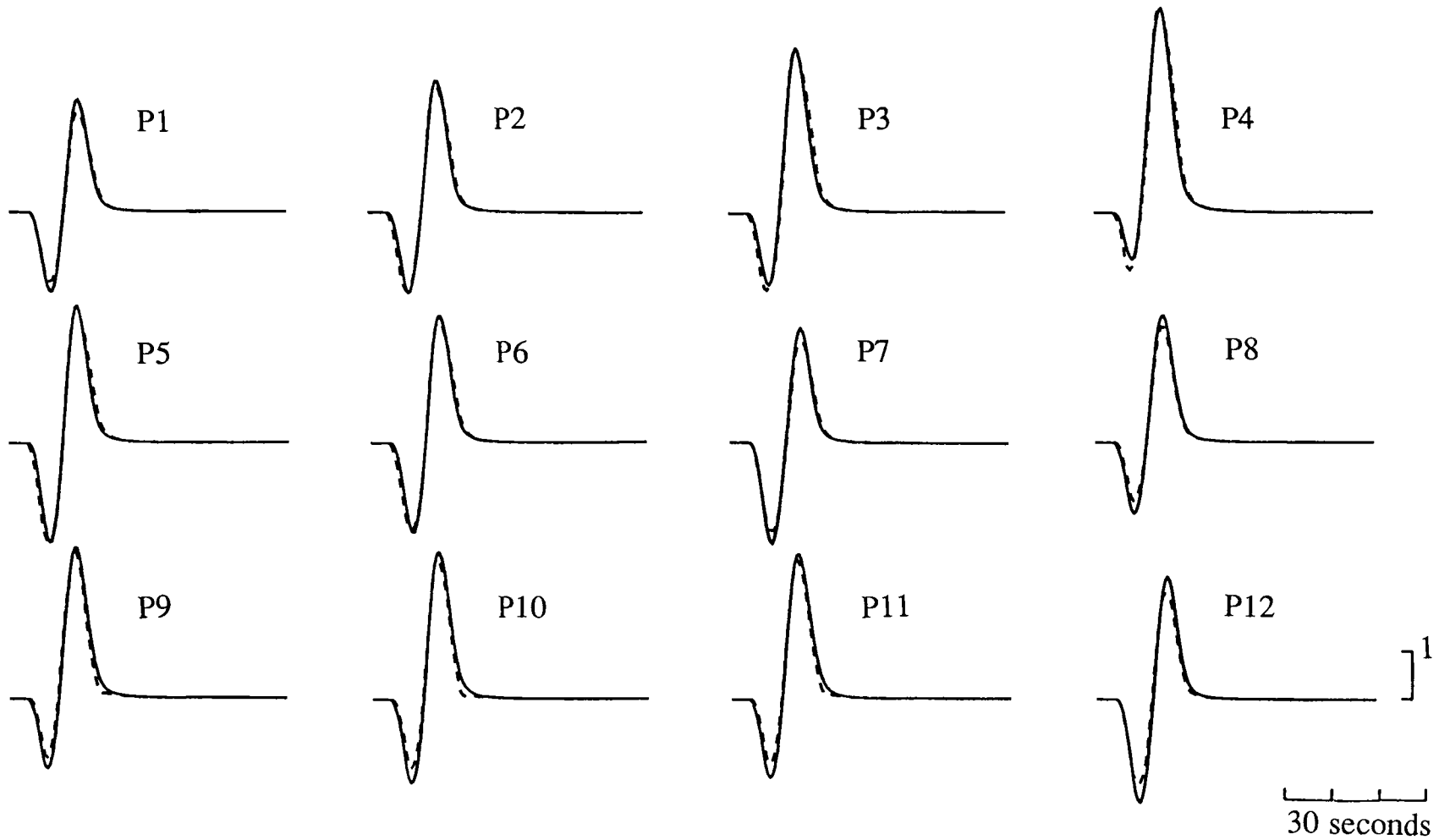
Figure 5.4   Effect of fault curvature on waveforms for bilaterally propagating ruptures. Solid line: planar model PLBI; dotted line: listric model LIBI. P waves.
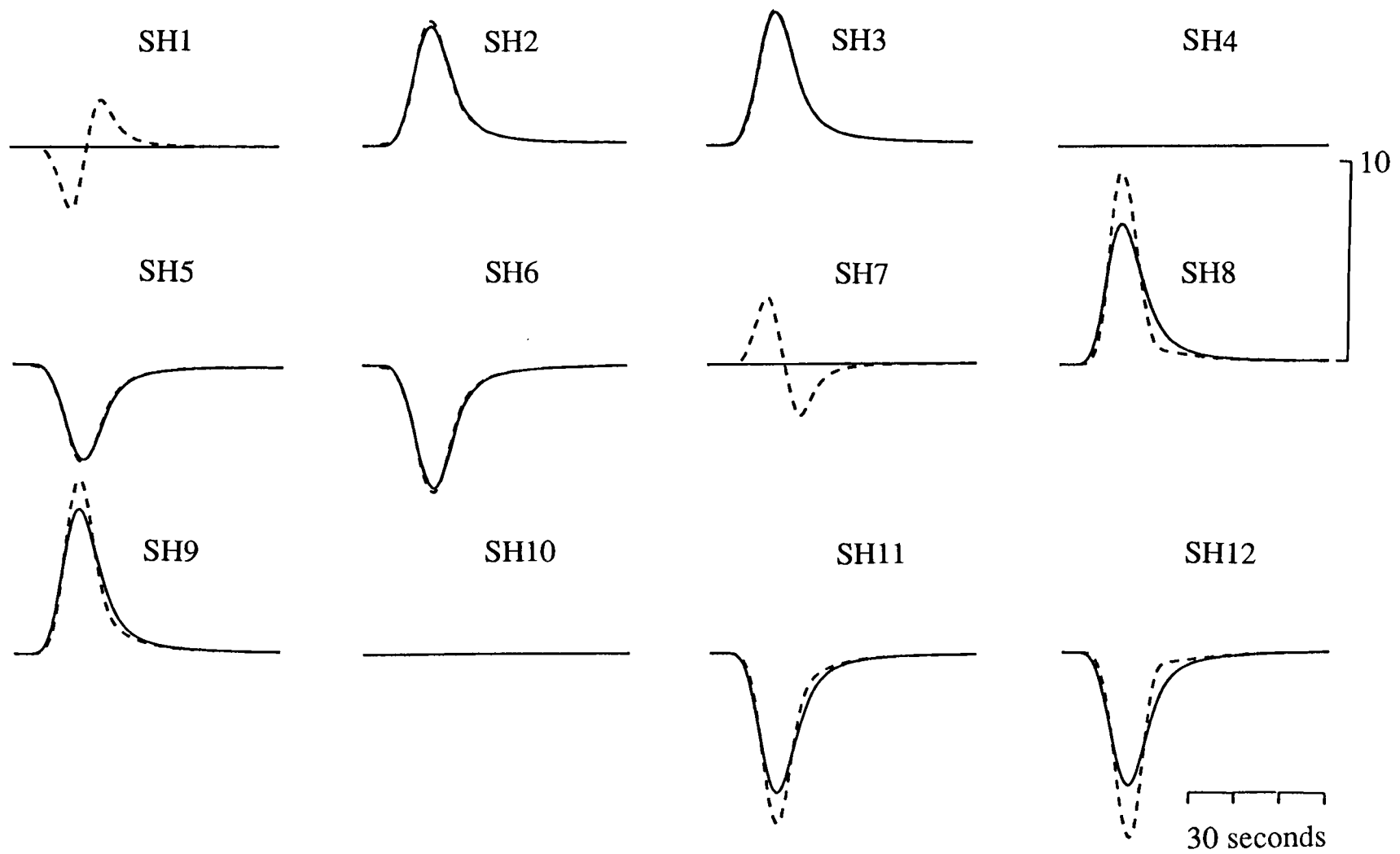
Figure 5.4   cont. SH waves.

SV1　　　SV2　　　SV3　　　SV4

SV5　　　SV6　　　SV7　　　SV8

SV9　　　SV10　　　SV11　　　SV12

30 seconds

10
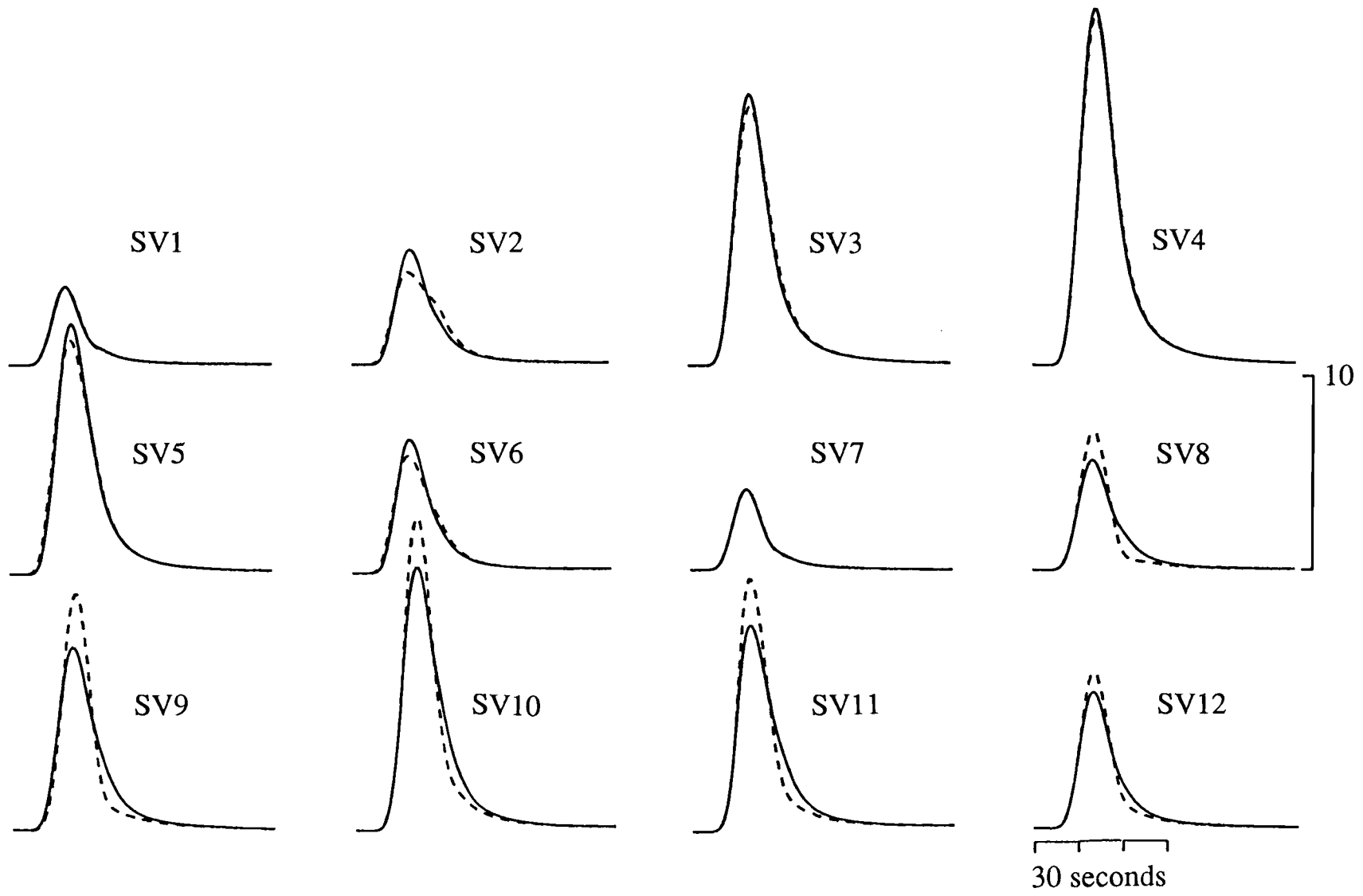
Figure 5.4　cont.　SV waves.
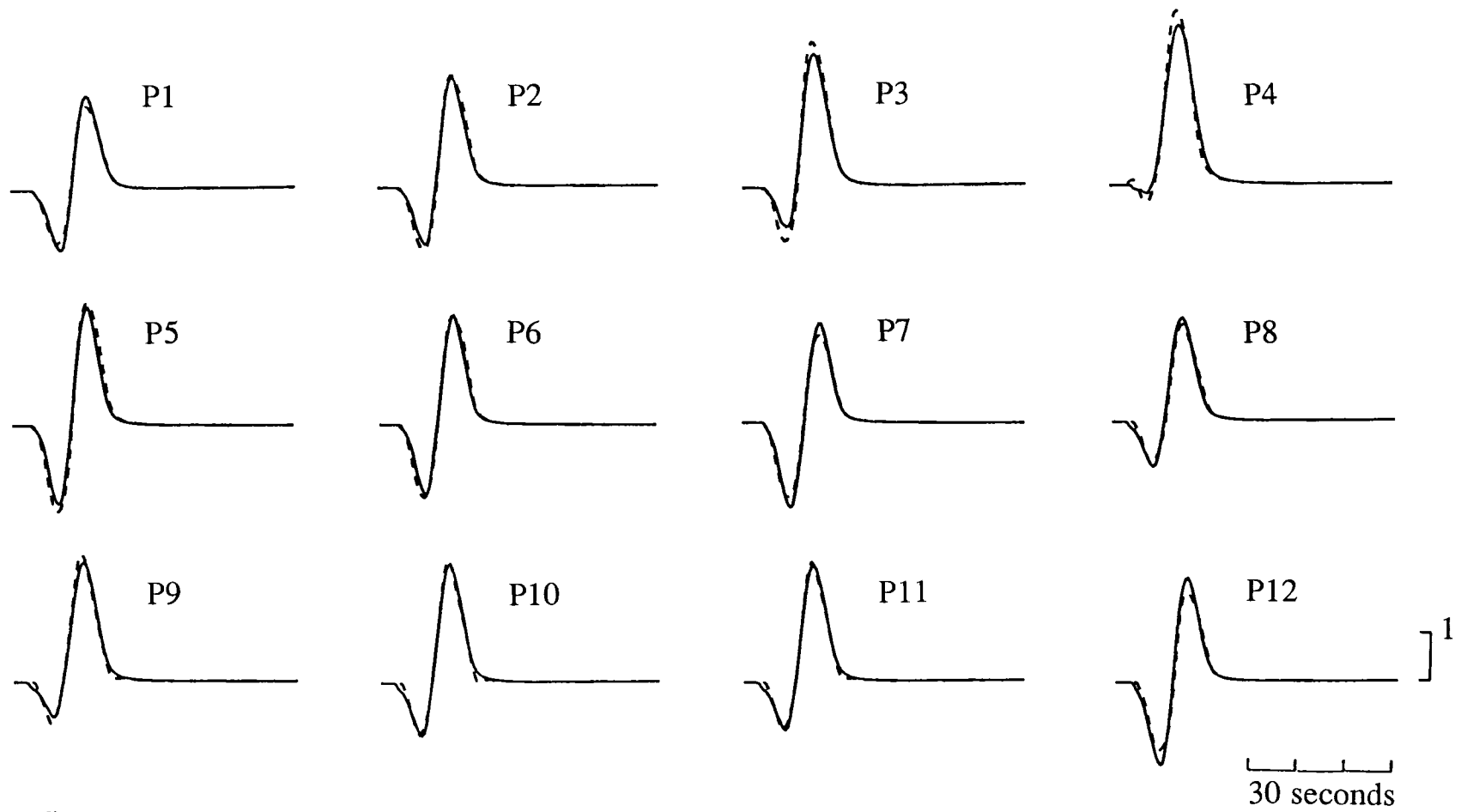
Figure 5.5   Effect of fault curvature on waveforms for downwards propagating ruptures. Solid line: planar model PLDO, dotted line: listric model LIDO. P waves.

SH1 SH2 SH3 SH4

SH5 SH6 SH7 SH8

10

SH9 SH10 SH11 SH12

30 seconds
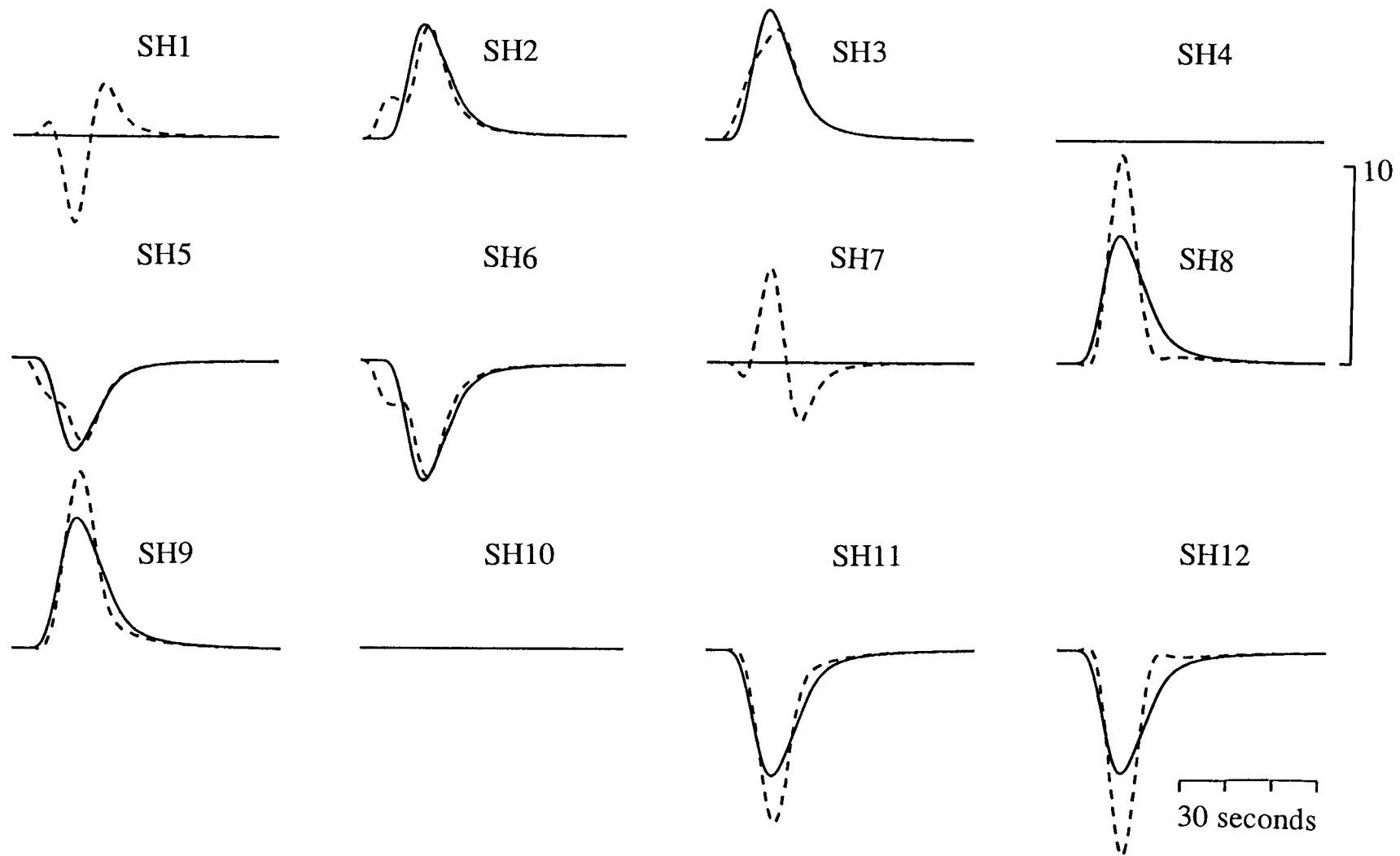
Figure 5.5   cont.   SH waves.
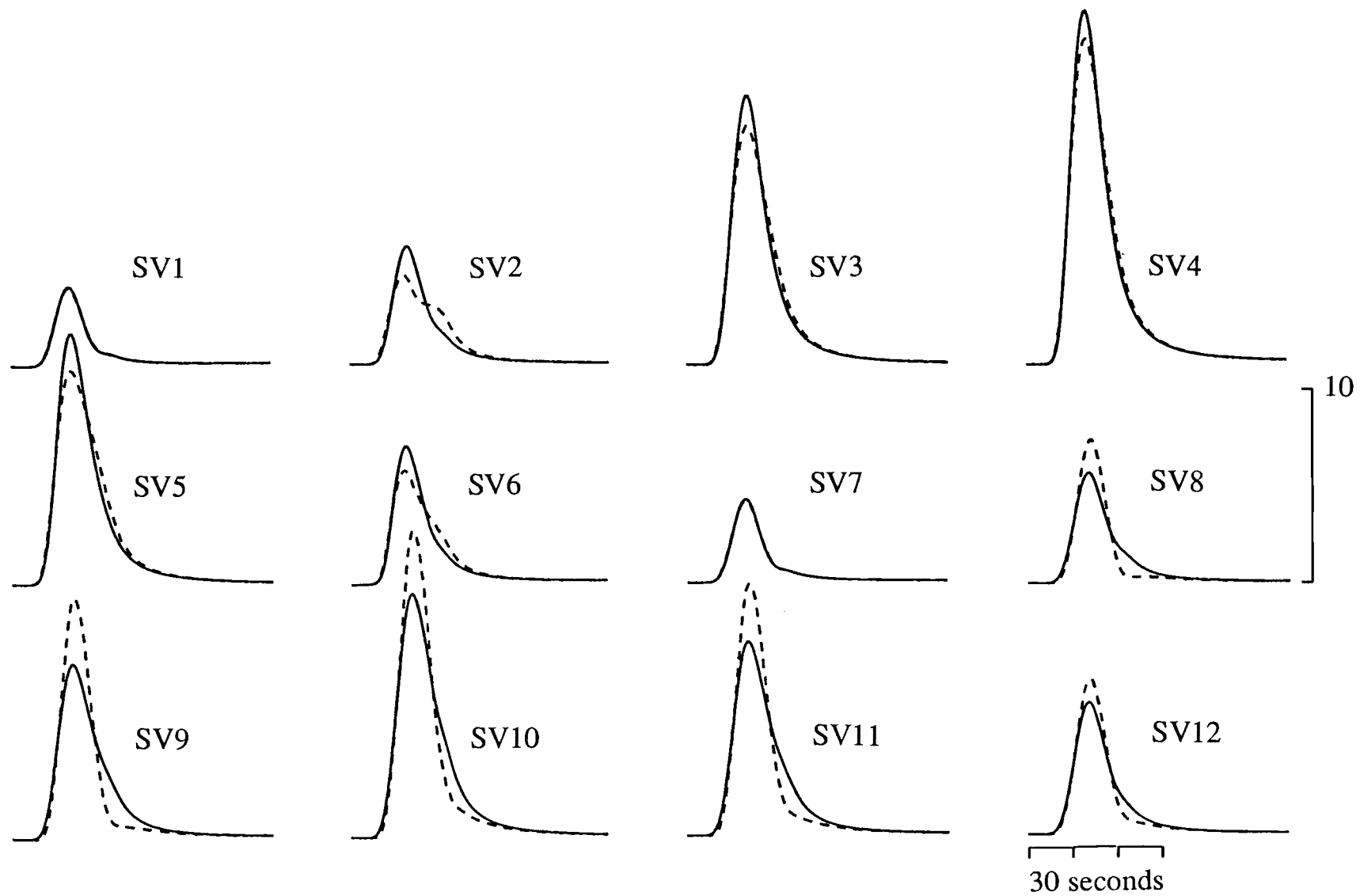
Figure 5.5   cont. SV waves.
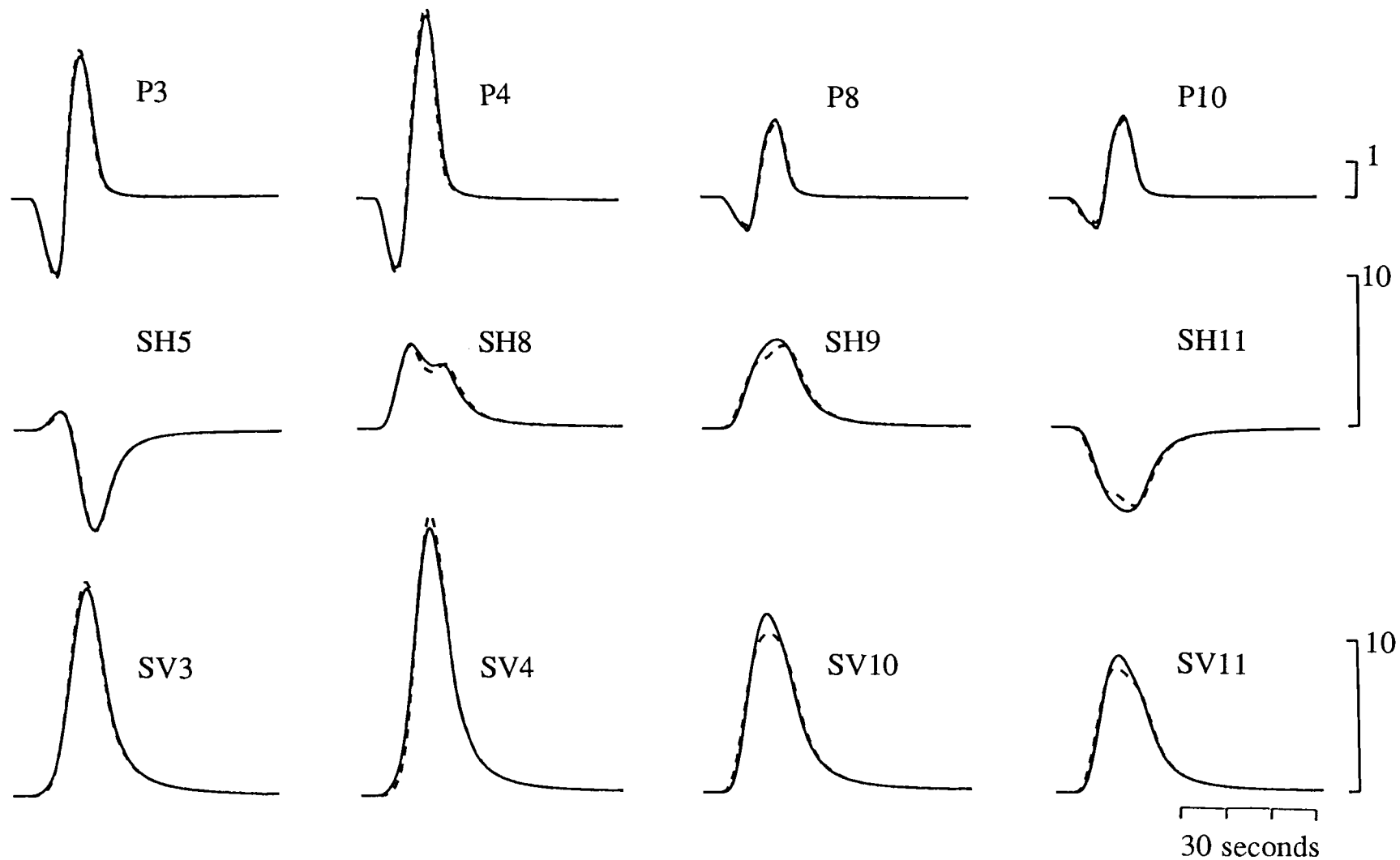
Figure 5.6   Effect of changes in lateral source distribution on waveforms. Solid line: listric model LIUP; dotted line: same model, but all sources located at the same lateral position. Stations showing the largest effects (perpendicular to strike) are shown.
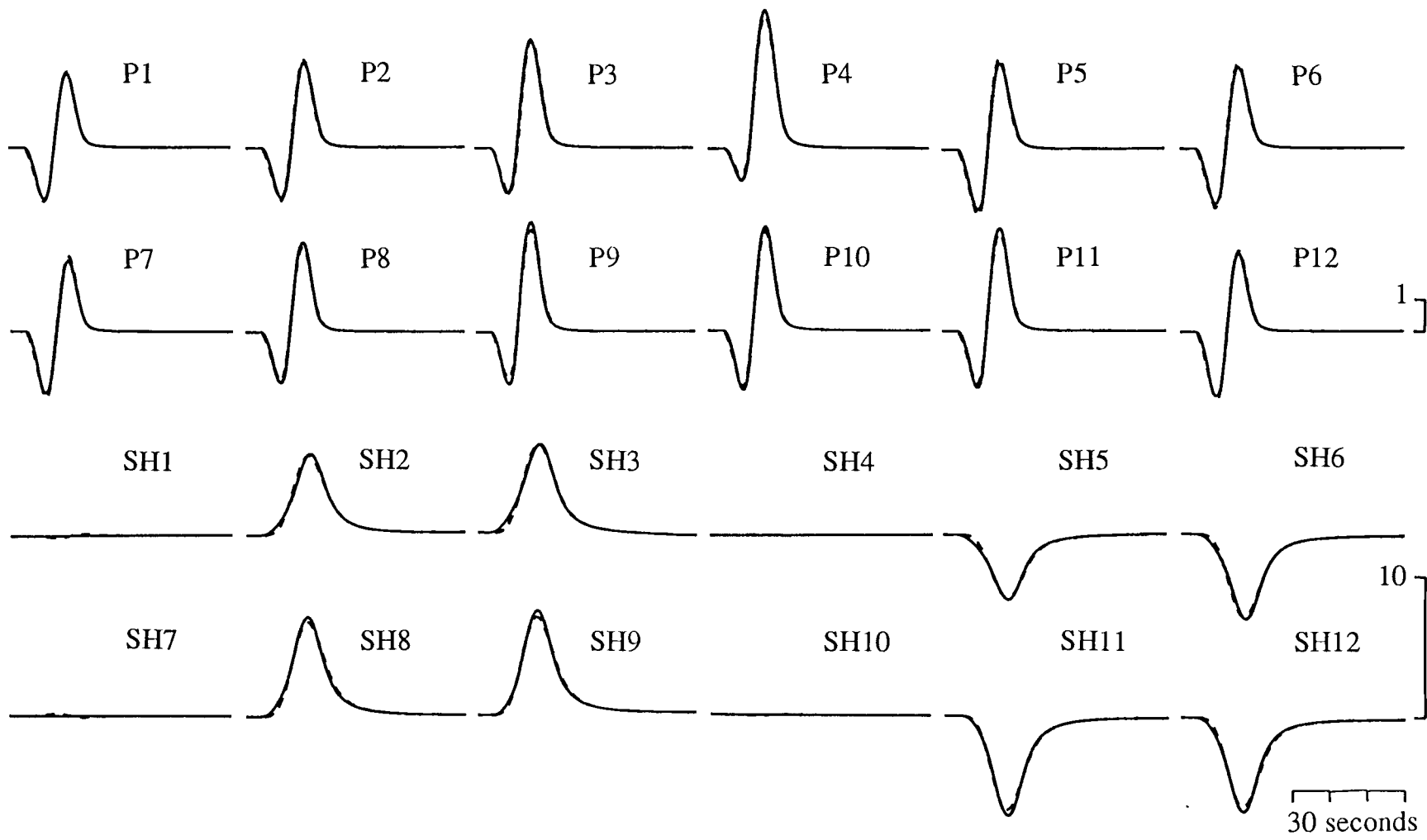
Figure 5.7   Point source solution for planar model PLUP. Solid line: PLUP; dotted line: best point source model.
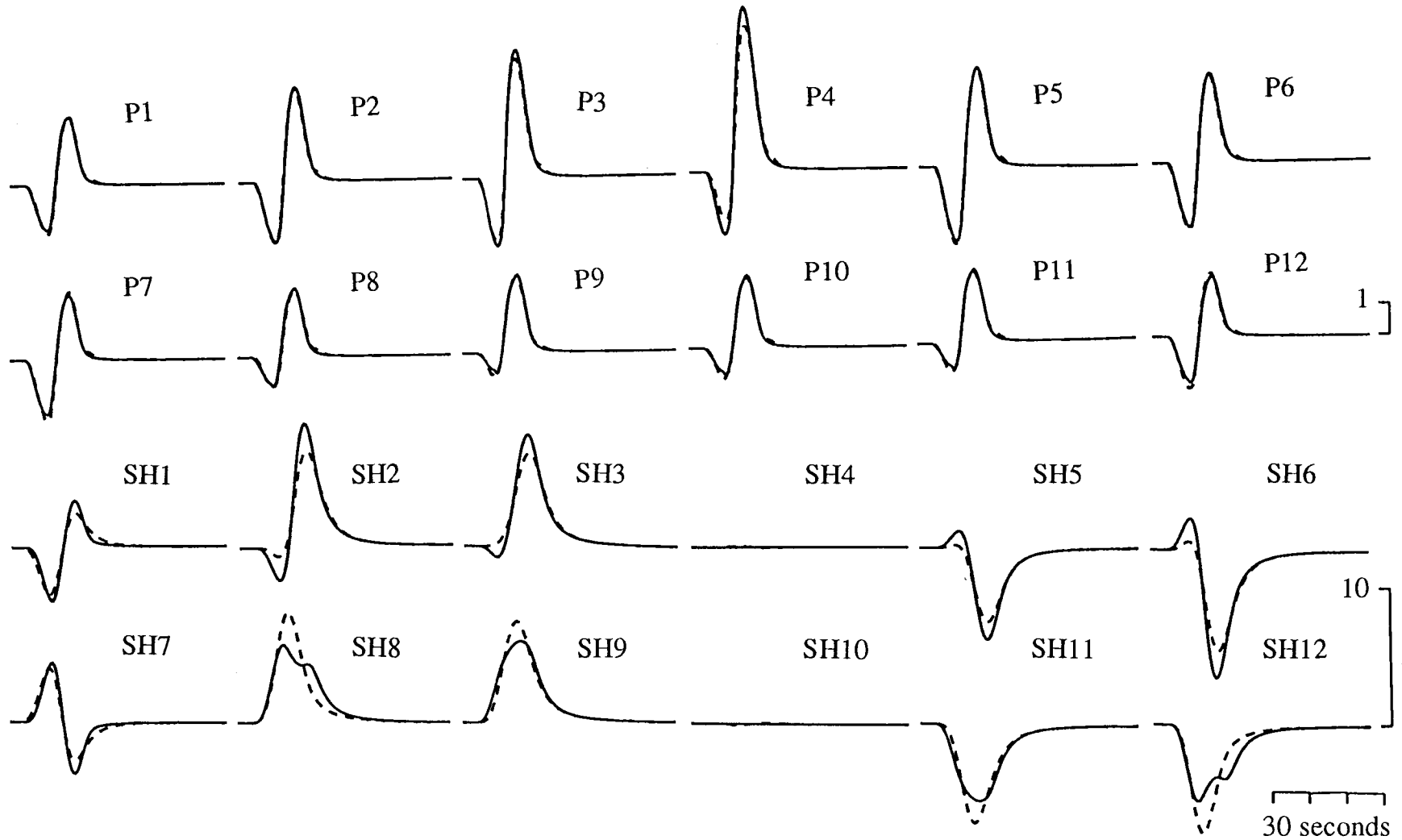
Figure 5.8   Point source solution for listric model LIUP. Solid line: LIUP; dotted line: best point source model.
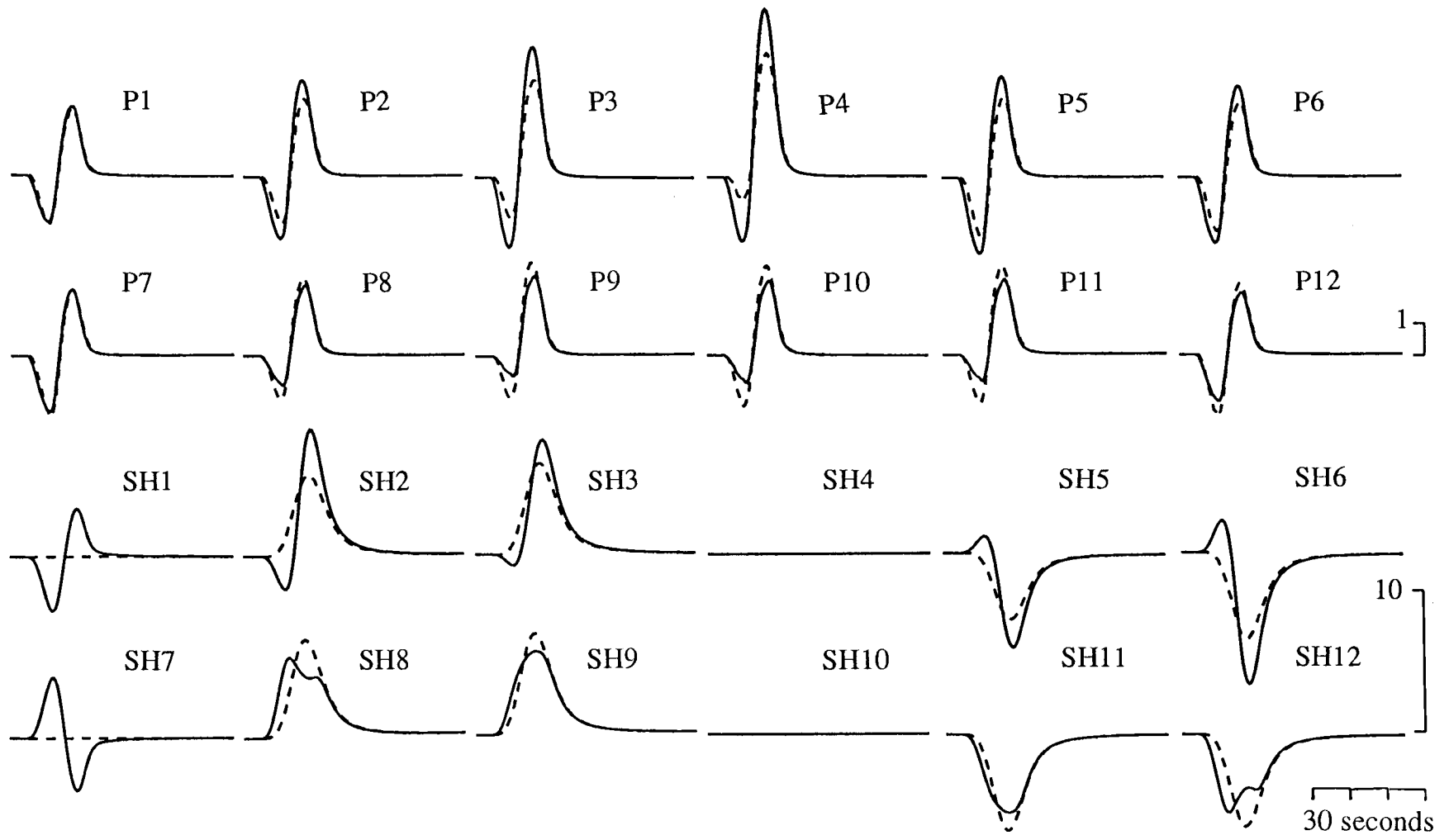
Figure 5.9   Expected (correct) centroid (dotted lines) overlain on model LIUP (solid lines). Compare with Figure 5.8.
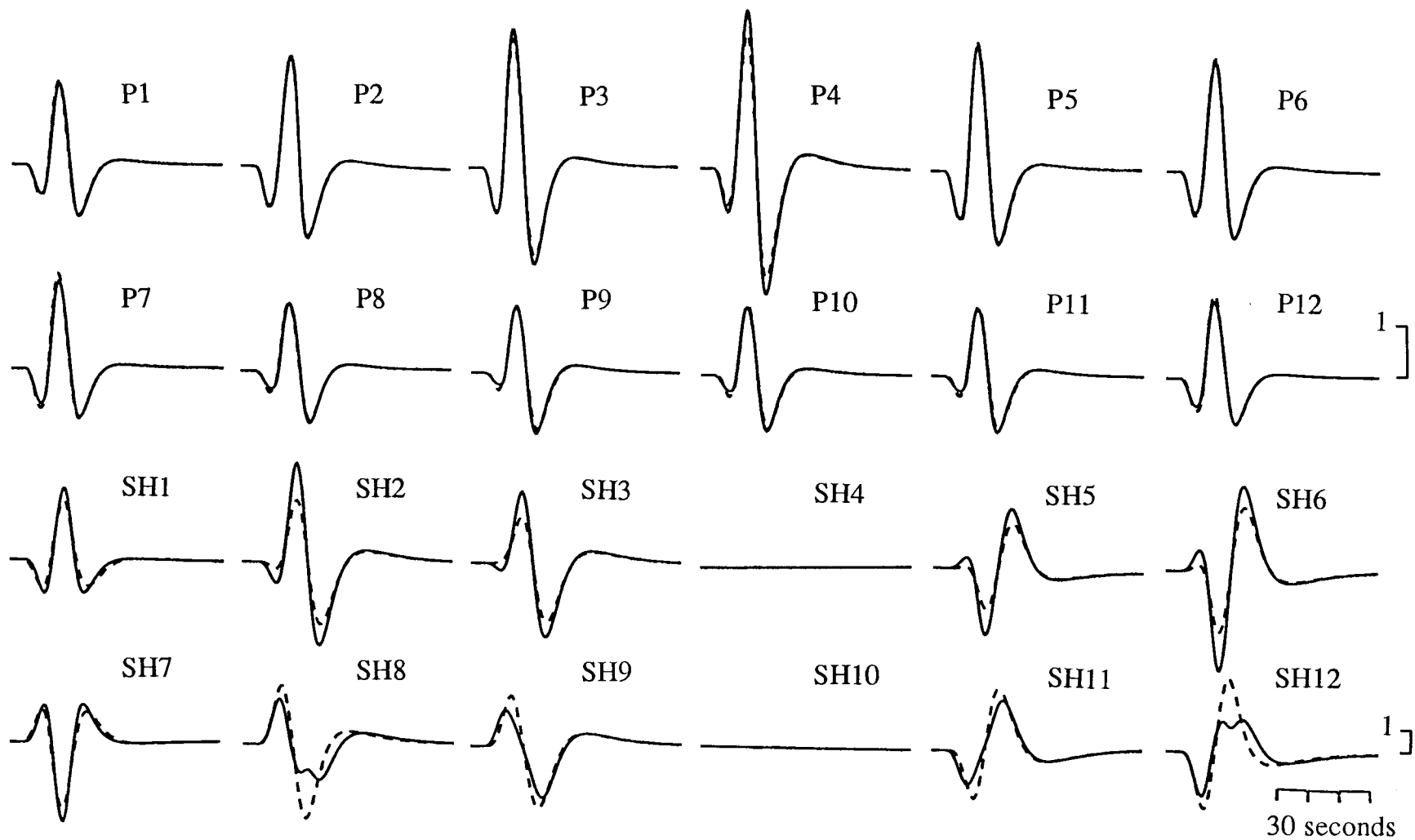
Figure 5.10 Point source solution (dotted line) for listric model LIUP-wwssn (solid line). Broadband seismograms convolved with WWSSN long-period instrument response.
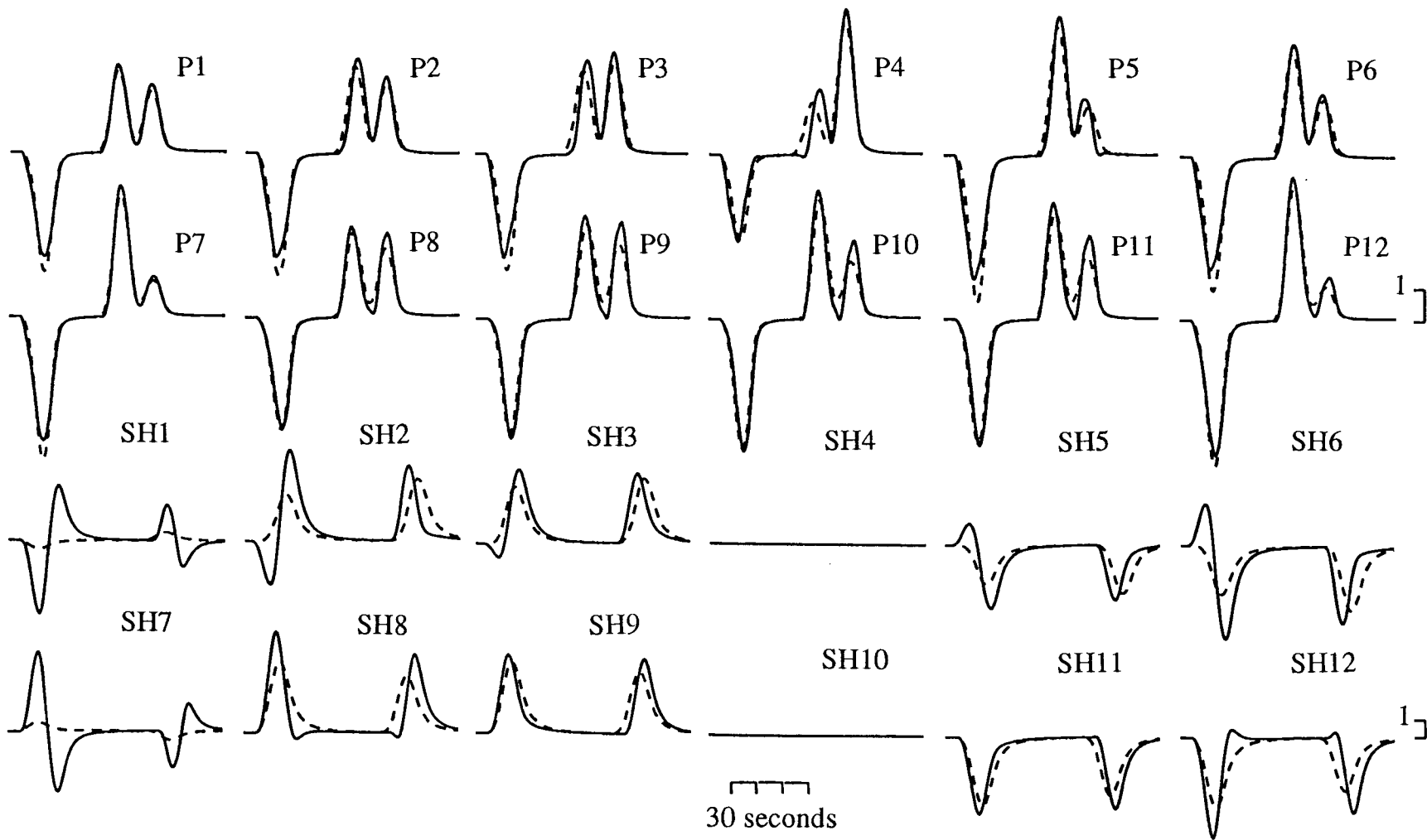
Figure 5.11 Point source solution (dotted line) for model LIUP-deep (solid line). Model LIUP shifted to a centroid depth of 100 km. Direct (P and S) and reflected phases (pP, sP, and sS) are well separated.

6. Results

6.1 Demirci, Alasehir and Gediz Earthquakes 1969-71

6.1.1 Introduction

A long sequence of earthquakes starting in March 1969 and continuing for more than 2 years occurred in the area of Gediz-Demirci-Alasehir in Asia Minor in western Turkey. Rapid continental extension has been observed in western Turkey (e.g., Westaway, 1990) and the graben system of western Anatolia, a region of complex faulting with major fault blocks bounded by normal faults (Tasdemiroglu, 1971; Westaway, 1990), is its major geological expression. A history of large normal faulting earthquakes is associated with this area (Allen, 1975) and more than 6000 aftershocks were recorded regionally following the first large Demirci earthquake of March 1969 (Ambraseys and Tchalenko, 1972). Only the two largest events, the 03/28/69 Alasehir and the 03/28/70 Gediz earthquakes caused casualties and produced observable surface faulting of several tens of kilometers in extent. Figure 6.1.1 shows the epicenters of the studied events, surface faulting associated with the two largest shocks and the fault plane solutions obtained from waveform inversion. A master event (Jackson and Fitch, 1979) and a joint epicenter determination (Dewey, 1976; North, 1977) technique have been used to relocate the teleseismically recorded aftershock sequences. The pattern of activity following the Demirci events is diffuse, an E-W (North, 1977; Jackson and Fitch, 1979) or a NW-SE (Dewey, 1976) trend have been suggested, but the small size of the source area makes it difficult to determine a direction. The Gediz aftershock sequence shows a more clear NW to SE trend (Dewey, 1976; North, 1977; Jackson and Fitch, 1979). The lack of aftershocks in the vicinity of the Alasehir epicentral region is noteworthy and enigmatic.

I have studied the seven largest events of the sequence (Table 4.1). Since the hypocenter parameters of the aftershocks were not derived from dense local network data and are therefore less reliable, I did not address the question of the depth extent of earthquakes for these events. Planar vs. listric faulting and the possibility for detachment faulting have been investigated for the Alasehir and Gediz (mainshock) earthquakes.

6.1.2 Demirci 03/23/69 and 03/25/69

<u>Demirci 03/23/69</u>

A few foreshocks occurring one day before the main shock of March 23, 1969 (M_S=5.6) mark the beginning of a sequence of earthquakes in the Demirci area which continued for the next several months. Another strong earthquake (M_S=5.5) in the vicinity of the main shock epicenter was recorded on March 25, 1969. No surface faulting was observed, but landslides and surface shaking caused considerable damage in the epicentral area. About 1700 houses were destroyed in Demirci and other towns further north in the Simav River valley (Ambraseys and Tchalenko, 1972, Canitz et al., 1982). The dominating tectonic structure is the east-west trending fault bounded Simav graben. On Landsat satellite photographs of the Simav River valley a prominent fault escarpment facing north is visible (McKenzie, 1978b). Southward dip of sediment layers in the Simav River valley may indicate domino-like block rotation of a major northward dipping fault (Westaway, 1990). Based on the distribution of damage, aftershock activity, and the structure of the Simav River valley with the river flowing along the northern boundary, Eyidogan and Jackson (1985) originally suggested that the activity was associated with a fault dipping southwards; however, Jackson (personal communication) now thinks that their interpretation was incorrect. Damage distribution is strongly related to populated areas and the aftershock epicenters are not well determined, therefore these data do not provide sufficient information to resolve the fault plane ambiguity. Contradicting structural and morphological observations do not shed light on this issue either.

The digitized long-period data were resampled with a sampling period of 0.3 s and high-pass filtered with a 3-pole butterworth filter with cut-off at 100 s; for the SH waves at AAE, NAI, BUL, WIN, and COL a cut-off of 50 s was used due to a higher noise level. The polarities of the horizontal components at the stations PRE and KBS were apparently reversed.

The simple long-period P and SH waveforms of the mainshock could be best fit by a point source located at a depth of 8.4 km with an almost trapezoidal source time function of 3 seconds duration (Figure 6.1.2). Strike, dip, and rake (values in parentheses are for the second nodal plane) are 296° (114°), 54° (36°), and 272° (267°), respectively, and the seismic moment is 6.8×10^{17} Nm (M_W=5.8). When inverting P waves only, the centroidal solution was very similar to the solution found by simultaneous inversion of P and SH waves (Table 6.1.1). Taking the uncertainties in crustal structure and the

averaging properties of the inversion into account, the first motion data agree well with the centroidal solutions (Figure 6.1.3). The agreement of the short-period first motion data with the centroid solution suggests that within the small rupture area of this event there is no significant change in fault dip. P wave modelling by Eyidogan and Jackson (1985) gives a similar orientation (112/34/270), depth (8 km), and duration (3.6 s), but a slightly higher moment (9.8×10^{17} Nm). From Rayleigh wave spectral amplitude analysis North (1977) obtains a moment of $9.1(\pm7.5) \times 10^{17}$ Nm. A first motion fault plane solution read from long-period vertical seismograms by McKenzie (1972), assuming a source in the upper mantle, is rotated and shows more right lateral slip and a steeper fault plane (70/46/242), but the data set used is rather sparse.

Demirci 03/25/69

The digitized data were resampled with a sampling period of 0.3 s, all data were high-pass filtered with a cut-off at 100 s except the P-waves for stations BUL and NOR where a cut-off of 50 s was used. The gain for station SHA as given on the WWSSN records is too small by a factor of two (1500 instead of 3000) as deduced by comparison with adjacent stations.

The large aftershock of March 25, 1969 ($M_S=5.5$) shows generally a lower signal to noise ratio than the main shock, especially for the observed S waves. This may partly be due to another small event occurring about 20 s before the large aftershock and a higher noise level during this day. S waves of many stations used seem to be quite nodal. However, similarities in wave shapes of S waves between this event and the main shock indicate a similar source mechanism. Inversion results obtained from P waves only differ significantly from simultaneous P and SH wave inversion results (Table 6.1.1), and do not satisfactorily match the observed SH waves. Inclusion of SH waves with a relatively good signal to noise ratio and wave shapes similar to the ones observed for the main shock, moves the centroid to a deeper position (9.9 km) and therefore decreases the source duration from 7 s to 5 s, the seismic moment (8.9×10^{17} Nm) becomes smaller, and the source orientation, especially the rake, changes. The centroid depth of the aftershock is probably slightly deeper than for the main shock. The preferred solution from the combined P and SH data set has a strike of 119° (308°), dip of 46° (44°), and rake of 264° (276°), respectively. The fit to the observed data for the combined P and SH data set is shown in Figure 6.1.4. Similarities in the strikes obtained for both events may indicate rupture on the same fault plane; however, antithetic faulting or faulting along subparallel faults is equally likely. The seismic moment of this aftershock (8.9×10^{17}

Nm, M_w=5.9) is actually higher than that of the main shock. Moment release appears to represent two distinct pulses of 2 s and 3 s duration. Eyidogan and Jackson (1985) from P wave modelling, find a fault orientation of 90/40/256 (288/51/281), the main difference being in strike. At a depth of 8 km and duration of 8 s they find a seismic moment of 17×10^{17} Nm. North (1977), using surface waves, also finds $18(\pm9.2)\times10^{17}$Nm, more than twice the moment I obtained. McKenzie (1972), assuming a source in the upper mantle obtains 90/40/254 (291/52/283) for strike, dip and, rake, respectively , which is also rotated with respect to my results. To test the sensitivity of the data to changes in strike, I inverted the combined P and SH data set for all of the above parameters, but kept the strike of one nodal plane fixed to 90°. The overall results are quite similar to the model where the strike was allowed to vary (Table 6.1.1), but the variance measuring the misfit increased by about 14%, indicating that the data set used is inconsistent with a 90° strike of the fault. Applying a t-test to the best-fitting model and the model where the strike has been held fixed shows that there is a statistically significant difference between the two models. A t of 1.87 (μ=1.102x10^{-3}, σ=3.276x10^{-3}, N=31) was found, indicating that at a 95% level of confidence the model where one nodal plane was held fixed at 90° is inadequate to match the data optimally. Due to a small foreshock, first motion arrivals especially for close stations and high-gain stations are often obscured, therefore the constraint provided from first motions is weak (Figure 6.1.3). The first motion data are compatible with a wide range of solutions, including the fault orientation obtained from body wave inversion, the results of Eyidogan and Jackson (1985), and McKenzie (1972). However, it is quite clear that the first motions preclude a very shallow dipping fault at its nucleation point.

Table 6.1.1 gives a summary of the results from this and other studies.

6.1.3 Alasehir 03/28/69

The upper Gediz river valley near Alasehir, approximately 80 km south of the Simav River valley, was strongly shaken by a M_S=6.5 earthquake just five days after the Demirci main shock. Heavy damage was observed in the villages located along the border of the upper Gediz River valley (Arpat and Bingöl, 1969; Ambraseys and Tchalenko, 1972; Canitez et al, 1982) and 40 to 50 people were killed (Arpat and Bingöl, 1969; Ambraseys and Tchalenko, 1972; Ritsema, 1979). Aftershocks were not observed teleseismically in the vicinity of the mainshock epicenter; however, seismic activity continued in the Demirci area further north. Allen (1975), based on Holocene fault scarps seen on satellite photographs, related the surface faulting with preexisting Holocene

faults. The Neogene basin in the hanging wall of the fault was downthrown to the north and showed about 30-36 km of surface faulting (Ambraseys and Tchalenko, 1972; Allen, 1975; Canitez et al., 1982), which was continuous along a WNW-trending 20 km long segment running from the town of Alasehir to Dereköy (Canitez et al., 1982). The epicenter determined by ISC is located close to the northwestern end of the continuous surface break, which may indicate rupture initiation at the northwestern terminus and predominantly unilateral rupture propagation towards SE. A 16 km long discontinuous segment of surface faulting runs from Alasehir southeast towards the town of Doguslar (Canitez et al., 1982). Maximum vertical displacements of about 15 cm were reported (Canitez et al., 1982).

Focal Mechanism

The digitized data were resampled with a sampling period of 0.5 s. Except for the P waves at the stations NDI (T ≤ 100 s) and BUL (T ≤ 60 s) no filtering was applied to the data. The horizontal components at PRE were reversed. The gain given on the WWSSN records for QUE was too large and for SHA too small by a factor of two and have been corrected.

The waveforms of this event are more complicated than the seismograms of the smaller Demirci earthquakes. A point source parameterization was first used to obtain the centroidal solution for this normal faulting event. The results are shown in Figure 6.1.5 and Table 6.1.2. Compared with fault plane solutions obtained from first motion data (McKenzie, 1972; Eyidogan and Jackson, 1985), the strike is slightly rotated towards a more northwestern direction (300°), a small right lateral slip component (rake: 263°) has been found, and the dip of the fault plane (41°) is slightly steeper. The shape of the source time function is roughly triangular with a relatively rapid rise and a slower decrease, the overall duration was about 15 s (Figure 6.1.6). The estimate of the seismic moment (128.5×10^{17}Nm) agrees with the moment estimate of $120(\pm 67) \times 10^{17}$Nm obtained from surface wave spectra (North, 1977). The centroid depth of 3.3 km is very shallow and shallower than for any of the other investigated earthquakes of this study. Figure 6.1.7 shows the plot of variance vs. centroid depth. The pronounced minimum at shallow depths may indicate unusual crustal structure in the vicinity of Alasehir, however, trying various different crustal models for the source region did not significantly alter or improve the fit or the results, therefore I kept the crustal half-space model. A 10% increase in the variance is probably a conservative estimate for the uncertainties in the centroidal parameters. The centroid depth is well resolved at very

shallow depths of 2-5 km. Strike, dip, and rake vary within that depth range by 8°, 3°, and 13°, respectively. The seismic moment estimates are within $103\text{-}136\text{x}10^{17}$Nm.

The centroidal solution provides a reasonably good fit, however, it fails to account for a large arrival about 20 s into the P-waves for African stations located south of the epicenter and for a double pulse in the first upward peak for Middle and North American stations located west of the epicenter; this double peak reduces to a kink in the second downward swing for north European stations and is also not matched. The shapes of the SH waves, having a frequency content shifted towards lower frequencies due to higher attenuation, are generally fit, however, amplitudes are not well matched for stations located west and north of the epicenter. More complicated source parameterizations are investigated next.

The ISC location of the epicenter in the northwestern part of the surface rupture area suggests a rupture propagating predominantly unilateral towards southeast. Line source approximations propagating either towards southeast or northwest along the strike of the fault were tested. To allow the observed 36 km of surface faulting to form during 15 s of rupture duration a rupture velocity of 2.4 km/s has been selected. As expected, a rupture model involving propagation in a northwestern direction (NW) is inferior to a southeastward (SE) propagating rupture; it fits even worse than the point source solution. Statistical testing shows that the SE model is significantly better at a confidence level of 99.5% than the NW model (t=3.387, μ=8.016x10^{-3}, σ=1.674x10^{-2}, N=50). Only the seismic moment and its distribution were included in this inversions. However, allowing also the orientation and depth for these propagating sources to vary, does not change the above conclusions. Figure 6.1.8 shows a comparison of the fits for azimuthally selected stations between the point source solution and the unilaterally propagating source models. The unilateral model still fails to produce the double pulse and the kink, respectively, for the P waves observed to the west and north; however, the widths of the pulses are closer to the observed ones. The amplitudes of the SH waves are generally matched better than for the point source solution.

In the next step a bilateral rupture model was studied. The inversion only included the seismic moment and its distribution along the fault segments away from the epicenter. I tried three different rupture speeds (1.5, 2.0, and 2.4 km/s) and the solutions were insignificantly different and all showed an improvement compared to the point source and unilaterally propagating models. The match of the synthetics to the observed seismograms is shown in Figure 6.1.8 for a rupture speed of 1.5 km/s, which accounts for the observed length of surface faulting. The kink observed for P waves at northern stations is now part of the synthetic seismograms. The double pulse observed to the west

does not show up; however, the width is now matched very accurately. The SH wave amplitudes are now well matched except for stations in North America where the fit deteriorated. The spatial moment distributions for different rupture velocities have very similar shapes. The total seismic moment is evenly distributed among the two segments which have approximately the same length for the respective rupture velocity (for slower rupture speeds, 2.0 and 1.5 km/s, the moment release along the southeastward part becomes slightly dominant). The rupture seems to first propagate towards northwest, most of the moment along this segment is released close to the nucleation point, and the rupture towards southeast is delayed by approximately 2 s.

From the distribution of the seismic moment of the bilateral rupture models there appear to be two distinct centers of moment release along the fault. Therefore a superposition of two point sources separated in space and time was tried next. First I inverted only for the seismic moment, keeping orientation, depth and relative location and timing of the subevents fixed. From the bilateral propagating models, a time delay of 2-4 s for the second subevent, and a location east-southeast at a distance of 10-20 km from the centroid of the first subevent were estimated. Inverting for the moment and moment distribution of the subevents essentially fixes their spatial and temporal relations to the estimated starting values and only small changes occur when these parameters are included in the inversion at a later step. Therefore the time delay and the spatial separation are not very well resolved. The azimuth of the second subevent, however, showed a stable direction eastsoutheast from the first subevent. The fit to the data (Figure 6.1.8) is very similar to the bilateral rupture models. Both subevents are of approximately the same size. To reproduce the two pulses for P waves at western stations it is necessary to allow the subevents to have different orientations. However, the results showed some dependence on the starting models. In general, the first subevent located in the northwest showed a more northerly strike and a small component of left lateral slip compared to the point source solution. The strike of the second subevent in the southeast became more east-west, and the right lateral strike-slip component increased. These results may be artifacts of the interplay of the inversion parameters and therefore I prefer the simpler, although slightly less well fitting, models.

In summary, the size of this earthquake and the more complicated waveforms which cannot be matched by a simple point source favor a model incorporating the finiteness effects. Unilaterally propagating ruptures towards southeast improve the fit slightly, however, a bilateral rupture model more adequately describes the data. The bilateral rupture model and the two point source description are almost equivalent and the results are very similar. These two models provide the correct width for the P waves observed at

American stations, but not the double pulse; they also produce the kink in the second downswing at observatories located north of the epicenter. Similarly the SH amplitudes and waveforms are best matched by these two models. This result is in agreement with the first two subevents of the model presented by Eyidogan and Jackson (1985), the relative locations and time delay are very similar. They obtain a double pulse at the North American stations because their first two subevents have slightly different orientation, however, these orientations are opposite to the ones inferred from the inversion of the data in this study. Their estimate of the seismic moment for these two sources of 106.2×10^{17} Nm is very close to the point source value (128.5×10^{17} Nm) of this study.

Short Period First Motion Data

The short period first motion data are in broad agreement with the centroidal results (Figure 6.1.9 solid lines). However, in order to account for the polarity at ATU (clear down) and the amplitudes of the first half cycle of the long period records at regional distances a small change in mechanism is necessary. A fault plane solution compatible with the short and long period first motion data is shown in Figure 6.1.9 (dotted lines). The fault trend is rotated by 5°, the dip is slightly shallower (39°), and the slip is left-lateral (280°) instead of right-lateral compared to the centroid solution. Uncertainties in crustal structure and the take-off angles of close stations influence the exact positions on the focal sphere, and may bias the first motion solution slightly.

A shallowing of the fault is precluded by the short period first motion data, assuming that the short period data sample the fault at the nucleation point at the base of the fault.

Detachment Faulting

None of the models described so far can explain the large amplitude arrivals of the P wave records about 20 s after the first motion onset observed at African stations located south of the epicenter. To explain these arrivals, Eyidogan and Jackson (1985) proposed a detachment-type source with a very shallow dipping fault plane and a long source time function located in deeper parts of the crust, near the brittle-ductile transition zone (Table 6.1.2). Waveforms at stations close to the steeply dipping auxiliary plane would not change much, whereas stations away from either nodal plane would be affected more. Eyidogan and Jackson (1985) did forward modeling of the wave shapes of the P waves, but they did not include the amplitude information and did not utilize the information provided by the SH waves at all. I recalculated the synthetic seismograms for their final

solution, which includes four subevents, the last two of them being low angle detachment faults, to investigate if this model can account for the observed amplitudes and if the SH waves are also matched (Figure 6.1.10). The P waves fit reasonably well, however, the amplitudes for the late arrival are not matched at African stations and some arrivals are strongly out of phase; such model would be eliminated by a formal inversion. The SH waves are not matched; the synthetic seismograms are too complicated and are out of phase and ringy at some stations.

Before rejecting the hypothesis of seismogenic slip along a detachment surface for this earthquake, it is certainly necessary to investigate further. A second point source resembling a pure normal faulting earthquake and with the strike of the centroid was added to the point source solution at twice the depth of the centroid and located at the down-dip projection of the main shock. A long source time function was assigned to the detachment source and inversions for the seismic moment and its distribution were carried out for models with a 0° and 10° dipping fault plane, respectively (Table 6.1.2). If a detachment source is required by the data, the solution should improve significantly even without the precise knowledge of the detachment dip. However, the inversion results for both models show no significant improvement and the large P wave arrivals at African stations are not matched. Some very low-level moment release of long duration on a detachment cannot be excluded by my data. However, the large amplitude late arriving energy especially at African stations, which was interpreted by Eyidogan and Jackson (1985) as originating from a detachment, is clearly incompatible with such a mechanism. Most likely, this arrival is due to crustal and upper mantle effects as will be discussed below.

Down-Dip Fault Geometry

To examine the fault surface for the presence of curvature, three point sources were distributed along the width of the fault to sample different depth segments of the fault. Following the procedure described in Chapter 3, three subsources were evenly distributed along the fault width at 1.1, 3.3, and 5.5 km depth. Upward propagating rupture was assumed and the subsources were delayed by 1.7 s with respect to each other, and a horizontal distance of 2.6 km at an azimuth of 210° separates them spatially. The strike (300°) obtained from the point source solution was assigned to each subsource. The seismic moments and rakes for the individual subsources were chosen such that the combination of the subsources results in exactly the same moment tensor as the point source. For a planar model, all subsources have the same dip obtained from the

centroidal solution, while for models with listric curvature, i.e. decreasing fault dip with depth, the shallowest source is steeper, the intermediate is held to the point source dip and the deepest source is less steep. Table 6.1.3 gives the parameterizations for some of the fault models.

For the Alasehir earthquake, the spatial and temporal separations of subsources for models with an upward propagating rupture are very small, due to the shallowness of the centroid depth, and it is therefore expected that the effects of fault geometry are very small and difficult to detect. Arrivals from different parts of the fault will be more separated for earthquakes with a larger fault width. The results of the distributed fault models where the curvature was prescribed are summarized in Table 6.1.4. Figure 6.1.11 shows the fit to the data at azimuthally selected stations for the planar model PL, a convex upward model LO4 with a 40° increase, and models LI3 and LI6 with a 30°, and 60° decrease of fault dip with depth. The variations seen for the P waves are only minor and the residuals for some stations are actually slightly smaller for the listric cases. The improvements seen for the SH waves are more obvious, however, are also azimuth dependent. SH waveform fits for stations to the west and northwest are worse for models with curvature, a 60° decrease of dip with depth is certainly precluded by the SH wave fits. Figure 6.1.11 shows stations which are the most sensitive to curvature, yet the effects are relatively small and only stations at certain azimuths clearly indicate that the SH waves are incompatible with large curvatures. Models which have smaller changes of fault dip with depth, of course, generate waveforms which are even less discernable from the fit of the planar case, therefore it is very difficult to estimate solely by eye which fault curvatures are 'precluded' or 'allowed' by the data. Applying a statistical test provides a means to discern the models, however, it is certainly advisable to use a very conservative estimate, i.e., a very high confidence level according to the t-test, before rejecting some of the models. From the data it cannot be excluded that the dip of the fault becomes steeper with depth. For a 40° increase of fault dip (model LO4), the planar model is only at the 75% level of confidence better, which is not sufficient to exclude model LO4. A 20° decrease of fault dip with depth (model LI2), however, produces a solution which is at the 95% confidence level worse than the planar case. Therefore a bound of concave upward listricity of 20° can be deduced for the Alasehir earthquake.

In a second set of tests, the fault dips of the subsources and their seismic moments were allowed to vary in the inversion after a stable distribution of the (fixed) moments for each subsource was reached. The resulting dip and moment estimates for each subsource for three starting geometries (planar, 40° concave, and 40° convex) are shown in Table 6.1.5. The results from different starting geometries are consistent despite the shallow

character of the earthquake and the proximity of the subsources to each other. The estimates for the shallowest source (1.1 km) are probably not reliable due to the insensitivity of the excitation functions at very shallow depths. The deeper sources provide probably a better estimate of existing fault curvature. A steepening of the fault seems more likely than flattening, which is consistent with the above results.

In summary, the small rupture width associated with this earthquake lumps contributions from different parts of the fault together. This severe overlap degrades the resolution of the parameters and hence the results must be viewed with caution. Some small amount of listric curvature of the fault surface is not precluded by the data, however, subhorizontal flattening of the fault is clearly not allowed. The distributed source tests indicate that, more likely, the fault steepens slightly with depth. However, neither the short period first motion data nor the centroidal solution support a significant change of fault dip at deeper parts of the fault.

Average Displacement

The average displacement derived from the seismic moment estimate of the point source (128.5×10^{17}Nm), assuming a fault length of 36 km, fault width of 10.5 km, and a rigidity of 3.4×10^{10} N/m^2, is 1 m, this is incompatible with the observed surface ruptures (20-25 cm displacement). The centroid depth is well resolved and the observed and estimated displacements cannot be reconciled even if the fault length is significantly longer than 36 km. It can be speculated that the ground displacement observed in alluvial deposits (see e.g., Arpat and Bingöl, 1969) was attenuated and distributed over a broader area. Geodetic measurements, however, which could substantiate distributed deformation are not available according to Arpat and Bingöl (1969). The possible flattening of the fault at shallow depths would also cause vertical displacements to become relatively smaller. Another possibility is that most of the moment release was confined to the deeper parts of the (shallow) fault.

6.1.4 Gediz Main Shock 03/28/70

A severe earthquake of magnitude M_S=7.2, the largest studied in this thesis, struck the Gediz area approximately 70 km east of Demirci. More than 1000 people lost their lives and many buildings collapsed or were heavily damaged (Tasdemiroglu, 1971; Ambraseys and Tchalenko, 1972; Ritsema, 1979; Canitez et al., 1982). Areas of most

severe damage were mainly restricted to regions with Neogene outcrops in the Gediz-Emet basin, where landslides were particularly abundant (Tasdemiroglu, 1971).

Approximately 50 km of complicated surface faulting, mostly following pre-existing faults or zones of weakness, were mapped by Tasdemiroglu (1971) and Ambraseys and Tchalenko (1972). An east-west trending fault scarp with the northern block downthrown and a more complicated approximately north-south trending en-echelon surface break structure with the eastern part downthrown are predominantly of normal faulting type. Maximum vertical displacements of up to 220 cm and maximum left-lateral displacements of 30 cm were measured (Ambraseys and Tchalenko, 1972), but these values were highly variable along the strike (Tasdemiroglu, 1971; Ambraseys and Tchalenko, 1972) and may have been accentuated by creep or aftershock activity (Ambraseys and Tchalenko, 1972).

A long sequence of aftershocks followed the main shock. Several aftershocks were large enough for long-period teleseismic body wave analysis and will be described in the next section. Because no local network was set up to record aftershocks, only regionally and teleseismically recorded aftershocks with less precise hypocenter determinations are available. Several workers (Dewey, 1976; North, 1977; Jackson and Fitch, 1979) relocated parts of the aftershock sequence. Dewey (1976) suggested that the epicenters of earthquakes in this region are systematically mislocated northwards by up to 16 km. The aftershock activity shows a broad northwest-southeast trending distribution about 100 km long (Dewey, 1976; North, 1977; Jackson and Fitch, 1979), which is significantly larger than the length of observed surface faulting. The lineation of aftershocks cuts obliquely across the area of complex surface breaks. Aftershock activity was concentrated NW and SE of the main shock epicenter (North, 1977; Jackson and Fitch, 1979). The three aftershocks studied here are located in the vicinity of the southeastern termination of surface ruptures associated with the main shock.

Jackson and Fitch (1979) suggested that a buried NW-SE trending fault, following the trend of the aftershock zone, is the primary feature, whereas the surface faulting followed secondary pre-existing zones of weaknesses near the surface.

Focal Mechanism

The body wave data were resampled with a sampling period of 0.5 s after digitizing and no filtering was applied. The horizontal components of station PRE had reversed polarities.

The best fitting point source solution is shown in Figure 6.1.12 and the source parameters are listed in Table 6.1.6. The fault orientation agrees well with the first motion solution obtained by McKenzie (1978b). The seismic moment estimate (505.2×10^{17}Nm, M_w=7.1) is similar to that found by Eyidogan and Jackson (1985) of (415×10^{17}Nm, sum of the first two subevents of their solution corresponding to my point source) and North (1977) ($300 \pm 96 \times 10^{17}$Nm).

The centroid is placed at 7.7 km depth. Figure 6.1.13 shows the variance of the misfit as a function of centroid depth. Using a variance increase of 10% as a crude measure, an acceptable centroid depth is between 5 and 12 km depth. In this depth range, strike, dip, and rake vary by 4°, 1°, and 5° respectively, and the seismic moment estimate ranges from 543×10^{17}Nm at 5 km to 408×10^{17}Nm at 12 km. The seismograms of the SH waves proved to be especially sensitive to the fault dip, and even small deviations were incompatible with the data. The duration of the source time function is about 21 s (Figure 6.1.14). The double downward pulse at the start of the P waves is caused by slow initial moment release, which increased abruptly approximately 3 s after the onset. The point source model is doing a surprisingly good job in fitting the data considering the complicated pattern of surface faulting.

As expected from the location of the main shock epicenter in the central region of the surface ruptures and the aftershock distribution (North, 1977; Jackson and Fitch, 1979), unilaterally propagating rupture models towards northwest and southeast did not improve the fit. A bilaterally propagating rupture (v_r = 1.5 km/s), where the orientation and depth were held at the point source values, improved the fit slightly. However, a two point source model or a bilateral rupture model where the orientations of the subevents are free, provides the best fit. In both cases (bilateral and two sources), the orientation of the first subevent is almost unchanged compared with the point source estimate, whereas the second rupture with a smaller seismic moment is trending almost purely north-south (Table 6.1.6). These models are in agreement with the observed surface ruptures. The improvement of the fit compared to the point source description is confined to later parts of the waveforms, where the complex model starts to fit a fourth downswing observed at American and European stations and generates the sharper second upswing observed at African stations.

Short Period First Motion Data

The fault plane solution is well constrained from the short period first motion data, and only the station HLW is slightly inconsistent with the centroid mechanism (solid line

in Figure 6.1.15). Uncertainties in source crustal structure and the take-off angle for the departing rays could probably account for this difference. However, a slight rotation of the fault towards NW (315°) and a small left lateral slip component (280°-285°) is consistent with the short period readings and the amplitudes of the first half cycle of the long period data at regional distances.

A significant change in fault dip is not supported by the first motion data.

Detachment Faulting

Faulting on a shallowly dipping detachment has been investigated in the same way as described in Chapter 3.2. Detachment type mechanisms with dips of 0° and 10° and allowed a long duration of moment release showed only a minor moment release and the improvement to the fit was insignificant. The model was not able to generate observed large P wave arrivals about 30 s after the onset at stations located northwest and north of the epicenter while matching the SH waves satisfactorily. The simple SH waveforms do not allow a complicated source time history. A complex source model proposed by Eyidogan and Jackson (1985), where five subevents are considered with the last being a 'detachment type' source, fits the shapes of the P waves reasonably well, but the amplitudes are not matched. The model breaks down completely, however, when the SH waves are included, whose amplitudes and waveshapes are not matched at all (Figure 6.1.16).

Down-Dip Fault Geometry

The centroid depth determined for the Gediz main shock (7.7 km) is much deeper than for the Alasehir event (3.3km) and therefore the expected width of the zone which ruptured during the earthquake is probably twice the width estimated for the Alasehir earthquake. Contributions from different parts of the fault should be sufficiently separated in space and time to examine effects caused by different fault geometries. The centroidal solution has been used in the same way as described in Chapter 3.2 to distribute three subsources evenly along the width of the fault at 2.6, 7.7, and 12.8 km depth. The subsources are laterally evenly spaced at 5.9 km intervals along an azimuth of 214° with the deepest subsource at the northeastern end.

In the first set of tests, a rupture propagating up-dip was generated and the second and third subsource are delayed by 2.6 and 5.2 s with respect to the first one and the curvature was prescribed. Figure 6.1.17 shows the fit to the waveforms for azimuthally

selected stations for four models: planar (PL), concave upward with 30° and 60° change in fault dip (LI3, LI6), and convex upward with 40° change in fault dip (LO4). Differences between the PL- and LO4-model are very small. P wave residuals are similar and only very subtle differences exist; the SH waves, however, show consistently a better overall fit for the planar model, especially for stations to the west and north of the epicenter (e.g., SCP, COL). Model LI6 can be rejected solely on the basis of P waves, since the polarities are wrong at the onset for stations to the south and the amplitudes and phase relations for the early parts of the P waves are generally less well matched than for the planar model. These discrepancies, however, are still small compared to the differences between the observed SH waves and the SH waves predicted by the model LI6.

For models with less listric curvature (e.g., LI3 model in Figure 6.1.17) the misfits are generally still larger than for the planar models, however, by eye it becomes very difficult to distinguish the quality of the fits. Therefore, a statistical test as described in Chapter 3.4 was applied to discern acceptable solutions from unacceptable ones. Results can be found in Table 6.1.7 (upper part). At the 95% level of confidence obtained from the t-test, it can be concluded that even a decrease in fault dip as small as 10° (along a fault more than 20 km wide) is not allowed by the data.

In the next set of tests, the dip is allowed to vary freely. The seismic moments of the subsources were constrained and, initially, only their moment distributions were determined. After a preliminary distribution was found, the seismic moments and fault dips of each of the subsources were also included. The results from models with initial planar, 40° concave, and 40° convex geometry are remarkably similar (Table 6.1.8). Despite of different initial fault curvatures, all models converge to an essentially planar geometry. The deepest and the intermediate depth subsources gave estimates varying by only 1° from the dip estimated from a single point source. The fault dip of the shallow subsource showed somewhat wider variations influenced by the starting model; however, the estimates of the dip in the uppermost part of the fault do not indicate significant steepening. The fault seems to be very planar, but most of the moment release seems to have occurred in the central part of the fault; this explains why the centroidal solution provides a good fit. A smaller moment release (about 1/3 of the overall moment) has been found for the lower part. The observed surface displacements are consistent with the moment release found for the shallowest subsource. Assuming a fault length of 50 km, fault width (only upper part!) of 8 km, rigidity of 3.4×10^{10} N/m^2, and seismic moment of 1×10^{19} Nm, provides an estimate of the expected average displacement of

about 0.7 m, the maximum vertical displacement measured was 2.2 m (Ambraseys and Tchalenko, 1972).

A bilaterally propagating rupture model has been used to further investigate the sensitivity of the conclusions derived above. Rupture nucleates at the intermediate depth source and the shallow and deep subsource are both delayed by 2.6 s. In Figure 6.1.18 different models are compared, the results of statistical testing are listed in Table 6.1.7 (lower part). The fits for the models differ less than for the case of upward propagating ruptures. Significant differences visible by eye are basically restricted to the SH waves recorded at stations to the west and north (e.g. SCP, COL). The planar fault geometries provide an equally good fit for ruptures starting at the base or at the center of the brittle layer. Statistical testing (Table 6.1.7) indicates a decrease in resolving power compared with a model simulating up-dip rupture propagation, which is expected, and a slightly wider range of possible fault curvatures is allowed. Using again the 95% confidence limit from the t-test to separate acceptable from non-acceptable models, a 20° increase or decrease of fault dip with depth is not allowed by the data even for a rupture nucleation in the center of the seismogenic layer.

Based on the results presented above there is no evidence for a significant shallowing of the fault surface with depth.

6.1.5 Gediz Aftershocks 04/16/70, 04/19/70, and 05/25/71

Many large aftershocks followed the mainshock of March 28, 1970. I studied three aftershocks with $M_w \geq 5.5$, all of which occurred in close spatial proximity to each other in the southwestern part of the aftershock zone.

Gediz 04/16/70

After digitizing, the seismograms were resampled with a sampling period of 0.3 s and high-pass filtered with a cut-off of 100 s. For the P waves from the stations KBL and QUE, and the SH waves from POO and AAE, a 50 s cut-off was applied. The gains at QUE (too large) and NIL (too small) were off by a factor of two, and the horizontal components at NIL were reversed.

The 04/16/1970 event is the smallest of the events studied; only stations relatively close to the epicenter and stations with a high gain showed a sufficient signal to noise ratio. The azimuthal coverage is good despite the smaller number of observations incorporated in the inversion. Differences in the radiation pattern between P and SH

waves make the usage of SH waves especially valuable in the case of a limited station coverage, where the SH waves further constrain the centroidal solution. A seismic moment of 2.6×10^{17} Nm (M_w=5.5) was found for a centroid depth of 7.8 km and source duration of 3 s. The orientation is 283/38/282 for strike, dip, and rake and agrees with the trend of the aftershock distribution. The fit to the waveforms is shown in Figure 6.1.19. The first motion data are compatible with the centroid orientation (Figure 6.1.20). The results of Eyidogan and Jackson (1985), who used the first motion fault plane solution determined by McKenzie (1978b), agree with my results (Table 6.1.9).

Gediz 05/25/71

The digitized waveforms were resampled (T=0.3 s) and low-pass filtered with a cut-off at 100 s. A 50 s and 35 s cut-off, respectively was applied to the data from stations SHK and ANP, due to a higher long-period noise level. The gains for the stations NIL (too small), QUE (too large), and SNG (too large) were off by a factor of two and have been corrected.

More seismograms with higher signal to noise ratio were available indicating a larger seismic moment release for this event. The point source solution satisfies the first motion data (Figure 6.1.20). The moment is 6.5×10^{17} Nm (M_w=5.8), the source duration is 3 s, and the depth of the centroid is 6.6 km. The strike (297°) of this aftershock is similar to the one obtained for the main shock, and is slightly more northerly than the two other aftershocks studied. The waveforms and their fits are shown in Figure 6.1.21. Eyidogan and Jackson (1985) found a very similar result, using the first motion solution from McKenzie (1978b) (Table 6.1.9).

Gediz 04/19/70

The data were resampled with a sampling period of 0.3 s. A high-pass filter (T≤100 s) was applied to all stations except ANP where a cut-off of 35 s was used. The horizontal components at PRE and NIL showed reversed polarity. The gain at NIL was increased by a factor of two.

The earthquake of 04/19/1970 was the most complicated of the aftershocks. The steeply northward dipping nodal plane is well constrained by first motion data (Figure 6.1.20). The best point source solution found for this event (Table 6.1.9, Figure 6.1.22), however, does not satisfy the first motion data and shows a more shallowly northward dipping nodal plane. Since the moment release occurs in two distinct phases, I

attempted to model the observed waveforms with a two source model. A second point source located at the same position as the first one was introduced, the duration of the first subevent was restricted to roughly coincide with the first phase of the moment release observed for the centroidal solution, and the second event was delayed to account for the second phase of the moment release. Since the depth of the subevents makes the inversion non-linear, I tried different source models while keeping the depth of the individual subevents fixed such that the centroidal depth remained unchanged at 9.6 km depth. Only the mechanism and the seismic moment were allowed to vary. The northward dipping nodal plane of the first subevent becomes steeper in all tested models, which is consistent with the first motion data. The model Sf, where the first subevent is shallower than the second is insignificantly (t=0.71, $\mu=0.554\times10^{-4}$, $\sigma=4.709\times10^{-4}$, N=36) better than the model Cf, where both depths were fixed to the centroidal depth. However, model Df, where the first subevent is deeper, is inferior to the model Cf at a 97.5% level of confidence (t=2.20) and to model Sf at a 90% level of confidence (t=1.56). Starting with model Cf and also inverting for the depth of the individual events yields a result very similar to model Sf. The data do not provide sufficient information to resolve the lateral positions of the two subevents. If both subevents occurred on the same northward dipping fault, this result indicates the possibility of flattening of the fault at depth. Since the lateral distribution is not known, alternative explanations are equally likely. Steepening of an antithetic fault with depth or complicated internal deformation along two different fault planes in a highly faulted and strained region are also possible. North (1977) and Jackson and Fitch (1979) found that aftershock activity is concentrated away from the mainshock epicenter. This could indicate that the rupture of the main shock ran into barriers at its northwestern and southeastern termination, e.g., manifested in the topographic high at the southeastern end of the surface rupture, and these regions released some of the accumulated strain in form of aftershocks.

This region is expected to have a highly complicated fault pattern (e.g., King and Nábělek, 1985). It is also interesting that the rupture appears to have propagated downward from the first subevent, not upward as would be expected for simple models based on the strength of the crust. This perhaps can also be explained in terms of expected heterogeneity of the barrier regions.

Figure 6.1.23 shows the fit of the data for model Cf. The improvement compared to the point source solution (Figure 6.1.22) is quite remarkable, especially for SH waves observed at North American and European stations. The combined moment of these two subevents corresponds to a moment magnitude of 5.9.

The first motion solution of McKenzie (1978b) is very similar to the orientation of the first subevent obtained from inversion. Eyidogan and Jackson (1985) also use a multiple event model for this aftershock. Their first two subevents are consistent with the results presented here. To account for complexities in later parts of the waveforms they add two more relatively shallow dipping sources. Their station distribution was very one sided, with 7 out of 9 stations located to the east of the earthquake and they did not incorporate SH waves. Including SH waves and additional P waves improves the azimuthal coverage of my data set significantly. However, a third source placed at greater depth did not improve the fit significantly and only a minor moment release is allowed.

6.1.6 Late Large Arrivals - Structural Effects

Detachment type faulting has been investigated for the Alasehir event and the Gediz mainshock. Later arrivals in the P waves about 20-30 s after the onset with a pronounced azimuthal dependance of their associated amplitudes have been interpreted by Eyidogan and Jackson (1985) as manifestations of seismogenic slip along a detachment surface. Including SH waves into their models showed that these complexities are not supported by the relatively simple observed SH waveforms (Figures 6.1.10, and 6.1.16). Additional models with a detachment type source were tested. However, no significant moment release could be found for either of the earthquakes, and the fit to the waveforms did not improve. Large arrivals at African stations were not matched by any of the models. Most probably they are due to propagation effects and not due to unmodelled source complexities. This is supported by Figure 6.1.24 which shows that the identical arrival can be observed for all events of the Gediz sequence at station AAE: it occurs at the same time relative to the maximum positive amplitude with only slight variations in the relative amplitude.

Effects of the crustal structure in the source region were investigated for the Alasehir earthquake. Layered models and especially layered models including a low-velocity zone improved the fits in the later parts of the seismograms slightly. However, correct amplitudes of the large arrivals were not generated by any the tested structures.

Table 6.1.1 Source Parameters of the Demirci Earthquakes

	strike deg	dip deg	rake deg	moment 10^{17}Nm	depth km	duration s	σ
03/23/69							
P	294	58	276	7.1	8.8	3	
P+SH (preferred)	296	54	272	6.8	8.4	3	
E&J	112 (292)	34 (56)	270 (270)	9.8	8	3.6	
McK, N	287	51	296	9.1±7.5			
03/25/69							
P	333	56	294	15.0	6.6	7	
P+SH (preferred)	307	44	276	8.8	9.9	6	0.26
P+SH	283*	43	280	8.9	10.1	6	0.30
E&J	90 (288)	40 (51)	256 (281)	17.0	8	8	
McK, N	288	51	281	18.0±9.2			

P - inverted only P waves. P+SH - inverted both P and SH waves. E&J - P waveform modelling by Eyidogan and Jackson (1985), values in parantheses are for second nodal plane. McK - first motion solution from KcKenzie (1972). N - moment estimate from North (1977). σ - normalized variance of residuals. "*":- strike of second nodal plane fixed to 90°, strike obtained by McK, E&J.

Table 6.1.2   Source Paramaters of the 03/28/1969 Alasehir Earthquake

	strike deg	dip deg	rake deg	moment 10^{17}Nm	depth km	duration s	Δt s	Δr km	Δaz deg	σ
P S	300	41	263	128.5	3.3	15				0.31
S E	300*	41*	263*	123.3	3.3*	15*				0.30
N W	300*	41*	263*	120.7	3.3*	15*				0.35
B I										0.29
southeast	300*	41*	263*	68.7	3.3*	12				
norhtwest	300*	41*	263*	54.4*	3.3*	12	2			
T S										0.29
	300*	41*	263*	56-71	3.3*	12				
	300*	41*	263*	58-71	3.3*	12	2-4	12-16	100-110	
DE	300*	0*	270*	27.2	6.7*	29	12	3.9*	30*	0.30
	300*	10*	270*	54.4	6.7*	39	12	3.9*	30*	0.30
E&J	281	34	270	62.5	6	6				
	318	32	302	43.7	6	6	3.8	11.4	104	
	281	2	270	31.2	10	8	9.0	11.0	62	
	281	10	270	62.5	10	14	14.0	16	73	
McK, N	287	29	270	120±67						

PS - point source solution. SE, NW - unilateral rupture towards southeast and northwest, respectively, rupture velocity $v_r = 2.4$ km/s. BI - bilateral rupture, $v_r = 1.5$ km/s. TS - two point source model. DE - detachment source with 0° and 10° dipping surface, respectively, locations derived relative to point source solution PS. E&J - P waveform modelling by Eyidogan and Jackson (1985), first subevent from first motion data. McK - first motion solution from KcKenzie (1972). N - moment estimate from North (1977). Δt, Δr, Δaz - time delay, distance and azimuth of subevent with respect to first subevent. σ - normalized variance of residuals. "*" - fixed.

Table 6.1.3 Parameters for some fault models of Tables 6.1.4, and 6.1.5.

	strike deg	dip deg	rake deg	moment 10^{17}Nm	depth km	duration s	Δt s	Δr km	Δaz deg
PL									
#1	300	41	263	42.8	5.5	12			
#2	300	41	263	42.8	3.3	12	1.7	2.6	210
#3	300	41	263	42.8	1.1	12	3.4	5.2	210
LO4									
#1	300	61	264	50.7	5.5	12			
#2	300	41	263	50.7	3.3	12	1.7	2.6	210
#3	300	21	264	50.7	1.1	12	3.4	5.2	210
LI4									
#1	300	21	266	64.1	5.5	12			
#2	300	41	263	64.1	3.3	12	1.7	2.6	210
#3	300	61	266	64.1	1.1	12	3.4	5.2	210

PL - planar fault model. LO4 - listric fault model with 40° increase of fault dip with depth (+40°). LI4 - listric fault model with 40° decrease of fault dip with depth (-40°). Δt, Δr, Δaz - time delay, horizontal distance and azimuth of subevent #2 and #3 with respect to first subevent. A kinematic rupture velocity of 3.1 km/s was assumed to calculate Δt.

Table 6.1.4   Alasehir, Down-Dip Geometry: 1. Dip and Seismic Moment Fixed.

	curvature deg	σ	t		μ 10^{-3}	s 10^{-2}	Mo 10^{17}Nm	rake deg
LO4	+40	0.314	**0.95**	•	1.06	0.78	50.7*	264*
LO2	+20	0.307	**-0.50**	•	-0.32	0.45	44.6*	263*
PL	0	0.308		•			42.8*	263*
LI2	-20	0.315	**1.75**		1.18	0.48	44.6*	263*
LI3	-30	0.324	**2.87**		3.05	0.75	47.0*	263*
LI4	-40	0.336	**3.31**		5.23	1.12	50.7*	264*
LI6	-60	0.388	**4.37**		15.20	2.46	64.1*	266*

LO - fault steepens with depth. PL - planar fault model. LI - fault flattens with depth. Rupture propagates upward from the base of the seismogenic layer. Curvature - increase (+) or decrease (-) of fault dip with depth in degree. σ - normalized variance of residuals. t - value obtained from t-test comparing listric models with planar model PL, negative value: other model fits better than model PL. μ,s - mean and standard deviation of differences of squared station residuals, for explanation see Chapter 3.4. Number of samples N=50. Value t has to exceed to be within certain confidence level: 60% - 0.25. 75% - 0.68. 90% - 1.30. 95% - 1.68. 97.5% - 2.01. 99% - 2.40. 99.5% - 2.68. 99.95 - 3.50. • - acceptable fits (95% confidence level). Mo - moment assigned to each individual subsource. rake - rake assigned to shallow and deep subsource, while subsource at centroid depth was assigned point source value (263°). * - fixed. All models have same moment tensor as point source.

Table 6.1.5 Alasehir, Down-Dip Geometry: 2. Dip and Seismic Moment Free.

	depth km	strike deg	rake deg	Start		Result	
				dip deg	moment 10^{17}Nm	dip deg	moment 10^{17}Nm
PL	5.6*	300*	263*	41	43	**46**	35
	3.3*	300*	263*	41	43	**32**	53
	1.1*	300*	263*	41	43	**67**	55
LI4	5.6*	300*	264*	21	51	**50**	30
	3.3*	300*	263*	41	51	**34**	74
	1.1*	300*	264*	61	51	**72**	42
LO4	5.6*	300*	264*	61	51	**47**	31
	3.3*	300*	263*	41	51	**39**	75
	1.1*	300*	264*	21	51	**73**	30

PL - planar start model. LI4, LO4 - listric start models. "*" - fixed. inverted for seismic moment and dip of each subsource, rupture propagating up-dip.

Table 6.1.6   Source Parameters of the 03/28/1970 Gediz Earthquake

	strike deg	dip deg	rake deg	moment 10^{17}Nm	depth km	duration s	Δt s	Δr km	Δaz deg	σ
PS	304	41	263	505.2	7.7	21				0.27
BIc										0.26
southeast	304*	41*	263*	309	7.7*	18				
northwest	304*	41*	263*	208	7.7*	21				
BIf										0.24
southeast	304	41	273	563	5.4	21				
northwest	360	36	253	214	5.2	18				
TS										0.24
	304	41	266	498	7.7*	18				
	358	37	247	116	7.7*	18	3.1	24	305	
DE	304*	0*	270*	43.6	15.4*	26	6.0	8.8*	34*	0.26
	304*	10*	270*	46.0	15.4*	24	6.0	8.8*	34*	0.26
E&J	308	35	270	109	10	6				
	270	35	250	306	10	5	4.0	11.4	120	
	270	25	270	164	10	6	8.5	11.1	95	
	90	60	230	77	10	3	15.0	10.1	90	
	270	20	270	219	15	14	24.0	23.8	34	
McK, N	308	35	270	300±96						

PS - point source solution. BI - bilateral rupture, v_r = 1.5 km/s, c: constraint, f: free. TS - two point source model. DE - detachment source with 0° and 10° dipping surface, respectively, locations derived relative to point source solution PS. E&J - P waveform modelling by Eyidogan and Jackson (1985), first subevent from first motion data. McK - first motion solution from KcKenzie (1978). N - moment estimate from North (1977). Δt, Δr, and Δaz - delay,distance, and azimuth of subevent with respect to first subevent. σ - normalized variance of residuals. "*" - fixed.

Table 6.1.7 Gediz, Down-Dip Geometry: 1. Dip and Seismic Moment Fixed. Results are Compared Statistically.

	curvature deg	σ	t	μ 10⁻¹	s 10⁻¹	Mo 10¹⁷Nm	rake deg
U-LO4	+40	0.31	**2.69**	1.82	3.82	199.2*	264*
U-LO3	+30	0.29	**2.49**	1.03	2.33	184.7*	263*
U-LO2	+20	0.27	**2.30**	0.50	1.23	175.4*	263*
U-LO1	+10	0.27	**1.73**	0.17	0.57	170.1*	263*
U-PL	0	0.26	●			168.4*	263*
U-LI1	-10	0.27	**2.39**	0.26	0.61	170.1*	263*
U-LI2	-20	0.28	**2.97**	0.77	1.47	175.4*	263*
U-LI3	-30	0.30	**3.18**	1.50	2.67	184.7*	263*
U-LI4	-40	0.32	**3.83**	2.43	3.59	199.2*	264*
U-LI5	-50	0.35	**4.19**	3.90	5.27	220.5*	265*
U-LI6	-60	0.41	**4.31**	6.24	8.19	251.9*	266*
B-LO4	+40	0.31	**2.45**	1.98	4.57	199.2*	264*
B-LO3	+30	0.29	**2.17**	1.20	3.14	184.7*	263*
B-LO2	+20	0.28	**2.07**	0.58	1.59	175.4*	263*
B-LO1	+10	0.27	**1.60** ●	0.17	0.59	170.1*	263*
B-PL	0	0.26	●			168.4*	263*
B-LI1	-10	0.27	**0.88** ●	0.10	0.66	170.1*	263*
B-LI2	-20	0.28	**2.21**	0.53	1.35	175.4*	263*
B-LI3	-30	0.29	**2.57**	1.08	2.38	184.7*	263*
B-LI4	-40	0.31	**2.82**	1.83	3.67	199.2*	264*
B-LI5	-50	0.33	**3.02**	3.00	5.61	220.5*	265*
B-LI6	-60	0.38	**3.13**	4.79	8.67	251.9*	266*

U - rupture propagates upward from base of seismogenic layer. B - rupture nucleates in central part of fault and spreads bilaterally up and down. LO - fault steepens with depth. PL - planar fault model. LI - fault flattens with depth. Curvature - increase (+) or decrease (-) of fault dip with depth in degree. σ - normalized variance of residuals. t - value obtained from t-test comparing listric models with planar model PL. μ,s - mean and standard deviation of differences of squared station residuals, for explanation see Chapter IV. Number of samples N=32. Value t has to exceed to be within certain confidence level: 60% - 0.26. 75% - 0.68. 90% - 1.31. 95% - 1.70. 97.5% - 2.04. 99% - 2.46. 99.5% - 2.75. 99.95 - 3.65. ● - acceptable fits (95% confidence level). Mo - moment assigned to each individual subsource. rake - rake assigned to shallow and deep subsource, while subsource at centroid depth was assigned point source value (263°). * - fixed. All models have same moment tensor as point source.

Table 6.1.8 Gediz, Down-Dip Geometry: 2. Dip and Seismic Moment Free

	depth km	strike deg	rake deg	Start		Result	
				dip deg	moment 10^{17}Nm	dip deg	moment 10^{17}Nm
PL	12.8*	304*	263*	41	168	42	103
	7.7*	304*	263*	41	168	41	246
	2.6*	304*	263*	41	168	45	183
LI4	12.8*	304*	264*	21	199	42	103
	7.7*	304*	263*	41	199	41	245
	2.6*	304*	264*	61	199	45	175
LO4	12.8*	304*	264*	61	199	41	98
	7.7*	304*	263*	41	199	41	265
	2.6*	304*	264*	21	199	39	181

PL - planar start model. LI4, LO4 - listric start models. "*" - fixed. inverted for seismic moment and dip of each subsource, rupture propagating up-dip.

Table 6.1.9   Source Parameters of the Gediz Aftershocks

	strike deg	dip deg	rake deg	moment 10^{17}Nm	depth km	duration s	Δt s	σ
04/16/1970								
PS	283	38	282	2.6	7.8	3		
E&J	280	31	260	2.7	8	4		
McK, N	280	31	260	4.4±0.9				
04/19/1970								
PS	278	50	267	7.1	9.6	6		0.38
Cf	279	63	282	3.0	9.6*	4		0.28
	290	42	265	5.4	9.6*	4	3.0	
Sf	278	62	284	3.3	7.1*	4		0.28
	292	44	266	5.4	11.1*	4	3.2	
Df	282	62	273	3.3	11.9*	4		0.30
	288	38	265	4.9	7.9*	4	3.6	
E&J	284	66	270	2.9	8	5		
	284	56	270	10.0	8	5	4.0	
	284	25	270	3.1	8	7	7.6	
	284	25	270	3.4	12	8	16.0	
McK	284	66	270					
05/25/1971								
PS	297	51	282	6.5	6.6	3		
E&J	298	55	283	9.5	6	3		
McK	298	55	284					

PS - point source, using P and SH waves. Cf, Sf, Df - two source models for the 04/19/1970 event. E&J - P waveform modelling by Eyidogan and Jackson (1985). McK - first motion solution from KcKenzie (1972). N - moment estimate from North (1977). Δt - delay of subevent with respect to first event. σ - normalized variance of residuals. "*":- fixed.
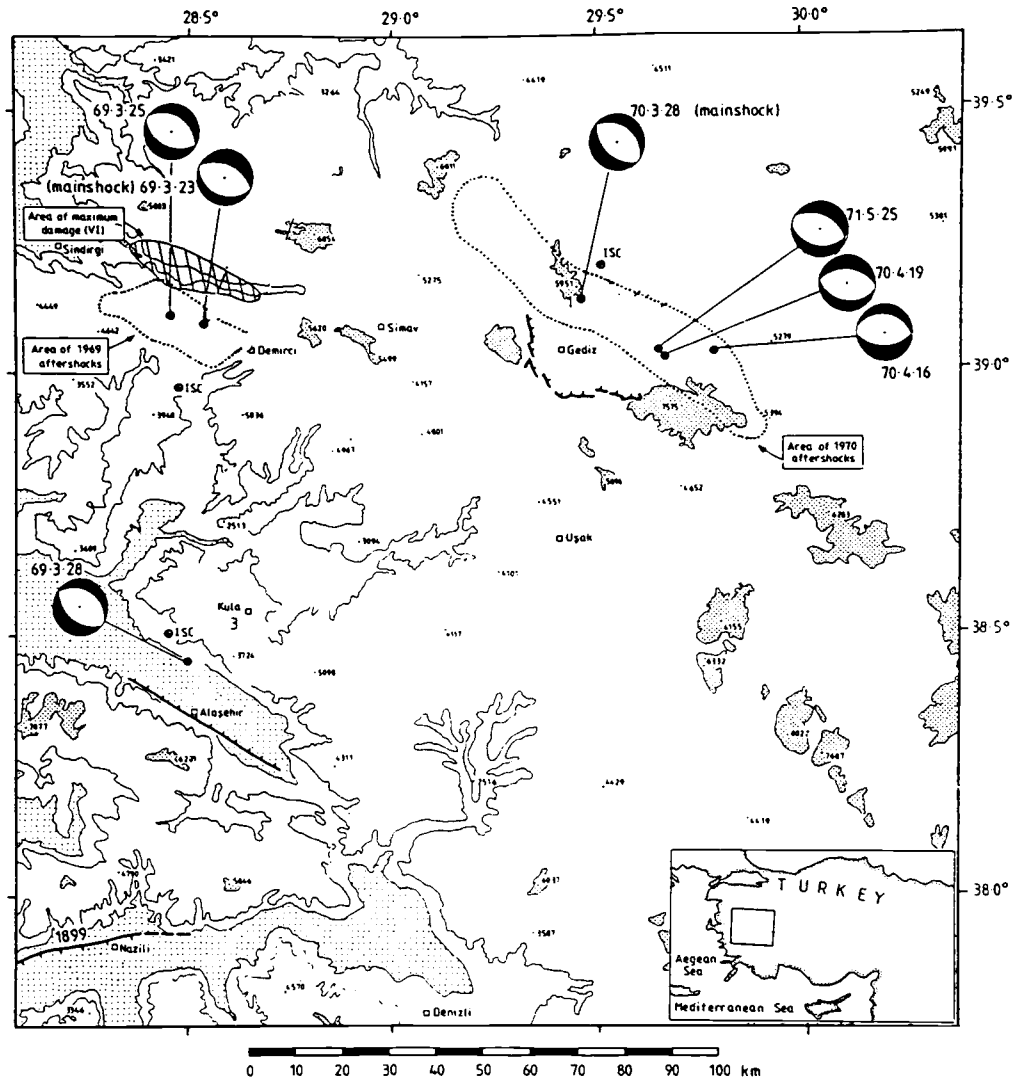
Figure 6.1.1   Map of the Demirci-Alasehir-Gediz area (from Eyidogan and Jackson, 1985). Areas lower than 1000 ft have light stippling and those higher than 5000 ft have dense stippling. Surface ruptures for the Aydin-Nazilli (1899), Alasehir (1969), and Gediz (1970) earthquakes are shown in a simplified manner with ticks on downthrown side. Fault plane solutions are from this study.

Demirci 03/23/1969

P

WWSSN/CSN (2) = 3.21 μm

0 10 20 30
time (s)

SH

Source Time Function

time (s)

WWSSN/CSN (2) = 1.69 μm

0 10 20 30
time (s)
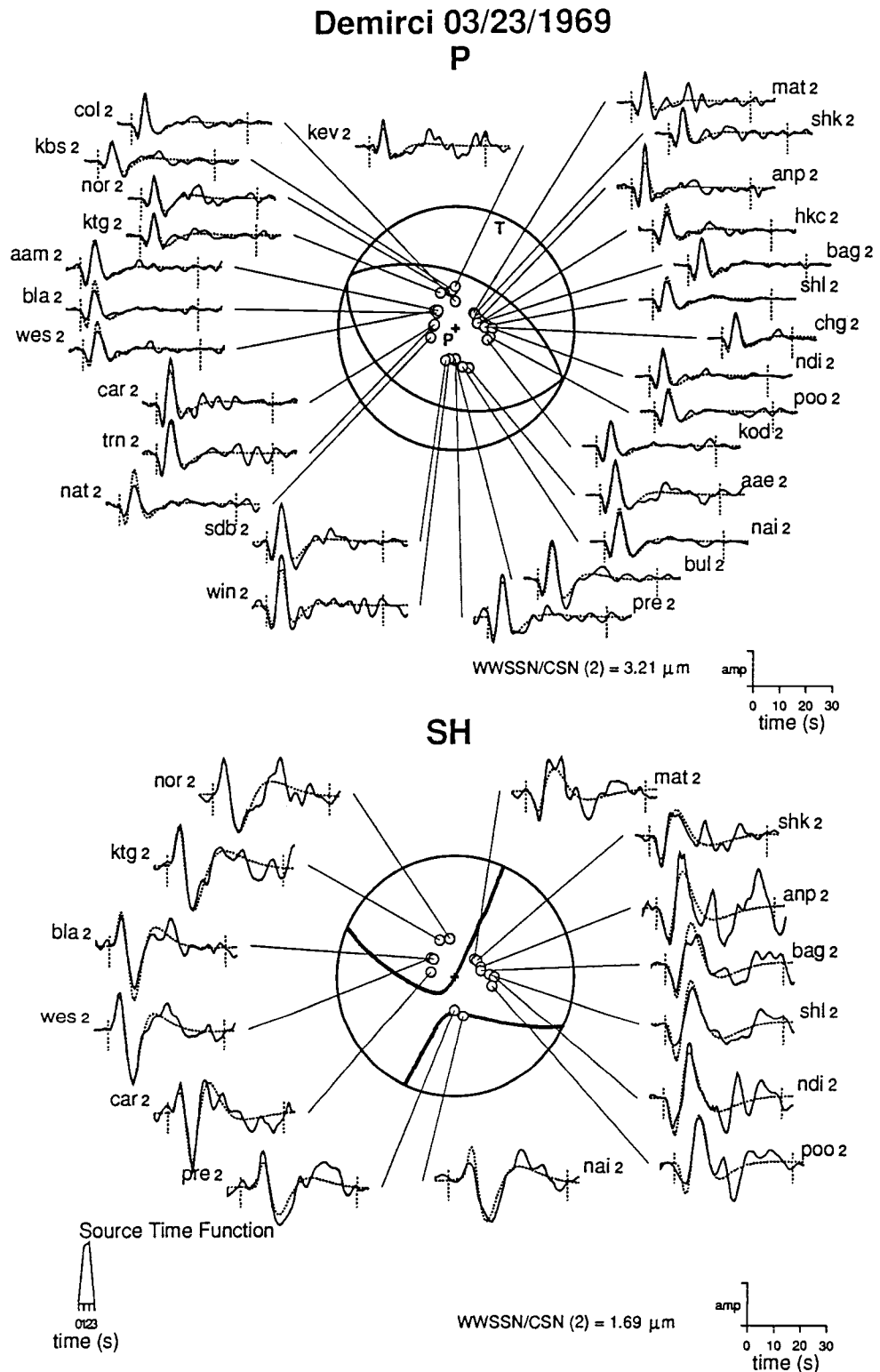
Figure 6.1.2 Point source solution for the 03/23/1969 Demirci earthquake. Solid lines: observed seismograms, dotted lines: synthetic seismograms. The source time function is shown in the lower left. The amplitude scales are in the lower right corner. The same layout has been used throughout this thesis.

03/23/1969

03/25/1969

+ Compressional

□ Dilatational

Figure 6.1.3   Short period first motion polarities for the 03/23/1969 and 03/25/1969 Demirci earthquakes. The fault plane solutions are from waveform inversion (Figures 6.1.2, and 6.1.4).
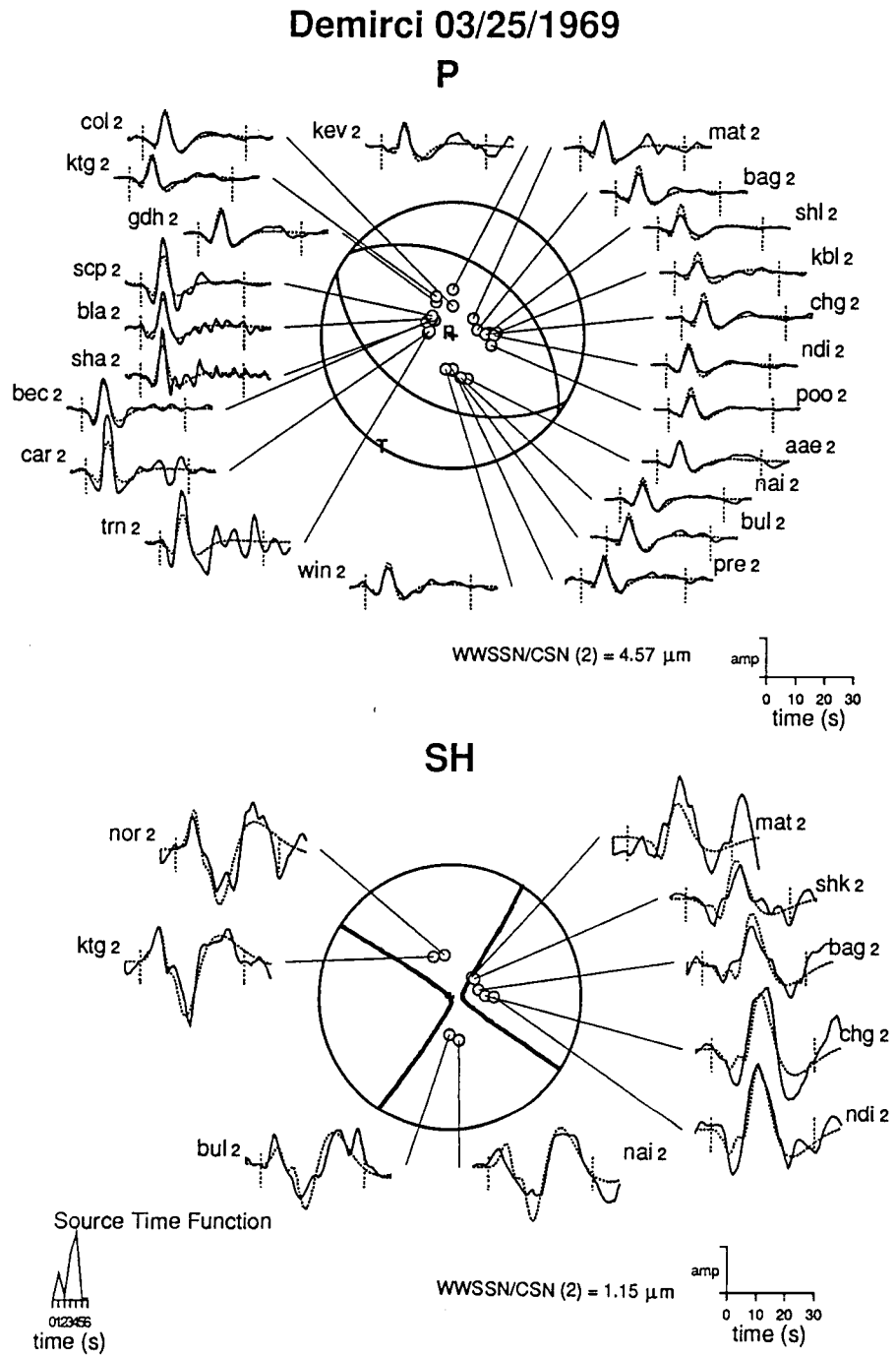
Figure 6.1.4   Point source solution for the 03/25/1969 Demirci earthquake.
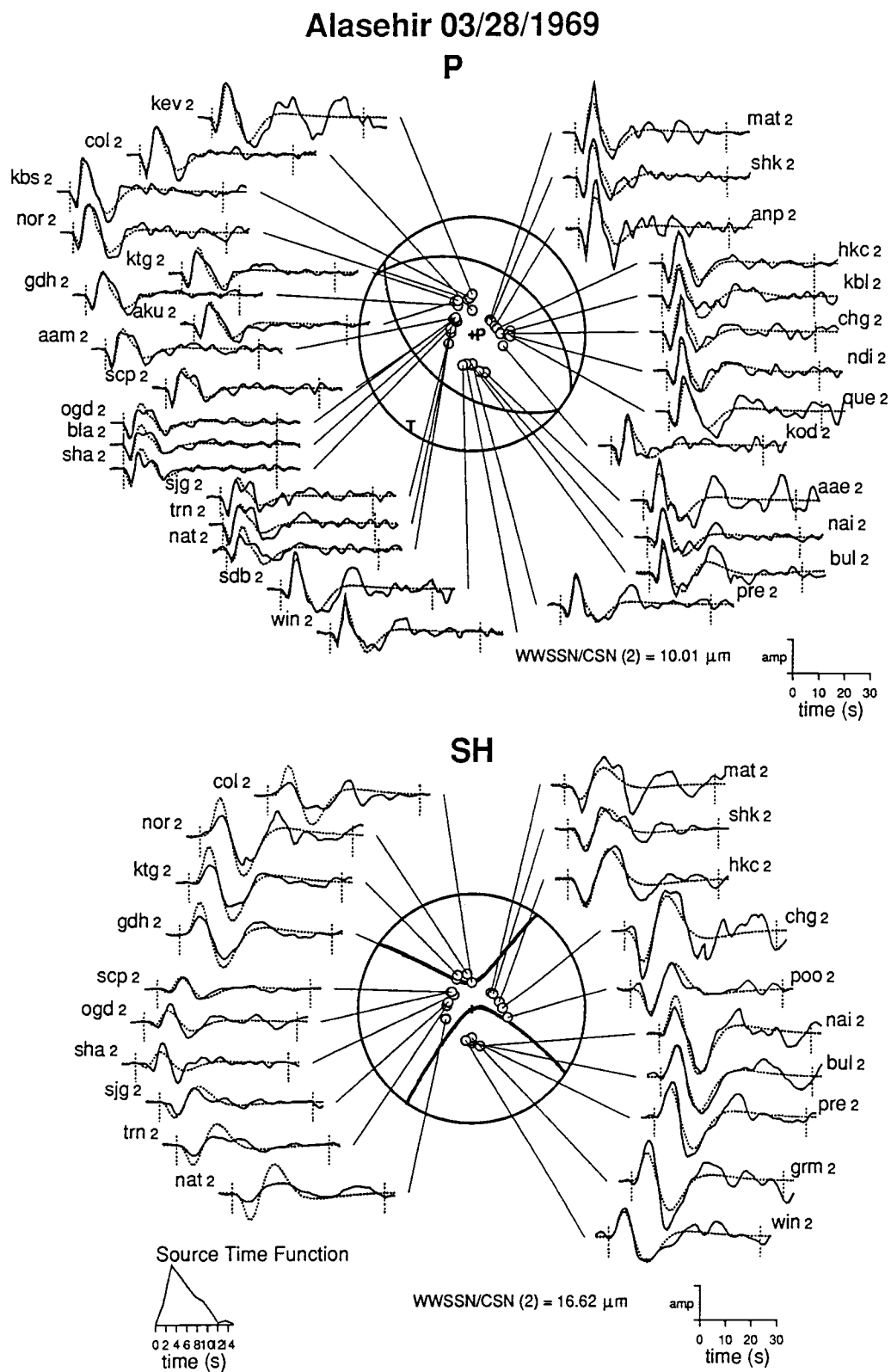
Figure 6.1.5   Point source solution for the 03/28/1969 Alasehir earthquake.

Alasehir - moment release rate
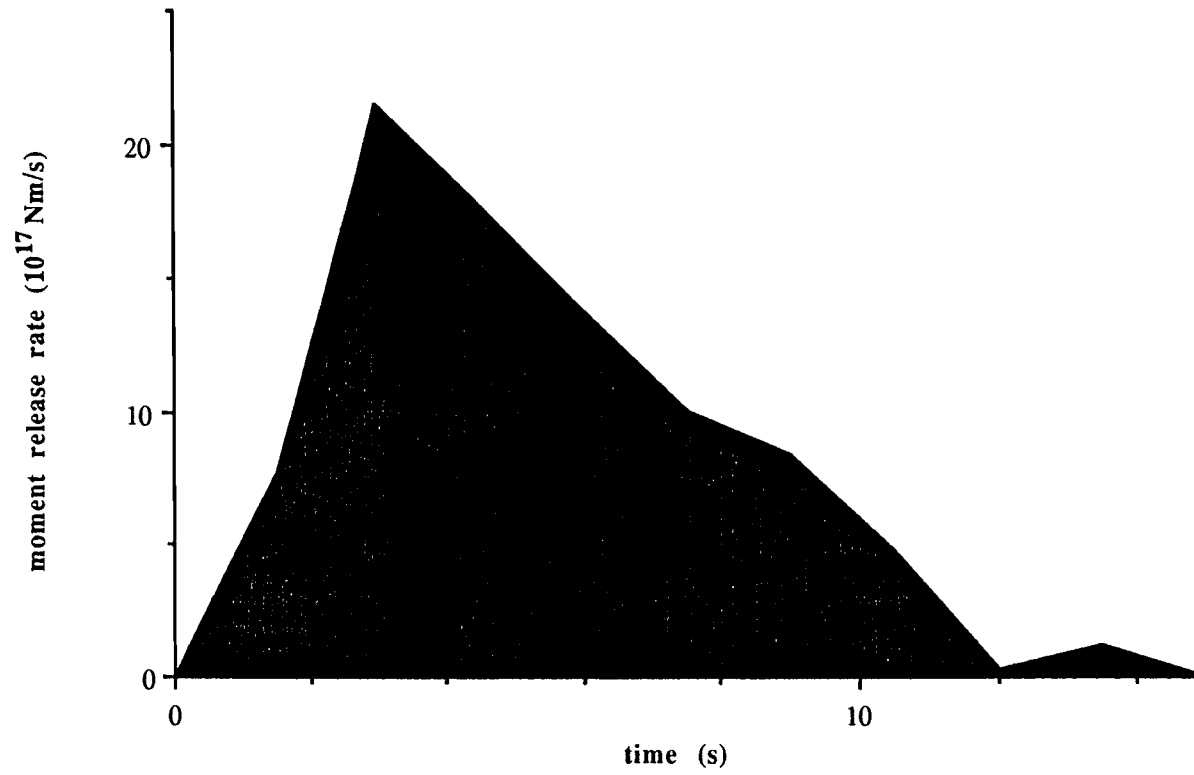
Figure 6.1.6   Seismic moment release rate.

Alasehir   03/28/1969
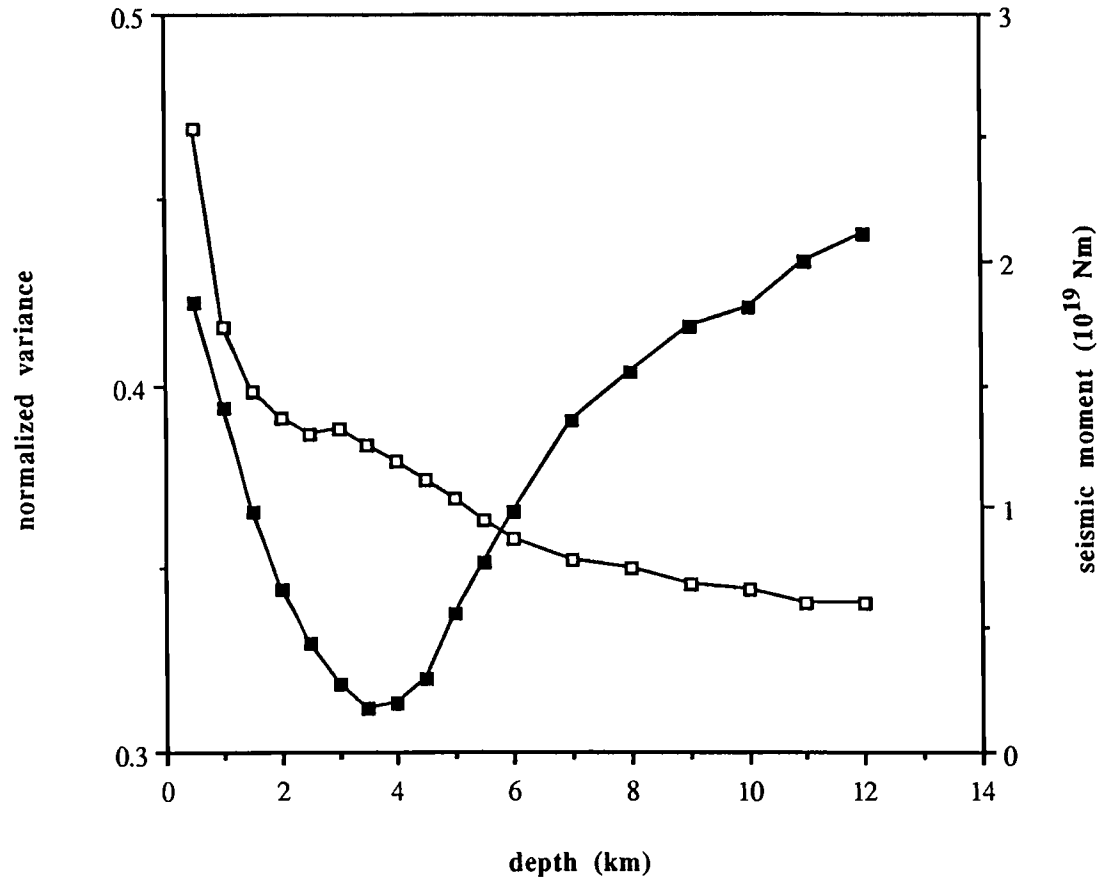
Figure 6.1.7   Residual variance (filled squares) and seismic moment (open squares) as a function of centroid depth.
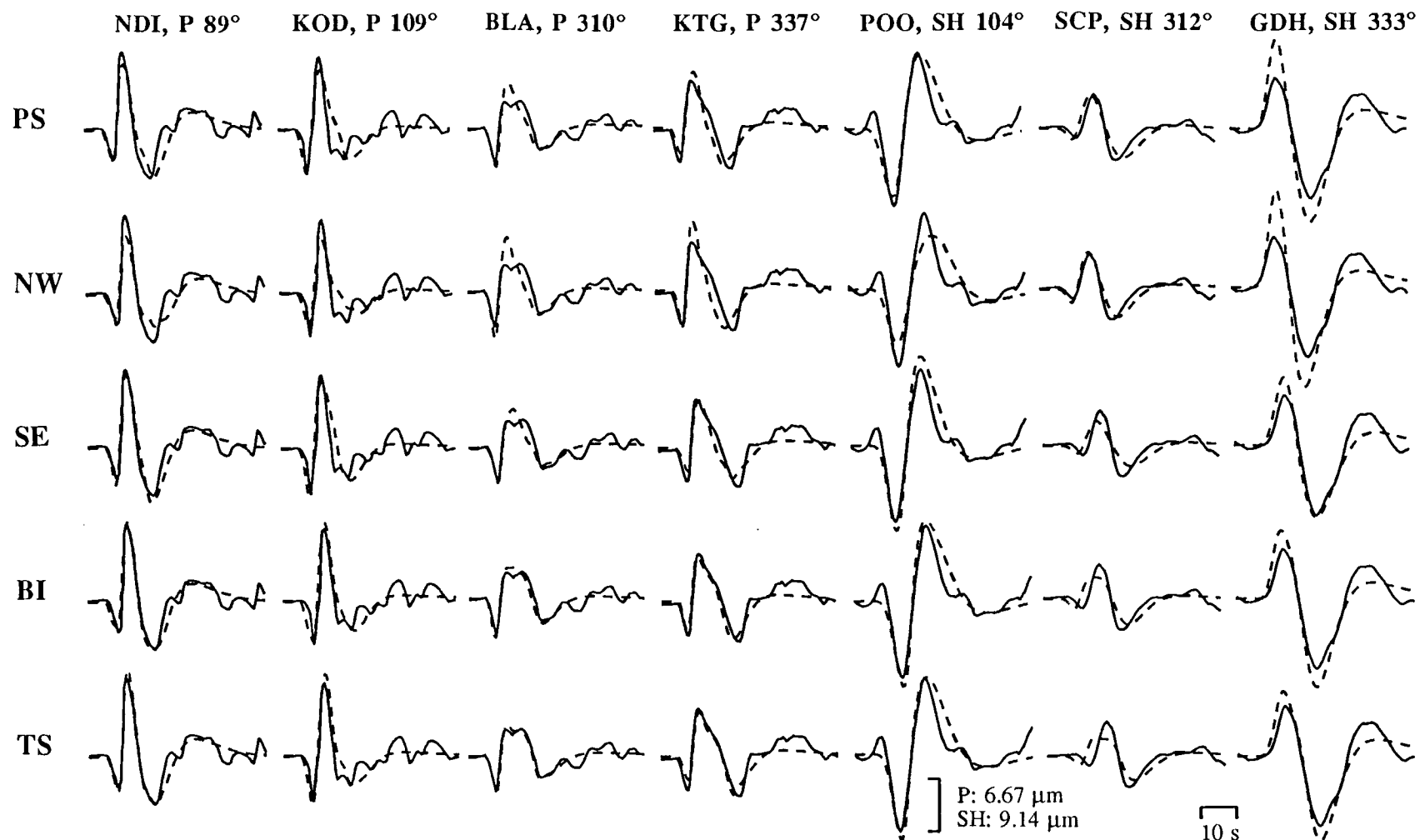
Figure 6.1.8 Comparison of P and SH waveforms for different source models. PS: point source. NW, SE: unilaterally propagating ruptures, towards NW and SE. BI: bilaterally propagating rupture. TS: two point sources. See Table 6.1.2 for details. Number next to station is the azimuth from the source.
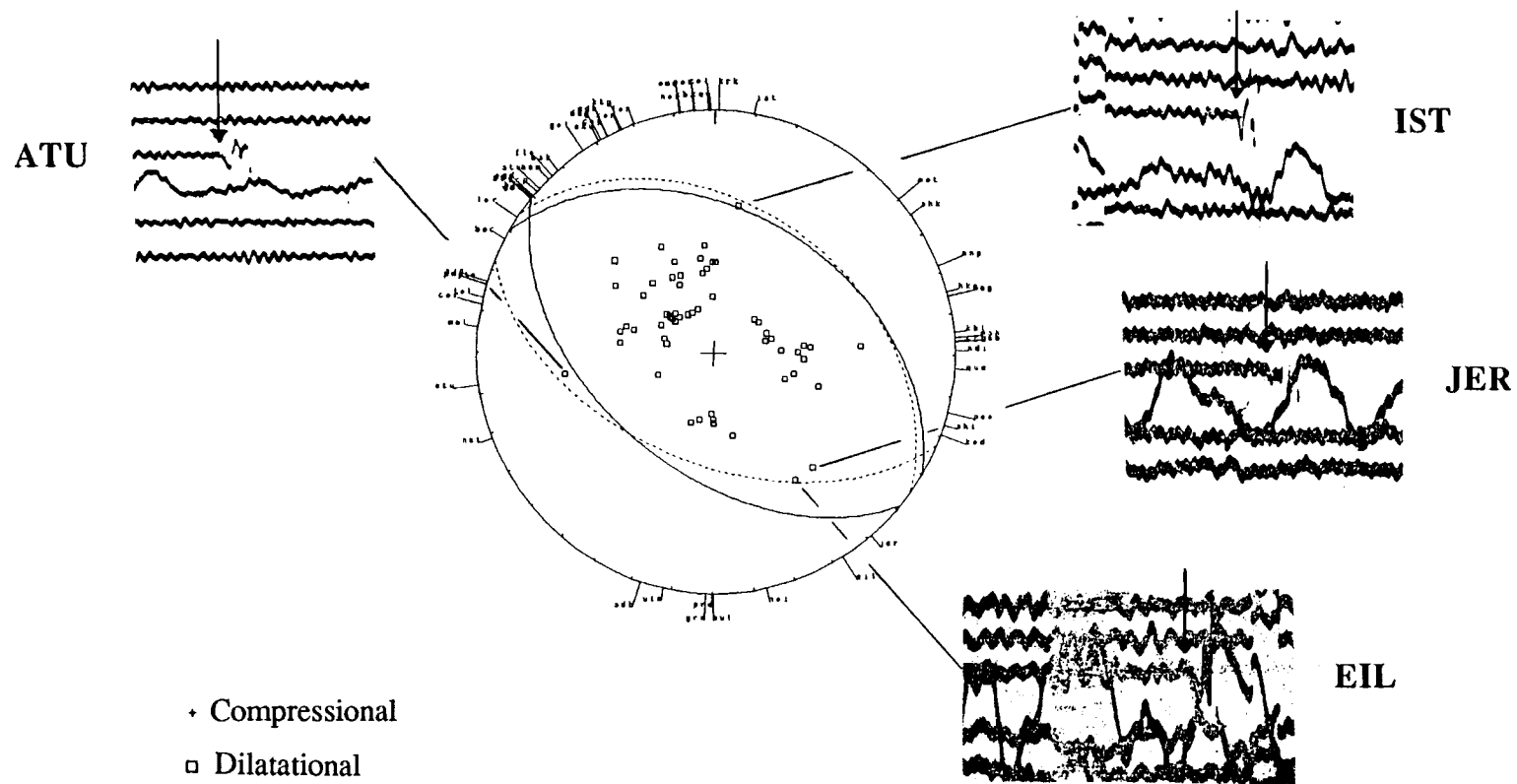
Figure 6.1.9   Short-period first motion data for the Alasehir earthquake. Critical stations close to the nodes are shown. Solid line: centroidal solution. Dotted line: fault plane solution compatible with the short period first motion polarities and the amplitudes of the first half cycle of the long-period data at regional distances (strike: 305°, dip:39°, and rake: 280°).
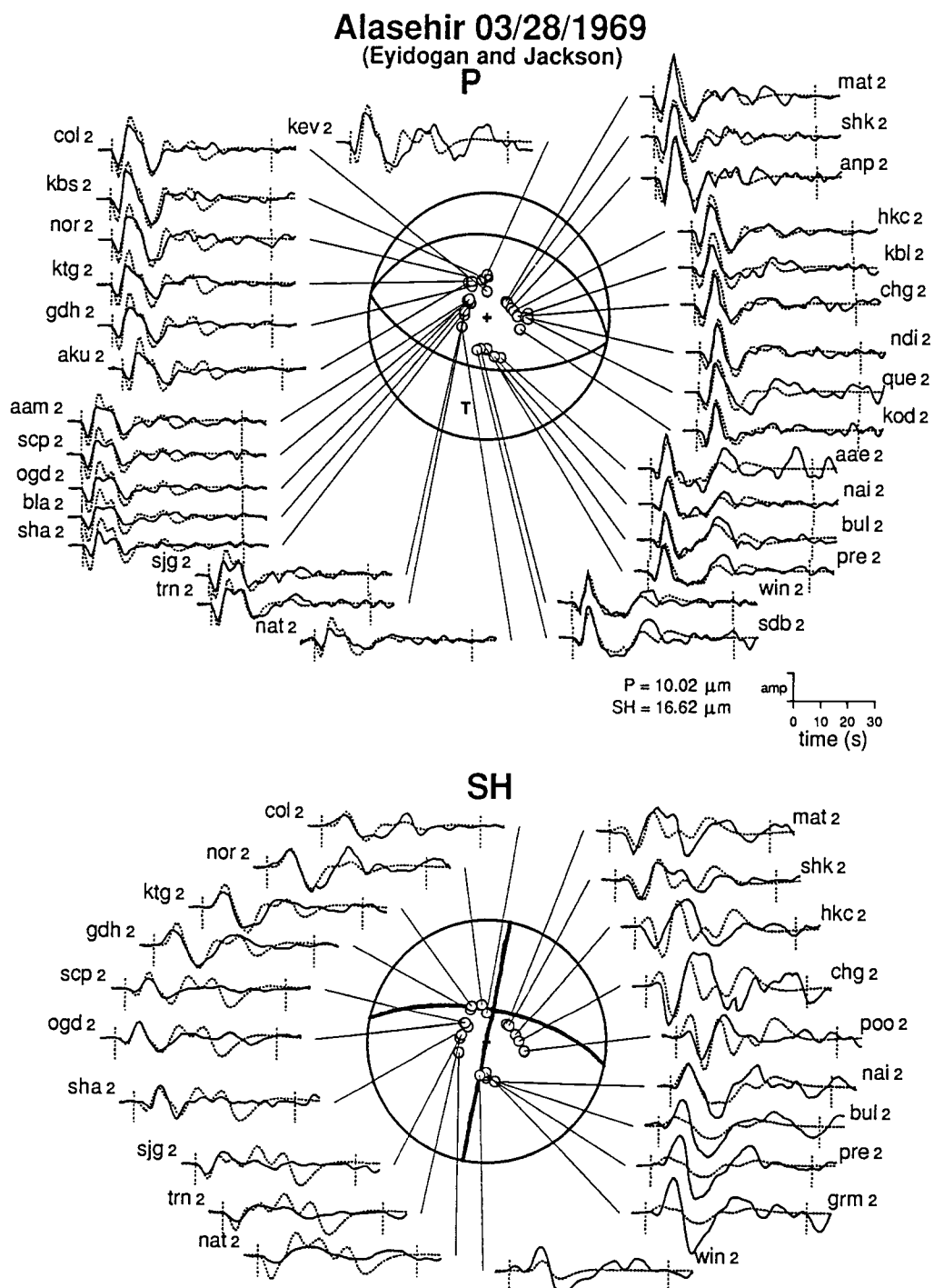
Figure 6.1.10 The synthetic seismograms (dotted lines) corresponding to the model presented by Eyidogan and Jackson (1985). The model consists of four subevents with the last two being shallow dipping detachment sources. The fault plane solution of the first subevent is shown. Note the poor SH wave fit.
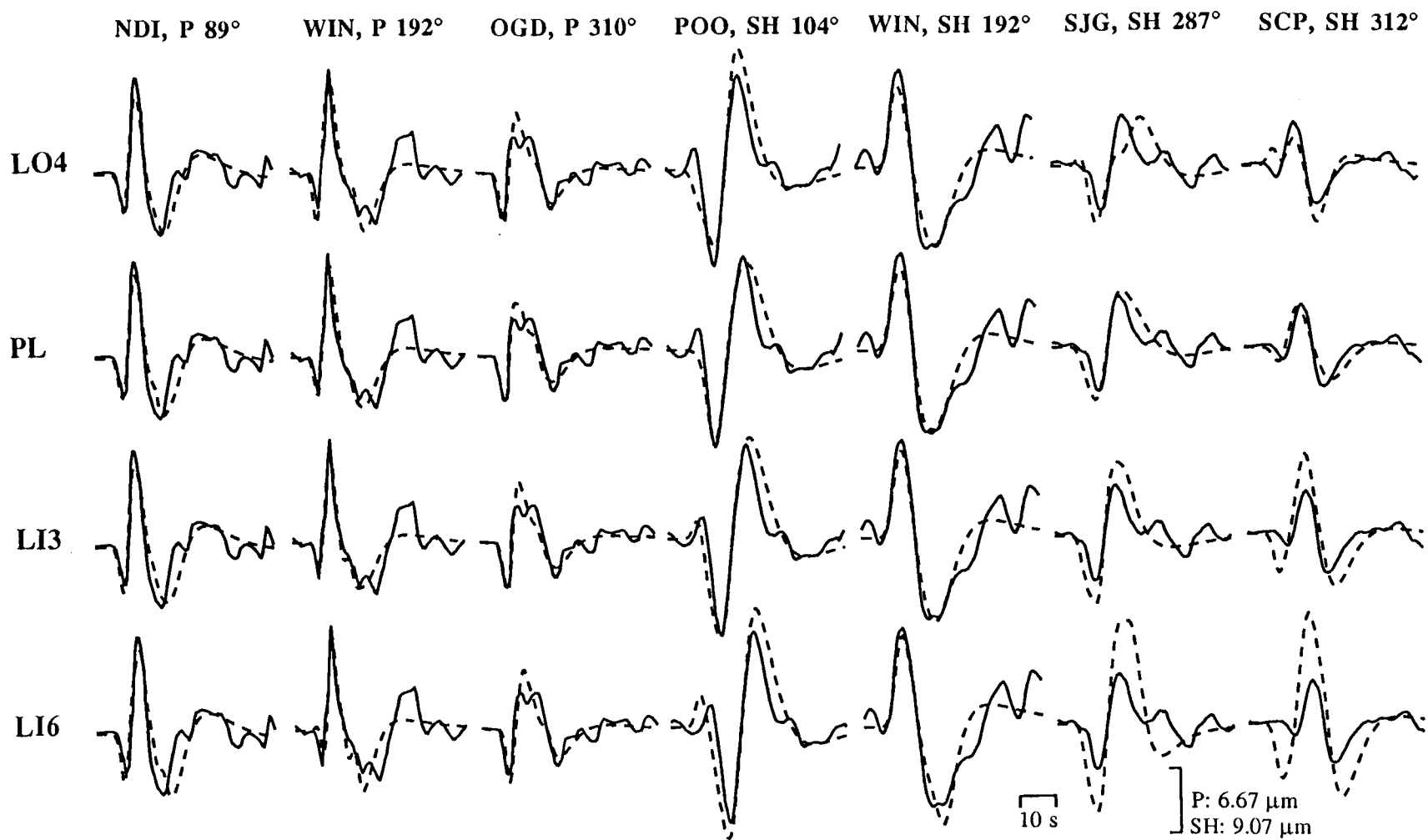
Figure 6.1.11 Comparison of P and SH waveforms for four fault models listed in Table 6.1.4 for the 03/28/1969 Alasehir earthquake. Number next to station is the azimuth from the source.
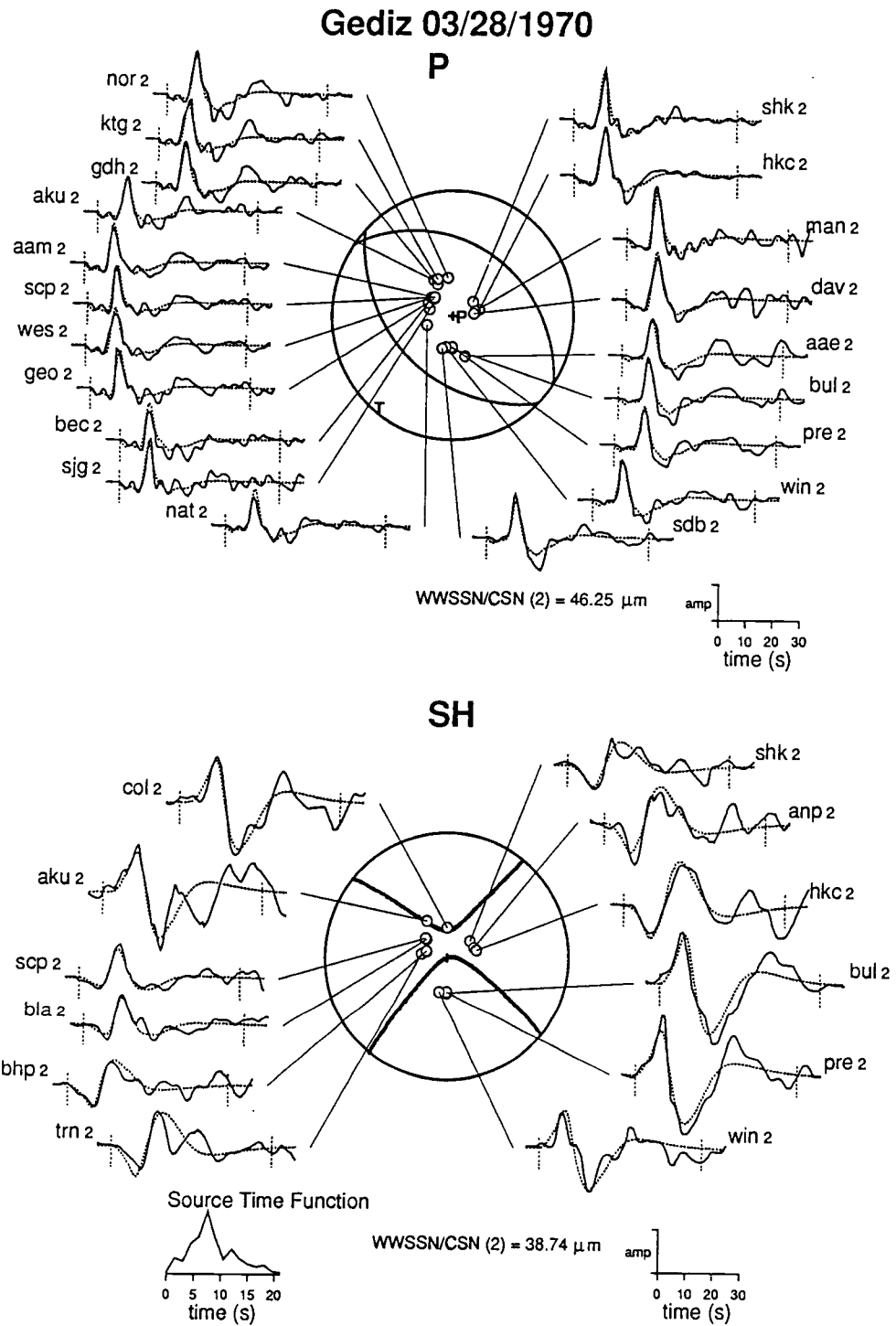
Figure 6.1.12 Point source solution for the 03/28/1970 Gediz earthquake.

Gediz   03/28/1970
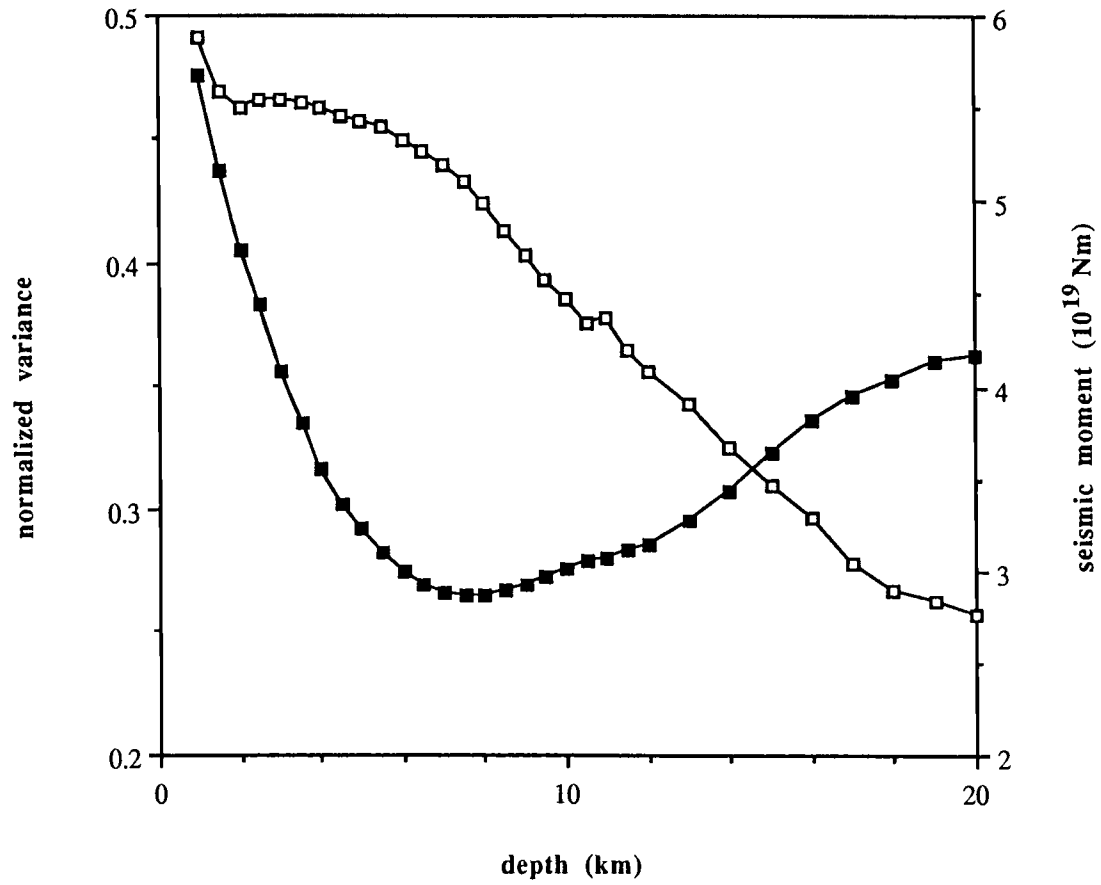
Figure 6.1.13 Residual variance (filled squares) and seismic moment (open squares) as a function of centroid depth.

Gediz - moment release rate
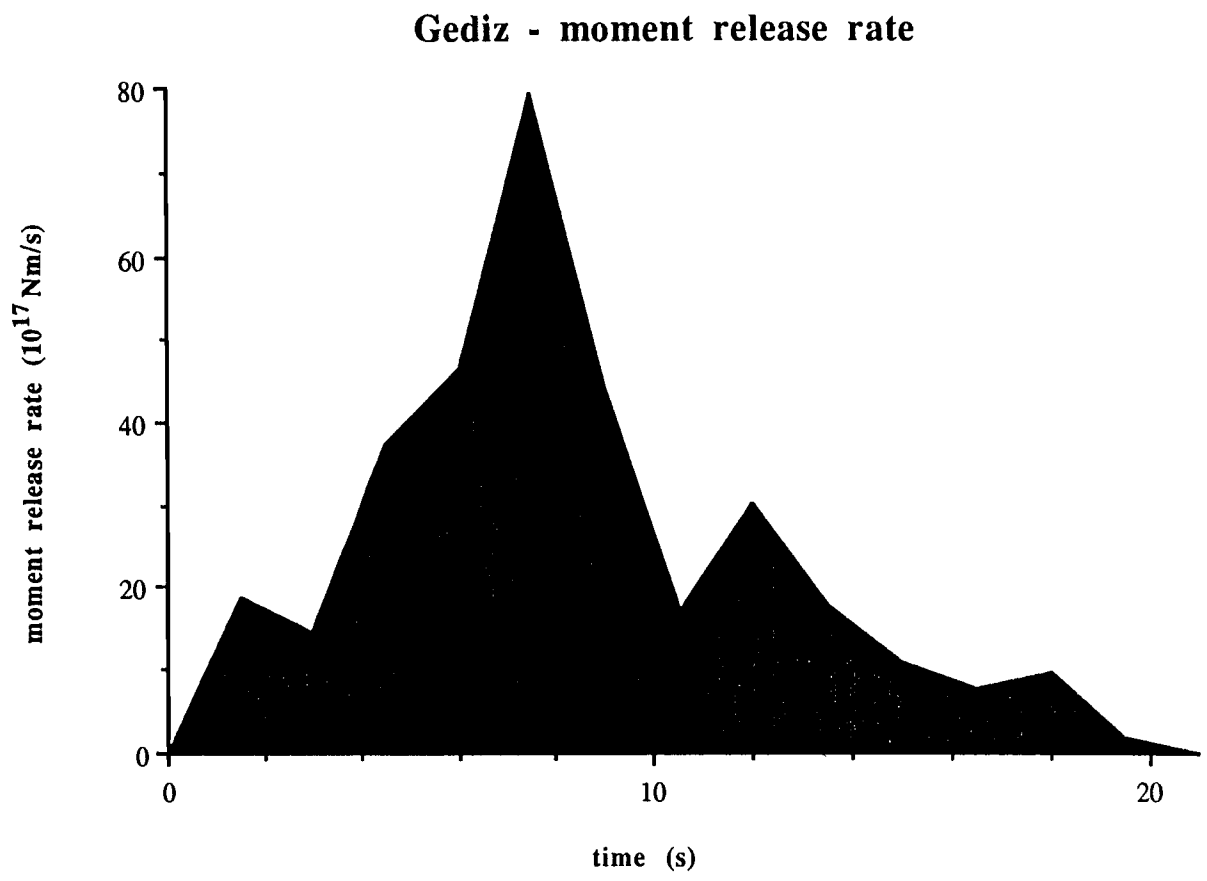
Figure 6.1.14 Seismic moment release rate. Note the emergent onset.
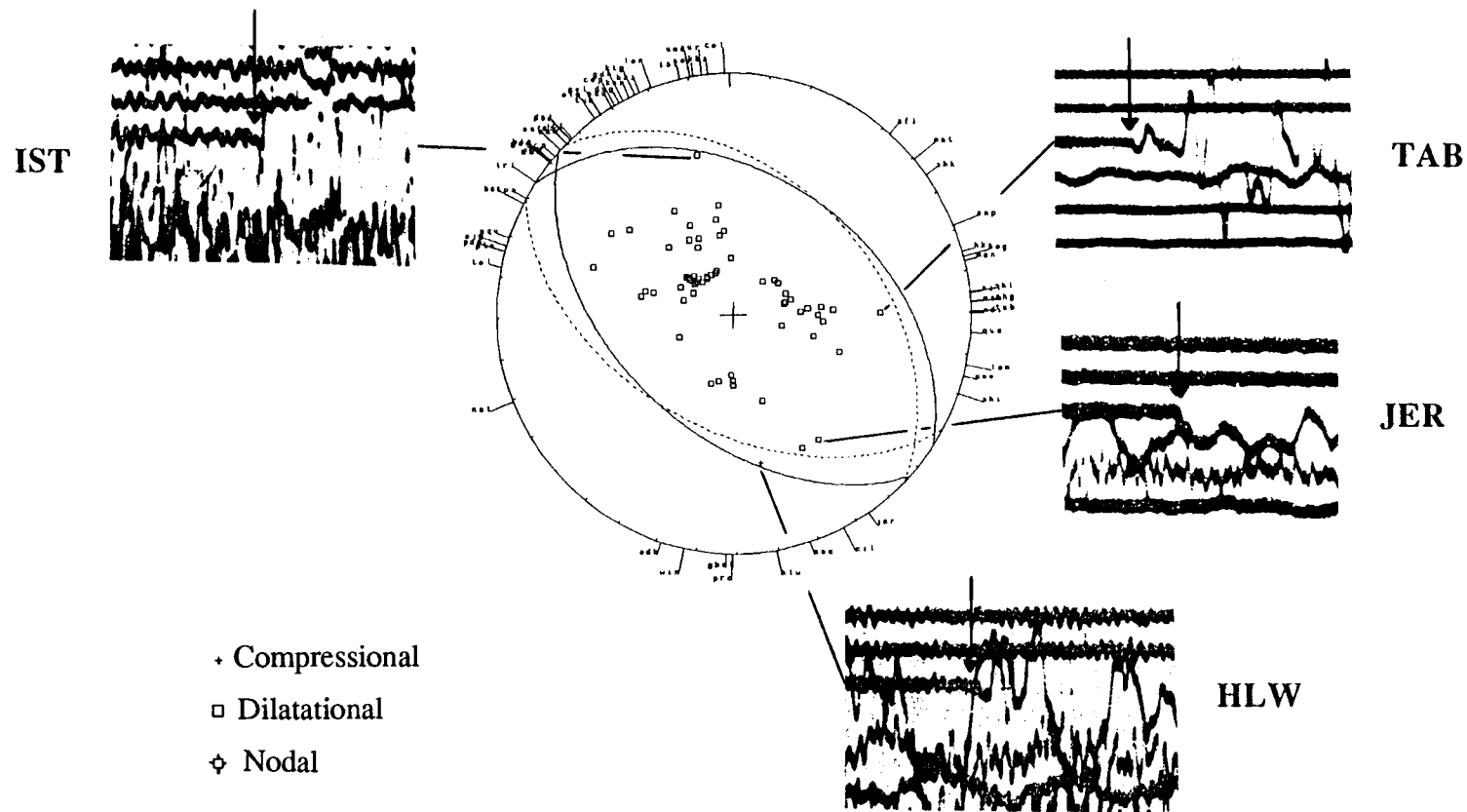
Figure 6.1.15 Short-period first motion data for Gediz main shock. Critical stations close to the nodes are shown. Solid line: centroidal solution. Dotted line: fault plane solution compatible with the short period first motion polarities and the amplitudes of the first half cycle of the long-period data at regional distances (strike: 315°, dip: 41°, and rake: 282°). HLW: short-period north-south component is shown, the backazimuth from the station to the epicenter is 351°, and the first motion polarity on the vertical component is therefore compressional.

Gediz 03/28/1970
(Eyidogan and Jackson)
P

WWSSN/CSN (2) = 73.22 μm   amp

0 10 20 30
time (s)

SH

WWSSN/CSN (2) = 74.76 μm   amp

0 10 20 30
time (s)
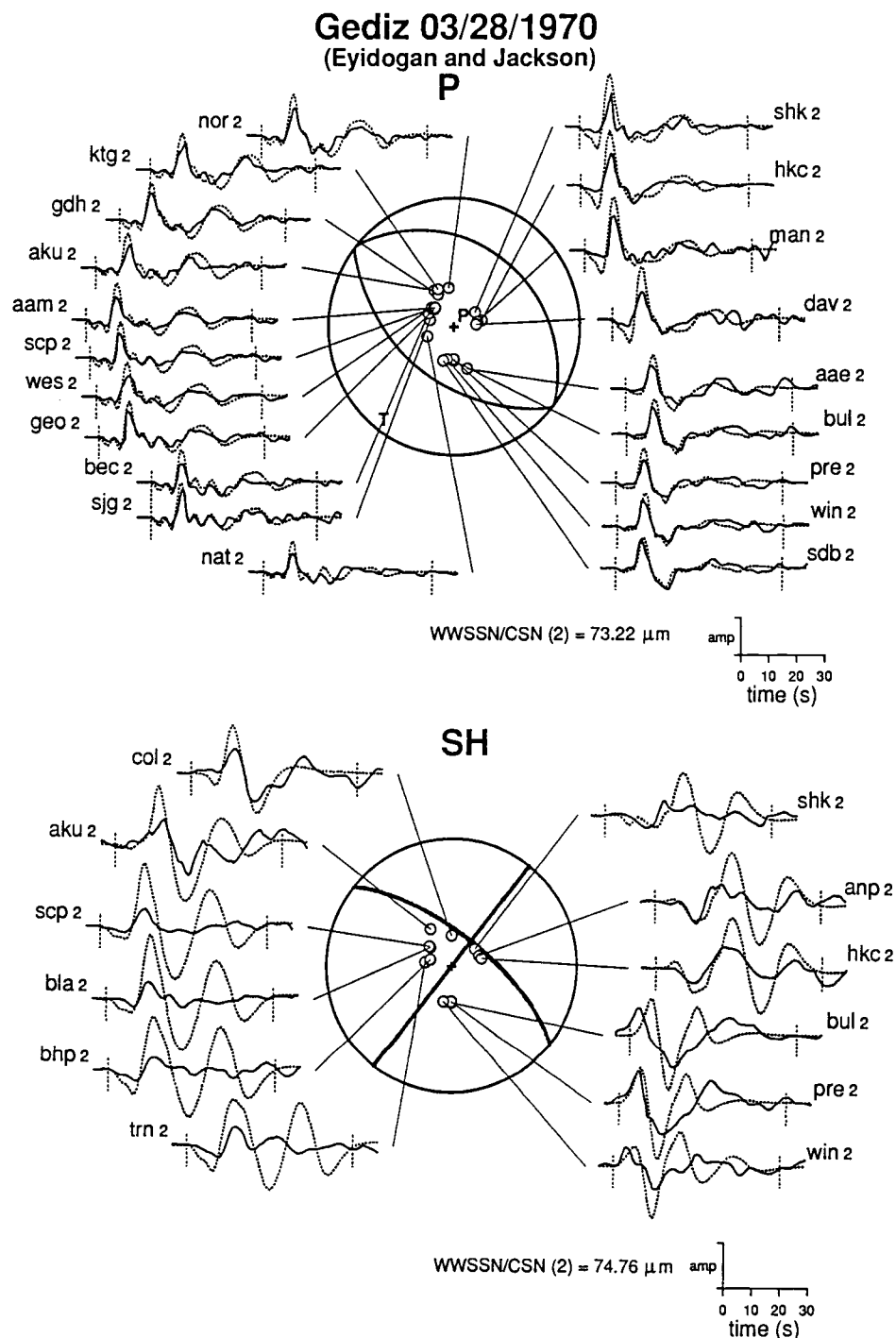
Figure 6.1.16 The synthetic seismograms (dotted lines) corresponding to the model presented by Eyidogan and Jackson (1985). The model consists of five subevents with the last and third to last being a shallow dipping detachment sources. The fault plane solution of the first subevent is shown. Note that the synthetic SH waves are completely incompatible with the observed waveforms.
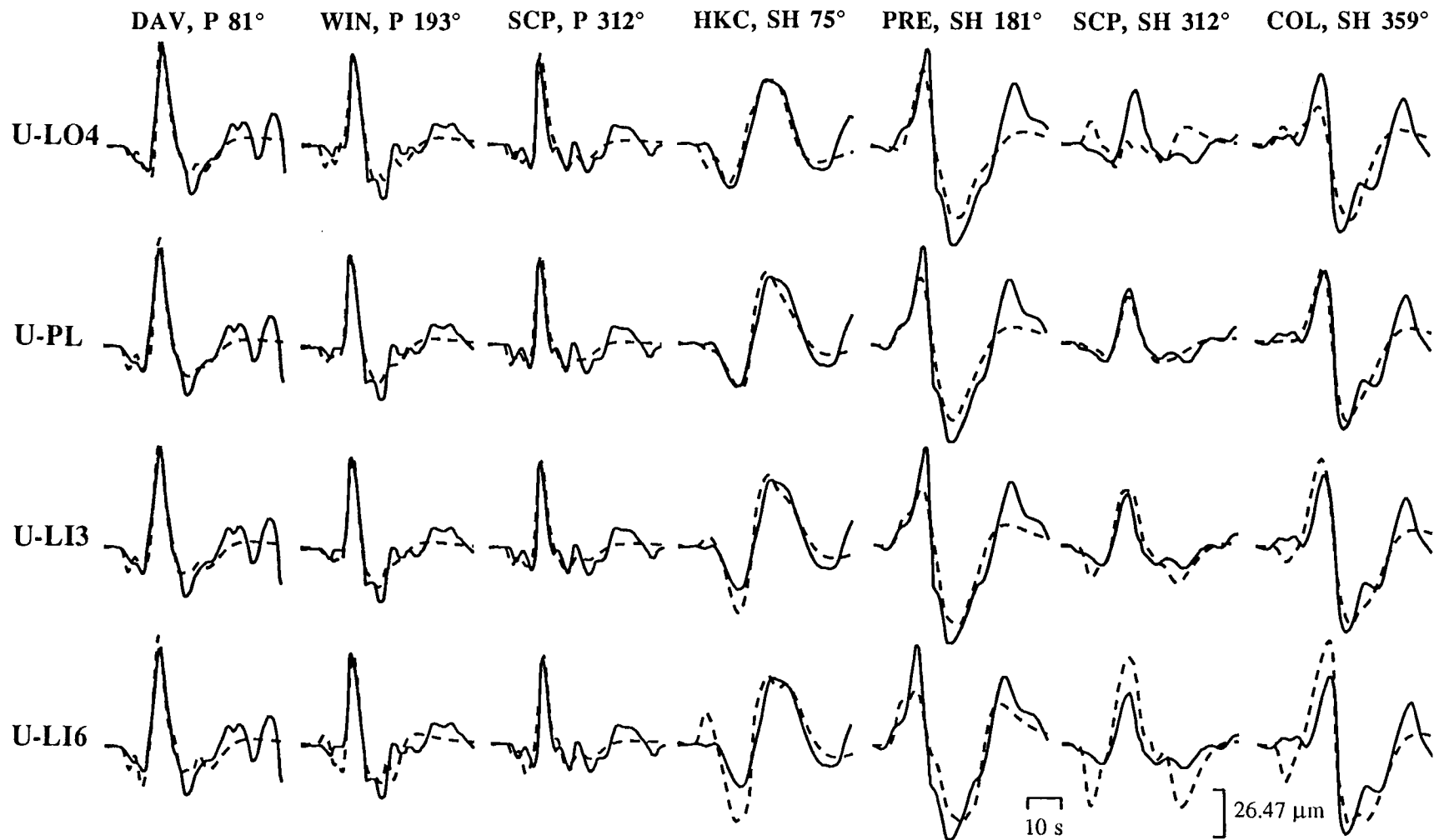
Figure 6.1.17 Comparison of P and SH waveforms for four fault models listed in Table 6.1.7 for the 03/28/1970 Gediz earthquake. Number next to station is the azimuth from the source. U: upward propagating rupture.
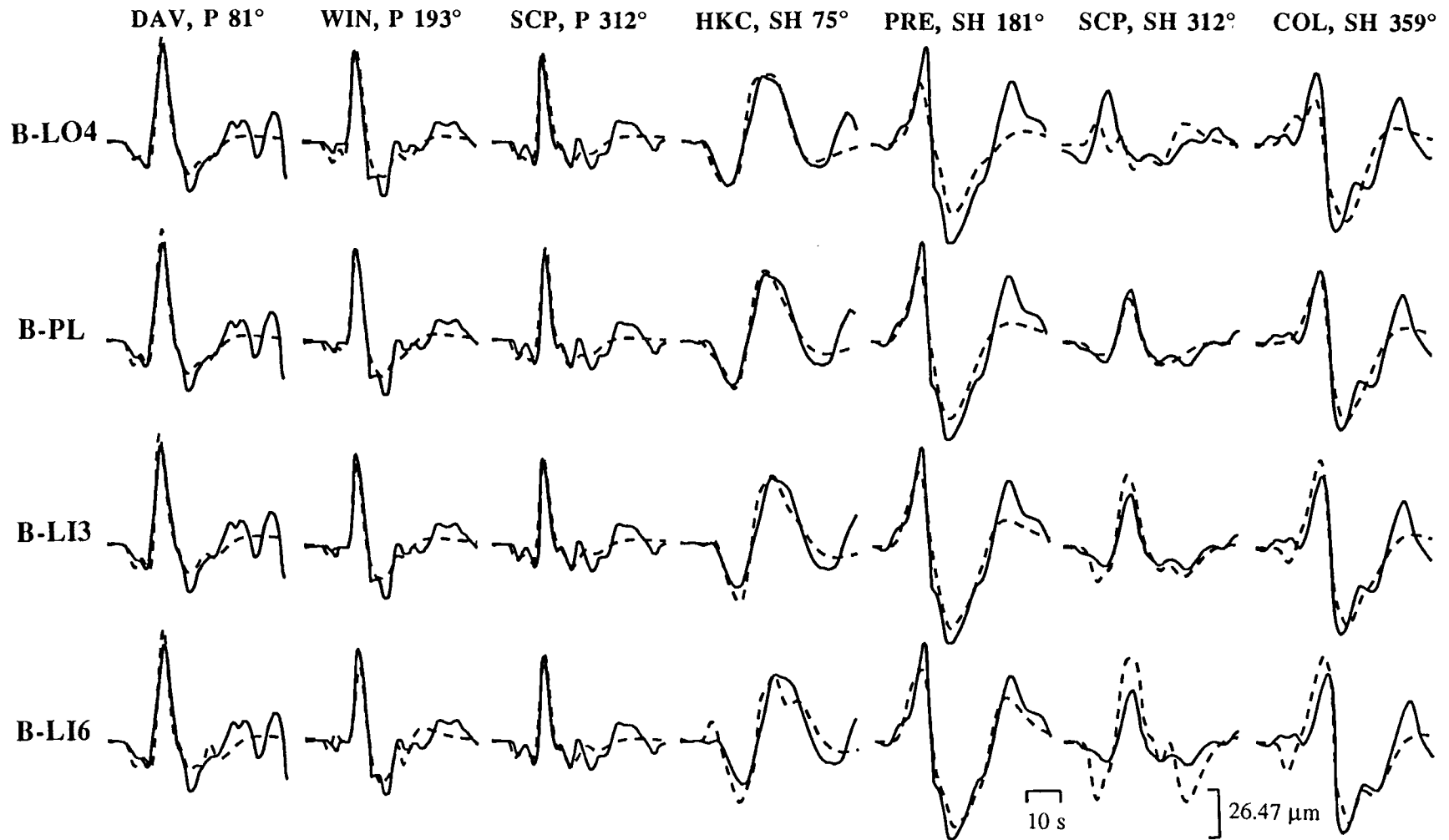
Figure 6.1.18 Comparison of P and SH waveforms for four fault models listed in Table 6.1.7 for the 03/28/1970 Gediz earthquake. Number next to station is the azimuth from the source. B: bilaterally propagating rupture.

Gediz 04/16/1970

P

nor 2

sjg 2

car 2

nai 2

P +

T

mat 2

bag 2

nil 2

shl 2

kbl 2

que 2

poo 2

aae 2

WWSSN/CSN (2) = 1.24 μm

amp

0 10 20 30
time (s)

SH

ogd 2

nai 2

nil 2

shl 2

kbl 2

ndi 2

poo 2

Source Time Function

0123
time (s)

WWSSN/CSN (2) = 0.67 μm

amp

0 10 20 30
time (s)
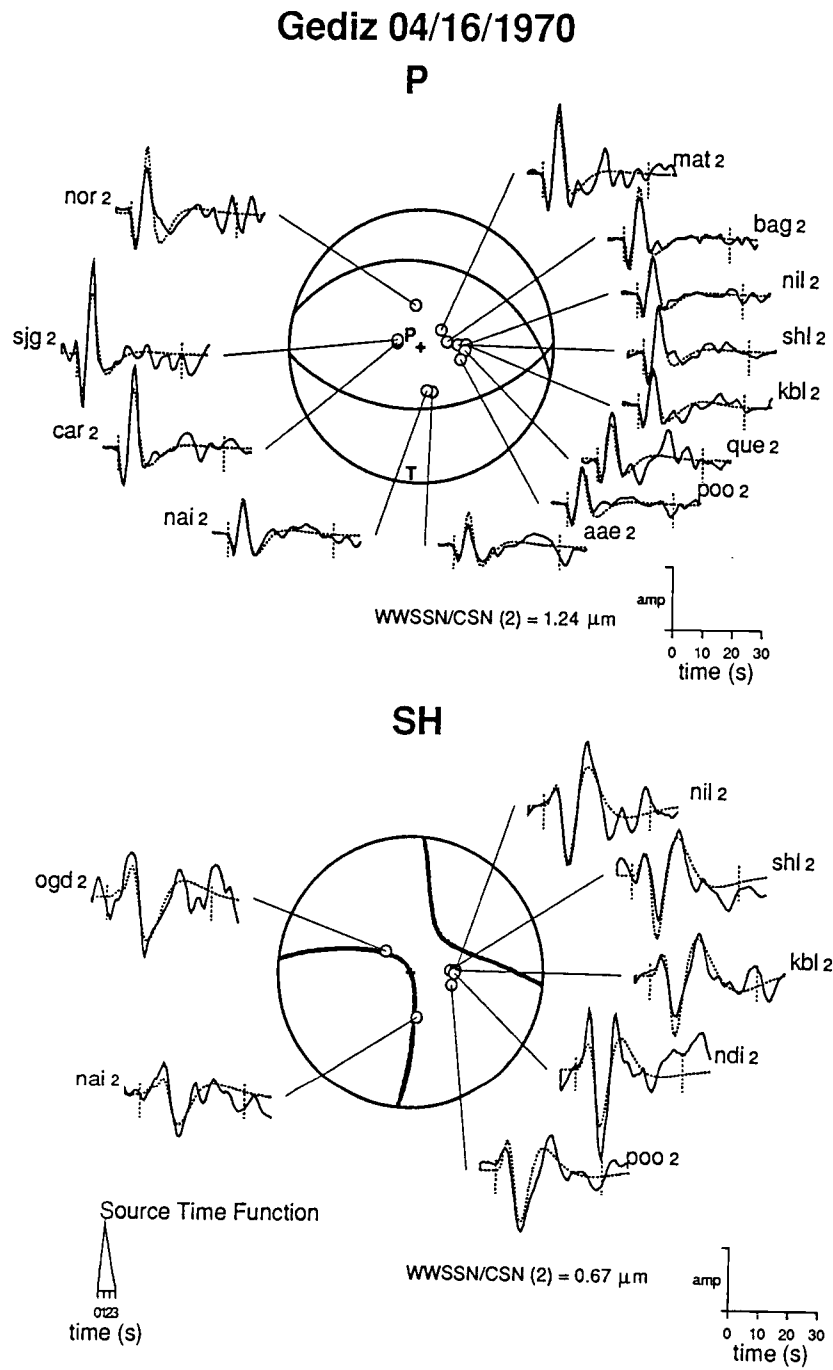
Figure 6.1.19 Point source solution for the 04/16/1970 Gediz aftershock.

04/16/1970

04/19/1970

05/25/1971

+ Compressional

□ Dilatational
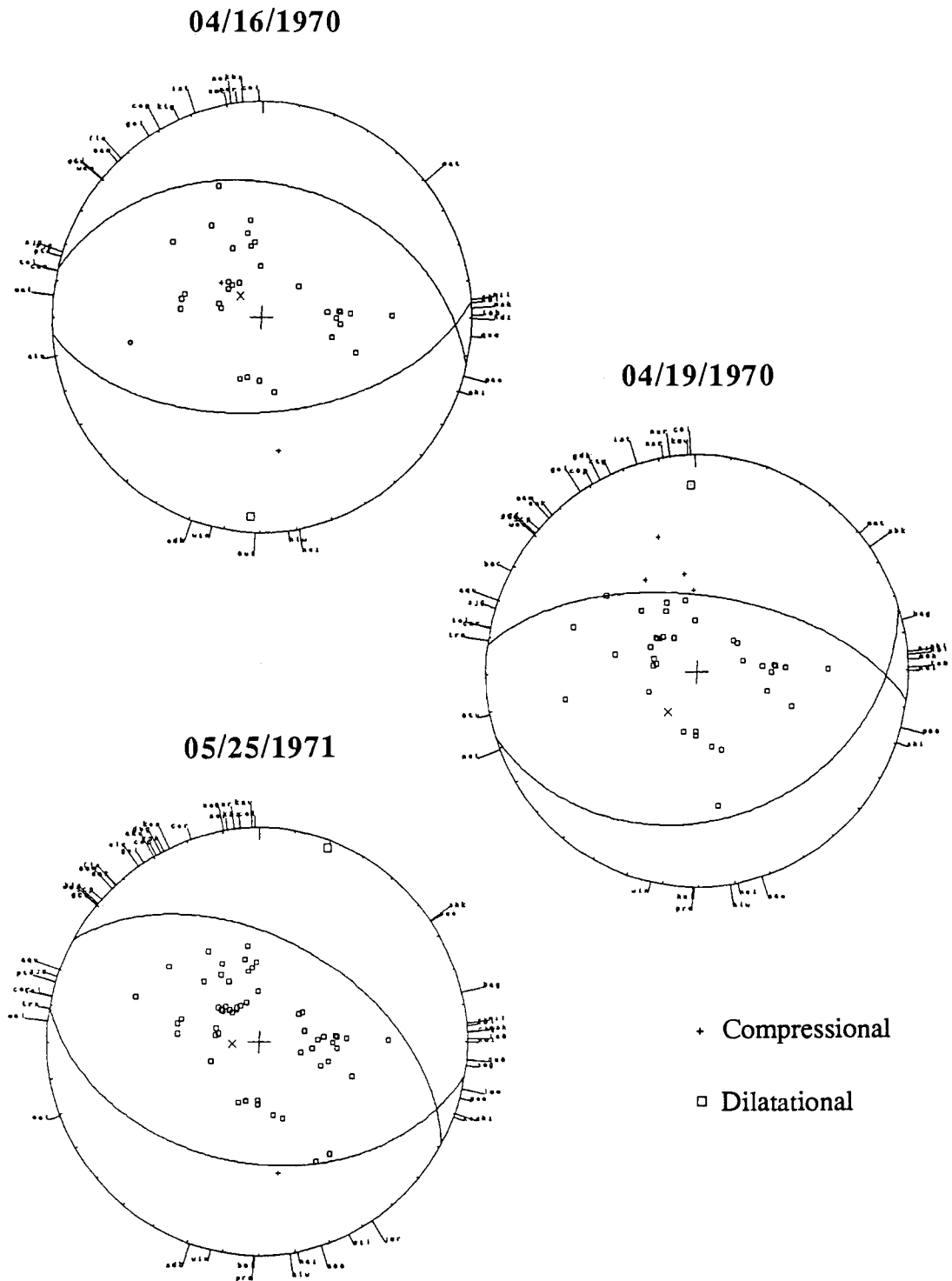
Figure 6.1.20 Short period first motion polarities for the 04/16/1970, 04/19/1970, and 05/25/1971 Gediz aftershocks. Fault plane solutions for the 04/16/1970 and 05/25/1971 aftershocks correspond to point source solution; for the 04/19/1970 aftershock, the first subevent of the two source model.
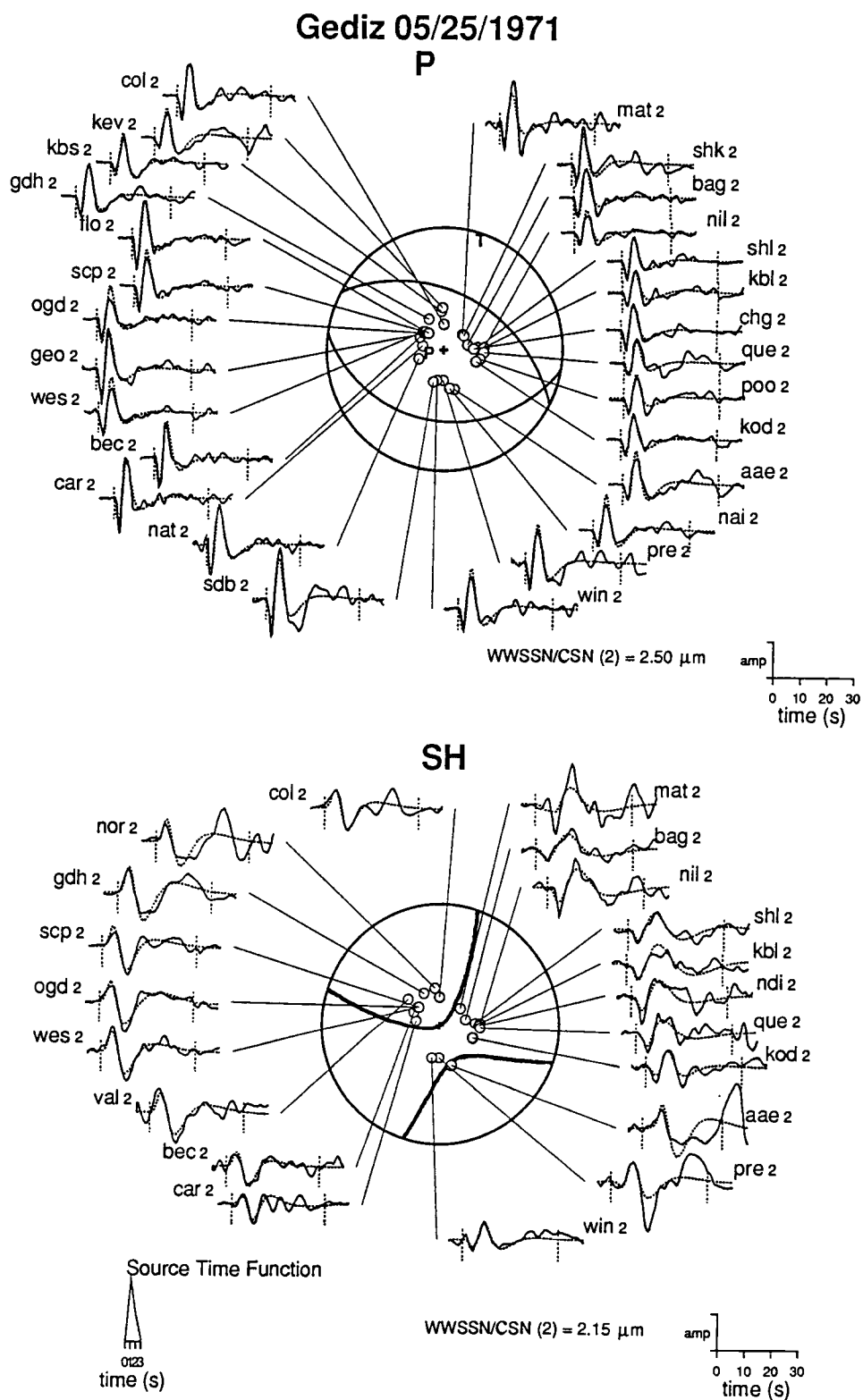
Figure 6.1.21 Point source solution for the 05/25/1971 Gediz aftershock.

Gediz 04/19/1970

P

WWSSN/CSN (2) = 2.39 μm

amp

0 10 20 30
time (s)

SH

Source Time Function

0123456
time (s)

WWSSN/CSN (2) = 1.78 μm

amp

0 10 20 30
time (s)
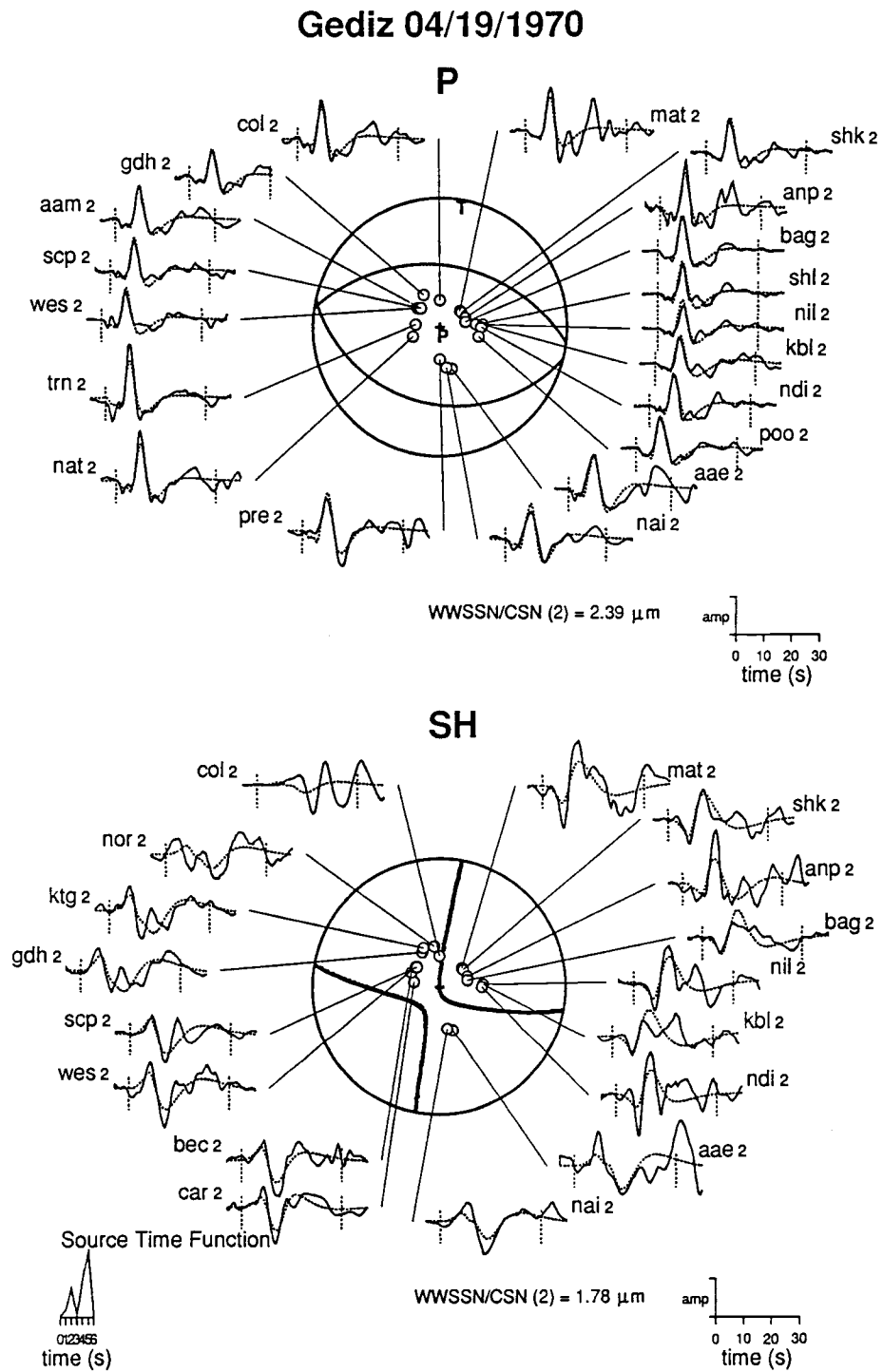
Figure 6.1.22 Point source solution for the 04/19/1970 Gediz aftershock.

Gediz 04/19/1970
2 source model
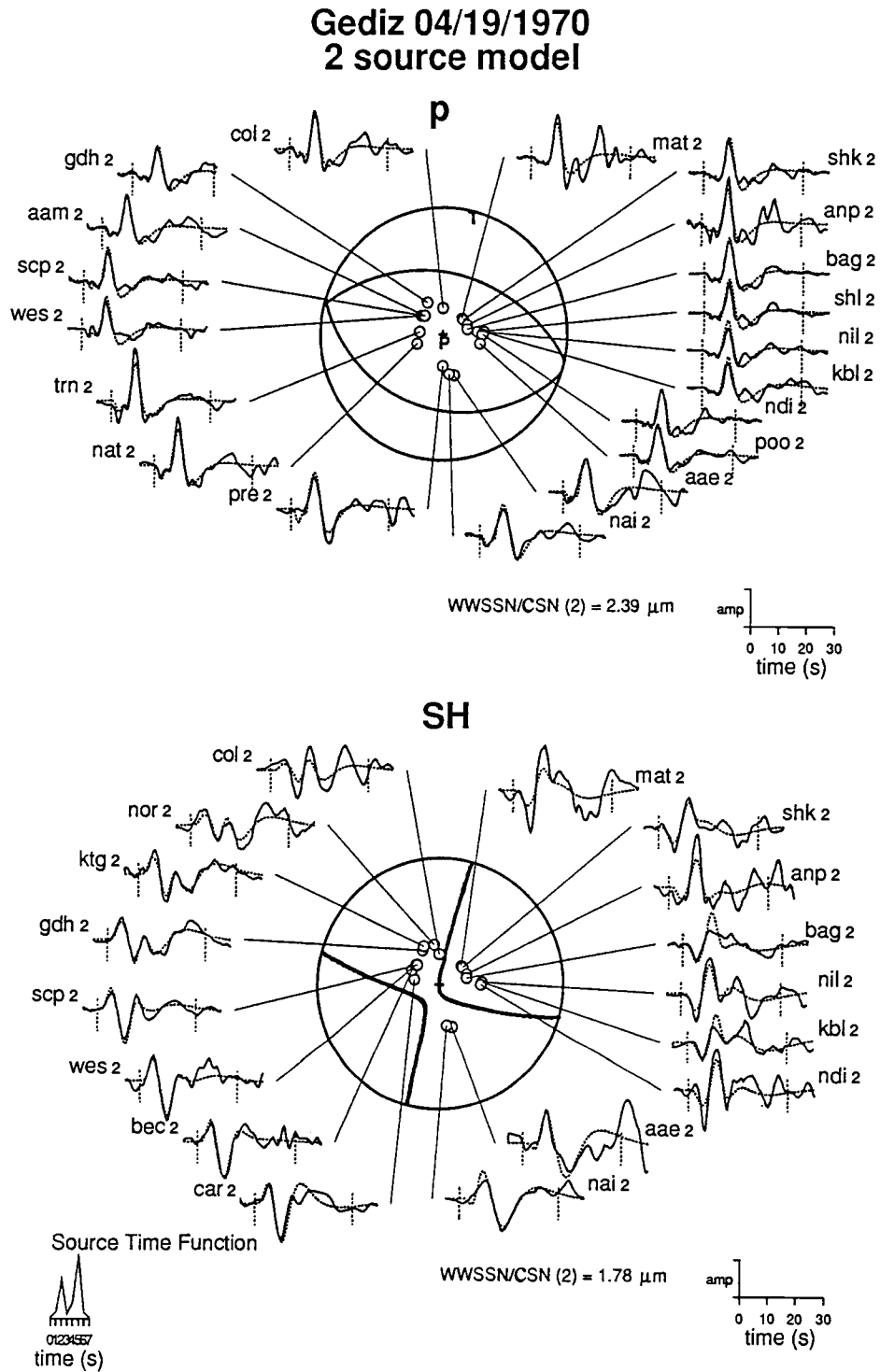
Figure 6.1.23 Two source model for the 04/19/1970 Gediz aftershock. Fault plane solution shown is the average of both subevents. Especially the fit for the SH waves improved significantly compared to the point source solution (Figure 6.1.22).
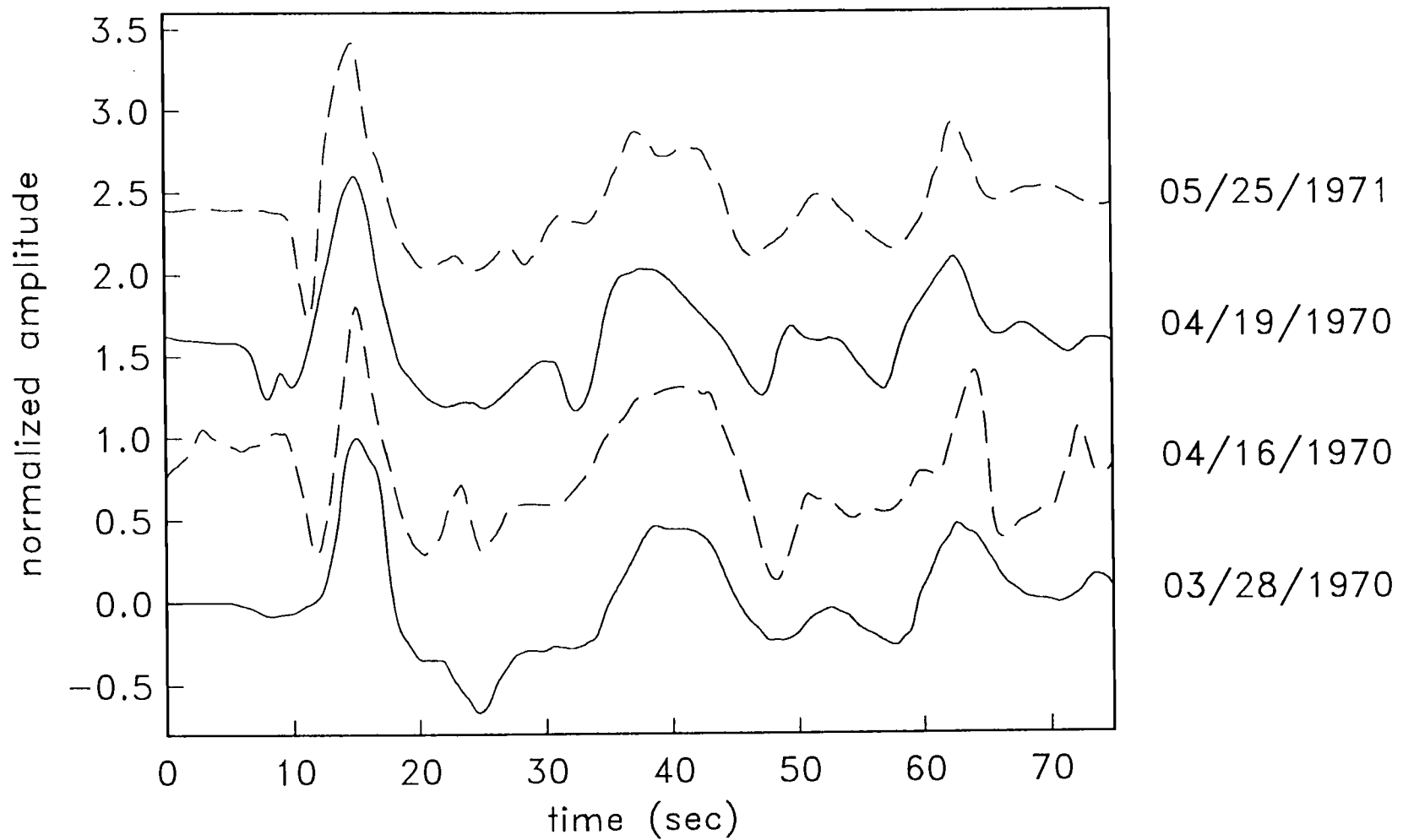
Figure 6.1.24 P waveforms observed at station Addis Ababa (AAE) for the Gediz earthquakes. Shown are the unfiltered, but normalized seismograms aligned with respect to their maximum amplitude. The waveforms consistently show a large arrival about 20 s after the peak. A source related origin of these arrivals can be excluded.

6.2 Thessaloniki 1978

6.2.1 Introduction

A strong earthquake of M_S=6.5 occurred in the area of Thessaloniki in northern Greece on June 20, 1978. The epicenter was located about 25 km east-north-east of the city, near the lakes Volvi and Langadha (Fig. 6.2.1). The main shock was preceded by a number of foreshocks. The largest of them on May 23, 1978 with a surface wave magnitude of M_S=5.8 will be studied in the next section. Numerous aftershocks with a size of up to $M_L \approx 4.5$ (Carver and Bollinger, 1981; Soufleris et al., 1982) were recorded by a local network of portable stations installed right after the occurrence of the main shock. The damage was most severe in the city of Thessaloniki and about 50 people were killed (Papazachos et al., 1979a; Ritsema, 1979).

Surface Faulting

The epicentral region consists of an E W-trending fault-bounded graben, the Mygdonian graben (Mercier et al., 1979; Papazachos et al., 1979a), which demonstrates the presence of recent extensional activity (McKenzie, 1978b). The dominant west to north-west striking and north to north-east dipping faults along the southern terminus of the graben separate two major geologic formations: the Axios-Vardar zone to the south and the Serbomacedonian massif to the north (Papazachos et al., 1979a). The following description of the surface faulting is based on work by Mercier et al. (1979, 1983) and Papazachos et al. (1979a). Surface faulting, which reactivated older neotectonic faults, accompanied the seismic activity. The foreshock of May 23 produced minor cracks which were not mapped (Soufleris and Stewart, 1981; Mercier et al., 1983). Surface ruptures were mapped following the main shock and three distinct groups of fissures showing predominantly normal faulting were observed between the lakes Volvi and Langadha. A NW-trending discontinuous surface break along the northern side of the graben of about 8 km length shows predominantly normal faulting behaviour with the southwestern part downthrown by up to 20 cm and a small left-lateral component of 2-3 cm. A second set of fractures with a visible length of about 12 km is situated along the southern side of the graben and strikes almost E-W; the northern block is downthrown with a maximum vertical displacement of about 30 cm and has a small right-lateral component. A smaller segment of surface rupture was observed between the above lines in the alluvial deposits of the valley trending approximately NW-SE. Mercier et al.

(1983) report a crack several hundred meters long observed in a northern suburb of Thessaloniki which appears to be associated with a large fault visible on Landsat photographs. Liquefaction and landsliding caused some of the fissures in the vicinity of the lakes and in the alluvial deposits. However, most of the surface rupture is thought to be of tectonic origin and striations along shear planes at bed rock sites along the southern boundary of the graben are clearly of tectonic origin. Opening and apparent reverse motion on some surface fissures on sloping grounds has been explained by Mercier et al. (1979, 1983) in terms of normal faulting that became overturned in the unconsolidated sediments at the surface. Mercier et al. (1979, 1983) measured the slip vector from cracks in sufficiently rigid sediments and deduced crustal stretching in a N-S to NNE-SSW direction, which corresponds very well with estimates of the direction of the tension axis derived from neotectonic faults, indicating reactivation of Quaternary faults during the 1978 earthquakes.

Aftershocks

The aftershock sequence was well recorded by portable seismograph networks from several institutions. The first stations were installed in the beginning of July 1978 and a network was operational for almost two months (Carver and Bollinger, 1981; Soufleris et al., 1982). Aftershock activity east of the main shock epicenter was mainly confined to locations within the Serbomacedonian massif north of the observed surface ruptures and composite fault plane solutions are of predominantly normal faulting type (Carver and Bollinger, 1981; Soufleris et al., 1982). The seismic activity west of the main shock epicenter is more diffuse and aftershocks are also observed within the Mygdonian graben beneath the lake Langadha (Carver and Bollinger, 1981; Soufleris et al., 1982). Composite fault plane solutions are mainly extensional; however, some strike-slip mechanisms are also found (Carver and Bollinger, 1981; Soufleris et al., 1982). This mixture of mechanisms is interpreted by Carver and Bollinger (1981) as splay faulting at the causal fault's western terminus. Hypocenter relocations of the main events (largest foreshocks, main shock, and largest aftershocks immediately following the main event before operation of the local network) by Soufleris and Stewart (1981), using the master event technique described by Jackson and Fitch (1979), and by Bollinger and Carver (1981), using a joint epicenter determination technique, place the hypocenters north of the observed traces of surface ruptures. The epicenter locations of the main events, as well as the aftershock distribution, suggest that the northward dipping fault bounding the graben at its southern side was the fault plane. Fault breaks along the northern boundary

of the graben may be associated with antithetic faulting at depth (Soufleris and Stewart, 1981).

6.2.2 Foreshock 05/23/78

The foreshock of May, 23, 1978 (M_s=5.8) was the largest earthquake of the fore- and aftershock sequence associated with the main shock of June, 20, and it radiated long-period waveforms of sufficient amplitude to be studied here. However, the amplitudes were relatively small and only waveforms with a good signal to noise ratio, usually associated with stations close to the epicenter or with high-gain stations, were utilized. The azimuthal coverage is not very good, and only one station (AAE) is located on the southern hemisphere of the focal sphere. Amplitudes at stations SHL and SHA were much larger than at adjacent stations and therefore I assumed that the gains for these stations were wrong by a factor of two. This improved the internal consistency of the data set. After removing the linear trends, all data were resampled with a sampling interval of 0.3 s. All SH waves were high-pass filtered (T≤100 s) and the P wave seismogram for SJG is high pass filtered with a cut-off of 50 s.

<u>Focal Mechanism</u>

The point source solution (Figure 6.2.2) indicates almost pure dip-slip motion along a fault trending approximately E-W with a centroid depth of about 5.3 km and a seismic moment of 4.4×10^{17} Nm (M_w=5.7) (Table 6.2.1). The overall fit is not very good, which is probably due to the small amplitudes of the waveforms; the errors introduced during digitizing are relatively more severe for small earthquakes with small amplitudes than for large events. The onset of the moment release is rather emergent; this can also be seen on the short period records, which have small arrivals preceding the main pulse by about 2-3 s. The triangular shape of the source time function with an emergent beginning and a relatively sharp drop has a duration of about 4 s; however, different alignments can change the shape and duration slightly; in particular alignments representing earlier starting times of the synthetic seismograms result in an even more emergent source time history. The depth is well resolved between 4-7 km depth, using a 10% variance increase as a measure for acceptance (Fig. 6.2.3). The variation of the other focal parameters within that depth range is quite small: strike, dip, and rake may differ by only 261±4°, 42±1°, and 270±3°, respectively, and the moment estimate varies between $3.9\text{-}4.7 \times 10^{17}$ Nm. These variations most probably underestimate the true uncertainties in the fault

orientation. The centroidal solution is compatible with the short period first motion data (Fig. 6.2.4). The first motion data, however would also allow a more steeply northward dipping nodal plane and a slightly more shallowly dipping southern one.

The CMT solution (Dziewonski et al., 1987a) of 261/54/274 for strike, dip, and rake and seismic moment of 5.7×10^{17}Nm obtained at a depth of 10 km agrees well with my results, with the exception of the steeper dip for the CMT mechanism. Papazachos et al. (1979b), from predominantly long-period first motion readings, obtained a normal faulting solution with a strike of 267° and fault dip of 54° respectively. Soufleris and Stewart (1981) found a similar result: strike: 277°, dip: 49°, and rake: 300°. The rake is not well resolved and could be changed to result in a smaller strike-slip component. My polarity readings from the short period instruments differ somewhat from theirs; station JER is interpreted as dilatational which, if true, constrains the auxiliary plane and the slip vector. Soufleris and Stewart (1981) interpreted the long period first motion polarity at JER as being compressional.

6.2.3 Mainshock 06/20/78

The mainshock of June 20, 1978 was well recorded at teleseismic distances and the azimuthal distribution of the stations is very good. I used 16 P-wave and 18 SH-wave seismograms to determine the rupture process of this earthquake. Following the digitizing, the data were resampled with a sampling period of 0.5 s. No filtering was applied to the data except for the SH wave seismogram of WIN which showed long period noise and was high-pass filtered (T≤60 s). The P wave amplitudes at KTG seemed to be inconsistent with observations of stations nearby and therefore the gain was increased by a factor of two. From the polarity of the incident P wave at NDI it was deduced that the long-period north-south channel had a reversed polarity.

Focal Mechanism

Figure 6.2.5 shows the point source solution. The P waves are not very sensitive to slight changes in the source orientation, however, the SH waves and their polarities at the onset constrain the solution (e.g. stations MAT, HKC, NAI, and WIN). The fit at WIN is not very good for either the P or the SH wave, which may be attributed to source complexity, lateral heterogeneities in the source region, or local or path related effects. The P wave at PRE looks remarkably similar; unfortunately no records of the foreshock from these stations were available to confirm (or reject) any of these possibilities (see also

Barker and Langston, 1981). The source mechanism indicates almost pure normal faulting with only a minor right-lateral component (rake: 264°) along an east-west trending fault (strike: 257°) dipping north at an angle of 41°. The seismic moment of 35.4×10^{17} Nm corresponds to a moment magnitude of $M_W = 6.3$. The source time function is of roughly a triangular shape with a duration of about 10 s (Figure 6.2.6). The centroid depth of 7 km is not well resolved (Figure 6.2.7) which was also encountered by Barker and Langston (1981). Using a variance increase of 10% as a cut-off, the allowable centroid is placed at a depth of 4-16 km. Within this depth range strike, dip, and rake vary only by 2°, 1°, and 5°, respectively. The estimate for the seismic moment, however, is affected more drastically, $21-40 \times 10^{17}$ Nm are possible within that depth range (Figure 6.2.7). The short-period first motion polarity readings (Figure 6.2.8) are consistent with the point source estimate. The nodal character of the onset at STU and JER constrains both nodal planes.

The possibility for propagating ruptures was investigated. Line sources propagating unilaterally towards east provided fits inferior to the point source. The match to the observed waveforms improved slightly for ruptures propagating towards west compared to the point source; the data, however, are not sensitive to the rupture speed. Papazachos et al. (1979a) suggested a SE to NW propagation of the rupture based on heavier damage towards the NW, but modeling results neither confirm nor reject this hypothesis unequivocally. A rupture propagating bilaterally away from its nucleation point did not improve the fit significantly as long as the mechanism was held fixed to the point source solution. Allowing the line sources moving in opposite direction to freely vary their source mechanisms showed strong parameter trade-offs and no further attempts were pursued.

Strong motion data from Thessaloniki show two distinct S-wave groups separated by 3-4 s according to Soufleris and Stewart (1981). The observed teleseismic long-periodic waveforms do not show such complexity due to the low-pass filtering effects along the travel path and of the instrument, and the source time function of the point source estimate is rather smooth. Inversions including a second point source were carried out; however, results proved to be highly dependent on the source parameters initially assigned to the two sources and their relative locations in space and time. Since no precise information about the spatial and temporal relations of the possible subevents could be established, there was no means of deriving any unique solutions and I did not continue further along this line.

The point source solution was therefore kept as the solution which provides a well constrained fit with the least amount of source complexity. The result is shown in Figure

6.2.5 and the parameters are summarized in Table 6.2.2 along with source parameters obtained by numerous other researchers.

Barker and Langston (1981) inverted for the source parameters using teleseismic body waves from 8 stations. At a centroid depth of 8 km they found a source orientation with a fault striking west-north-west and dipping 52° towards north. A left-lateral strike slip component to the normal faulting is indicated by the rake of 298°. They obtained a seismic moment of 5.7×10^{17}Nm and a skewed triangular source time function of about 6-8 s duration. The orientation of their solution is incompatible with some of the SH wave polarities and waveforms in my data set. Barker and Langston used only two SH waveforms.

Soufleris and Stewart (1981) used also long-period, teleseismic body waves to infer the source orientations. With a trial-and-error forward modelling technique they confirmed their first motion fault plane solution: the fault strikes 278°, has a dip of 46°, and the rake of 300° implies a normal motion with some oblique left-lateral strike-slip. A source depth of 6±2 km was inferred. Soufleris and Stewart (1981) also obtained an estimate of the seismic moment of $5.2\pm1.8 \times 10^{17}$Nm with a duration of the trapezoidal source time function of 9±1.5 s.

Papazachos et al. (1979b) used mainly long-period first motion data and obtained a normal faulting mechanism with a strike of 265° and the fault dipping towards north at an angle of 36°.

The Harvard CMT solution (Dziewonski et al., 1987a) at a depth of 10 km is of almost pure normal faulting character. A strike of 286° and a dip of 43° were obtained. The half-duration of 4.2 s and the seismic moment of 27.1×10^{17}Nm agree with my results.

Kulhánek and Meyer (1979) measured the P- and S-wave spectra from UPP and KIR. Following the seismic source model of Brune (1970, 1971) and Hanks and Wyss (1972) they obtained a seismic moment estimate of 87×10^{17}Nm and a average displacement of 25 cm from the P wave spectra of KIR; estimates from the UPP data are about four times larger. The moment and displacement are probably overestimated, since strong upper mantle phases due to triplications are present in the distance range of these two stations (KIR: 27°, UPP: 19°).

Bürstle and Müller (1983) used an extended reflectivity method to model the Love waves recorded at Gräfenberg (GRF) to determine a seismic moment of 3.4×10^{17}Nm and a duration of 10 s. They utilized the source orientation found by Soufleris and Stewart (1981).

Stavrakakis et al. (1987) used the method of Kikuchi and Kanamori (1982) to investigate the multiple source character of the Thessaloniki earthquake. Fixing the mechanisms of the subevents to the Soufleris and Stewart (1981) solution they obtained a seismic moment of 33.3×10^{17}Nm and a source duration of the main subevent of 9 s. They found three significant subevents based on the moment release rate function. The second and third occurred about 15 and 24 s after the first subevent. However, the simple waveforms do not support their results and tests using a long source time function showed that no significant moment release occurred outside the 10 s window of the main energy release.

Carver and Bollinger (1981) calculated the dip of the fault plane from the average depth of the aftershocks (8 km) and the distance between the surface breaks and the main shock epicenter (5 km), indicating a fault dipping northward with 58°. Based on the first motion fault plane solution of Papazachos et al. (1979b) with a dip of 36°, they suggested that the fault is of listric geometry, flattening with depth.

My results are generally compatible with most of the results presented by other investigators. Using a more complete data set compared to other studies, especially the incorporation of many SH waves, constrains the source orientation and the good azimuthal sampling should provide a trustworthy point source estimation. The slight change in strike to a west-south-west direction is caused by SH wave polarities and waveshapes. The estimated dip from the inversion was very stable throughout all inversions and tests. The moment estimates, source durations, and centroid depths are in agreement with other studies. The similarity in the source mechanisms of the fore- and the mainshock could imply that both earthquakes ruptured along the same fault plane. The fault plane solutions from waveform modelling show N-S extension, which is in agreement with the geologic record (Mercier et al., 1979, 1983) and tectonic models of the Aegean (e.g. McKenzie, 1978b).

Detachment Faulting

Faulting on a shallowly dipping detachment surface has been studied in the way described in Chapter 3.2. The detachment sources dipping with either 0° or 10° placed at twice the centroid depth were allowed to have a very long source time function. In the first attempts, these subevents were not delayed with respect to the point source. However these shallow dipping sources showed no moment release at all for the first 14 s. The possible moment release for the detachment sources was rather small and the fit to

the observed waveforms did not improve significantly. Results are summarized in Table 6.2.2.

Down-Dip Fault Geometry

The centroid depth of 7 km indicates that the rupture width should be sufficiently wide to allow contributions from different parts of the fault to be well separated in time for ruptures nucleating at the base of the brittle upper crust. Three point sources at 11.6, 7, and 2.3 km depth were distributed along the width of the fault. Models for ruptures propagating up-dip were tested for different fault geometries with varying amounts of curvature as described for the Alasehir and Gediz events. The second (7 km) and third (2.3 km) subsource were delayed by 2.2 s and 4.4 s with respect to the deep initial source. Their lateral separation is 5.4 km and shallower subsources are positioned almost south of the first event. The composite moment tensor of the subsources was constrained to be consistent with the point source moment tensor.

In the first step, the inversions included only the distribution of the seismic moment, while the total amount of seismic moment release was constraint for each subsource. The waveforms at azimuthally selected stations for four different fault geometries are shown in Figure 6.2.9. Differences between the fits are small, especially for P waves. For large decreases of fault dip (LI6 model), the first motion polarity changes its sign for stations toward south (e.g. AAE) which is not compatible with the data. The SH waves show more clearly the shortcomings of listric fault geometries compared with the planar case. Stations roughly in the direction of fault strike (e.g. MAT, SHL, and FVM) are especially sensitive to different models, whereas stations away from the strike direction (e.g. NAI) are not. The t-test was used to differentiate acceptable and unacceptable solutions quantitatively, the results are shown in Table 6.2.3. From the statistical test, models with an increase in fault dip by 40° with depth can be rejected (95% confidence level). Less than 30° of decrease in fault curvature is allowed by the data based on the 95% confidence level obtained from the t-test.

In the second set of tests I inverted for the distribution of the seismic moment for each subsource as done above. After a stable solution was found, but before realigning the synthetic and the observed seismograms, the seismic moment and later the dip of each subsource were also inverted for. Table 6.2.4 shows the results obtained from three starting models (planar, 40° increase and decrease of fault dip respectively). The shallow source was very unstable and no consistent results for the dip and seismic moment of this subsource could be found. The deeper sources are more stable, since the surface

reflected phases are more separated from the direct phases. The estimated distribution of the seismic moments depends on the starting model. This could reflect the influence of the dip and moment estimated for the shallowest source on the deeper subsources, which possibly biases the results. The estimated dips for the two deeper sources, however, are relatively stable and a significant decrease of fault dip with depth is not apparent, which agrees with the more constrained inversion results listed in Table 6.2.3.

Depth Extent of Rupture

The aftershock activity of the Thessaloniki earthquake has been well recorded by a local network of portable seismographs. The hypocentral depths of the 413 'best' located aftershocks from the studies by Carver and Bollinger (1981) and Soufleris et al. (1982) are shown in Figure 6.2.10. Most of the aftershocks are located at a depth of 3-12 km. Doubling the centroid depth provides a rough estimate of the depth extent of faulting for the main shock. The value of 14 km indicates that the rupture may have penetrated to depths where almost no aftershocks occurred.

To obtain a more detailed estimate of the depth extent of brittle faulting during the main shock, I used a planar fault model and distributed five point sources at equal spacings along the width of the fault and inverted for the time history and seismic moment of each source. From the above investigation of the fault geometry no compelling evidence for a significant amount of fault curvature could be deduced. As a starting model I used the point source depth and distributed three sources equidistant within twice the centroid depth in the same way as done when studying the fault geometry. Then two more sources with the same vertical spacing were added at the bottom of the original model, resulting in sources at 2.3, 7, 11.6, 16.3, and 20.9 km depth. More information about the depth at which the moment release drops to small values was sought by 'perturbating' the above model. The deepest source was moved upward and downward in 0.45 km increments and the depth of the other sources was linearly adjusted such that they remained equidistant. Rupture nucleation was assumed to occur at 10-12 km depth, close to the base of the main aftershock activity. Barker and Langston (1981) compared arrival times of surface reflected phases from short-period seismograms with synthetic seismograms at various depths, and deduced a nucleation depth of about 11±1 km, supporting my choice. Figure 6.2.11 shows the seismic moment release (normalized with respect to the width of the respective fault segment) vs. depth of the subsources. For depths between 4-16 km the moment release seems to be rather uniform, and decreases between 16 and 19 km. Below about 19 km the moment release seems to be

negligible. At shallow depths, interference between direct phases and surface reflections causes instabilities. The solutions are certainly not unique and no emphasis will be placed on specific details of the moment release with depth. However, from the various models it seems to be quite clear that a significant part of the moment release occurred up to depths of around 16 km. This depth could be off by a few kilometers since the crustal half-space model used to generate the synthetics is certainly an oversimplification of the true crustal structure, especially for the deeper parts of the crust. However, the same crustal half-space velocity of 6.0 km/s used to calculate the synthetic seismograms was found by Soufleris et al. (1982) to result in aftershock locations with the smallest rms-residuals. The difference in the depth extent of the aftershock activity and the main shock rupture is therefore probably real and not caused by different crustal models.

The aftershock distribution and the extent of the main shock rupture follow the model presented by Scholz (1987) and Tse and Rice (1986). For depths above 3 km and below 12 km stable frictional behaviour is present and prevents the nucleation of earthquakes. The main-shock rupture, however, seemed to dynamically penetrate into the zone characterized by velocity-strengthening and stable frictional behaviour. The few aftershocks located within this zone can be explained in terms of heterogeneities in the material and stress concentration caused by the main shock rupture.

Table 6.2.1 Source Parameters of the 05/23/1978 Thessaloniki Foreshock

	strike deg	dip deg	rake deg	moment 10^{17}Nm	depth km	duration s
P S	261	42	270	4.4	5.3	4
CMT	261	54	274	5.7	10	2.0[1]
Pb	267	54				
S & S	277	49	300			

PS - point source solution. CMT - Dziewonski et al (1987) moment tensor inversion. Pb, S&S - Papazachos et al. (1979b), Soufleris and Stewart (1981) first motion fault plane solution. [1] - half-duration.

Table 6.2.2 Source Parameters of the 06/20/1978 Thessaloniki Earthquake

	strike deg	dip deg	rake deg	moment 10^{17}Nm	depth km	duration s	Δt s	Δr km	Δaz deg	σ
PS	257	41	264	35.4	7.0	10				0.345
DE	257*	0*	270*	3.9	13.9*	18	14.0	8.0*	347*	0.339
	257*	10*	270*	4.2	13.9*	18	14.0	8.0*	347*	0.339
B&L	280±7	55±3	298±5	57	8	6-8				
S&S	278	46	300	52±18	6±2	9±1.5				
Pb, K&M	265	36		87						
CMT	286	43	272	27.1	10	4.2[1]				
B&M				34		10				
C&B, S		58		33.3		9				

PS - point source solution. DE - detachment source with 0° and 10° dipping surface, respectively, locations derived relative to point source solution PS. B&L - Barker and Langston (1981). S&S - Soufleris and Stewart (1981). Pb - Papazachos et al. (1979b). K&M - Kulhánek and Meyer (1979). CMT - Dziewonski et al. (1987a). B&M - Bürstle and Müller (1983). C&B - Carver and Bollinger (1981). S - Stavrakakis et al. (1987). Δt, Δr, and Δaz - delay, distance, and azimuth of subevent with respect to point source. σ - normalized variance of residuals. "*" - fixed. [1] - half-duration.

Table 6.2.3 Thessaloniki, Down-Dip Geometry: 1. Dip and Seismic Moment Fixed. Results are Compared Statistically.

	curvature deg	σ	t	μ 10^{-3}	s 10^{-2}	Mo $10^{17}Nm$	rake deg
LO4	+40	0.383	**1.83**	1.80	0.57	14.0*	265*
LO2	+20	0.363	**0.36** ●	0.29	0.48	12.3*	264*
PL	0	0.359	●			11.8*	264*
LI2	-20	0.389	**1.52** ●	2.37	0.91	12.3*	264*
LI3	-30	0.443	**2.31**	6.21	1.56	12.9*	264*
LI4	-40	0.501	**2.82**	10.31	2.13	14.0*	265*
LI6	-60	0.763	**3.07**	29.19	5.55	17.7*	266*

LO - fault steepens with depth. PL - planar fault model. LI - fault flattens with depth. Rupture propagates upward from the base of the seismogenic layer. Curvature - increase (+) or decrease (-) of fault dip with depth in degree. σ - normalized variance of residuals. t - value obtained from t-test comparing listric models with planar model PL. μ,s - mean and standard deviation of differences of squared station residuals, for explanation see Chapter 3. Number of samples N=34. Value t has to exceed to be within certain confidence level: 60% - 0.26. 75% - 0.68. 90% - 1.31. 95% - 1.70. 97.5% - 2.04. 99% - 2.46. 99.5% - 2.75. 99.95 - 3.65. ● - acceptable fits (95% confidence level). Mo - moment assigned to each individual subsource. rake - rake assigned to shallow and deep subsource, while subsource at centroid depth was assigned point source value (264°). * - fixed. All models have same moment tensor as point source.

Table 6.2.4 Thessaloniki, Down-Dip Geometry: 2. Dip and Seismic Moment Free

	depth km	strike deg	rake deg	**Start**		**Result**	
				dip deg	moment 10^{17}Nm	dip deg	moment 10^{17}Nm
PL	11.6*	257*	264*	41	12	**38**	8
	7.0*	257*	264*	41	12	**42**	26
	2.3*	257*	264*	41	12	**?**	0
LI4	11.6*	257*	265*	21	14	**38**	14
	7.0*	257*	264*	41	14	**48**	20
	2.3*	257*	265*	61	14	**99**	3
LO4	11.6*	257*	265*	61	14	**41**	13
	7.0*	257*	264*	41	14	**40**	16
	2.3*	257*	265*	21	14	**-111**	12

PL - planar start model. LI4, LO4 - listric start models. "*" - fixed. Inverted for seismic moment and dip of each subsource, rupture propagating up-dip.
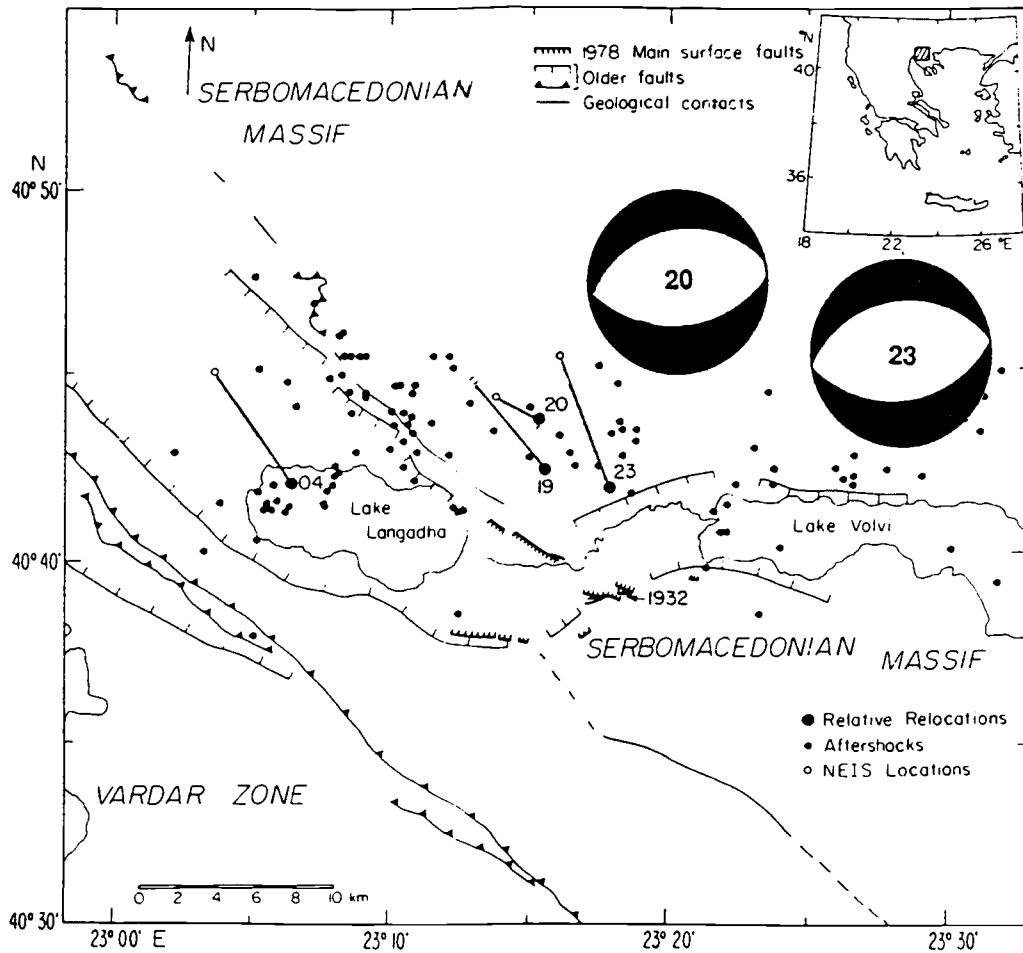
Figure 6.2.1   Tectonic setting of the 1978 Thessaloniki earthquake sequence (from Soufleris and Stewart, 1981). Surface ruptures associated with the main shock which are probably of tectonic origin are shown with heavy hatched lines on downthrown side. Aftershock distribution and main shock relocations from Soufleris and Stewart (1981). Focal mechanisms are from this study.

Thessaloniki 05/23/1978

P

WWSSN/CSN (2) = 1.49 μm   amp

0 10 20 30
time (s)

SH

Source Time Function

01234
time (s)

WWSSN/CSN (2) = 1.10 μm   amp

0 10 20 30
time (s)
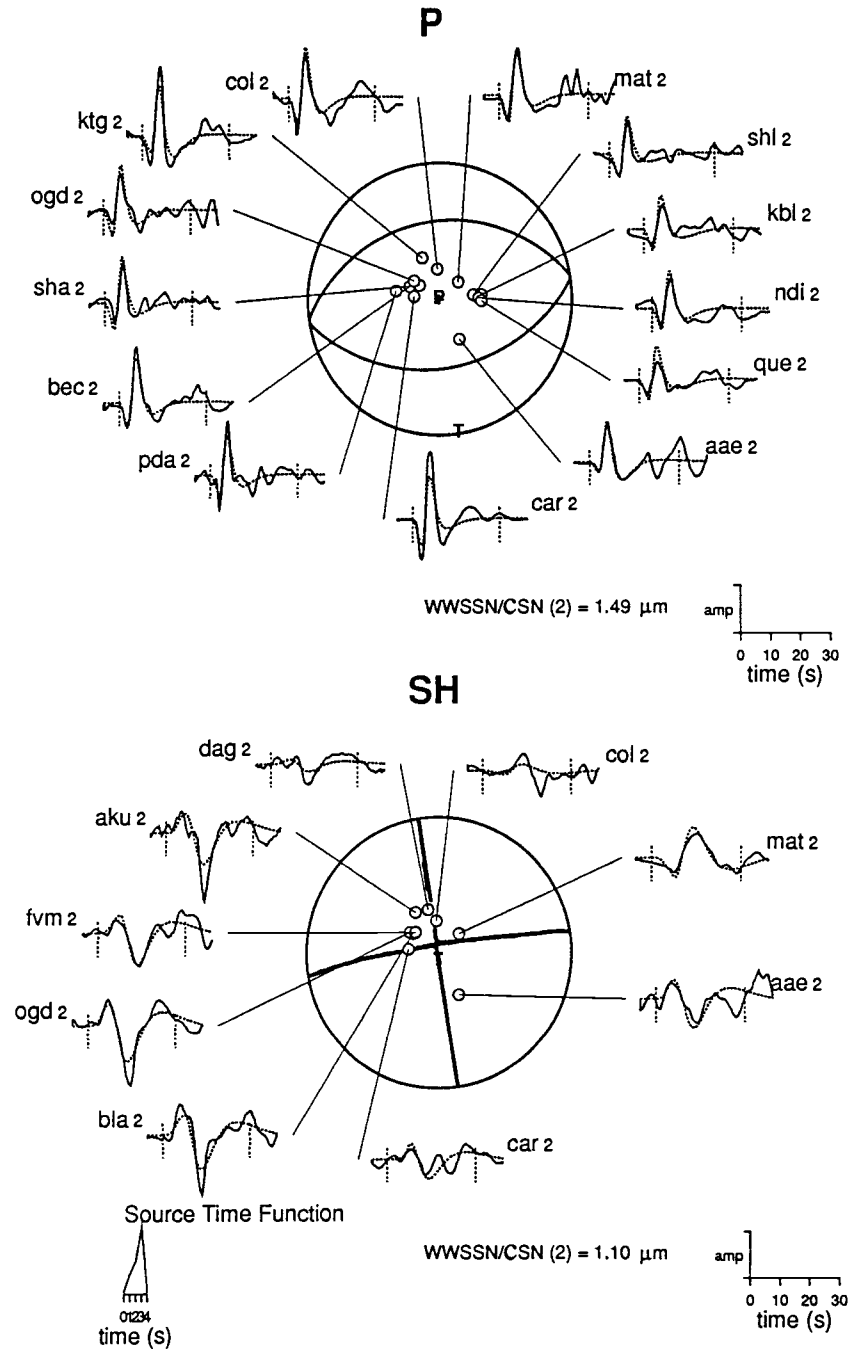
Figure 6.2.2   Point source solution for the 05/23/1978 Thessaloniki foreshock.

Thessaloniki 05/23/1978
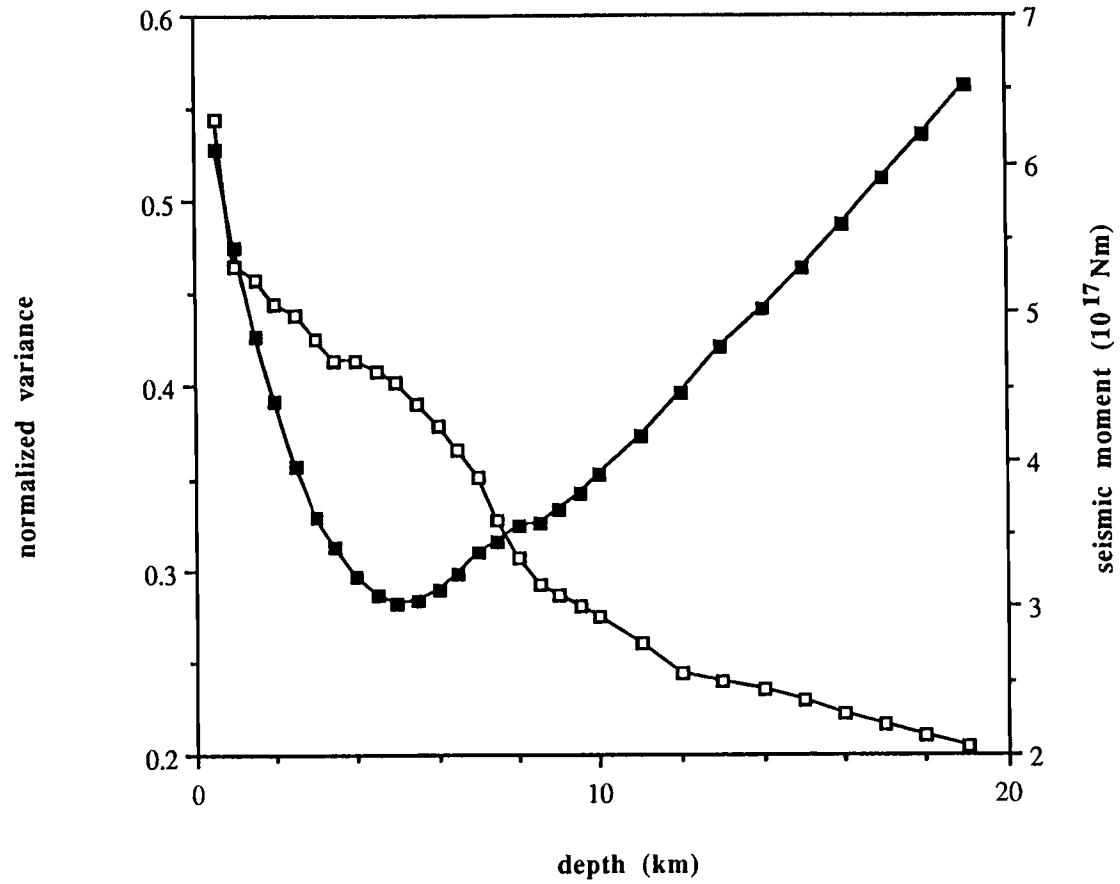
Figure 6.2.3 Residual variance (filled squares) and seismic moment (open squares) as a function of centroid depth.

Thessaloniki   05/23/1978

+ Compressional

□ Dilatational

✧ Nodal

Figure 6.2.4   Short-period first motion polarities. Fault plane solution from waveform inversion (see Table 6.2.1 and Figure 6.2.2) is consistent with the first motion data.

Thessaloniki 06/20/1978

P

WWSSN/CSN (2) = 5.26 μm

amp

0 10 20 30
time (s)

SH

Source Time Function

0 2 4 6 810
time (s)

WWSSN/CSN (2) = 5.63 μm

amp

0 10 20 30
time (s)
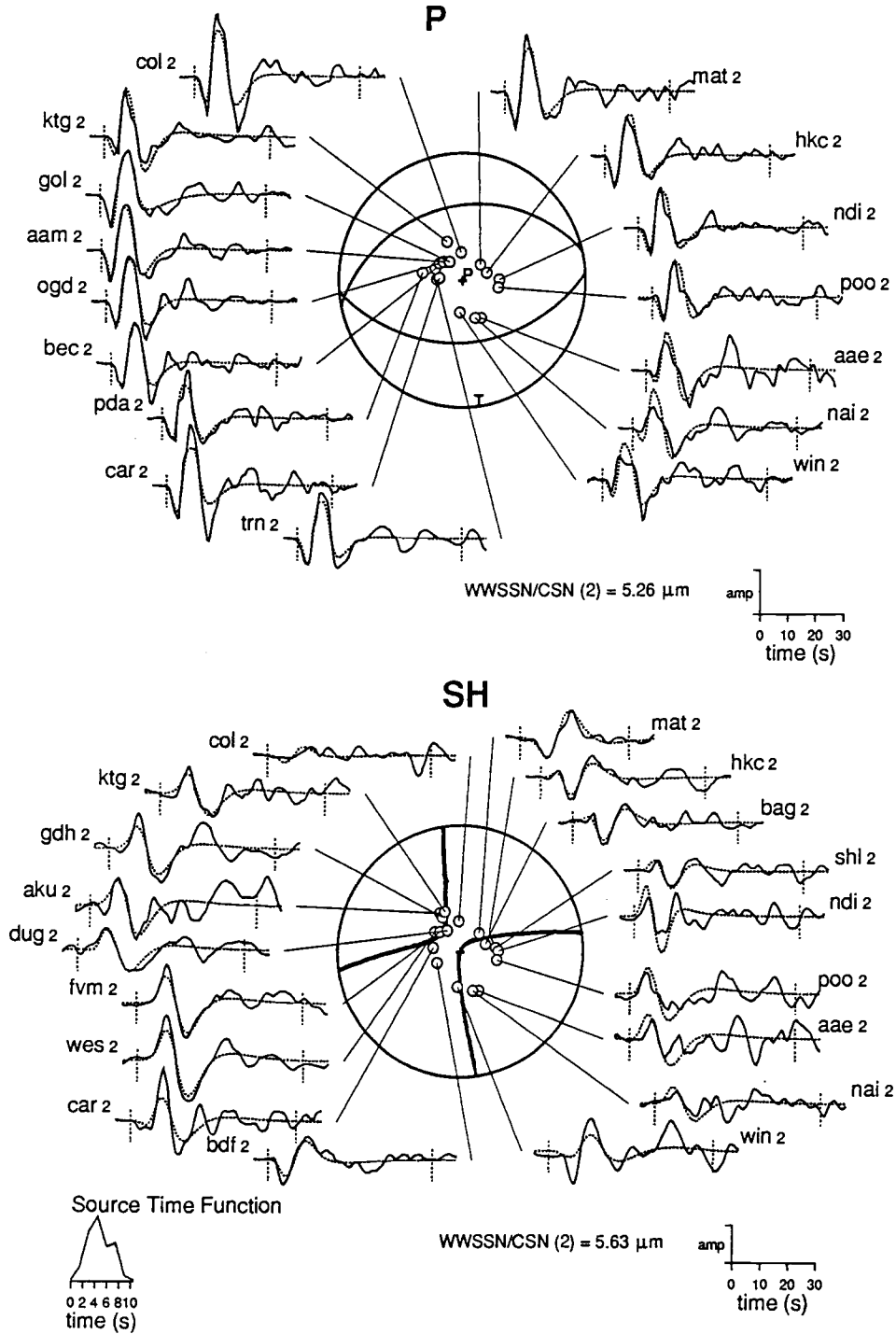
Figure 6.2.5 Point source solution for the 06/20/1978 Thessaloniki earthquake.

Thessaloniki - moment release rate
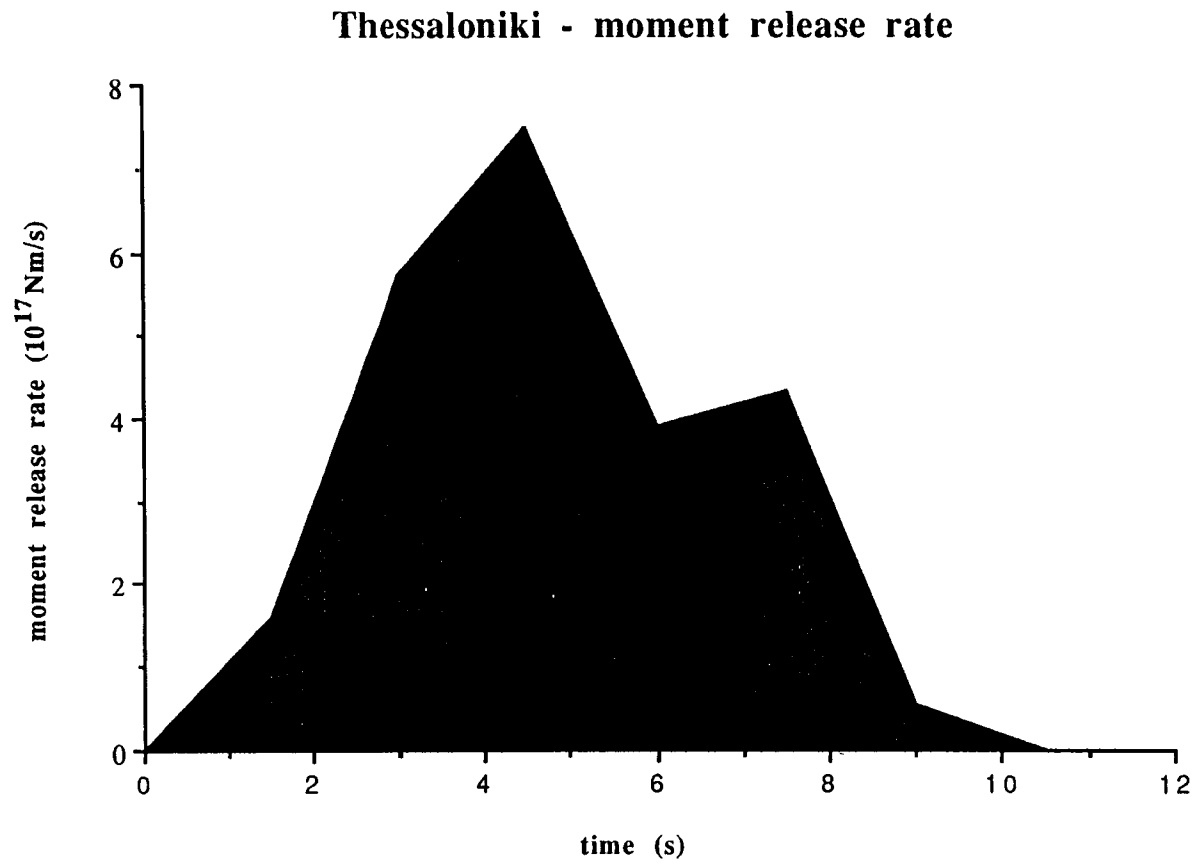
Figure 6.2.6   Seismic moment release rate.

Thessaloniki   06/20/1978
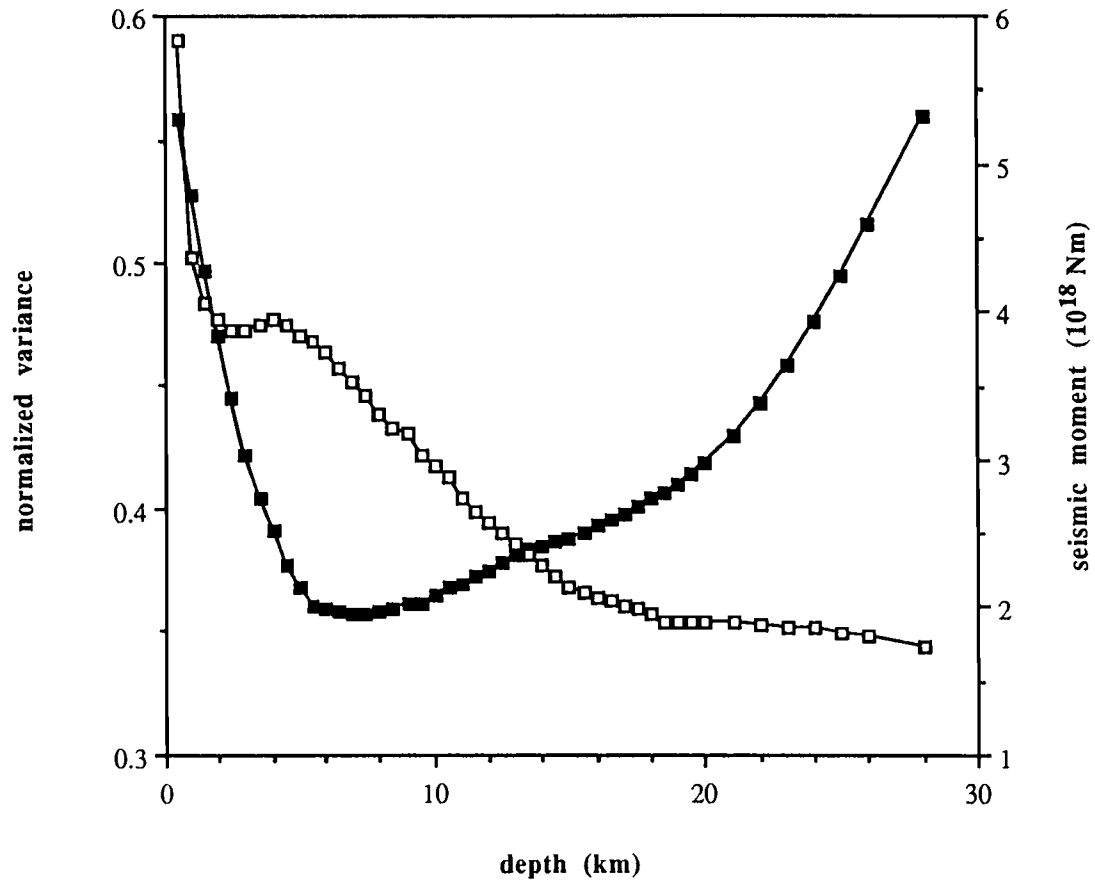
Figure 6.2.7   Residual variance (filled squares) and seismic moment (open squares) as a function of centroid depth.

STU

NUR

JER

+ Compressional

□ Dilatational

◇ Nodal
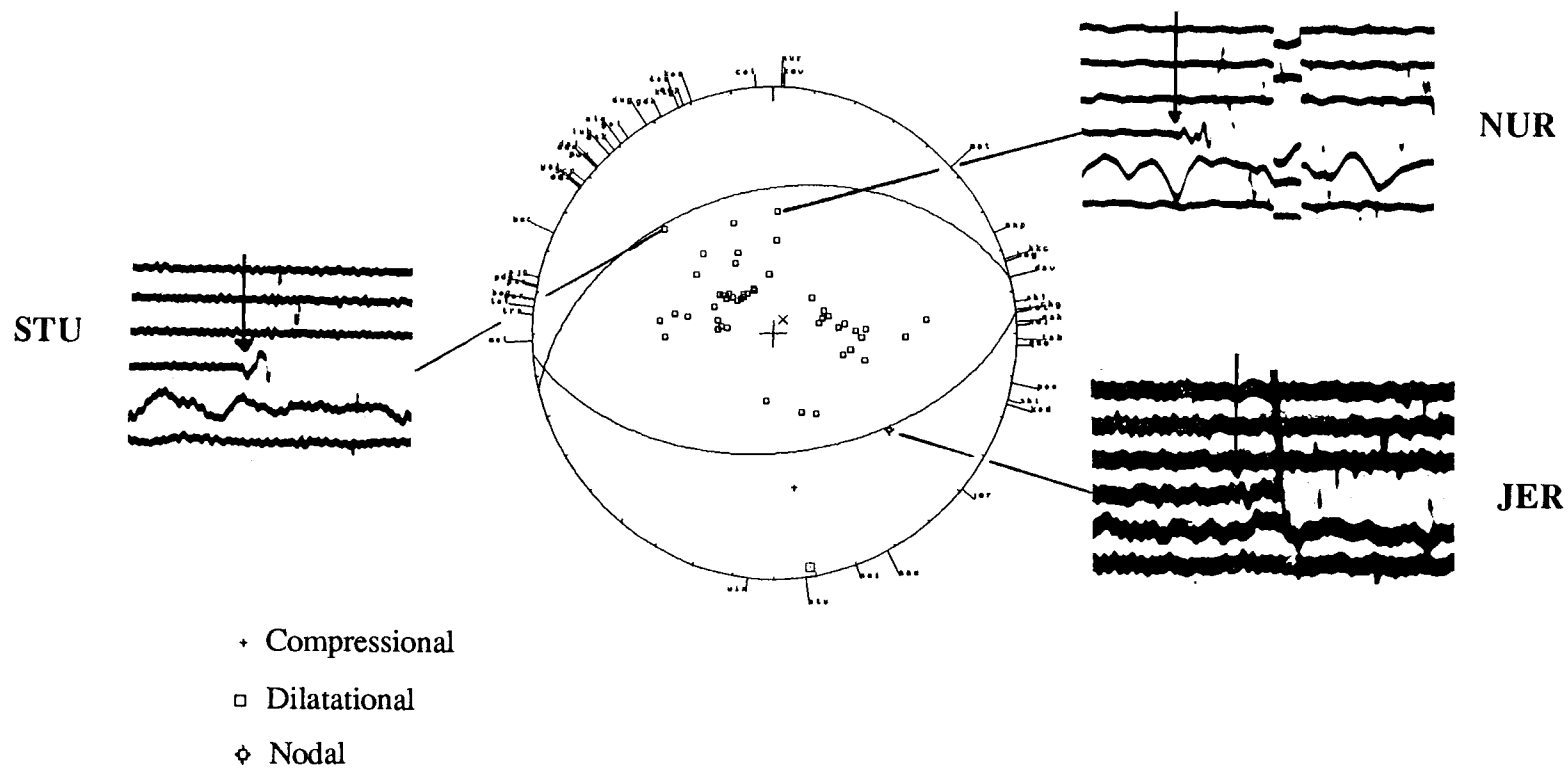
Figure 6.2.8 Short-period first motion polarities. Fault plane solution from waveform inversion (see Table 6.2.2 and Figure 6.2.5) is consistent with the first motion data. Critical stations close to the nodes are shown.
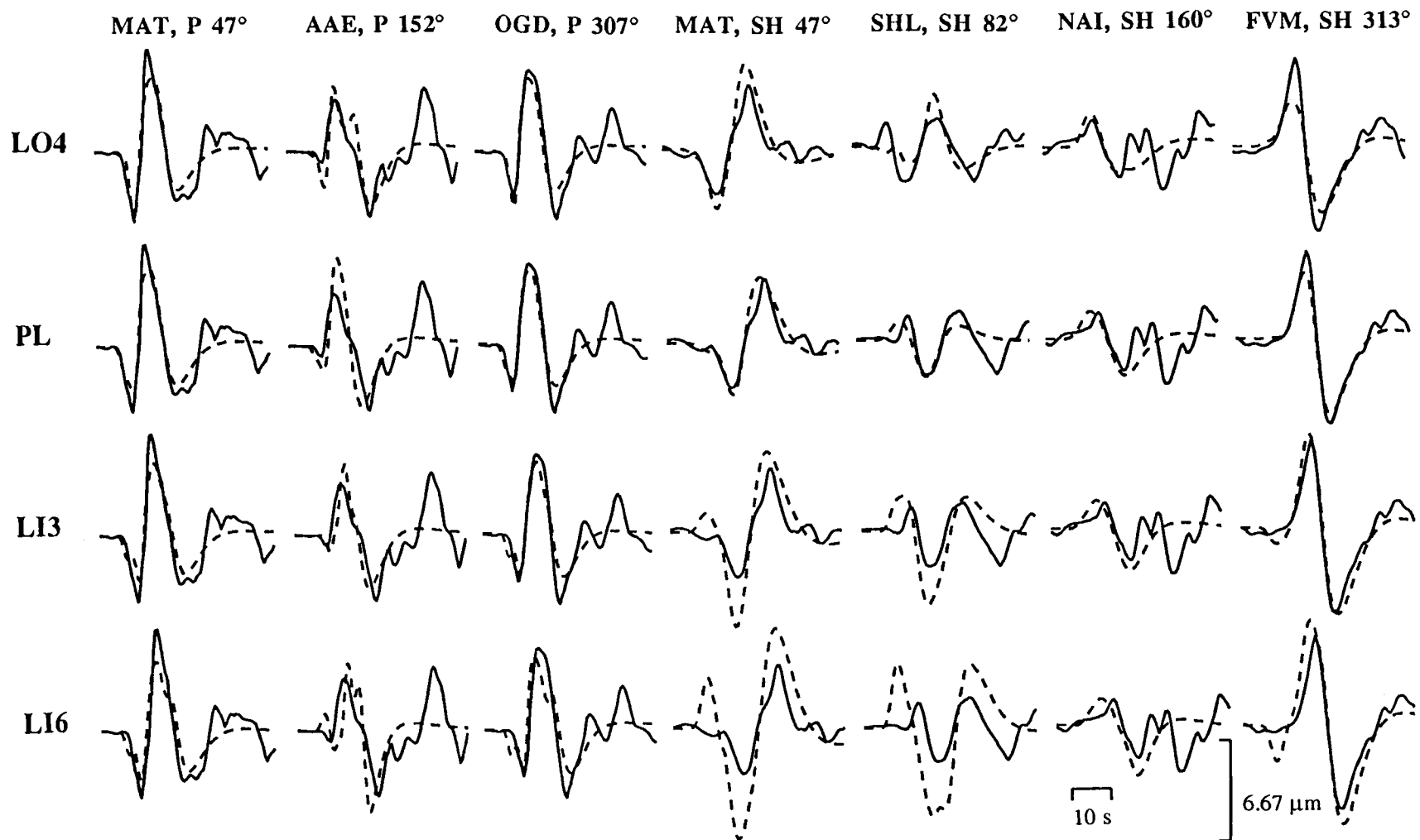
Figure 6.2.9 Comparison of P and SH waveforms for four fault models listed in Table 6.2.3 for the 06/20/1978 Thessaloniki earthquake. Number next to station is the azimuth from the source.
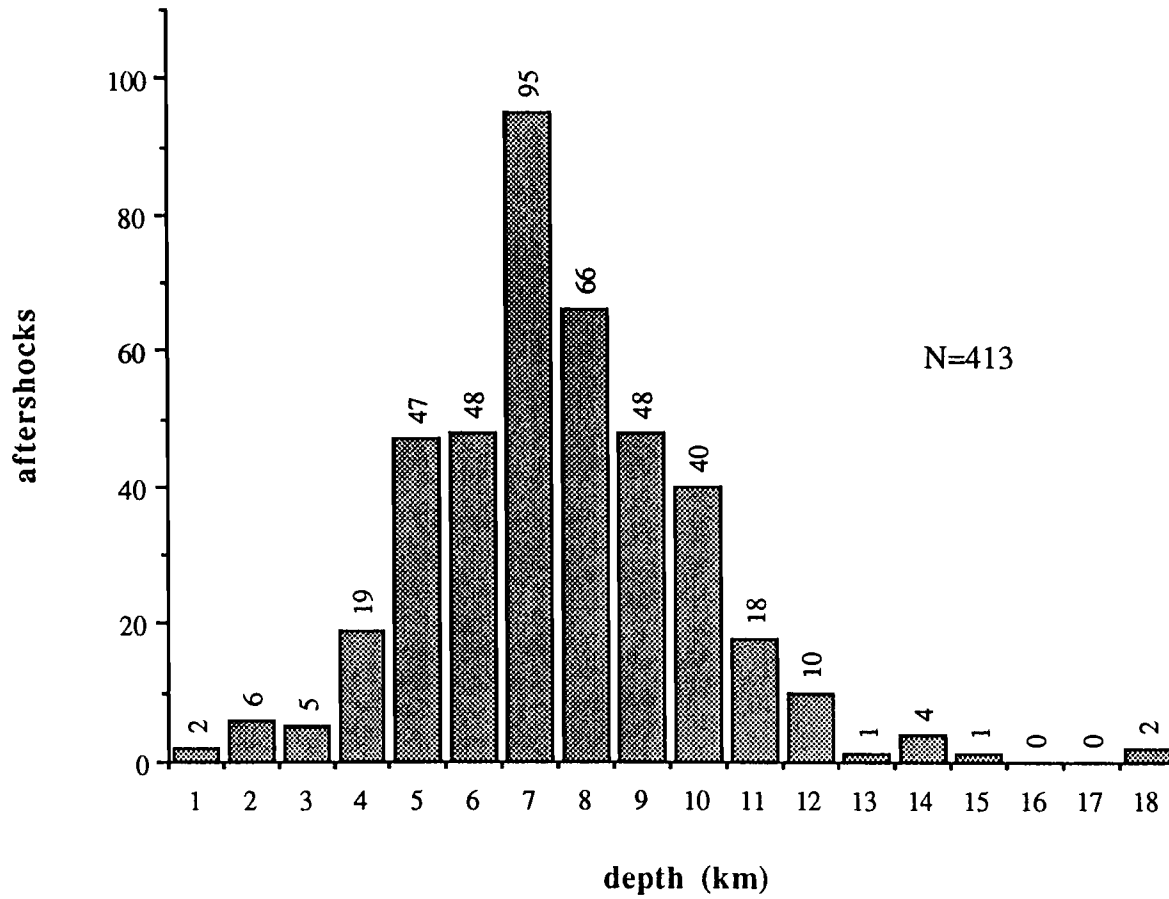
Figure 6.2.10 Aftershock depth distribution. Data are from Carver and Bollinger (1981) and Soufleris et al. (1982). Only a few aftershocks occur above 3 and below 12 km depth. N: total number of aftershocks included in histogram.
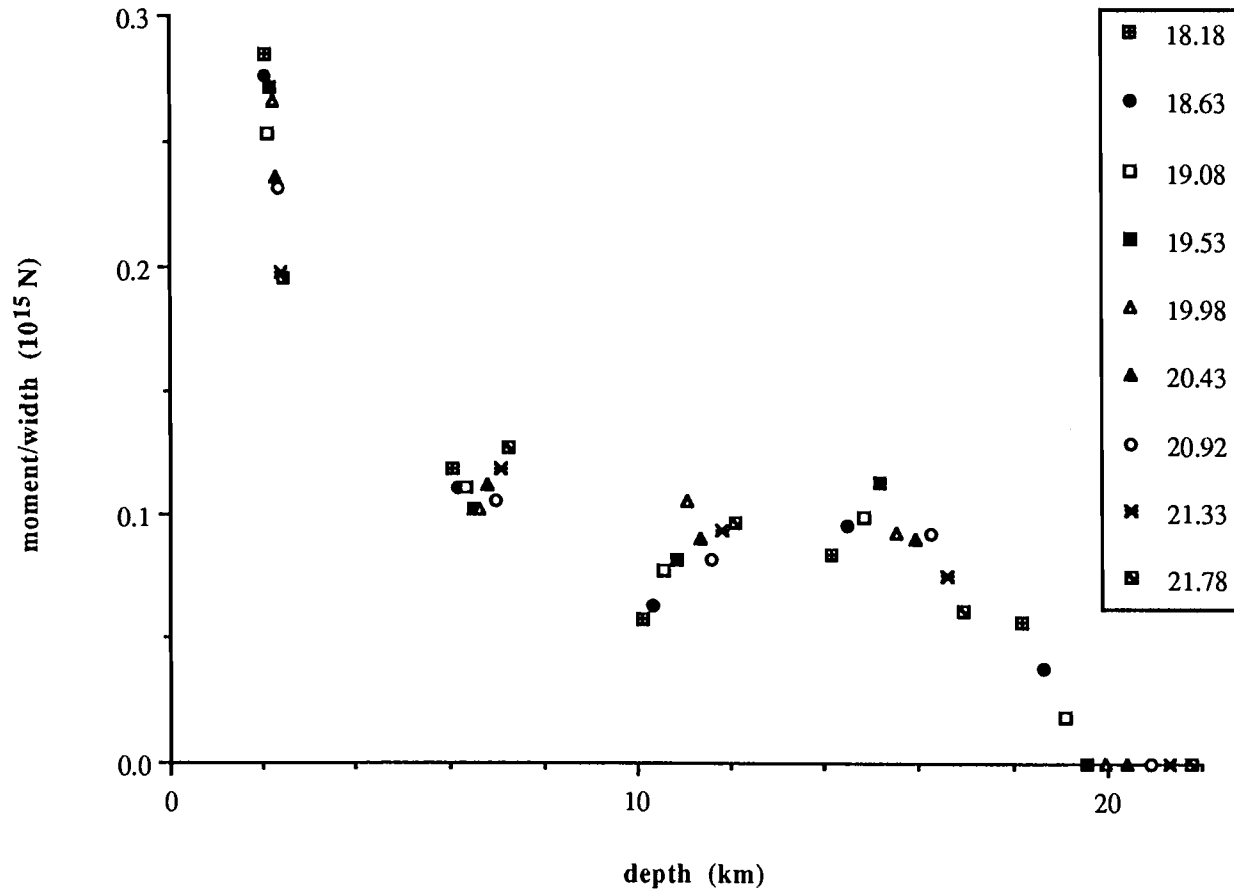
Figure 6.2.11 Seismic moment release vs. depth for the 06/20/1978 Thessaloniki earthquake. The figure is a compilation of 9 inversions in which 5 equally-spaced point sources were used. The numbers in the legend correspond to the deepest source of each model. Moment release extends to about 18 km depth.

6.3   Corinth 1981

6.3.1   Introduction

The easternmost part of the Gulf of Corinth about 60 km west of Athens was shaken by a strong earthquake (M_S=6.7) on February 24, 1981 without any preceding foreshock activity. About 5 hours later on February 25, a second strong earthquake (M_S=6.4) occurred in the same region. Many aftershocks followed these two main shocks and on March 4, 1981 another strong shock (M_S=6.3) occurred (Fig. 6.3.1). About 20 people were killed by the earthquake and several hundred sustained injuries (e.g. Papazachos et al., 1984). Several thousand houses were destroyed or damaged beyond repair and unprecedented damage occurred in Athens where about 500 houses collapsed, more than 5000 people were made homeless, and the Parthenon sustained minor damage (Ambraseys and Jackson, 1981, 1990). A more extensive description of the damage can be found in Ambraseys and Jackson (1981).

The epicenters of the main shocks are aligned west to east with the first event being the westernmost. A master event technique (Jackson and Fitch, 1979) has been used by Taymaz et al. (1991) to relocate the main events. The additional information of a locally (and teleseismically) well recorded aftershock provided a mean to position the epicenters in an absolute sense. Their results show that the first two events are located off-shore in the Alkyonides Gulf, whereas the March 4 event occurred just on-shore on the eastern extension of the gulf. These relocations are slightly shifted towards the east but are still within 5 km of earlier relocations based on a smaller data set by Jackson et al. (1982) and place the epicenters a few kilometers to the southwest of the locations provided by the USGS.

The Gulf of Corinth is an E-W trending active asymmetric graben structure situated in the back-arc of the Hellenic subduction zone. Single- and multi-channel marine seismic reflection profiles west of the epicentral area exhibit WNW-ESE trending normal faults which run parallel to the coastline and bound the Gulf of Corinth graben (Brooks and Ferentinos, 1984; Myrianthis, 1984). Vertical throws of 1.5 to 3.5 km are estimated (Myrianthis, 1984) and indicate ongoing and repeated extension. A description of the structural evolution of the eastern part of the Gulf of Corinth was presented by Vita-Finzi and King (1985), they used geomorphological and archaeological data in conjunction with radiometric dating of molluscs to decipher the uplift and subsidence history of the shore line. The development of the fault system and its eastward progression are discussed in Jackson et al. (1982) and King et al. (1985).

Surface Faulting

Surface ruptures on pre-existing faults associated with the 1981 earthquake sequence were mapped by several groups and the subsequent summary of observations is taken from Abstracts of the International Symposium on the Hellenic Arc and Trench (1981), Jackson et al. (1982), Papazachos et al. (1985), Ambraseys and Jackson (1990), and Taymaz et al. (1991), and a more detailed description can be found in these sources. The surface faulting attributed to the first two main events had a pure normal faulting character downthrown to the north along the north facing slopes of the Gerania mountains. A 12 km long segment of almost continuous surface rupture trends roughly WSW-ENE and an average vertical displacement of 90 cm was reported. Smaller and more discontinuous displacements were mapped on a 5-7 km long segment offset to the north of the above mentioned ruptures. Fault dips measured on these surface breaks of 45°±15° (Taymaz et al. 1991) are consistent with the slope of the escarpment that forms the northern face of the Gerania mountains. However, for relative important downthrows (0.5-1.5 m) which permit continuous deformation and sliding of unconsolidated sediments along cracks, it may not be simple to derive the fault dip from the opening vectors and uncertainties can be large, as pointed out by Sorel et al. (1981). A fault outcropping on land in the NW part of the Perakora peninsula showed a small displacement of about 10 cm over a 1 km long segment. It is not clear which surface ruptures correspond to which earthquake since both events occurred during the same night, before reconnaissance teams could measure the effects caused by the first shock. A small sea-wave was reported in coastal areas near the town of Skinos immediately after the main shock, which could indicate underwater tectonic dip-slip movement. Jackson et al. (1982) therefore suggested that the first event occurred on a fault which outcrops underwater, and that the second event caused the surface faulting. However, subbottom profiler data showed a submarine sediment slump in the eastern part of the Alkyonides Gulf (Perissoratis et al., 1984). Destruction of fishing nets of trawling boats following the main phase of earthquake activity indicates changes in sea-floor relief where the mass flow was probably triggered by earthquake shaking. Perissoratis et al. (1984) suggested that the main shock of February 24 caused the slumping which was responsible for the observed small tsunami.

The third major shock of March 4 occurred on an antithetic normal fault dipping towards the south. Faults scarps were observed in the vicinity of the town of Kaparelli on the northeast coast of the Gulf of Alkyonides with the southern block being downthrown by 60 cm on average. One segment with E-W trend immediately south of

Kaparelli coincides with a geologically known normal fault and affects bedrock. The maximum observed vertical throw is 1.2 m. A second segment, which is offset by about 3 km to the southwest, extends at least to the coast. The surface breaks are discontinuous with a total length of about 12 km and purely normal.

Aftershocks

Many aftershocks were recorded. Kim et al. (1984) observed a west to east migration of teleseismically recorded aftershocks, which follows the shift in activity of the major events towards the east. A local network of up to 14 seismograph stations was in operation for about 4 weeks starting immediately after the third event. The locations of the 133 best recorded aftershocks are presented in King et al. (1985) (Fig. 6.3.1). The depth distribution of the aftershocks is shown in Figure 6.3.2. The quality of the estimated depths is poor (±4 km) for some events according to King et al. (1985), and the shallowest aftershock which was located with a formal uncertainty of less than ±2 km is 3.6 km deep. Most aftershock were located between the normal faults bounding the Gulf of Corinth graben and did not lie on the main fault planes or in the footwall of the north dipping fault (for cross-sections see Figures 2 and 3 in King et al. (1985)). Only a few aftershocks were recorded near the epicenter of the first event, and they were deeper than the remaining shocks. Some bias in the recorded activity and estimated hypocenter depths due to insufficient station coverage towards west is possible. Most of the aftershocks were clustered in the vicinity of the surface breaks of the third event and were shallower than 13 km.

Previous Work

Source parameters of the Corinth earthquake sequence have been obtained by a number of researchers and the relevant focal parameters in conjunction with my results are summarized for each earthquake separately in Tables 6.3.1, 6.3.4, and 6.3.7.

Papazachos et al. (1984) constructed first motion fault plane solutions from short- and long-period data. Estimates of the seismic moment and the fault dimensions were extracted from far field displacement spectra by Stavrakakis et al. (1991). Centroid moment tensor solutions (CMT) from long-period body and mantle waves are given in Dziewonski and Woodhouse (1983) and Dziewonski et al. (1988). Forward modelling of teleseismic P waves was utilized by Jackson et al. (1982) to verify their first motion focal solutions and to obtain estimates of the centroid depths and the seismic moments.

Kim et al. (1984) did forward modelling of body wave pulses to constrain the first motion focal solutions. Azimuthal differences in waveform widths for the first and second event are interpreted as effects of rupture propagation towards W-NW. Small foreshocks triggering the main events are inferred from slow rise times of the source time functions and the emergent seismogram onsets; the slow rise times and the duration of the source time functions indicate overall slow moment release.

Bezzeghoud et al. (1986) used the mechanisms obtained by Kim et al. (1984) and applied a modified version of Kikiuchi's and Kanamori's (1982) method to deconvolve the source time history of the earthquakes from broadband ($1 \text{ s} \leq T \leq 15$ s) seismograms. A small precursor preceded all three main events. Based on apparent directivity in the waveforms a rupture propagation E to W has been suggested for the 03/04/1981 event.

Taymaz et al. (1991) obtained the source parameters by formal inversion of P and SH wave data using the same routine as I did. Since their data set is also very similar to mine it is no surprize that our estimated source orientations are quite similar.

6.3.2   Corinth 02/24/81

This first and strongest event of the Corinth earthquake sequence (M_S=6.7) was well recorded teleseismically and 27 P- and 16 SH-wave seismograms were used to investigate the source mechanism and rupture history. For this earthquake (and the following ones) digital data from the GDSN network are available. I used a mixture of long-period analog and broad-band digital recordings. This provides a better station coverage and should also increase the stability of the inversion since different sensors and frequencies are used and therefore systematic errors are more likely to cancel. Since only 8 digitally recording stations operated in the proper distance range, I did not attempt to use these higher quality data independently.

The analog data were resampled at a sampling period of 0.3 s after digitizing and high-pass filtered ($T \leq 100$ s). The SH wave data from WES and the P and SH data from WIN were not filtered.

The instrument response was removed from the digital data to form broadband displacement records. Due to long-period instabilities, all broadband records were high-pass filtered at T=100 s. The P-wave seismograms were either derived from the combined long- and short-period data sets or the intermediate period data channel. These data contain high frequencies and the resulting records are broadband from the Nyquist frequency. Intermediate period channels at SCPD and LOND were also used to derive SH broadband records ($0.6 \text{ s} \leq T \leq 100$ s). All other SH wave broadband records and

the P wave record for TATO are solely derived from the long-period data channel and the high frequency cut-off was therefore chosen to be 5 s. The data streams at KAAO were multiplexed incorrectly and the vertical and E-W channel were exchanged.

Focal Mechanism

The point source solution is shown in Figure 6.3.3. The fit to the waveforms is equally good for WWSSN and GDSN data. The causative fault trends E-W (strike: 268°) and dips at 39° towards north, the rake of 284° indicates the presence of a small left-lateral component to the normal faulting. The fault strikes obtained earlier (Jackson et al. (1982); Dziewonski and Woodhouse (1983); Kim et al. (1984); Papazachos et al. (1985); and Dziewonski et al. (1988)) are oriented more towards WNW (strike: 285°-300°). However, the orientation of the fault plane is well constraint by the SH waves and is consistent with the most recent investigation by Taymaz et al. (1991). The first upward swing observed for SH waves at stations to the east (e.g. MAJO, TATO, NIL) and their amplitudes are difficult to explain with a more northerly fault strike. The short period first motion fault plane solution does not constrain the fault planes very well, which is due to the lack of readings from regional and local stations (Fig. 6.3.4a). The estimated seismic moment of 105.2×10^{17}Nm corresponds to a moment magnitude of $M_w=6.6$. The source time function (Fig. 6.3.5) shows a very emergent onset of the moment release during about the first 4 s of the rupture. Most of the energy is released during the next 6 seconds which is followed by a long tail of about 10 s duration. A relatively long rupture duration with a slow rise has been also reported by Bezzeghoud et al. (1986), Kim et al. (1984) and Taymaz et al. (1991). Kim et al. (1984) and Bezzeghoud et al. (1986) argued that the small onset may represent a small foreshock which triggered the main event. While this cannot be excluded with the available data, slow rupture initiation could equally well explain the observed emergent beginning. The centroid depth is well resolved (Figure 6.3.6). A 10% increase in the residual variance places the centroid between 6-12 km depth. Strike, dip, and rake vary within this depth range by 5°, 1°, and 4° respectively, which may be used as an error estimate for the fault orientation. The seismic moment estimates vary between $87-117 \times 10^{17}$Nm in that depth range.

An east to west propagation of the rupture was suggested by Kim et al. (1984) based on the small differences in the seismogram widths at different azimuths. The point source SH synthetic seismograms at stations to the east are slightly too narrow (Figure 6.3.3), which could support their argument. Line source parameterizations were applied, and during the inversions the source orientation, centroid depth and duration were constrained

to the point source estimates. Inversion where the source orientation and centroid depth were freed after a stable source time function was found provided almost identical results. Slow kinematic rupture speeds (v=1.0 km/s) provided slightly better fits than faster ruptures (2.0 km/s) for both east to west and west to east propagation. Ruptures propagating towards west proofed to be slightly better than towards east for all rupture speeds tested (1.0, 1.5, and 2.0 km.s). For a rupture speed of 1.0 km/s it was found that a rupture propagating towards west is significantly better than towards east at the 99% level of confidence (t-test). However the improvement compared to the point source solution is insignificant (Table 6.3.1).

Bilaterally propagating ruptures were investigated next. Again, first, the source orientation was constrained. Differences in rupture speed (1, 1.5, 2 km/s) did not affect the solutions. The point source solution, however, fits equally well. The number of free parameters increases significantly when the source orientations are included in the inversion, the improvements, however, were only very small.

Rupture propagation effects are relatively small for this earthquake and no unique answer to the question if the rupture propagated bilaterally or unilaterally could be found. The propagating line source parameterization, where the length is assumed to be much larger than the width, is not very well suited for this event. Assuming that the centroid is located at the center of the fault (even distribution of the energy over the entire fault), the width is about 27 km, which is of the same order as the rupture length. Different parameterizations may be warranted to deduce the direction of rupture propagation.

Detachment Faulting

The easternmost morphological manifestation of the extending Gulf of Corinth is the antithetic faulting which was also activated during the third main event of the earthquake sequence. King et al. (1985) suggest that antithetic faulting precedes the surface appearance of the main faulting and, in order to explain the aftershock distribution, propose motion on a shallow northward dipping, deep seated aseismic normal fault. Did it move seismically immediately following the main rupture?

Detachment type sources (with either 0° or 10° shallow dipping fault) were added to the centroidal solution at twice the centroidal depth. The parameters can be found in Table 6.3.1. Only the seismic moment of the detachment fault was inverted for and all other parameters were kept fixed. In order to pick up later arrivals in the waveforms, the inversion window length was increased to 50 s. The normalized variance of the residuals of the centroidal solution changes to 0.285. Only a small amount of moment release

(about 10% of the moment released during the main rupture) was acceptable by the data for both experiments. The detachment source with a 0° and 10° dipping fault plane, respectively, produced a normalized variance of 0.266 and 0.272, which is only slightly better than the point source considering the vastly increased number of free parameters. Therefore there is no compelling evidence for seismogenic rupture along a detachment source. The data do not exclude a small moment release, but effects not source related - e.g. crustal structure - may more readily account for the late arriving energy.

Down-Dip Fault Geometry

Following the description in Chapter 3.2, three sources were distributed along the width of the fault at 2.9, 8.6, and 14.3 km depth. Rupture nucleation at the base of the seismogenic layer was assumed. The subsources at 8.6 and 2.9 km were delayed by 2.9 s and 5.8 s, and separated by 7 km and 14 km horizontally south of the first subsource, respectively. The strike of the centroid solution was assigned to each subsource. The moment tensor sum of the three subsources was constrained to the centroidal moment tensor. Fault curvature is modelled by assigning different dips to the individual subsources. This affects the moment tensor sum in a way analogous to the absolute value of a sum of vectors, which depends on the direction of the individual vectors. Therefore the seismic moments of each subsource, which were assumed to be the same for each subsource, and the rake of the shallow and deep subsource were calculated numerically for each fault model resembling a different fault curvature. The dip and rake of the centroid source were assigned to the subsource situated at the centroidal depth (8.6 km).

In the first set of tests only the distribution of the seismic moments of each subsource were allowed to vary. The results are shown in Figure 6.3.7 for four different fault geometries and a summary of the tests is listed in Table 6.3.2. Variations in the quality of the fit are very small and azimuthally dependent. P wave polarities at southern stations (e.g. WIN) are incompatible with very shallow fault dips at the nucleation depth (e.g. model LI6). SH waves to the east and west show large misfits for all curved fault models compared to the planar model (PL), whereas stations to the south are not sensitive. This is caused by the change in the radiation pattern of SH waves as the rupture moves upward along a curved fault, where stations in strike direction are more affected than perpendicular to it. The opposite is true for P waves, especially when the fault dip becomes so shallow or steep that some onsets change their polarity and are then inconsistent with the observed data. The model with a planar fault geometry (all subsources have a fault dip of 39°) results in the smallest residual variance. Only models

with a 10° increase (LO1) or decrease (LI1: dip of deep source is 34° and of shallow source is 44°) in fault dip with depth were not significantly worse than the planar model at the 95% level of confidence (t-test) and all other more curved fault geometries are less likely.

In the next step, I first inverted only for the distribution of the subsource moments. After a stable distribution was found, but before realigning, the seismic moment and later the dip of each subsource were included in the inversion. I used a planar, a 40° concave, and 40° convex starting model (Table 6.3.3) to investigate the effects on the final results caused by the geometry of the starting model. The results were remarkably stable (Table 6.3.3). The results for the shallow subsource are probably unreasonable due to the severe interference of direct and reflected phases. The shallow dip of this source is incompatible with the observed morphological expression of the normal faulting in the Gulf of Corinth. However, the deeper parts of the fault, where the excitation functions are more sensitive and the estimated parameters are probably more reliable, show an almost planar geometry. An apparent very small decrease of fault dip (3°) for the deepest source with respect to the intermediate source is within the resolution uncertainties. It also seems that most of the seismic moment was released in the central part of the fault, and the deeper parts released only a smaller part of the radiated energy.

This tests show no evidence for any significant listric fault curvature in the case of upwards propagating earthquake ruptures.

Depth Extent of Rupture

The aftershock activity of the Corinth earthquake sequence was recorded by a network of up to 14 portable seismograph stations starting on March 5, 1981 until the end of March 1981. The hypocenter-depth distribution for 133 'best' recorded aftershocks taken from King et al. (1985) are shown in Figure 6.3.2. King et al. (1985) note that the hypocenter depths for some of the events may be in error of up to 4 km. Especially shallow events are affected since the reliability of depth estimates depend on the relative distance of the closest station to the hypocenter. The shallowest event located with an uncertainty of ±2 km is at 3.6 km depth. The deep activity is confined to the western edge of the station network (see Figure 2 in King et al. 1985) and the depth estimates are less reliable there. However, the first main shock of February 24 has a relatively deep centroid (8.6 km) and aftershocks at 16-19 km depth could be a real feature of this region. Most of the activity, however, is shallower than 13 km.

Five point sources with source parameters and distribution as described in Chapter 3.2 were used to investigate the depth of coseismic faulting. Figure 6.3.8 shows the seismic moment release vs. depth of the subsources. Sources closest to the centroid depth contain most of the moment release, which agrees with the tentative results of the moment distribution obtained when investigating the fault geometry. Assuming that the small moment release of the shallowest subsource is real opens the question if this relatively deep event actually reached the surface and if so if it caused all of the observed surface faulting. A drop in moment release at around 15 km probably indicates the depth below which only minor moment release occurs.

This depth of about 15 km is slightly deeper than the cut-off of aftershock activity at around 13 km depth. The hypocenter data for the aftershocks were calculated using a half-space crustal velocity of 5.7 km/s (King et al., 1985), which is close to the velocity used in the far field modeling here (6.0 km/s), therefore no bias should be introduced and the difference of the aftershock activity and the depth extent of main shock rupture could be real.

6.3.3 Corinth 02/25/81

The analog and digital data set consists of 24 P- and 16 SH-waves seismograms. A common resampling interval of 0.3 s was applied to all data. Except station WIN, where no filtering was applied, all analog data were high-pass filtered with a cut-off at 100 s. The digital data are broadband from 100 s to a low-pass cut-off period that depends on the data available and their quality. Short- and long-period data were combined to obtain the broadband displacement records for P waves; therefore the low-pass corner frequency is identical with the Nyquist frequency (T=0.6 s). The intermediate period channel was available for station SCPD, the instrument response was removed from this data stream for the P and SH waves, and the resulting records are broadband from T = 0.6 s to 100 s period. All other SH waves and the P wave from station TATO have a high frequency cut-off at T = 5 s, since only data from the long-period channels were available for these phases. The vertical and E-W data streams were incorrectly multiplexed at station KAAO; this has been corrected.

Focal Mechanism

The point source solution is shown in Figure 6.3.9. The fault strike of 246° is rotated with respect to the first event (268°), which is constrained mainly by changes in

amplitude of observed SH waves at MAJO, TATO, and GDH. The estimated fault dip is 44° towards north, and a rake of 276° indicates almost pure normal faulting. Using a 10% increase of variance as an estimate of the parameter uncertainties, shows that the centroid depth of 6.7±3 km is well resolved. Figure 6.3.10 shows a plot of the normalized variance vs. centroid depth. Strike, dip, and rake vary by up to 6°, 2.5°, and 12° within that depth range. The estimated seismic moment (35.2±4.8x10^{17} Nm) corresponds to a moment magnitude of 6.3. Results of previous studies generally agree with my results. However, the strike and rake of the CMT solutions (Dziewonski and Woodhouse, 1983; Dziewonski et al., 1988) are incompatible with my results, and the differences of the estimated strike are similar to the ones for the first event (see Table 6.3.1), which may indicate some station bias in the CMT solutions. The rake estimated from P wave forward modeling and first motion data by Jackson et al. (1982) indicates a significant component of right lateral strike-slip motion; however, only eight P wave seismograms were used and the rake is probably not resolved well. Their moment is smaller than the estimate here by a factor of about two, which also can be attributed to their sparse data set. The source time function with a slow rise and a long tail looks quite similar to the one found for the first event (Fig. 6.3.11). The overall duration is about 15 s, but most of the moment was released during approximately 5 s following the 3 s long emergent onset. Similar results for the source time history were also found by Kim et al. (1984), Bezzeghoud et al. (1986), and Taymaz et al. (1991).

Kim et al. (1984) propose a rupture propagation towards the west based on waveform complexities. I used unilaterally and bilaterally propagating line source parameterizations to investigate rupture propagation; during these inversions the fault orientation and depth were held fixed at the centroidal values. Unilateral ruptures did not improve the fit, ruptures moving towards the west were insignificantly better than ruptures towards the east. Different rupture speeds (1.0, 1.5, and 2.0 km/s) produced almost identical results. Ruptures propagating bilaterally improved the fit very slightly. Again the results were not sensitive to rupture speed. For bilateral rupture models, the westward propagating part was always delayed by 2-3 s; however, a larger moment release was assigned to it. Table 6.3.4 shows a summary of the rupture models. The effects due to rupture propagation are small for this event, which may indicate a bilateral (or circular) rupture propagation. The fault length to width ratio is again small and therefore the line source parameterization is probably not suitable.

Detachment Faulting

A detachment source (dip either 0° or 10 °) was added at twice the centroidal depth to the point source solution, and I inverted for the seismic moment of the detachment source while keeping all other parameters fixed. The inversion window length was increased to 50 s (point source variance becomes 0.345) to include later parts of the waveforms which may be due to seismic slip immediately following the main rupture. A long duration of the source time history was assigned a priori to the detachment source. No continuous moment release could be found, which indicates that only non-source related signals were fitted. The sum of the possible contributions to the seismic moment is, however, quite small and is about 10% of the point source moment estimate. The normalized variance was reduced to 0.337, and 0.334 by adding a 0° and 10° detachment source. The synthetic seismograms did not match the observed waveforms significantly better than the point source solution. A detachment source is therefore not required by the data.

Down-Dip Fault Geometry

Three sources were distributed as described in Chapter 3.2 at 11.1, 6.7, and 2.2 km depth. Upwards propagating rupture was assumed. The subsources at 6.7 and 2.2 km depth were delayed by 2 s and 4 s respectively with respect to the first source and their lateral position is 4.5 and 9 km southeast of the deepest subsource. The remaining parameters were derived and assigned to the subsources as described earlier.

All parameters except the distribution of the seismic moment for each subsource were held fixed during the first set of inversions. A summary of the results for different fault geometries is listed in Table 6.3.5 and Figure 6.3.12 shows the match of some of the waveforms. The differences are very minute and, based mainly on the SH waves, only the model with a 60° decrease of fault dip with depth (LI6) can be clearly rejected. The result of the planar model was compared statistically to the results of other fault geometries. At the 95% level of confidence from the t-test only fault geometries having a 40° increase (LO4) or 60° decrease (LI6) in dip along the width of the fault can be rejected.

In the next set of inversions, first the amount of the seismic moments and later the dips of the subsources were included after a stable distribution of the moments within each subsource was found. Table 6.3.6 shows the results for three starting geometries (planar, 40° concave and convex). Except for the shallow subsource at 2.2 km depth, the results are quite independent of the starting values. The dip of the shallow subsource is

not consistent with the surface expressions associated with the earthquakes of February 24 and 25. The dip values of the two deeper subsources indicate some small amount of shallowing (6-7°). However, the deepest subsource is associated with only a small moment release compared to the source at 6.7 km depth. Extrapolating this shallowing over the whole fault width suggests a 10-20° decrease of dip with depth. However, no unique conclusion can be drawn from these results and the fault could equally likely be planar or even slightly convex upwards. Available short period first motion data do not help to constrain a possible range of solutions (Figure 6.3.4b). The dip of the point source (44°) suggests that the fault remains relatively steeply dipping at greater depths, based on the results of the synthetic modeling indicating that the excitation functions sample the fault parameters at deeper parts of the rupture. However, the seismic moment was evenly distributed along the width of the idealized fault for the numerical modeling examples. This may not be true for this earthquake, and inversions including the seismic moment (Table 6.3.6) indicate that the deepest source contributed only in a minor way to the overall seismic moment (see also Figure 6.3.13). Therefore the point source fault dip may actually be an estimate of the true dip around the centroidal depth and may not contain any information about the dip at depth.

Depth Extent of Rupture

Five point sources were used to infer the depth extent of coseismic faulting as described in Chapter 3.2. The distribution of the sources and their parameters are with respect to a planar fault geometry and are derived from the point source solution. As discussed in the preceding paragraph, this assumption may not be valid, however, the main effect is caused by incorrect dip estimates for the shallowest and deepest subsource, which are probably small as long as the curvature is not very large.

Figure 6.3.13 is a compilation of 10 inversions. Unlike the first event of the Corinth earthquake sequence, the major moment release was not restricted to centroidal depths, but extended to shallower depths. The moment release drops rapidly below a depth of 10 km and no seismic radiation below 12 km depth could be detected. The aftershock depth distribution (Fig. 6.3.2) indicates that the seismogenic rupture did not extend below common aftershock depths.

6.3.4 Corinth 03/04/81

The combined analog and digital data set for this earthquake consists of 24 P- and 14 SH-wave records which were all resampled at a sampling period of 0.3 s. All analog data are high-pass filtered (T≤100 s). Amplitudes of P wave records from the stations BAG and SHA were considerably different compared to neighboring stations, I assumed that the gains were given incorrectly and changed them to 1500 (BAG) and 3000 (SHA). Broadband displacement records were derived from the digital recordings. Short- and long-period data were available for the P wave seismograms and the combined seismograms are broadband from the the Nyquist frequency to 100 s. At TATO no short-period data were available and only the long-period channel was used to generate the broad-band seismogram; since the instrument is not recording high-frequency signals accurately a band-pass filter (5 s ≤ T ≤ 100 s) was applied after the instrument response was deconvolved from the long-period signal. No short-period recordings of the S wave group were available, therefore all SH broadband displacement records are derived in the same way as described for TATO. The intermediate period channel at SCPD recorded the P wave, and was used on its own to generate a broadband signal (0.6 s ≤ T ≤ 100 s). The vertical and E-W channel were incorrectly multiplexed at KAAO.

Focal Mechanism

The point source solution is shown in Figure 6.3.14. The fault plane is uniquely determined by the surface faulting and represents antithetic faulting with respect to the two earlier ruptures. The centroidal solution provides an estimate of fault strike, dip and rake of 50°, 45°, and 264°, respectively. The centroid is located at about 5.6 km depth and therefore is the shallowest of the three main Corinth earthquakes. Figure 6.3.15 shows a plot of the normalized variance vs. centroid depth. The pronounced minimum indicates that the depth is well resolved. Using again a 10% increase of variance as a cut-off requires the centroid to be between 4.5-8 km depth. The estimated dip remains almost constant within that depth range (±0.5°); strike and rake, however, can vary by up to 9°, and 12°, respectively. The seismic moment estimate at the best point source depth is 23.1×10^{17} Nm (M_w=6.2) and varies between 20.8-23.8×10^{17} Nm in the above depth range. The source time function (Fig. 6.3.16) is very similar to the ones obtained for the first two events of this sequence and shows an emergent beginning (about first 2 s) followed by the bulk of the moment release of about 5-6 s duration, and a tail with low moment release (4-5 s duration). The overall duration of 12 s with an emergent onset is

comparable with results obtained by Bezzeghoud et al. (1986), Kim et al. (1984) and Taymaz et al. (1991).

The sampling of the SH waves on the focal sphere is somewhat uneven for my data set with only two stations in North America (WES and SCPD), both of which are relatively noisy. However, the nodal character of the SH waves at MAJO, TATO, and GDH allows only minor rotation of the fault orientation and constrains the focal mechanism. The fault orientation of Taymaz et al. (1991) obtained from body wave inversion is almost identical to my result.

The two continuous surface breaks observed in the field trend roughly east-west, and only the area of diffuse and small (10 cm, Jackson et al. (1982)) surface ruptures connecting the two segments shows the trend obtained from the waveform modeling in this study. Jackson et al. (1982) utilize more (regional and/or long period) first motion data which constrain the auxiliary plane, but not the fault plane. Their P wave forward modeling apparently is based on the first motion data to constrain the auxiliary plane and on the trend of the surface faulting to constrain the fault plane. This explains the E-W strike and the relatively significant left-lateral strike-slip component (rake: 290°) of their mechanism which is not in agreement with their own surface observations. Studying their solution also shows that the amplitude ratio of the first to second downswing of the synthetic P waves is opposite to the observed WWSSN pulses: e.g. stations to the east (SHK, BAG, NDI, KOD) have a larger second than first downswing contrary to their synthetics.

The depth estimate (29 km) of the CMT solution by Dziewonski and Woodhouse (1983) is probably biased by the very long period waves included in their inversion; their source orientation, however, is compatible with results presented here. The first motion solution of Papazachos et al. (1984) has only the auxiliary plane well constrained, which can explain the discrepancies in estimated strike.

The estimated seismic moment by Jackson et al. (1982) is too small by a factor of two which is probably caused by the forward modeling procedure and the relatively small numbers of stations used. Stavrakakis et al. (1991) do not correct for surface reflected phases when they derive the moment estimates from the amplitude spectra, which may lead to a bias especially for very shallow sources.

Bezzeghoud et al. (1986) see some directivity in the waveforms and suggest an E to W propagation of the rupture. Line source parameterizations, which are probably not suited for an earthquake with a rupture length of 12-15 km and a rupture width of about the same size, did not improve the fit for either unilaterally nor bilaterally propagating ruptures. It can only be speculated that the rupture may have nucleated in the zone of

diffuse surface ruptures which may have acted as a geometrical barrier and then propagated bilaterally towards NE and SW along two fault segments with slightly different orientations. Near field data could probably shed more light on this issue.

Detachment Faulting

A shallow dipping source (0° or 10°) at twice the centroid depth was added to the point source solution, and inversions looking only for the seismic moment of this second source were performed. The inversion window length was enlarged to 50 s to include later parts of the waveforms. No continuous moment release was observed for either of the detachment sources, which makes it very unlikely that such a rupture occurred. The variance decreases only insignificantly when the detachment sources are added to the point source. Therefore no evidence for seismogenic slip along a detachment surface immediately following the main rupture is present in the data.

Down-Dip Fault Geometry

Three subsources were placed at 9.3, 5.6, and 1.9 km depth. Upwards propagating rupture was assumed and the second and third subsource are delayed by 1.6 and 3.2 s with respect to the initial source at 11.1 km depth. The lateral spacing between the sources is 3.7 km at an azimuth of 320°, the deepest source is located towards the southeast. The other parameters were derived and assigned to the subsources as described earlier.

Following the usual procedure, in the first set of inversions the three subsources were assigned different dips to resemble faults with a varying degree of curvature. The geometry and the amount of seismic moment of each subsource was held fixed during this inversions. Figure 6.3.17 shows the fit at azimuthally selected stations for several of the fault geometries tested. A complete list of the results can be found in Table VI.3.8. Similarly to the 02/25/1981 event, the differences are rather small for different fault geometries. Only stations at certain azimuths are affected noticeably. P waves hardly show any differences for the fault geometries, the fit becomes not acceptable only for a fault curvature of 60° (LI6 model in Figure 6.3.18) based on African stations which are located roughly perpendicular to the fault strike and therefore are most sensitive to variations in fault dip. For SH waves this is expected for stations along the fault strike. This can be seen in Figure 6.3.18, where the fits become significantly worse for curved

fault geometries at stations TATO and CHTO. Using the t-test it was found that a 20° increase or 30° decrease of fault dip can not be excluded at a 95% level of confidence.

Different starting geometries (planar, 40° concave and convex) were used in a second set of tests, where the seismic moments and later the dips of the subsources were included in the inversion after a stable distribution of the seismic moment within each subsource was found. The models and the respective results are shown in Table 6.3.9. The results for this earthquake apparently depend on the starting model, at least when using model LO4 as original geometry, therefore any conclusions based solely on this test are less reliable. Again the results for the shallowest source will be disregarded due to the mentioned insensitivity of the excitation functions to determine fault dips for very shallow sources. The dip of the intermediate depth source is very stable and basically coincides with the centroid estimate (45°). The estimated dip of the subsource at 11.1 km depth is for all three starting geometries steeper than the source located at the centroid depth. However, the differences may be small (5°), if it is assumed that only the results obtained from model LO4 are biased and not the others.

Probably the only relatively safe conclusion is that there is no significant decrease in fault dip. From the above tests and the estimated centroidal fault dip there is no evidence for required fault curvature.

Depth Extent of Rupture

Five equally-spaced sources resembling a planar fault geometry were distributed. The parameterization chosen follows the description in Chapter 3.2. Only the seismic moments of each source was inverted for, and the source spacings were varied (but kept equidistant) to obtain information about the depth extent of the rupture. Figure 6.3.18 is a compilation of 8 inversions. Most of the moment seems to have been released at shallow depths. This may represent instabilities due to the shallowness of the source. Or, in the light of the observed surface ruptures (60 cm on average), could account for the relatively large breaks. For a fault length of 12 km, a rigidity of 3.4×10^{10} N/m^2, and fault dip of 45° at shallow depths, the surface displacement will be in the order of 45-70 cm if the seismic moment of about 12-14×10^{17} Nm associated with the shallowest source is evenly distributed over the uppermost 3.5-4.5 km depth.

For deeper parts the radiated seismic energy decreases steadily, reaches a low level at about 10 km depth, and continues down to a depth of 15-16 km. Below 18 km depth no moment release has been observed. The aftershocks in the eastern part of the Gulf of

Corinth and associated with this earthquake are mostly shallower than 12 km. It appears that the March 4th shock did rupture significantly deeper than that.

6.3.5 Summary

The centroidal parameters of the three major events ($M_S > 6$) of the Corinth earthquake sequence were determined by body wave inversion. The source orientations are well constrained by SH waves near nodes and indicate ongoing north-south extension of the Gulf of Corinth. The main events are aligned E-W with activity stepping towards east (Jackson et al., 1982; Taymaz et al., 1991). Estimated strikes of the second and third event are rotated counterclockwise with respect to the first by 20° and 30°. The causative faults therefore trend in a more NE-SW direction compared to the E-W trend of the first event. The changes in source orientation are well constrained by SH waves (e.g. MAJO, TATO). Fault trends at the southern boundary of the graben show an E-W to NNE-WSW direction and are consistent with the strikes of the first and second event. The two segments of surface rupture along the northern boundary of the graben associated with the third event trend roughly NNE-SSW and do not quite agree with the average source mechanism. The antithetic faulting of this event may be influenced or controlled by the main north dipping fault, and this could cause the discrepancy between surface faulting and faulting at depth.

The source time functions of all three events are remarkably similar. The emergent character of the energy radiation makes it more difficult to read the short period arrivals correctly. The two smaller events appear to have a slightly shorter emergent onset, which may be an artifact due to undetected very small earlier arrivals. In Figure 6.3.19 a better 'cross-correlation' of the rupture histories of the three events was sought, this resulted in a 1.5 s delay for the second and third source compared to their source time functions found by waveform inversion. The emergent beginning (1.5-4 s) is followed by a sharp rise in moment release which lasts for about 4-6 s and a long (4-9 s) tail of low moment release. Bezzeghoud et al. (1986) and Taymaz et al. (1991) also find the similarity. Kim et al. (1984) also note the emergent onset of the source time functions and their long durations. Kim et al.(1984) and Bezzeghoud et al. (1986) interpret the the slow start as being due to small foreshock activity triggering the main events. Or in a sense, minor activity leads a critically strained asperity to fail.

King et al. (1984) suggested the existence of a shallow dipping non-seismogenic fault at depth to account for the surface morphology at the eastern end of the Gulf of Corinth, which is dominated by the presence of southward dipping antithetic faults. No

evidence for activity during any of the main shocks along this buried surface could be found from waveform modeling.

The down-dip geometry of the faults was investigated by distributing three point sources along the width of the fault. Models with fixed fault geometries, but optimally distributed seismic moments within each of the subsources showed that a planar fault geometry provides a slightly better fit than curved models for all three events. Comparing the results statistically, however, reveals that the geometries of the 02/25/1981 and the 03/04/1981 shocks are not well constrained and a relatively large fault curvature of up to 60° and 40° respectively is possible. The waveforms of the 02/34/1981 event do not permit a fault curvature of 20° or more. Tests where the dips of subsources were allowed to vary during the inversions indicate only minor variations of fault dip for the two deeper sources, and there is no indication of flattening of the faults into subhorizontal detachment surfaces. The shallow subsource did not provide reliable results, which is probably caused by the interference of direct and reflected phases.

Five point sources were distributed equidistant to determine the depth extent of faulting. Aftershock activity extends to about 13 km depth (Figure 6.3.2). For the 02/25/1981 event the moment release drops to zero at about 12 km depth. Moment release to a depth of about 15-16 km has been observed for the 02/24/1981 and the 03/04/1981 events, which is slightly deeper than most of the aftershocks. This could indicate that the rupture for these events actually extended into the semi-brittle field. This supports the mechanism proposed by Scholz (1988) where velocity-strengthening behaviour prevents the generation of small aftershocks in the zone of stable friction and only large shocks can dynamically penetrate into it.

Table 6.3.1   Source Parameters of the 02/24/1981 Corinth Earthquake.

	strike deg	dip deg	rake deg	moment 10^{17}Nm	depth km	duration s	Δt s	Δr km	Δaz deg	σ
P S	269	39	284	105.2	8.6	18				0.22
W	269*	39*	284*	104.6	8.6*	18*				0.22
E	269*	39*	284*	104.5	8.6*	18*				0.22
B I										0.22
east	269*	39*	284*	60.0	8.6*	14				
west	269*	39*	284*	47.4	8.6*	12				
DE	269*	0*	270*	11.9	17.1*	35	4	10.6*	358*	•
	269*	10*	270*	9.5	17.1*	35	4	10.6*	358*	•
P, B	287	40	280	101	6	8-15				
S				150						
D&W	283	44	288	129	10	10[1)]				
D	285	37	294	90	10	6[1)]				
J	300	42	286	72.8	10	8				
K	285	40	290	81	12	10				
T	264	42	289	87.5	12	12				

PS - point source solution. W, E - unilateral rupture towards west and east, respectively, rupture velocity $v_r = 1.0$ km/s. BI - bilateral rupture, $v_r = 1.0$ km/s. DE - detachment source with 0° and 10° dipping surface, respectively, locations derived relative to point source solution PS. P - Papazachos et al. (1985), first motion solution. B - Bezzeghoud et al. (1986), moment and duration. S - Stavrakakis et al. (1991). D&W - Dziewonski and Woodhouse (1983). D - Dziewonski et al. (1988). J - Jackson et al. (1982). K - Kim et al. (1984). T - Taymaz et al. (1991). Δt, Δr, Δaz - time delay, distance and azimuth of subevent with respect to first subevent. σ - normalized variance of residuals. "*" - fixed. • - see text. [1)] - half duration.

Table 6.3.2   Corinth, 02/24, Down-Dip Geometry: 1. Dip and Seismic Moment Fixed. Results are Compared Statistically.

	curvature deg	σ	t	μ 10^{-2}	s 10^{-2}	Mo 10^{17}Nm	rake deg
LO4	+40	0.326	**3.70**	8.34	14.74	41.6*	282*
LO2	+20	0.259	**2.28**	2.04	5.87	36.5*	284*
LO1	+10	0.249	**1.54** ●	0.96	4.09	35.4*	284*
PL	0	0.239	●			35.0*	284*
LI1	-10	0.249	**1.51** ●	0.99	4.30	35.4*	284*
LI2	-20	0.257	**1.70**	1.72	6.63	36.5*	284*
LI3	-30	0.271	**2.24**	3.00	8.78	38.4*	283*
LI4	-40	0.294	**2.87**	5.10	11.65	41.6*	282*
LI6	-60	0.383	**3.26**	13.27	26.69	55.4*	278*

LO - fault steepens with depth. PL - planar fault model. LI - fault flattens with depth. Rupture propagates upward from base of seismogenic layer. Curvature - increase (+) or decrease (-) of fault dip with depth in degree. σ - normalized variance of residuals. t - value obtained from t-test comparing listric models with planar model PL. μ,s - mean and standard deviation of differences of squared station residuals, for explanation see Chapter 3. Number of samples N=43. Value t has to exceed to be within certain confidence level: 60% - 0.26. 75% - 0.68. 90% - 1.30. 95% - 1.68. 97.5% - 2.02. 99% - 2.42. 99.5% - 2.70. 99.95 - 3.55. ● - acceptable fits (95% confidence level). Mo - moment assigned to each individual subsource. rake - rake assigned to shallow and deep subsource, while subsource at centroid depth was assigned point source value (284°). * - fixed. All models have same moment tensor as point source.

Table 6.3.3 Corinth, 02/24, Down-Dip Geometry: 2. Dip and Seismic Moment Free

	depth km	strike deg	rake deg	Start dip deg	Start moment 10^{17}Nm	Result dip deg	Result moment 10^{17}Nm
PL	14.3*	268*	284*	39	35	**35**	10
	8.6*	268*	284*	39	35	**38**	73
	2.9*	268*	284*	39	35	**13**	48
LI4	14.3*	268*	282*	19	42	**35**	10
	8.6*	268*	284*	39	42	**38**	73
	2.9*	268*	282*	59	42	**13**	48
LO4	14.3*	268*	282*	59	42	**35**	10
	8.6*	268*	284*	39	42	**38**	73
	2.9*	268*	282*	19	42	**13**	48

PL - planar start model. LI4, LO4 - listric start models. "*" - fixed. inverted for seismic moment and dip of each subsource, rupture propagating up-dip.

Table 6.3.4 Source Parameters of the 02/25/1981 Corinth Earthquake

	strike deg	dip deg	rake deg	moment 10^{17}Nm	depth km	duration s	Δt s	Δr km	Δaz deg	σ
P S	246	44	276	35.2	6.7	15				0.21
W	246*	44*	276*	34-35	6.7*	15*				0.21
E	246*	44*	276*	35	6.7*	15*				0.21
B I										0.20
east	246*	44*	276*	12-15	6.7*	15				
west	246*	44*	276*	21-23	6.7*	11	2-3			
DE	246*	0*	270*	3.1	13.4*	29	5	6.8*	336*	•
	246*	10*	270*	3.9	13.4*	30	5	6.8*	336*	•
P, B	243	41	260	35	5	15-17				
S				48						
D&W	261	40	286	43	18.4	5[1)]				
D	264	34	309	38	10	6[1)]				
J	248	42	245	16.8	8	4				
K	250	42	280	27	7	7				
T	241	44	275	39.7	8	12				

PS - point source solution. W, E - unilateral rupture towards west and east, respectively, rupture velocities $v_r = 1.0$-2.0 km/s. BI - bilateral rupture, $v_r = 1.0$-2.0 km/s. DE - detachment source with $0°$ and $10°$ dipping surface, respectively, locations derived relative to point source solution PS. P - Papazachos et al. (1985), first motion solution. B - Bezzeghoud et al. (1986), moment and duration. S - Stavrakakis et al. (1991). D&W - Dziewonski and Woodhouse (1983). D - Dziewonski et al. (1988). J - Jackson et al. (1982). K - Kim et al. (1984). T - Taymaz et al. (1991). Δt, Δr, Δaz - time delay, distance and azimuth of subevent with respect to first subevent. σ - normalized variance of residuals. "*" - fixed. ° - see text. [1)] - half duration.

Table 6.3.5 Corinth, 02/25, Down-Dip Geometry: 1. Dip and Seismic Moment Fixed. Results are Compared Statistically

	curvature deg	σ	t	μ 10⁻³	s 10⁻²	Mo 10¹⁷Nm	rake deg
LO4	+40	0.258	**2.60**	3.66	0.89	13.9*	275*
LO2	+20	0.226	**0.42** ●	0.26	0.40	12.2*	276*
PL	0	0.220	●			11.7*	276*
LI2	-20	0.218	**0.05** ●	0.04	0.46	12.2*	276*
LI4	-40	0.222	**0.54** ●	0.70	0.82	13.9*	275*
LI5	-50	0.235	**1.04** ●	2.38	1.45	15.4*	274*
LI6	-60	0.342	**2.22**	15.28	4.35	17.5*	274*

LO - fault steepens with depth. PL - planar fault model. LI - fault flattens with depth. Rupture propagates upward from base of seismogenic layer. Curvature - increase (+) or decrease (-) of fault dip with depth in degree. σ - normalized variance of residuals. t - value obtained from t-test comparing listric models with planar model PL. μ,s - mean and standard deviation of differences of squared station residuals, for explanation see Chapter 3. Number of samples N=40. Value t has to exceed to be within certain confidence level: 60% - 0.26. 75% - 0.68. 90% - 1.30. 95% - 1.68. 97.5% - 2.02. 99% - 2.42. 99.5% - 2.70. 99.95 - 3.55. ● - acceptable fits (95% confidence level). Mo - moment assigned to each individual subsource. rake - rake assigned to shallow and deep subsource, while subsource at centroid depth was assigned point source value (276°). * - fixed. All models have same moment tensor as point source.

Table 6.3.6 Corinth, 02/25, Down-Dip Geometry: 2. Dip and Seismic Moment Free

	depth km	strike deg	rake deg	Start dip deg	Start moment 10^{17}Nm	Result dip deg	Result moment 10^{17}Nm
PL	11.1*	246*	276*	44	12	**36**	4
	6.7*	246*	276*	44	12	**43**	25
	2.2*	246*	276*	44	12	**21**	12
LI4	11.1*	246*	275*	24	14	**37**	4
	6.7*	246*	276*	44	14	**43**	22
	2.2*	246*	275*	64	14	**29**	12
LO4	11.1*	246*	275*	64	14	**36**	4
	6.7*	246*	276*	44	14	**43**	23
	2.2*	246*	275*	24	14	**20**	13

PL - planar start model. LI4, LO4 - listric start models. "*" - fixed. inverted for seismic moment and dip of each subsource, rupture propagating up-dip.

Table 6.3.7   Source Parameters of the 03/04/1981 Corinth Earthquake

	strike deg	dip deg	rake deg	moment 10^{17}Nm	depth km	duration s	Δt s	Δr km	Δaz deg	σ
PS	50	45	264	23.1	5.6	12				0.16
SW	50*	45*	264*	23	5.6*	12*				0.16
NE	50*	45*	264*	23	5.6*	12*				0.17
BI										0.16
northwest	50*	45*	264*	12	5.6*	12*				
southeast	50*	45*	264*	12	5.6*	12*				
DE	50*	0*	270*	2.3	11.1*	30	4	5.6*	140*	•
	50*	10*	270*	3.5	11.1*	30	4	5.6*	140*	•
P, B	62	47	260	19	8	8-10				
S				48						
D&W	58	49	265	34.8	29	7[1]				
D	39	55	246	28	10	4[1]				
J	90	52	290	9.7	8	4				
K	67	47	275	22	7	7				
T	50	45	270	27.0	4	12				

PS - point source solution. SW, NE - unilateral rupture towards southwest and northeast respectively, rupture velocity $v_r = 1.0$ km/s. BI - bilateral rupture, $v_r = 1.0$ km/s. DE - detachment source with 0° and 10° dipping surface, respectively, locations derived relative to point source solution PS. P - Papazachos et al. (1985), first motion solution. B - Bezzeghoud et al. (1986), moment and duration. S - Stavrakakis et al. (1991). D&W - Dziewonski and Woodhouse (1983). D - Dziewonski et al. (1988). J - Jackson et al. (1982). K - Kim et al. (1984). T - Taymaz et al. (1991). Δt, Δr, Δaz - time delay, distance and azimuth of subevent with respect to first subevent. σ - normalized variance of residuals. "*" - fixed. • - see text. [1] - half duration.

Table 6.3.8 Corinth, 03/04, Down-Dip Geometry: 1. Dip and Seismic Moment Fixed. Results are Compared Statistically.

	curvature deg	σ	t	μ 10^{-3}	s 10^{-2}	Mo 10^{17}Nm	rake deg
LO4	+40	0.186	2.27	1.52	0.89	9.1*	265*
LO2	+20	0.164	0.79 •	0.23	0.18	8.0*	264*
PL	0	0.161	•			7.7*	264*
LI2	-20	0.166	0.63 •	0.22	0.21	8.0*	264*
LI3	-30	0.179	1.66 •	0.90	0.33	8.5*	265*
LI4	-40	0.199	2.06	1.90	0.57	9.1*	265*
LI5	-50	0.231	2.11	3.40	0.99	10.1*	266*
LI6	-60	0.349	2.76	9.21	2.06	11.6*	267*

LO - fault steepens with depth. PL - planar fault model. LI - fault flattens with depth. Rupture propagates upward from the base of the seismogenic layer. Curvature - increase (+) or decrease (-) of fault dip with depth in degree. σ - normalized variance of residuals. t - value obtained from t-test comparing listric models with planar model PL. μ,s - mean and standard deviation of differences of squared station residuals, for explanation see Chapter 3. Number of samples N=38. Value t has to exceed to be within certain confidence level: 60% - 0.26. 75% - 0.68. 90% - 1.30. 95% - 1.68. 97.5% - 2.02. 99% - 2.42. 99.5% - 2.70. 99.95 - 3.55. • - acceptable fits (95% confidence level). Mo - moment assigned to each individual subsource. rake - rake assigned to shallow and deep subsource, while subsource at centroid depth was assigned point source value (264°). * - fixed. All models have same moment tensor as point source.

Table 6.3.9   Corinth, 03/04, Down-Dip Geometry: 2. Dip and Seismic Moment Free

	depth km	strike deg	rake deg	Start		Result	
				dip deg	moment 10^{17}Nm	dip deg	moment 10^{17}Nm
PL	9.3*	50*	264*	45	8	49	4
	5.6*	50*	264*	45	8	44	15
	1.9*	50*	264*	45	8	65	7
LI4	9.3*	50*	265*	25	9	49	3
	5.6*	50*	264*	45	9	44	15
	1.9*	50*	265*	65	9	65	7
LO4	9.3*	50*	265*	65	9	61	4
	5.6*	50*	264*	45	9	44	18
	1.9*	50*	265*	25	9	10	5

PL - planar start model. LI4, LO4 - listric start models. "*" - fixed. inverted for seismic moment and dip of each subsource, rupture propagating up-dip.
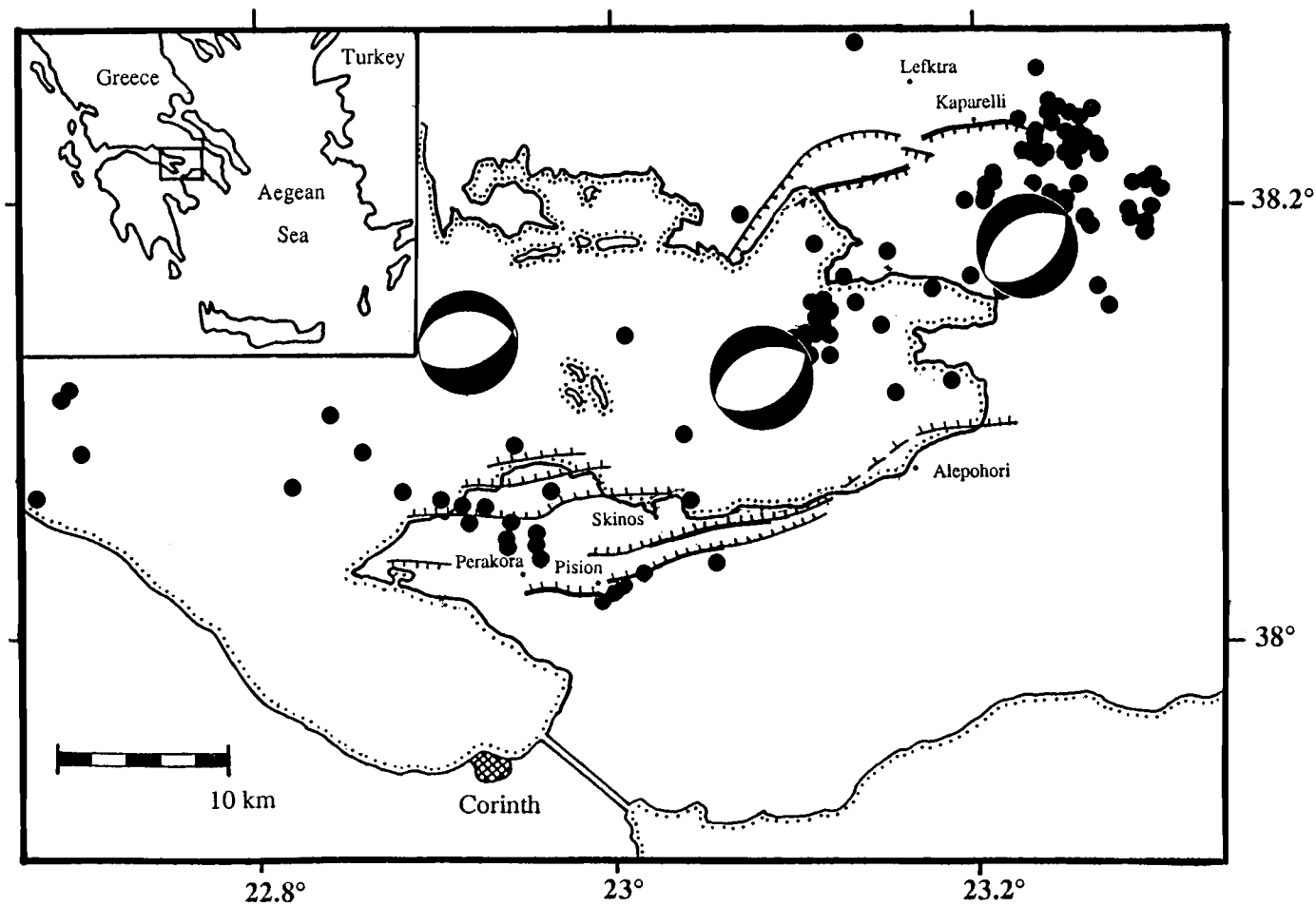
Figure 6.3.1 Map of the Corinth area, modified from King et al. (1985). Aftershock locations from King et al. (1985). Heavy solid lines with ticks on downthrown side mark surface faulting associated with the Corinth earthquake sequence. Focal mechanisms from this study centered on relocated epicenters (Taymaz et al., 1991).
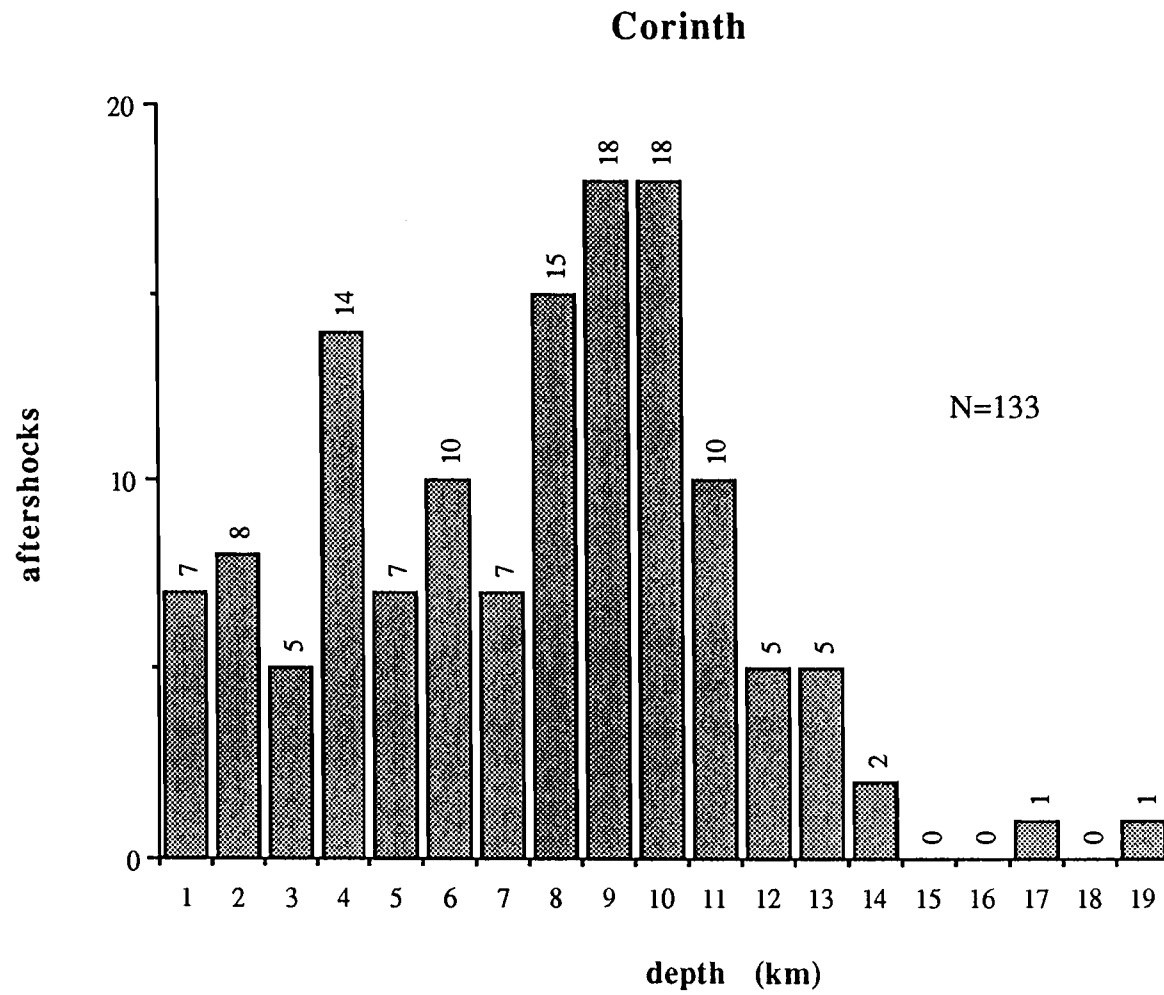
Corinth

Figure 6.3.2   Aftershock depth distribution. Data are from King et al. (1985). Only a few aftershocks occurred below 13 km depth. N: total number of aftershocks included in histogram.
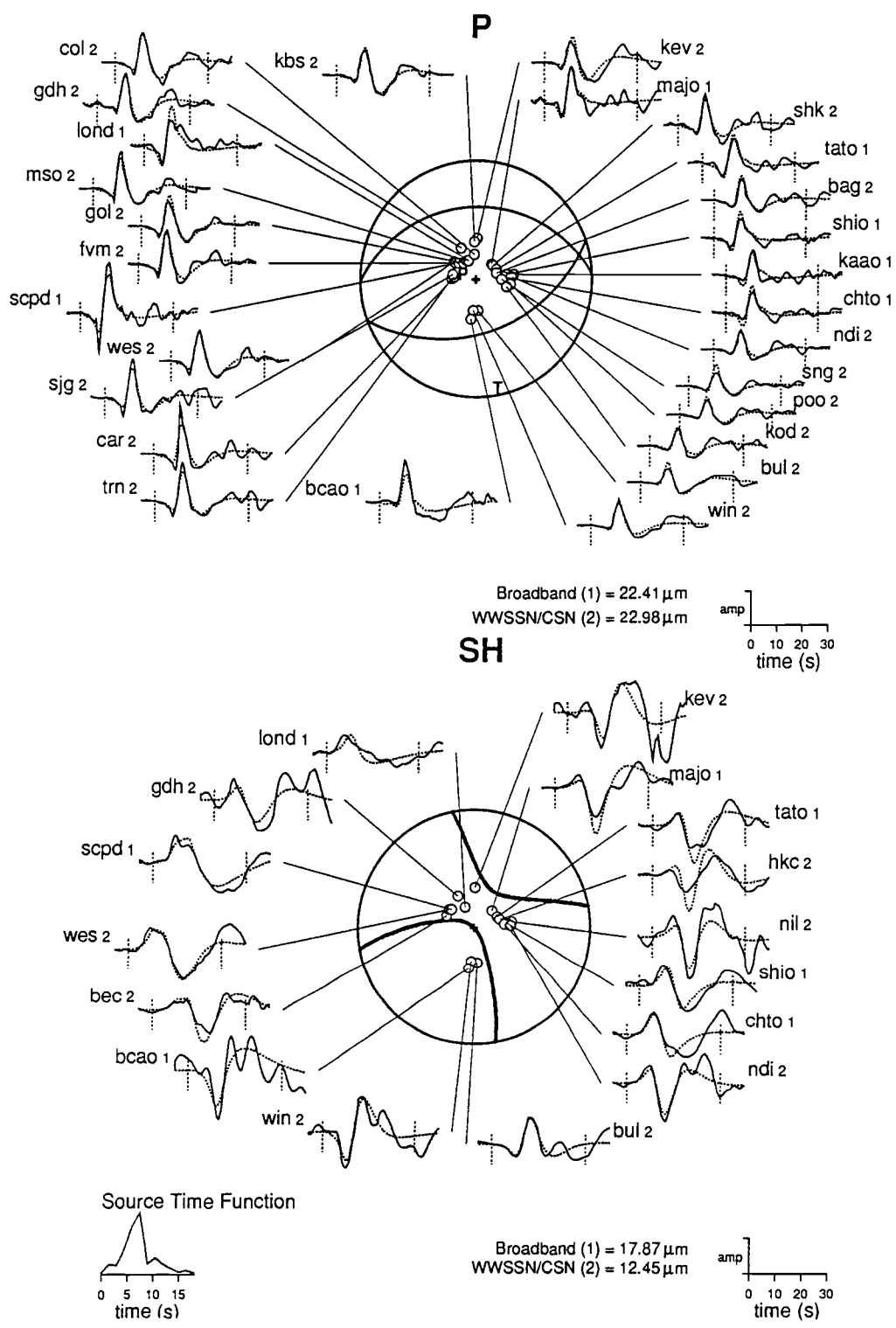
Corinth 02/24/1981

P

Broadband (1) = 22.41 μm
WWSSN/CSN (2) = 22.98 μm

SH

Source Time Function

Broadband (1) = 17.87 μm
WWSSN/CSN (2) = 12.45 μm

Figure 6.3.3   Point source solution for the 02/24/1981 Corinth earthquake.   Digital broadband and analog long-period data are included.

02/24/1981

02/25/1981

03/04/1981
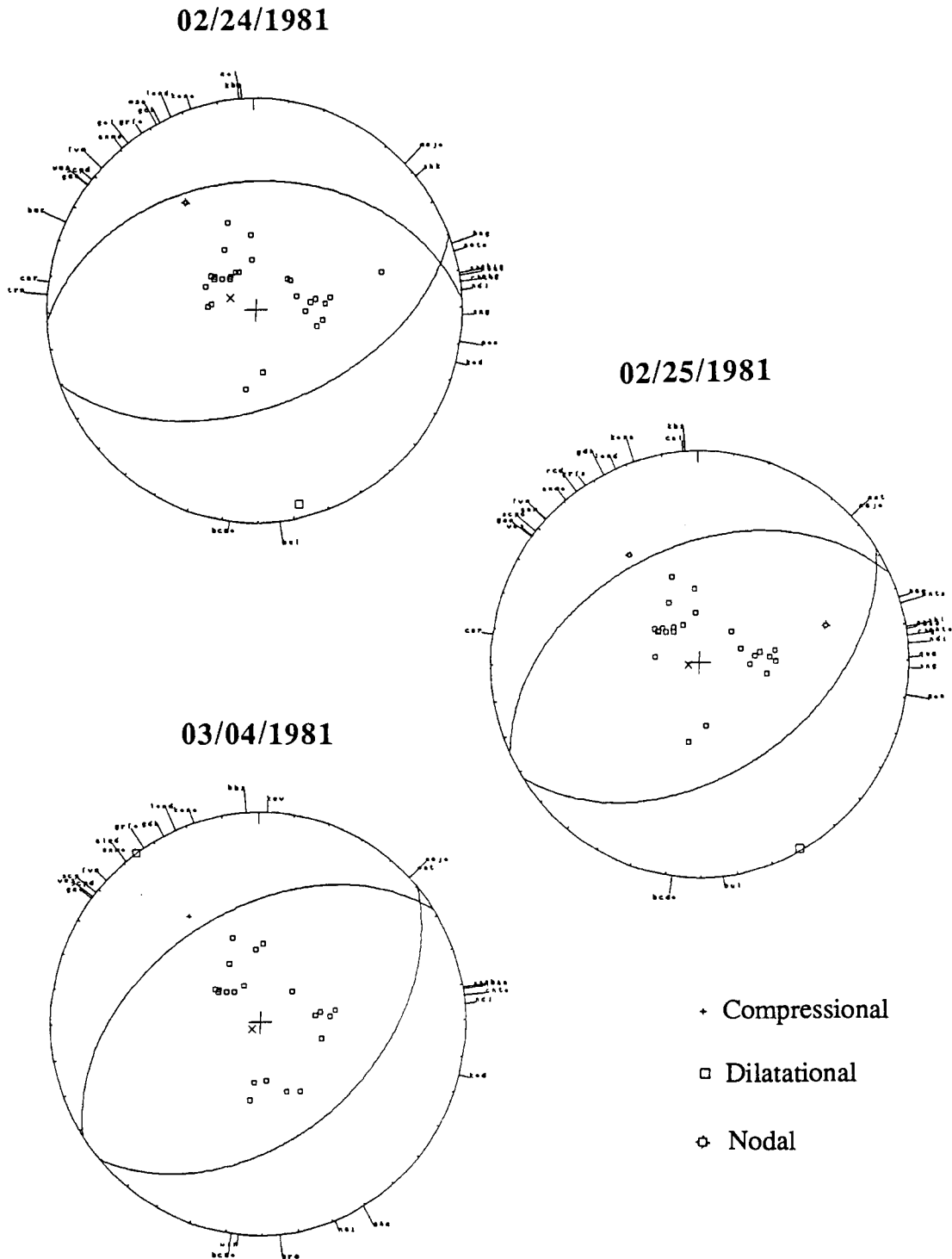
+ Compressional

□ Dilatational

✧ Nodal

Figure 6.3.4 Short period first motion polarities. a) 02/24/1981, b) 02/25/1981, and c) 03/04/1981. Fault plane solutions from waveform inversion (solid line) (Table 6.3.1, 6.3.4, and 6.3.7) are not tightly constrained by first motion data due to the lack of stations at regional distances.
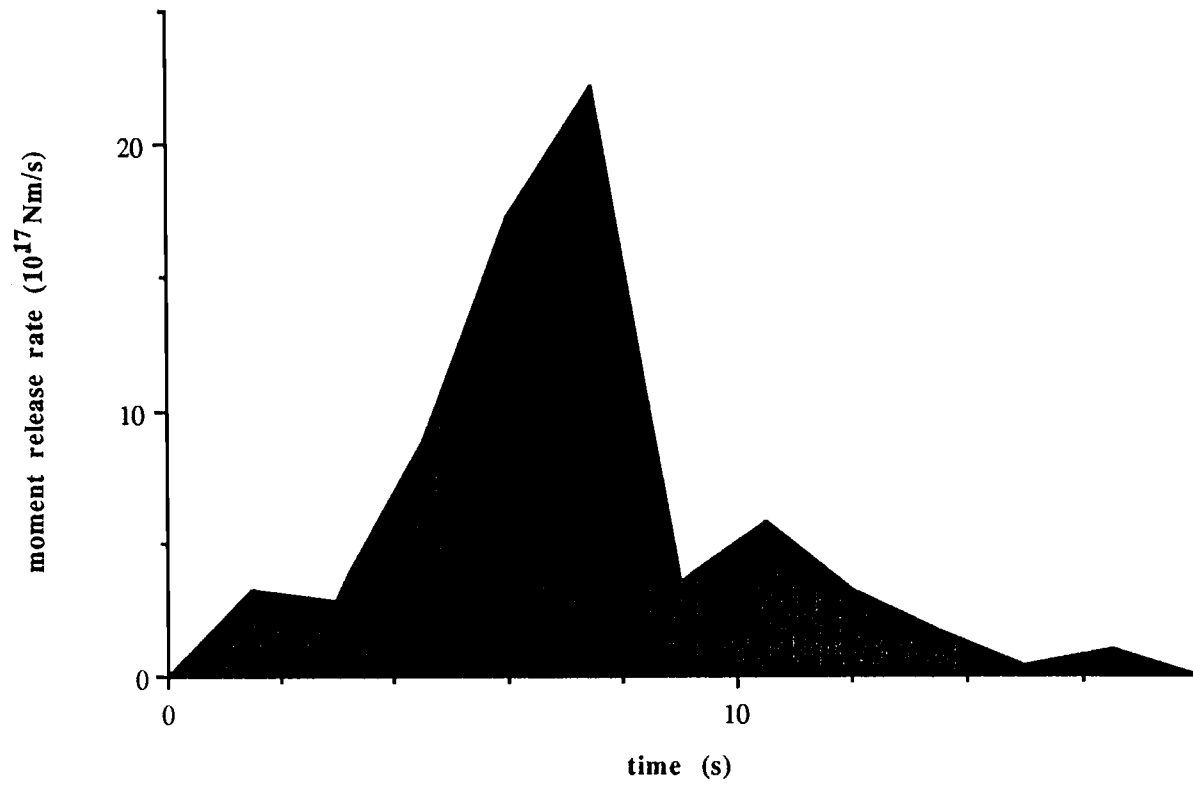
Corinth 02/24/1981 - moment release rate

Figure 6.3.5 Seismic moment release rate. Note the emergent onset and the long tail.
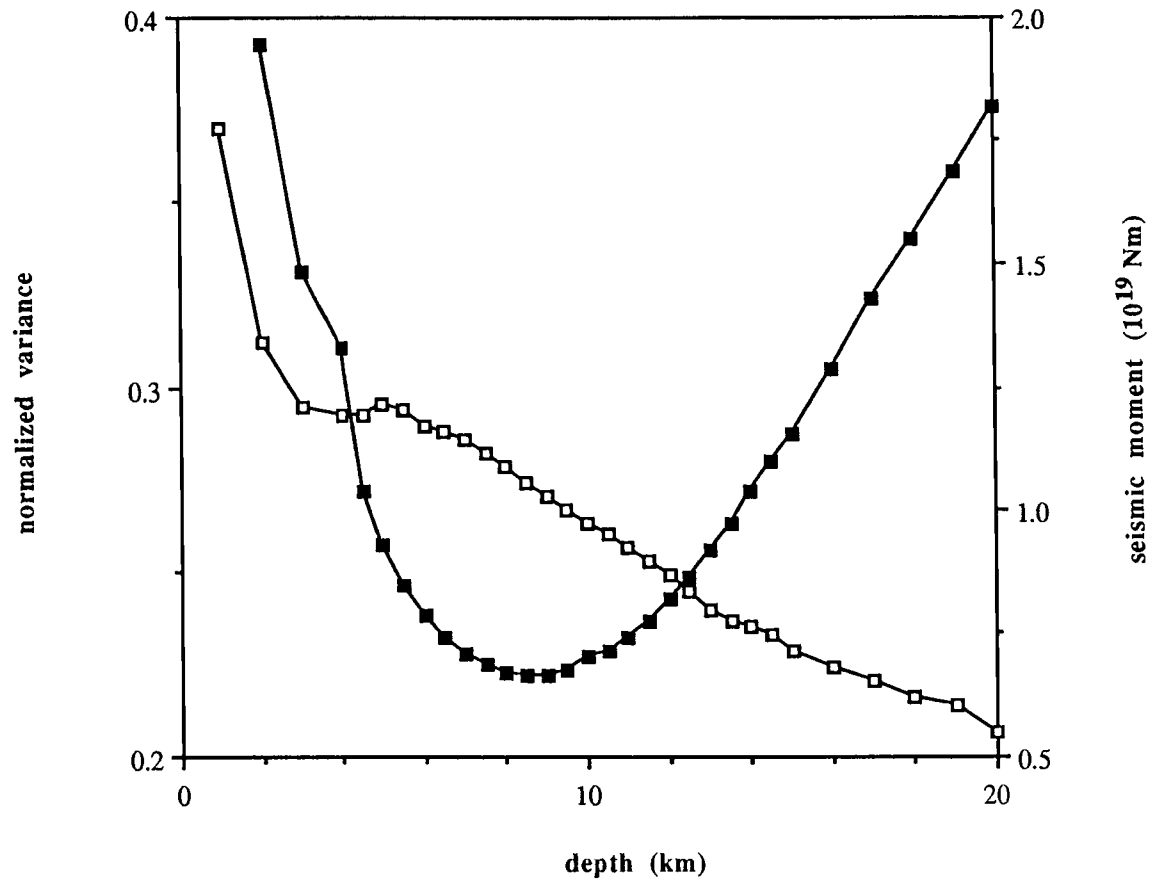
Corinth 02/24/1981

Figure 6.3.6 Residual variance (filled squares) and seismic moment (open squares) as a function of centroid depth.

MAJO, P 47°   WIN, P 186°   KBS, P 357°   TATO, SH 65°   WIN, SH 186°   BEC, SH 295°   WES, SH 307°

LO4

PL

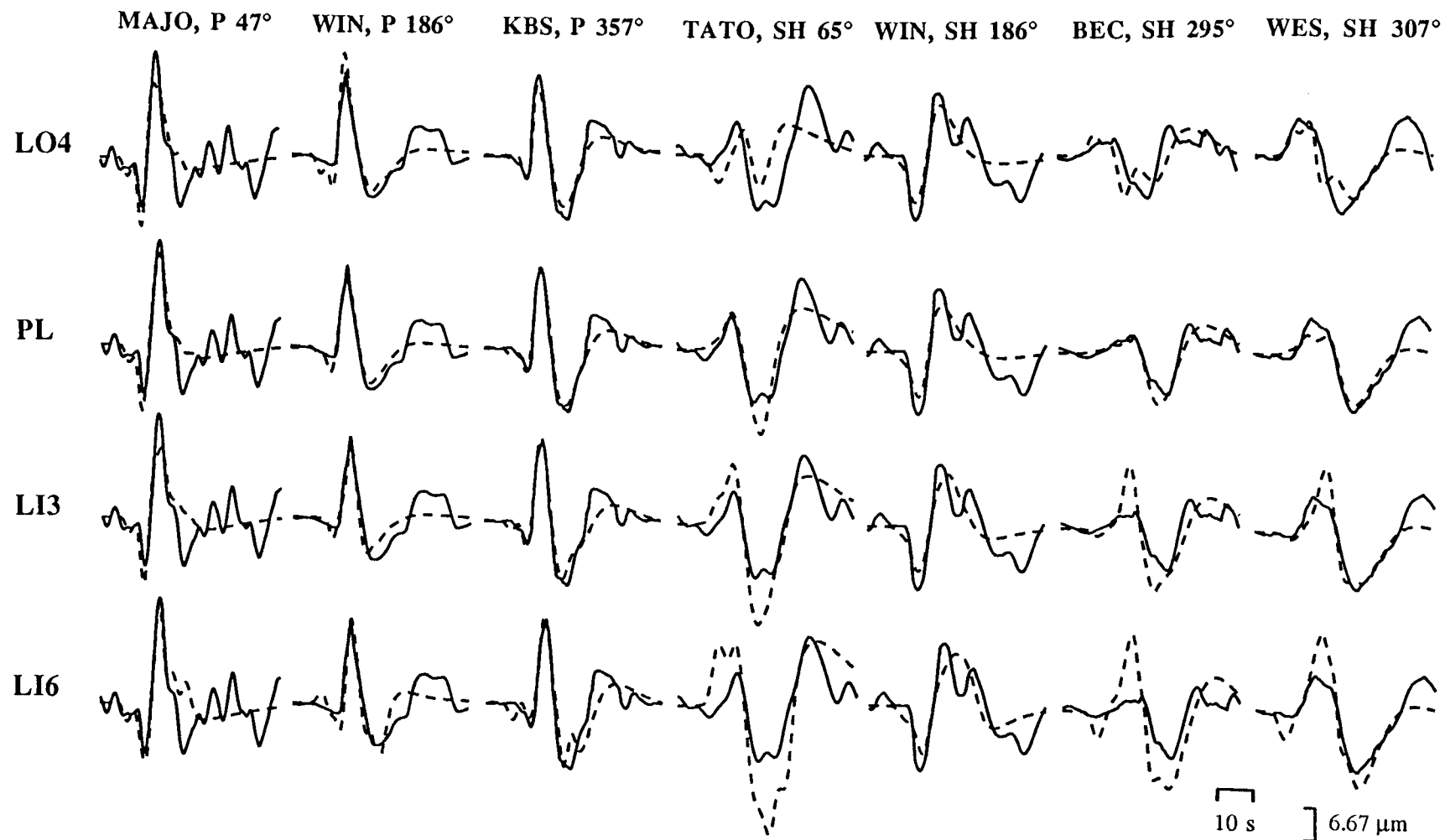LI3

LI6

10 s   ] 6.67 μm

Figure 6.3.7   Comparison of P and SH waveforms for four fault models listed in Table 6.3.2 for the 02/24/1981 Corinth earthquake. Number next to the station is the azimuth from the source.
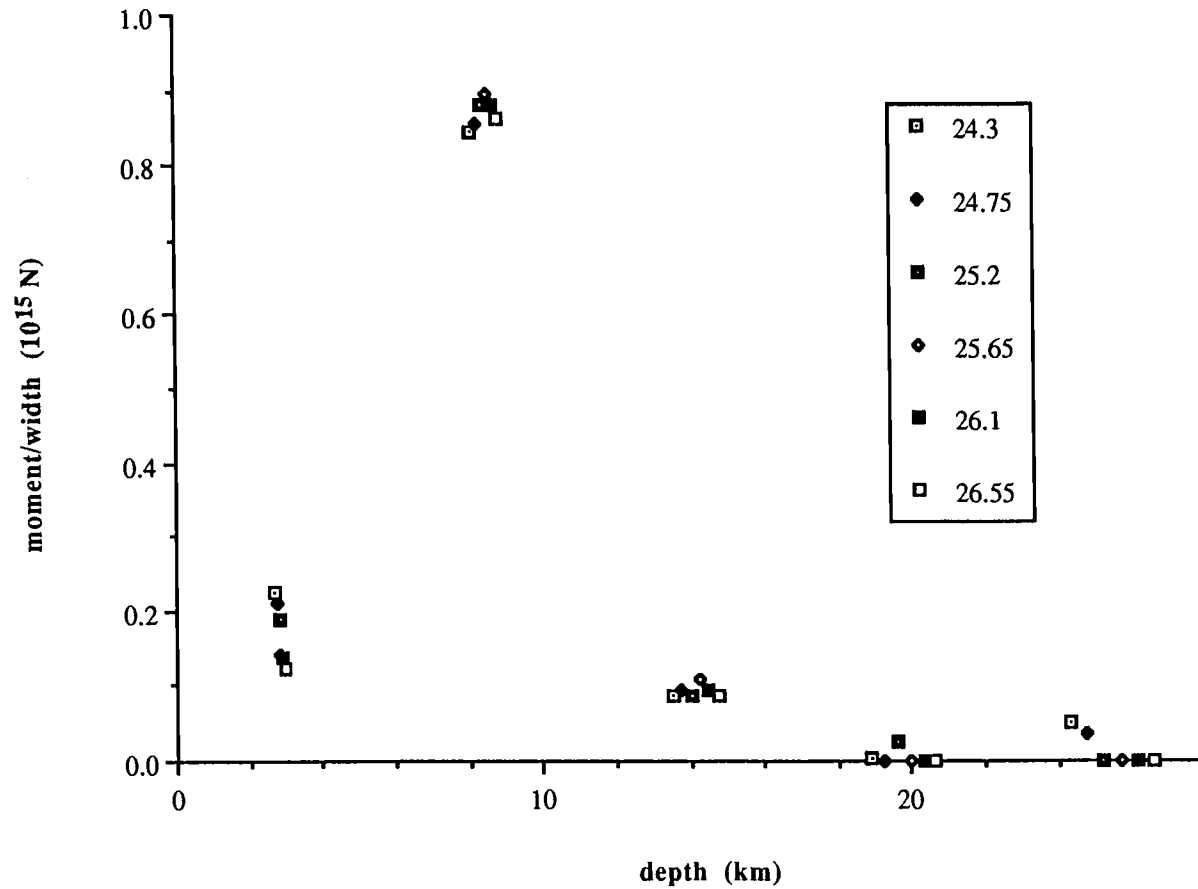
177

Figure 6.3.8   Seismic moment release vs. depth for the 02/24/1981 Corinth earthquake. Figure is a compilation of 6 inversions in which 5 equally spaced sources were used. Number in legend corresponds to depth of the deepest source of each model. Moment release is observed at least to 15 km depth.
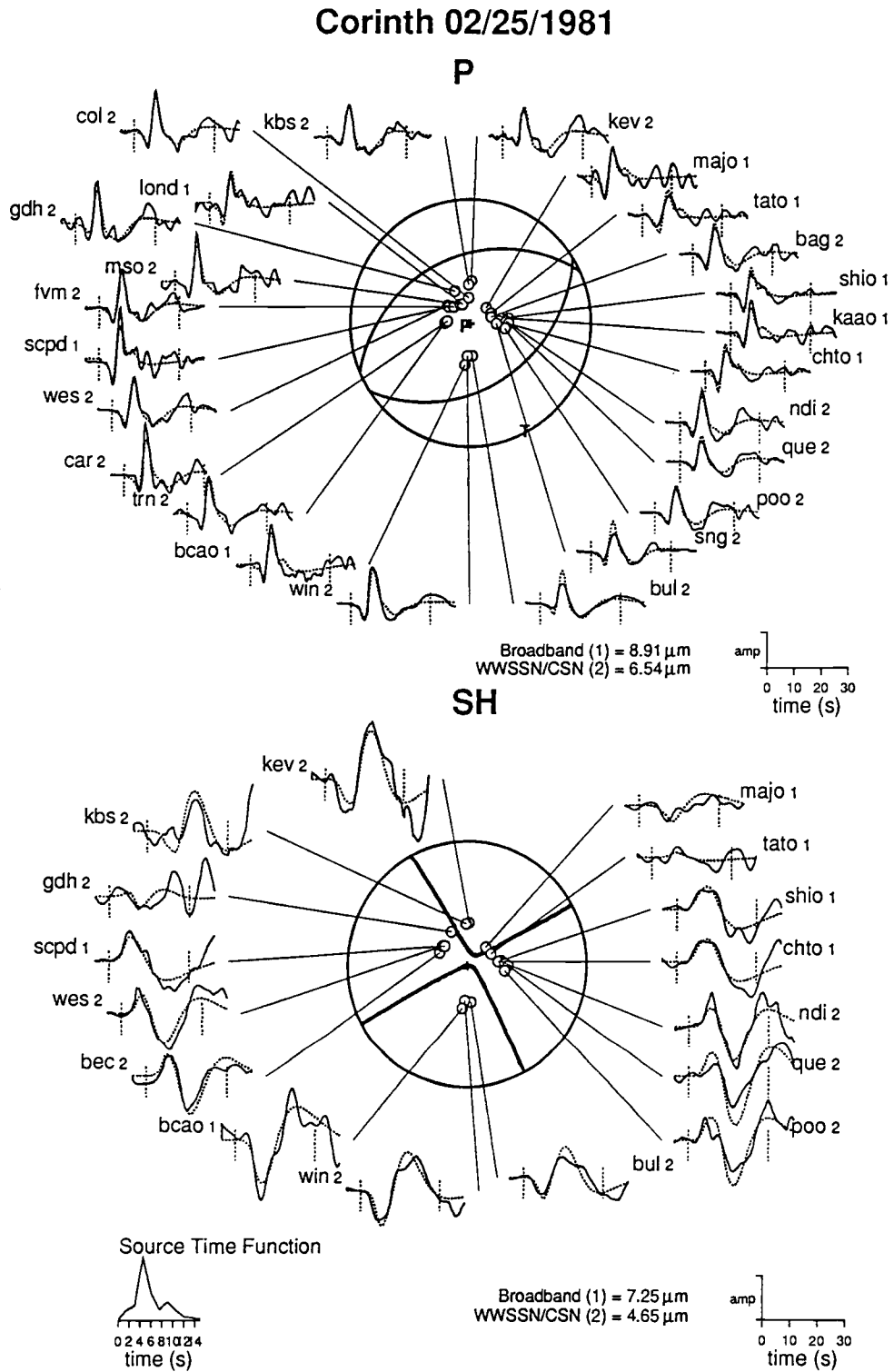
Corinth 02/25/1981

P

Broadband (1) = 8.91 μm
WWSSN/CSN (2) = 6.54 μm

amp

0 10 20 30
time (s)

SH

Source Time Function

0 2 4 6 81012 4
time (s)

Broadband (1) = 7.25 μm
WWSSN/CSN (2) = 4.65 μm

amp

0 10 20 30
time (s)

Figure 6.3.9   Point source solution for the 02/25/1981 Corinth earthquake.
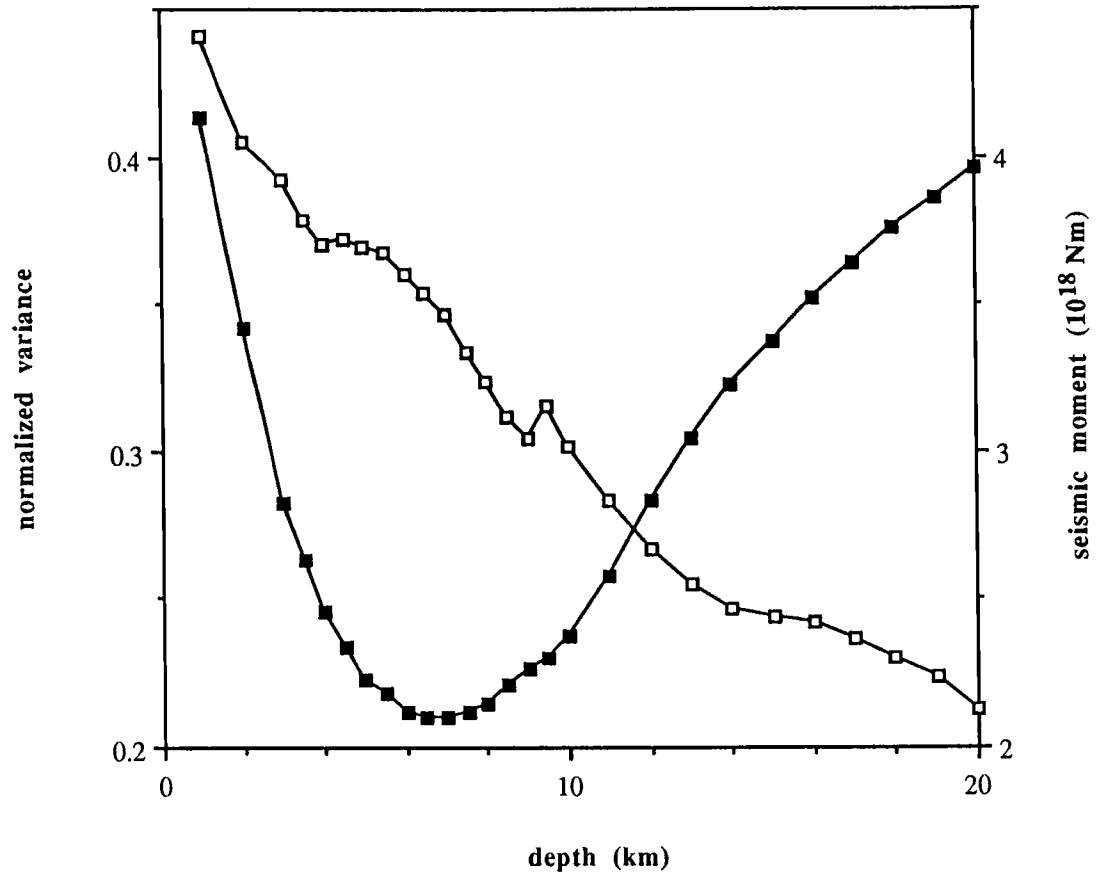
Corinth 02/25/1981

Figure 6.3.10 Residual variance (filled squares) and seismic moment (open squares) as a function of centroid depth.

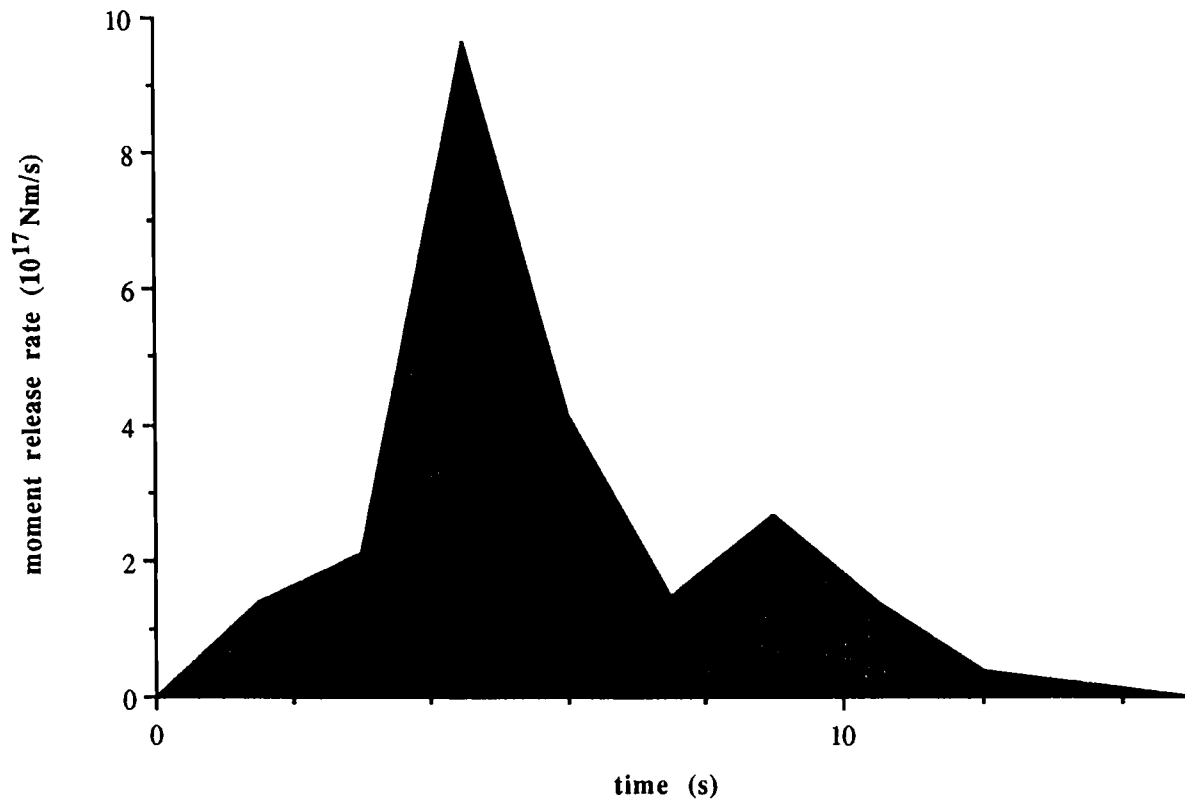Corinth 02/25/1981 - moment release rate

Figure 6.3.11 Seismic moment release rate. Note the emergent beginning and long tail.

MAJO, P 47°   WIN, P 186°   KBS, P 357°   MAJO, SH 47°   SHIO, SH 81°   WIN, SH 186°   SCPD, SH 309°

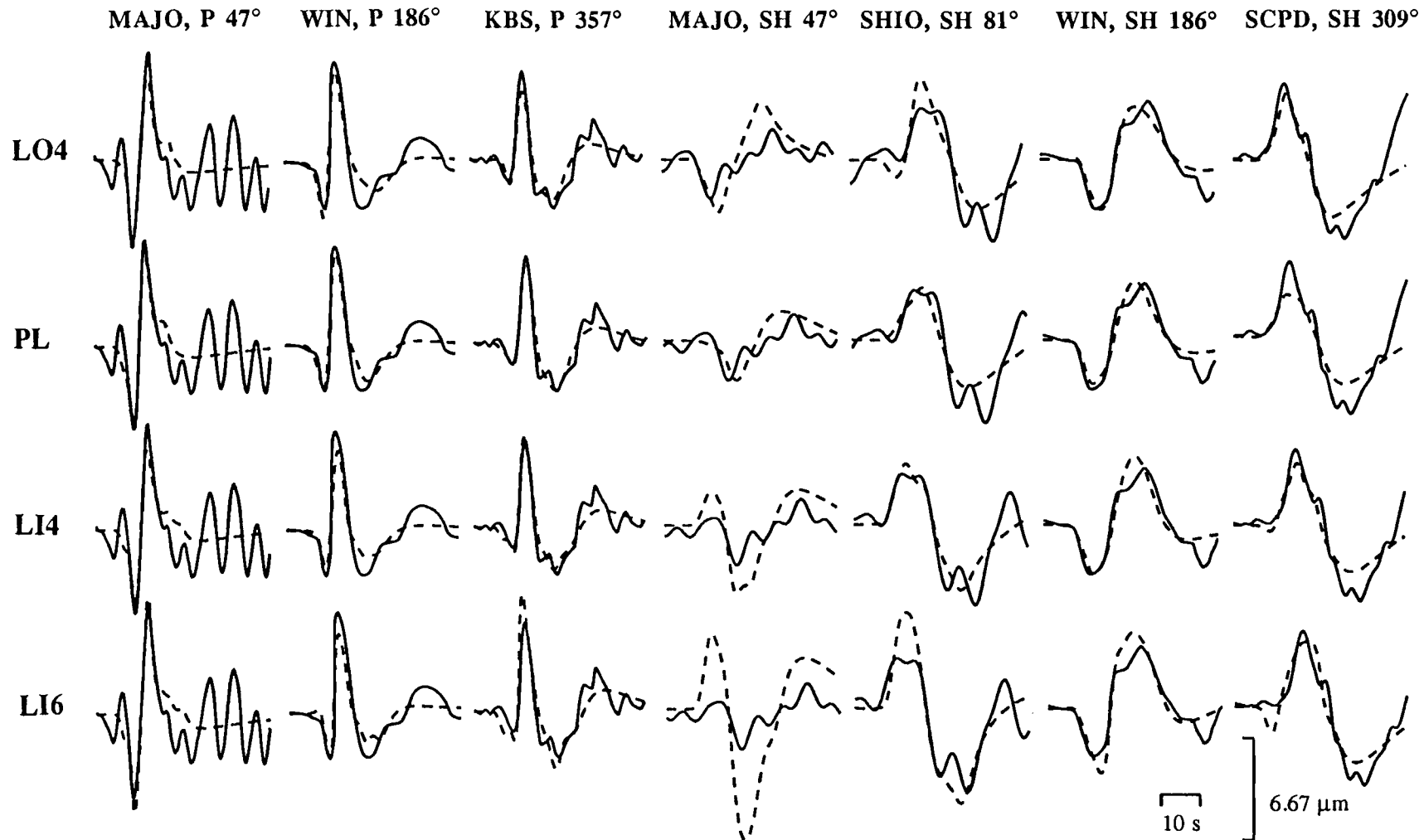LO4

PL

LI4

LI6

10 s

6.67 μm

Figure 6.3.12 Comparison of P and SH waveforms for four fault models listed in Table 6.3.5 for the 02/25/1981 Corinth earthquake. Number next to station is the azimuth from the source.

Corinth 02/25/1981 - moment vs. depth
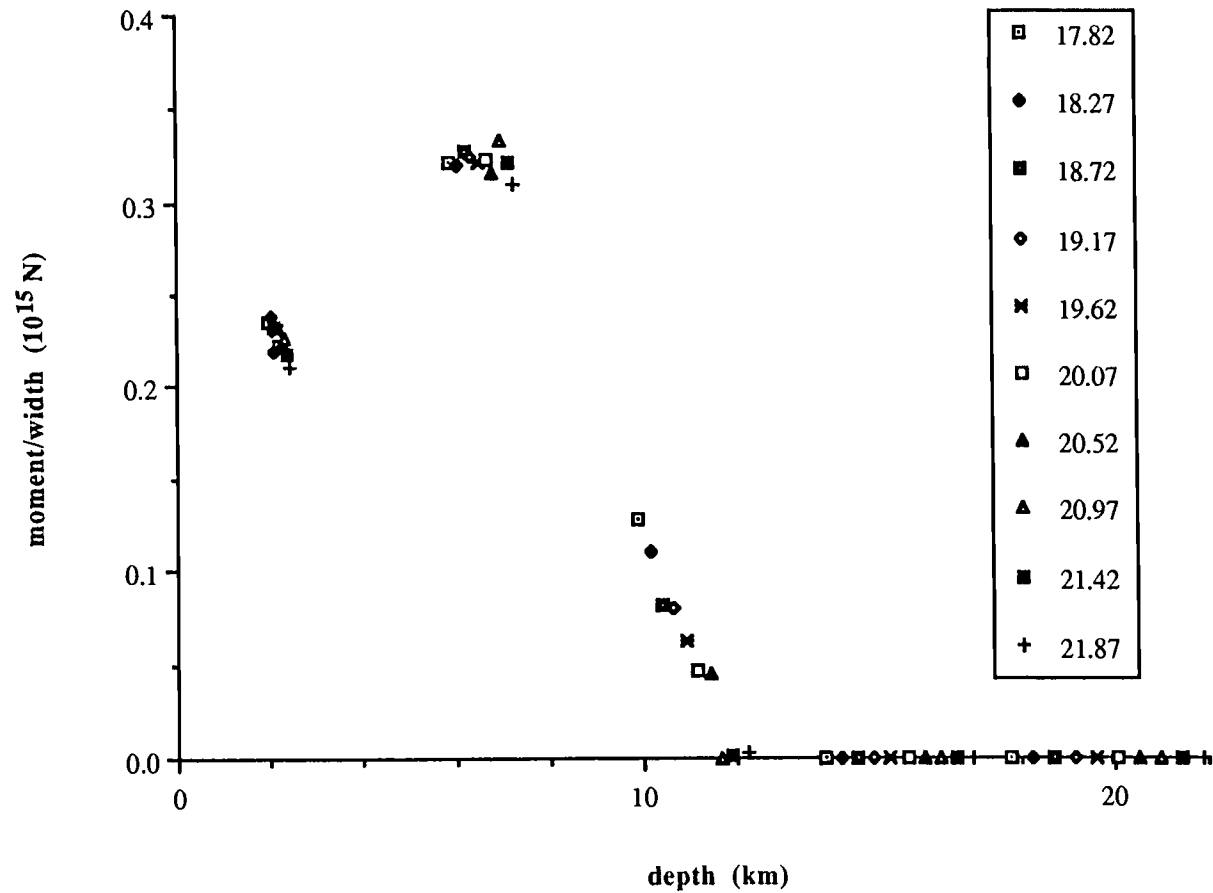
Figure 6.3.13 Seismic moment release vs. depth for the 02/25/1981 Corinth earthquake. The figure is a compilation of 10 inversions in which 5 equally spaced sources were used. No moment release below 12 km is apparent.

Corinth 03/04/1981

P

Broadband (1) = 4.19 μm
WWSSN/CSN (2) = 3.45 μm

amp

0 10 20 30
time (s)

SH

Source Time Function

0 2 4 6 8 10 12
time (s)

Broadband (1) = 4.49 μm
WWSSN/CSN (2) = 3.97 μm

amp

0 10 20 30
time (s)

Figure 6.3.14 Point source solution for the 03/04/1981 Corinth earthquake.

Figure 6.3.15 Residual variance (filled squares) and seismic moment (open squares) as a function of centroid depth.

Corinth 03/04/1981 - moment release rate
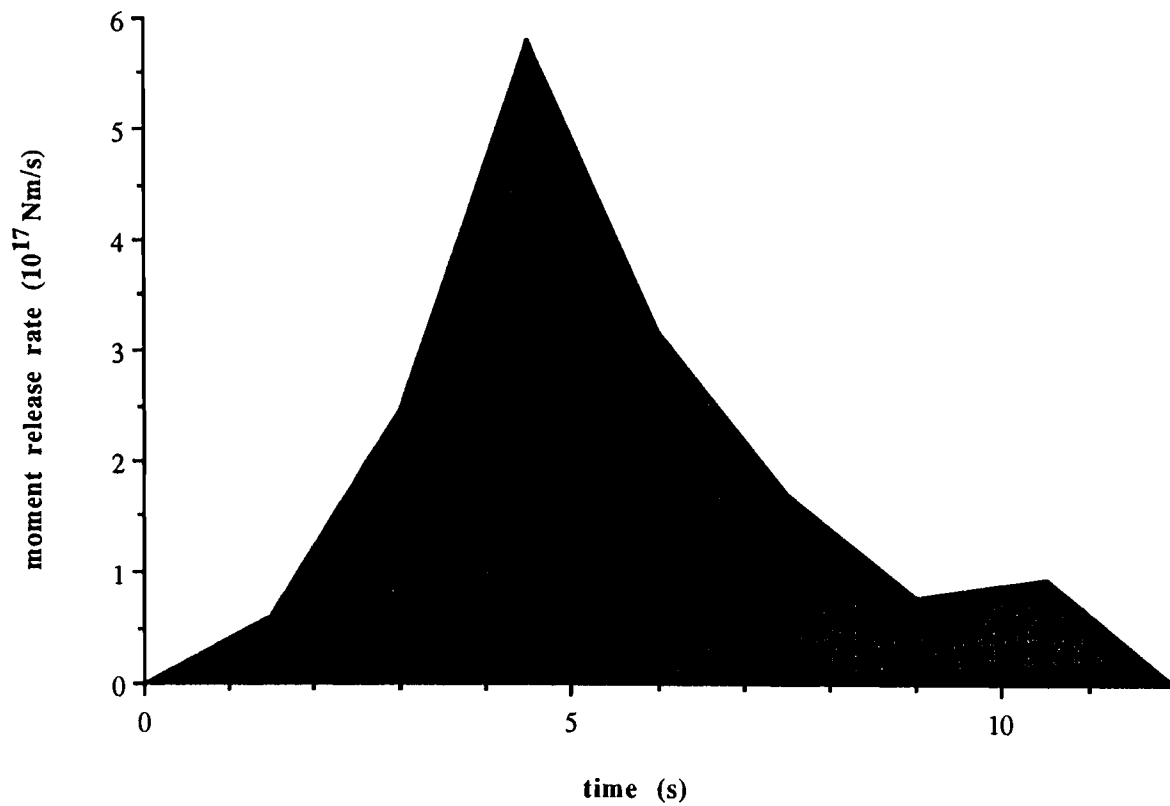
Figure 6.3.16 Seismic moment release rate for the 03/04/1981 Corinth earthquake. Note the emergent onset and the long tail.

MAJO, P 47° PRE, P 175° KBS, P 357° TATO, SH 65° CHTO, SH 83° PRE, SH 175° WES, SH 307°

LO4

PL

LI3

LI6

6.67 μm

10 s
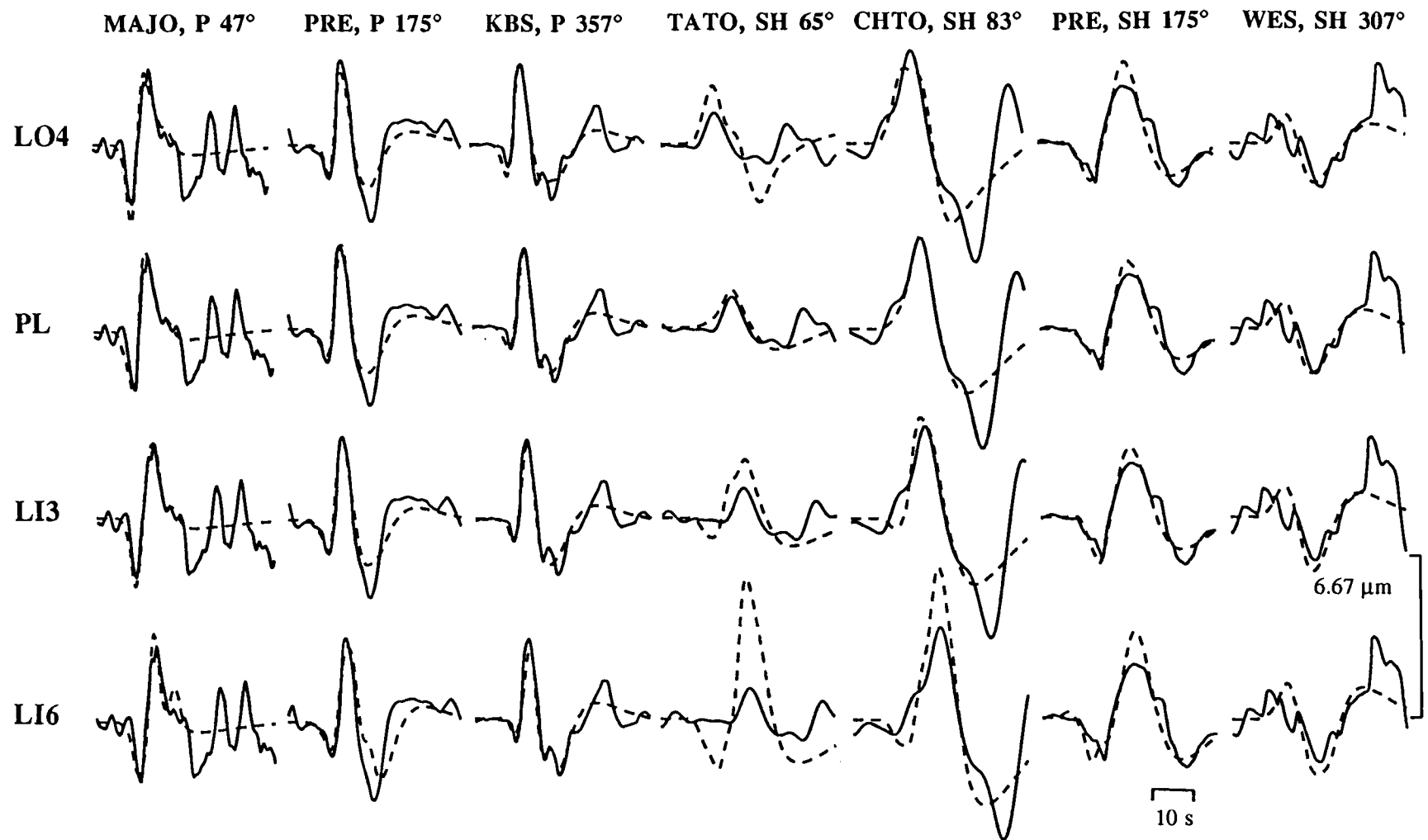
Figure 6.3.17 Comparison of P and SH waveforms for four fault models listed in Table 6.3.8 for the 03/04/1981 Corinth earthquake. Number next to station is the azimuth from the source.
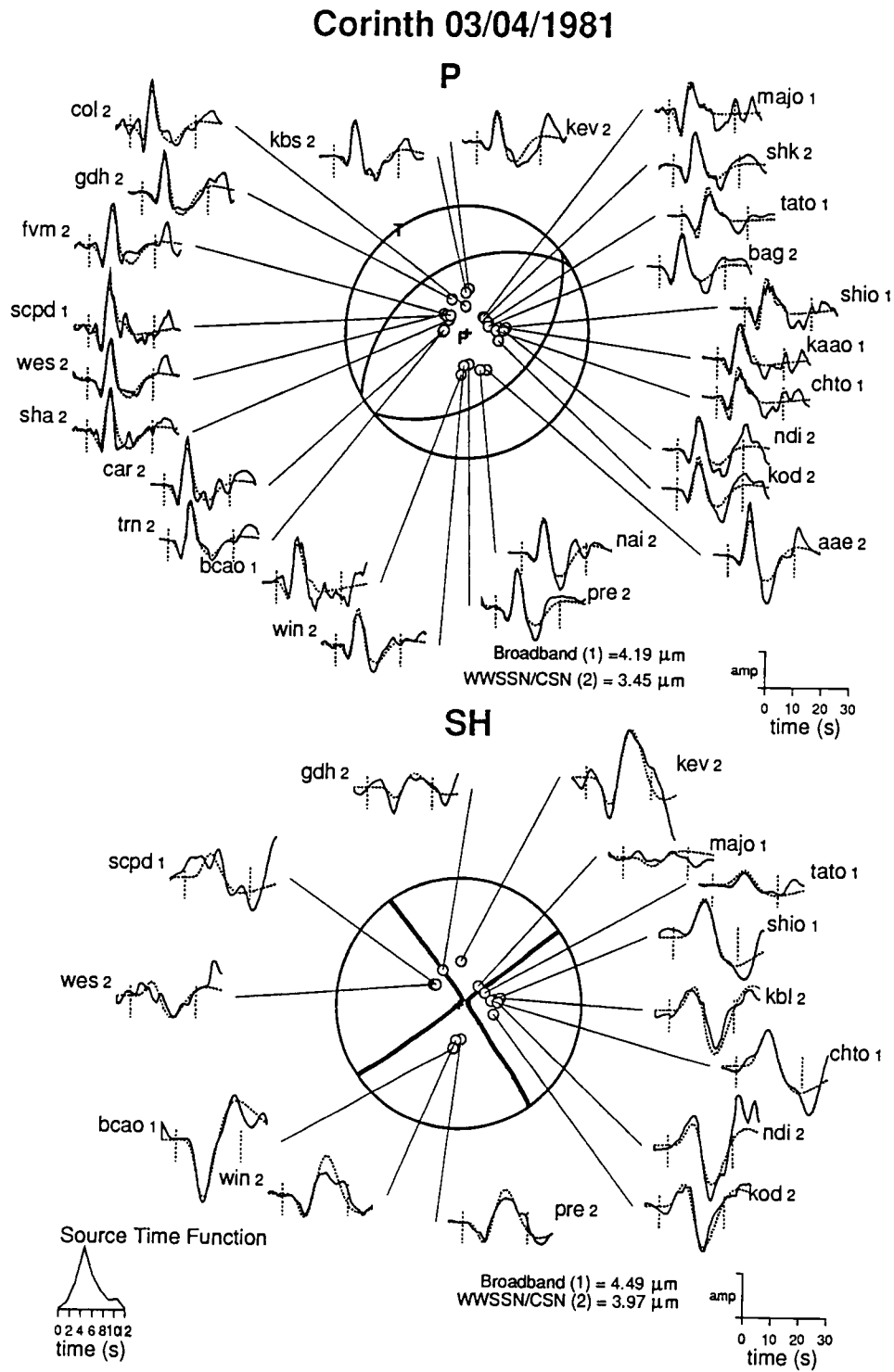
Figure 6.3.18 Seismic moment release vs. depth for the 03/04/1981 Corinth earthquake. The figure is a compilation of 8 inversions in which 5 equally spaced sources were used. The moment release continues to depths of about 16 km.

Corinth - source time functions
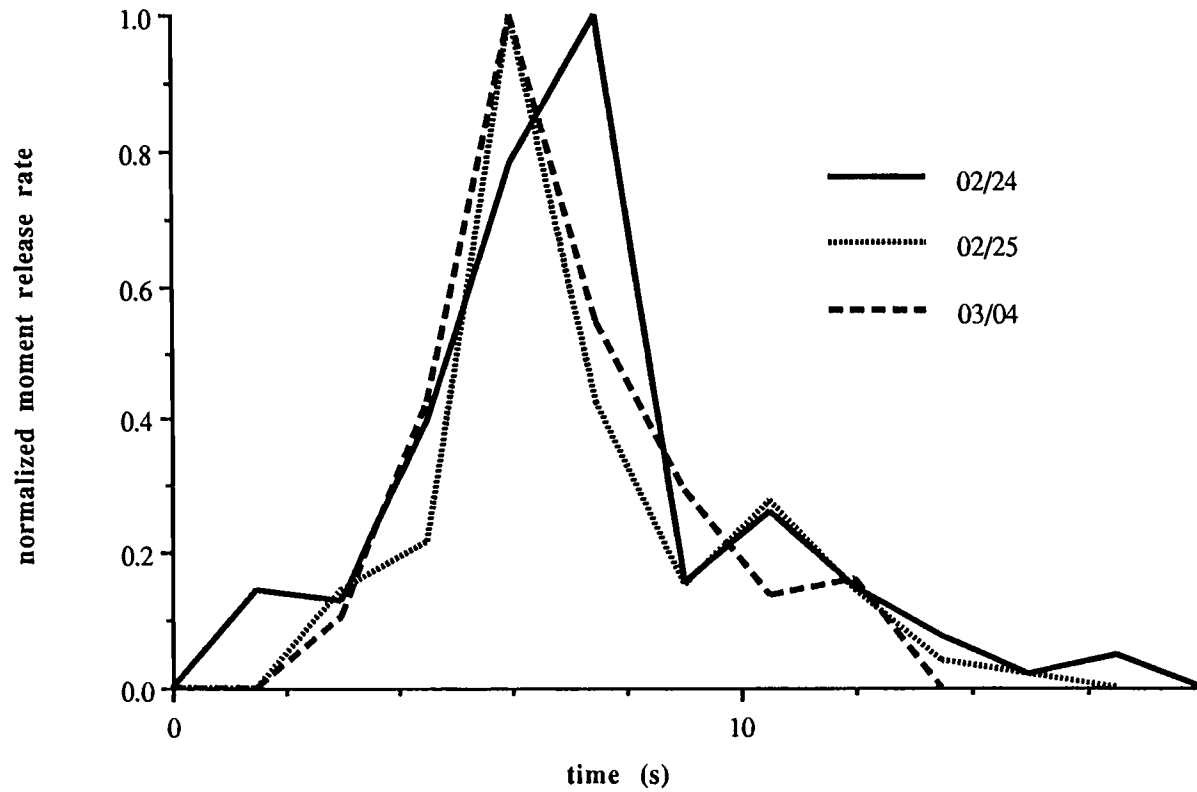
Figure 6.3.19 Comparison of the source time functions of the Corinth earthquakes. The rupture histories of the second and third event were delayed by 1.5 s with respect to Figs. 6.3.11 and 6.3.16 to obtain a better cross-correlation. Note the similarity of all source time functions.

6.4 Kalamata 09/13/1986

Introduction

A relatively large (M_S=6.2) earthquake occurred on September 13, 1986 in the southern part of the Peloponnesus peninsula. The epicenter is located about 10 km north of the city of Kalamata (Figure 6.4.1), and is constrained by strong motion data recorded in Kalamata. Considerable damage was sustained and 21 people were killed by earthquake related causes (Anagnostopolous et al., 1987; Delibasis et al., 1987; Papazachos et al., 1988). The town of Eleochori about 6 km northeast of Kalamata where more than 70% of the houses collapsed was abandoned by its inhabitants (Anagnostopolous et al., 1987; Papazachos et al., 1988). The earthquake occurred in the early evening (local time 20:24) of a late summer Saturday when many people were outdoors, which certainly spared the life of many inhabitants. Differences in soil conditions are the main cause for rapidly changing damage distribution within Kalamata, which is built on alluvial deposits; damage decreases towards the south and west with the heaviest damages in the northern part of the city (Anagnostopolous et al., 1987; Delibasis et al., 1987; Gariel et al., 1991). However, Gariel et al. (1991) computed synthetic accelerograms for a multiple circular crack model and showed that a heterogeneous faulting process can also cause large variations in ground motion within a small area near the fault plane.

The largest aftershock (M_S=5.4) on September 15 caused additional damage in Kalamata due to its proximity. Records from an accelerograph in the town hall of Kalamata indicate that the epicentral distance was just about 1 km, still within the city limits (Anagnostopolous et al., 1987; Delibasis et al., 1987). The maximum acceleration during the main shock reached 0.27 g on the transverse component (Anagnostopolous et al., 1987). The strong motion duration is estimated to be between 3 s as deduced by Gariel et al. (1991) from visual inspection and 5.8 s, the time span during which the acceleration exceeded 0.05 g (Delibasis et al., 1987). The strong motion data do not show multiple arrivals of S waves indicating a relatively simple rupture history (see e.g. Anagnostopolous et al., 1987 or Gariel et al., 1991).

Surface Faulting

The southern Peloponnesus is dominated by NNW-SSE trending ranges and basins which probably extend southward into the Aegean Sea (Figure 6.4.1). A fault in the

western foothills of the Tayghetos mountains with a local NNE-SSW trend bounding the eastern side of the Gulf of Messiniakos broke during the earthquake of September 13 (Papazachos et al., 1988; Lyon-Caen et al., 1988). It may be interesting to note that the ancient city of Sparta, located just about 40 km east of Kalamata, was severely destructed by a major earthquake in 464BC; in a recent paper, Armijo et al. (1991) relate a normal-fault fault scarp along the eastern foothills of the Tayghetos mountains to this event. The following description of the observed surface faulting is mainly based on work published by Lyon-Caen et al. (1988) and additional work by Papazachos et al. (1988) and Mariolakis et al. (1989). Surface breaks were observed along the fault bounding the Tayghetos mountains which represent the uplifted footwall. The ruptures are continuous for about 4.5 km and became discontinuous for another 1.5 km north of Eleochori. The fissures are usually some tens of centimeters west of the fault plane within sediments. They show a small throw of 6-18 cm and are generally steep (70-90°). Lateral slip components are small and thought to be of local origin. As explained by Mercier et al. (1979, 1983) for surface ruptures associated with the Thessaloniki earthquake(s), these steep attitudes are probably caused by the reduction of cohesion in the unconsolidated sediments near the surface, which faciliates motion along steeper or even overturned surfaces. Slickensides in bedrock clearly indicate a tectonic origin, and it is assumed that the steeper breaks within the sediments merge with the fault at a few meters depth. The road from Kalamata to Eleochori was crossed by a small surface break and brecchias of different age near this site indicate reactivation of the neotectonic fault. This conclusion is also supported by the morphology of the Tayghetos mountains, which are the result of successive footwall uplift due to normal faulting. The northern end of the observed surface ruptures coincides with a major left step of the normal fault system bounding the plain of the Pamisos river. Lyon-Caen et al. (1988) speculate that this offset is located along an older zone of transverse fractures. It is interesting that the epicenter of the main shock is probably at the northern end of the aftershock zone and is close to this left step of the fault system. Minor ground ruptures were observed in unconsolidated Quaternary deposits along the beach of the village Verga southeast of Kalamata. In contrast to Papazachos et al. (1988), these have been interpreted as gravitational slides by Lyon-Caen et al. (1988).

Aftershocks

The aftershock sequence was recorded by portable seismograph networks starting five days after the mainshock. A very detailed description can be found in Lyon-Caen et

al. (1988) and also in Papazachos et al. (1988). The aftershock distribution is shown in Figure 6.4.2. The epicenters follow roughly a north-south trend and cover an area of about 15 by 10 km. The northern cluster of high aftershock concentration is in the vicinity of the main shock epicenter and another cluster has been recorded close to the surface ruptures in the broader vicinity of the largest aftershock. These zones are separated by a narrow gap of minor activity (see also Figure 13 in Lyon-Caen et al, 1988). Aftershock activity extends to a depth of about 11-12 km with most of the deeper shocks located towards the northwest where shallow seismicity was relatively low (Figure 6.4.2). The cross-section, perpendicular to the strike of the fault (Figure 6.4.2), also delineates a fault dipping towards northwest at an angle of about 45° (Papazachos et al., 1988; Lyon-Caen et al., 1988) with additional activity within the deformed footwall especially for events from the southern more diffuse 'cluster'. Most of the aftershocks show a fault plane solution consisting of a steeply dipping P-axis and an almost horizontal T-axis trending towards E, compatible with the main shock; however, thrust-type events in the footwall were also reported as well as strike-slip and normal faulting events with a T-axis rotated counterclockwise (Lyon-Caen et al., 1988).

Previous Results for the Main Shock

Papazachos et al. (1988) used P wave first motion data to construct a fault plane solution. Their result (strike: 204°, dip: 51°, rake: 303°) implies E-W extension accompanied by a small amount of sinistral strike-slip motion. Estimating the width (15 km), length (11 km), and average displacement (12 cm) of the fault, and the rigidity (3×10^{10} N/m^2) of the neighboring rock, they derived a seismic moment of 6×10^{17}Nm. Based on surface observations of steeply dipping fault breaks and their (average) fault plane solution, Papazachos et al. (1988) suggest listric curvature of the fault surface.

Another first motion fault plane solution was presented by Delibasis et al. (1987), which also indicates E-W extension with a minor left-lateral strike slip component (strike: 173°, dip: 50°, rake: 280°).

Sipkin and Needham (1989) obtain a focal mechanism with a strike, dip, and rake of 200°, 41°, 307°, respectively, from moment tensor inversion. At a depth of 21 km their estimate of the seismic moment is 6.6×10^{17} Nm. The Harvard CMT solution (Dziewonski et al, 1987b) shows a steeper dip (56°) and the fault trend is more SW-NE (221°), whereas the rake (304°) is very similar to the one found by Sipkin and Needham (1989). They estimate a seismic moment of 9.8×10^{17} Nm at a depth of 15 km with a half-duration of 3.4 s. The long period moment tensor inversions are relatively

insensitive to centroid depth. It is hardly possible to explain the observed surface faulting for an event of this size with such centroid depths.

Stavrakakis et al. (1989) use the far-field displacement source model proposed by Brune (1979, 1971) and Hanks and Wyss (1972) to calculate the seismic moment, fault length, and average displacement from the P and S wave spectra. They obtain a seismic moment of 19×10^{17} Nm and 2.2×10^{17} Nm, an average displacement of 15 cm and 9 cm, and a fault length of 22 and 11 km from teleseismic P- and S-wave spectra, respectively. The moment estimate from the P wave data is considerably larger than estimates from any other study, but not taking the surface reflected phases into account may lead to this overestimation.

Lyon-Caen et al. (1988) used the same inversion routine as used in this study to model long period P and SH waveforms, and their results are therefore very similar to mine. They obtain a strike, dip, and rake of $201°$, $45°$, and $283°$, respectively. At a centroid depth of 5 km their estimated seismic moment is 7.9×10^{17} Nm with a source duration of 4 s.

The results of previous studies are summarized in Table 6.4.1 together with my results.

Data

The data set for this earthquake consists of a combination of analog WWSSN and digital GDSN data. All analog data were high-pass filtered with a 3-pole butterworth filter with a cut-off at 100 s and resampled at a sampling interval of 0.3 s. Broad-band displacement seismograms were derived from the digital records by removing the instrument response and combining long- and short-period records, the resulting records are broad band from the Nyquist period of 0.6 s to 50 s. The P wave record at TATO was derived from the short-periods only ($0.6 \text{ s} \leq T \leq 10$ s) due to instabilities of the combined deconvolution. The SH wave records for MAJO, TATO, RSNY, and COLD were derived from the long-period data only due to the absence of short period horizontal instruments at these sites ($5 \text{ s} \leq T \leq 50$ s). The supposedly broad-band intermediate channel at the stations RSON, RSSD, and RSNT was also used separately to obtain broadband records, the P waves at RSON and RSSD are broad-band from the Nyquist period up to 100 s, whereas the P- and SH-wave records at RSNT are broad-band up to 50 s. The broad-band digital waveforms are considerably more complex due to their higher frequency content. Using only the long-period data to generate the SH-broad-band waveforms resulted often in unstable and ringy waveforms probably caused by the

relatively small size of the earthquake and the instrument responses therefore magnifying unwanted noise. These data were rejected.

<u>Focal Parameters</u>

The point source solution found by simultaneous inversion of P and SH waves is shown in Figure 6.4.3. The orientation (strike: 201°, dip: 45°, and rake: 284°) of the centroid is in good agreement with the short period first motion data (Figure 6.4.4) and the fault dip as outlined by the aftershock distribution (Figure 6.4.2). The centroidal depth of 6.2 km is well resolved (Figure 6.4.5), a conservative error bound (10% increase in variance) places the centroid between 4 and 9.5 km depth, the moment within this bound is $7\pm1.1\times10^{17}$Nm (M_w=5.8). The dip is very stable over the entire depth range, the strike can vary by about $\pm4°$, and the rake by about $\pm5°$. The source time history shows a very emergent beginning, followed by a roughly triangular shaped moment release function with a sharp cut-off, the duration of the main part is about 4 s. This emergent beginning is evident in the short-period records which show small arrivals preceding the main arrival by about 3 s. Lyon-Caen et al. (1988) suggest that the main shock initiated within the zone offsetting the en echelon fault system which bounds the Pamisos plain in a left step, either due to a small foreshock triggering the main event or as the main shock itself with a small initial moment release due to complex deformation within this zone. Results presented by Lyon-Caen et al. (1988) are basically identical to my results. They used the same waveform inversion routine with a slightly smaller data set and without using broad-band data. Models involving a larger left-lateral strike-slip component (Papazachos et al., 1988; Sipkin and Needham, 1989; Dziewonski et al., 1987b) are not supported by my data. Effects of rupture propagation are very small, unilaterally propagating ruptures towards NNE and SSW were indistinguishable from the point source results, as expected from the size of the earthquake and the lateral extent of the aftershock distribution. Proposed propagation of the main shock unilaterally towards south (Papazachos et al., 1988; Lyon-Caen et al., 1988) deduced from the epicenter locations of the main shock and largest aftershock as well as from aftershock clustering and surface faulting, could not be substantiated with the data set available and the method used. The focal mechanism implies E-W extension oblique to the Hellenic arc in contrast to the results of the other earthquakes in this thesis which showed N-S extension. Changes in the boundary conditions due to the incipient collision of the African margin with the Hellenic arc probably changes the regional tectonic regime in the vicinity of the subduction zone (Lyon-Caen et al., 1988).

Due to the small size and duration of this earthquake, I did not attempt to investigate the fault geometry. However, from the short-period first motion data, sampling the fault orientation at the nucleation point of the rupture and from the centroidal description obtained from waveform modelling no discrepancy is present, suggesting that the fault surface is not significantly curved. Apparent steep dips of the surface ruptures probably do not represent the true dip of the fault plane (Mercier et al., 1979, 1983; Lyon-Caen et al., 1988) as assumed by Papazachos et al. (1988).

Depth Extent of Rupture

The aftershock sequence was well recorded. Lyon-Caen et al. (1988) recorded more than hundred aftershocks per day between 09/18-09/27/1986 with an extensive network of sixteen stations. The aftershock-depth distribution shown in Figure 6.4.6 is compiled from Lyon-Caen et al. (1988) (133 aftershocks where a fault plane solution could be constructed) and from Papazachos et al. (1988) (additional 25 aftershock hypocenters), who operated a five station network for about two days. The aftershock activity is concentrated between 2-11 km depth, and no hypocenter was located below 13 km depth.

Five sources were distributed as described in Chapter 3.2. Figure 6.4.7 shows the combined results of 11 models, with the depth of the deepest source ranging from 15.3 to 19.8 km. Estimating the width (14-16 km) and length (8-12 km) of the fault plane from the aftershock distribution provides an estimate of the expected average surface displacement (μ=3.4x10^{10} N/m^2, Mo=7x10^{17} Nm) of 11-18 cm, which is larger than observed. This behaviour can be expected for a medium sized earthquake where most of the energy is radiated in the vicinity of the centroid. The results from distributing sources follow that pattern: relatively low moment release close to the surface (very shallow sources, however, show again instabilities as observed for the Thessaloniki earthquake) with a concentration in the proximity of the centroidal depth. Below a depth of about 12 km no significant moment release was observed. Sources placed below 17 km depth show again a very small but insignificant amount of moment release associated with them. This may be caused by parameter inference, fitting of noise such as unmodelled crustal reverberations and is probably not real. The bulk of the aftershocks extends down to a depth of about 11 km, which almost coincides with the depth of 12 km below which no significant moment release was observed for the main shock rupture. This indicates that the Kalamata earthquake was not strong enough to penetrate far into the semi-brittle field in contrast to the Thessaloniki main shock. The discrepancy between observed surface faulting and the expected average value also supports the idea of Scholz (1988)

and Tse and Rice (1986) that intermediate sized earthquakes rupture only within the region of velocity weakening material behaviour.

Table 6.4.1   Source Parameters of the 09/13/1986 Kalamata Earthquake

	strike deg	dip deg	rake deg	moment 10^{17}Nm	depth km	duration s
P S	201	45	284	7.0	6.2	4
LyC	201	45	283	7.9	5	4
CMT	221	56	304	9.8	15	3.4[1]
S & N	200	41	307	6.6	21	
P	204	51	303	6.0		
D, S	173	50	280	2.2-19		

PS - point source solution. LyC - Lyon-Caen et al. (1988) waveform inversion. CMT, S&N - Dziewonski et al (1987), Sipkin and Needham (1989) moment tensor inversion. P, D - Papazachos et al. (1988), Delibasis et al. (1987) first motion fault plane solution. S - Stavrakakis et al. (1989) spectral estimate of moment. [1] - half-duration.
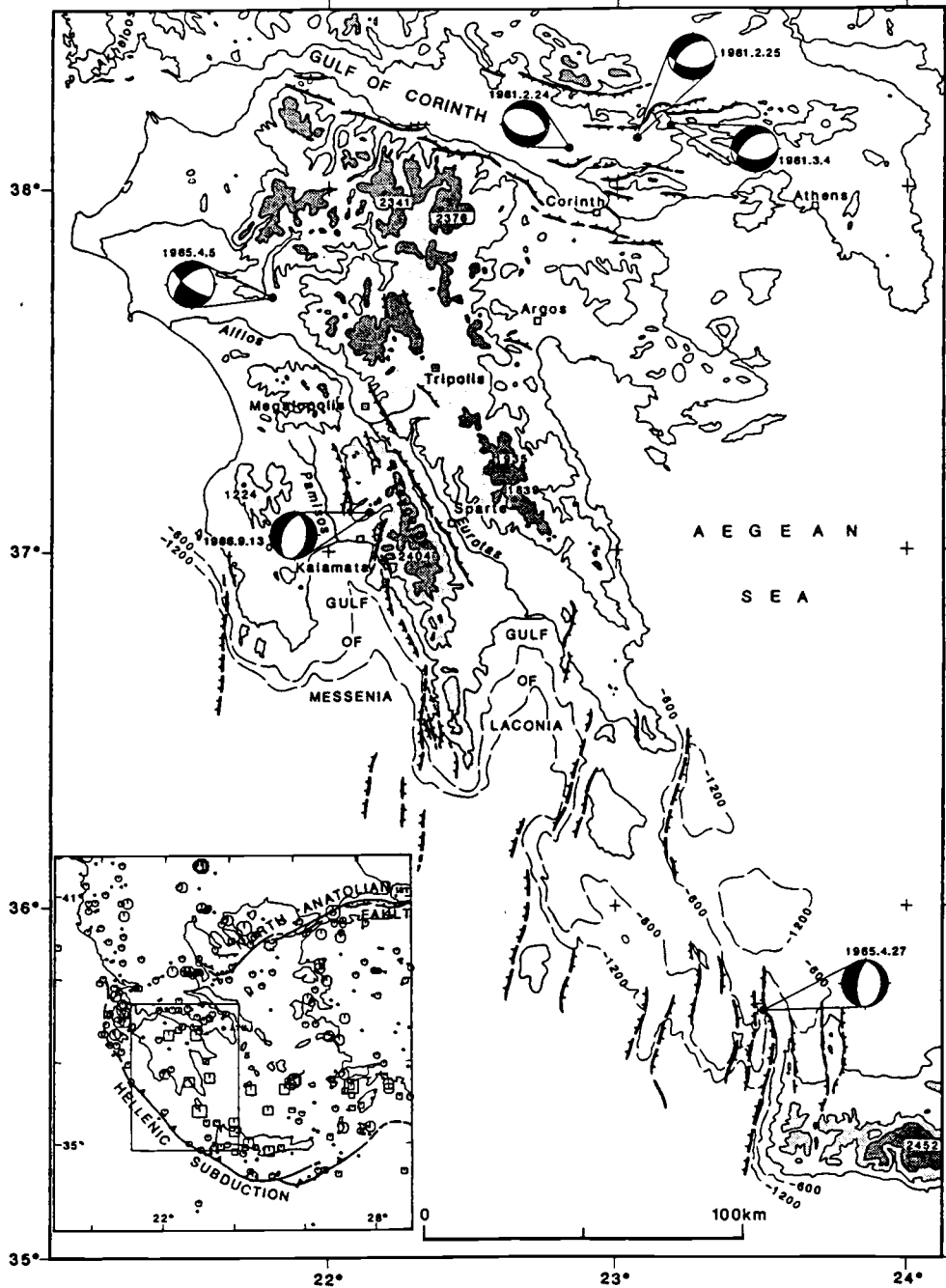
Figure 6.4.1 Seismotectonic map of the Peloponnesus and adjacent areas (from Lyon-Caen et al., 1988). Fault plane solutions are from McKenzie (1972) (04/05/1965), Jackson et al. (1982) (02/24, 02/25, and 03/04/1981), and Lyon-Caen et al. (1988) (04/27/1965, 09/13/1986). Normal faults are shown with ticks on the downthrown side. Inset shows tectonic framework of the Aegean and earthquakes with magnitude larger than 5.0 from 1900-1986.

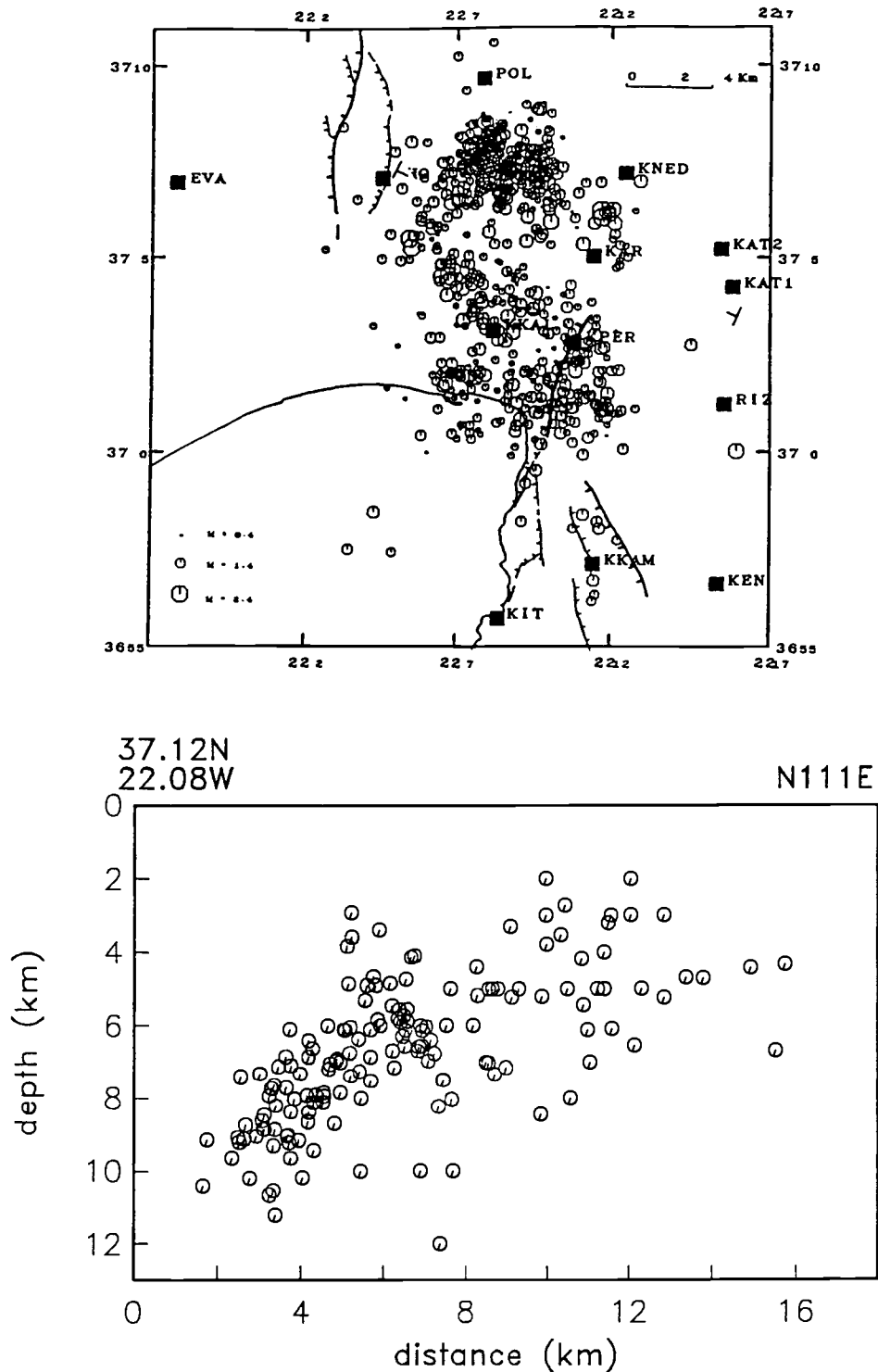Figure 6.4.2 Aftershock distribution. a) map view of 740 located events. Heavy line with ticks on downthrown side is observed surface rupture. From Lyon-Caen et al. (1988). b) cross section of 158 aftershocks perpendicular to strike of fault as determined by waveform inversion (hypocenter data from Lyon-Caen et al., 1988; Papazachos et al., 1988).
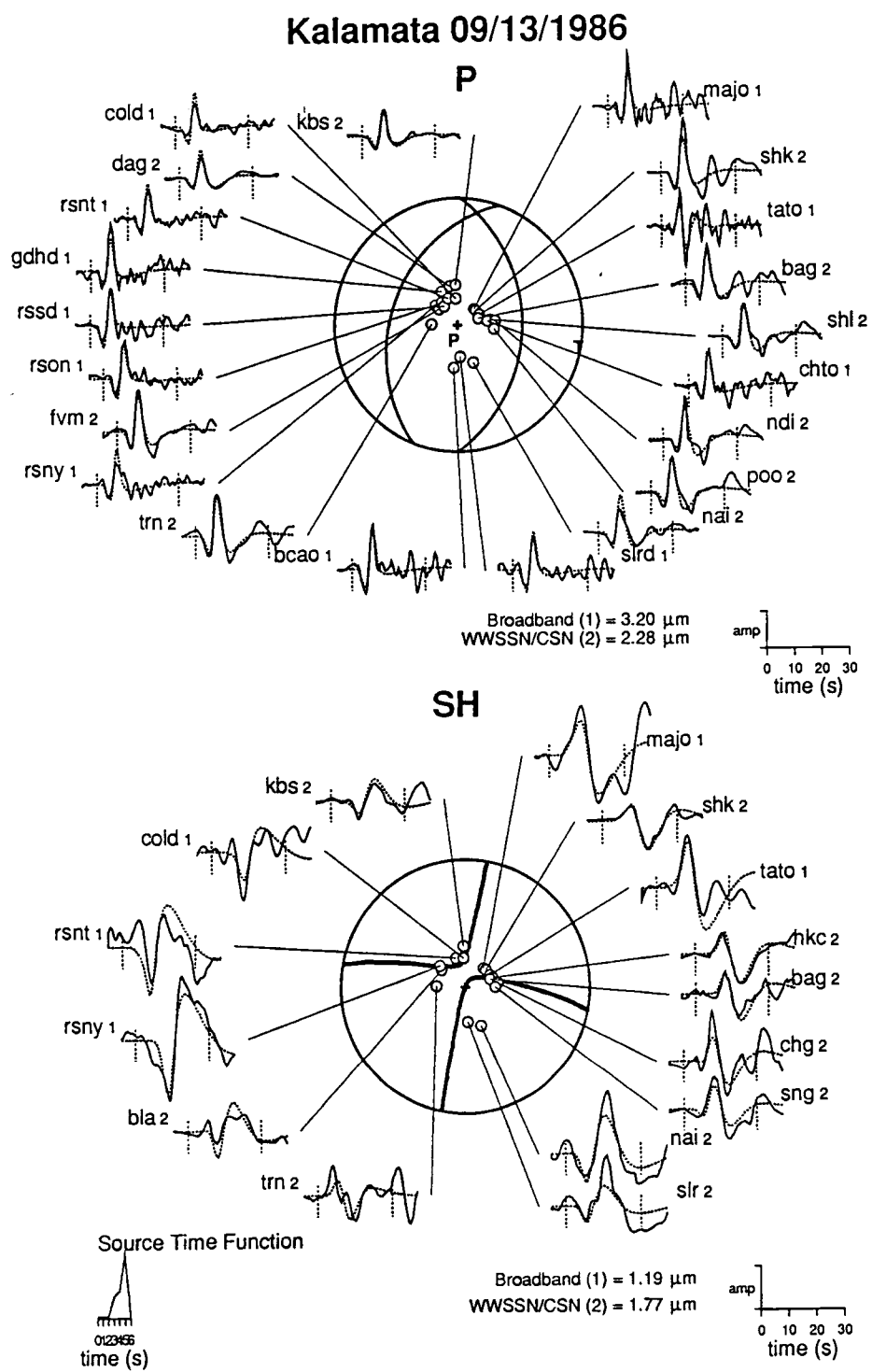
Figure 6.4.3   Point source solution for the 09/13/1986 Kalamata earthquake.

Kalamata   09/13/1986

+ Compressional

□ Dilatational

◇ Nodal
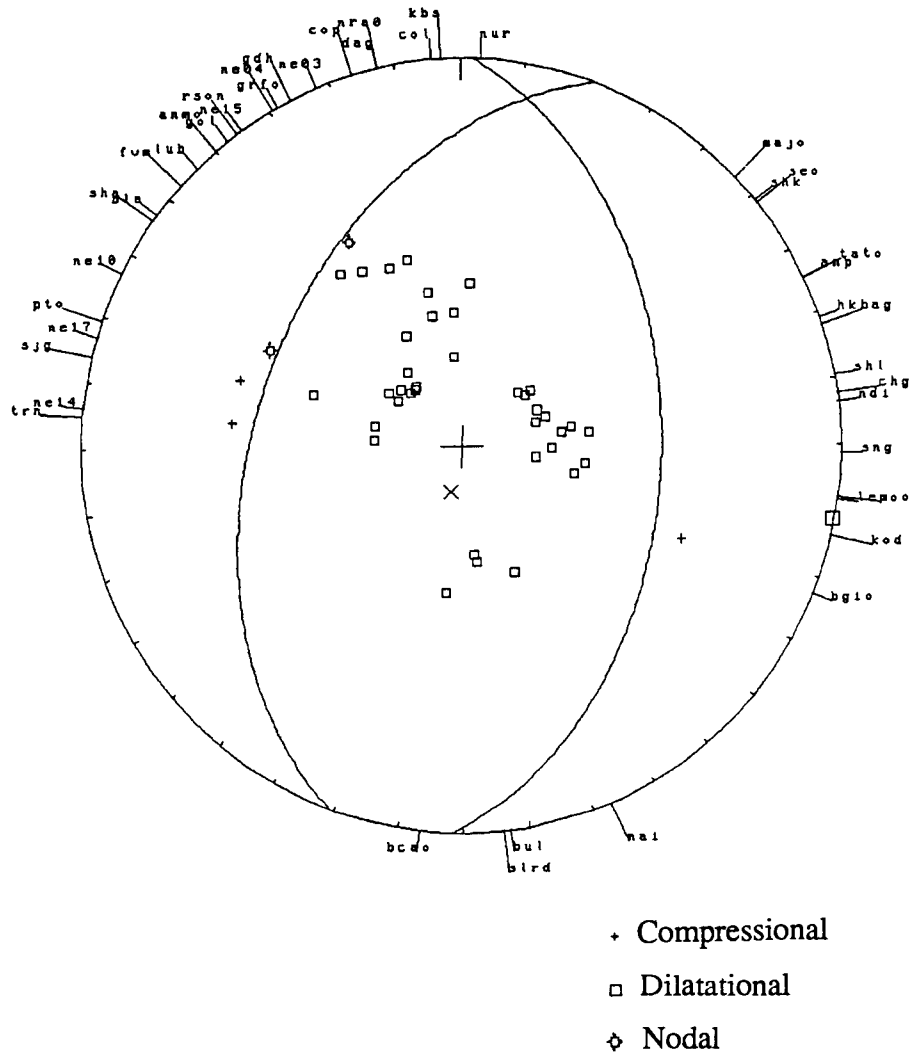
Figure 6.4.4   Short-period first motion polarities for the Kalamata earthquake. Fault plane is well constrained. Centroidal solution (solid line) is consistent with first motion data.

Kalamata 09/13/1986
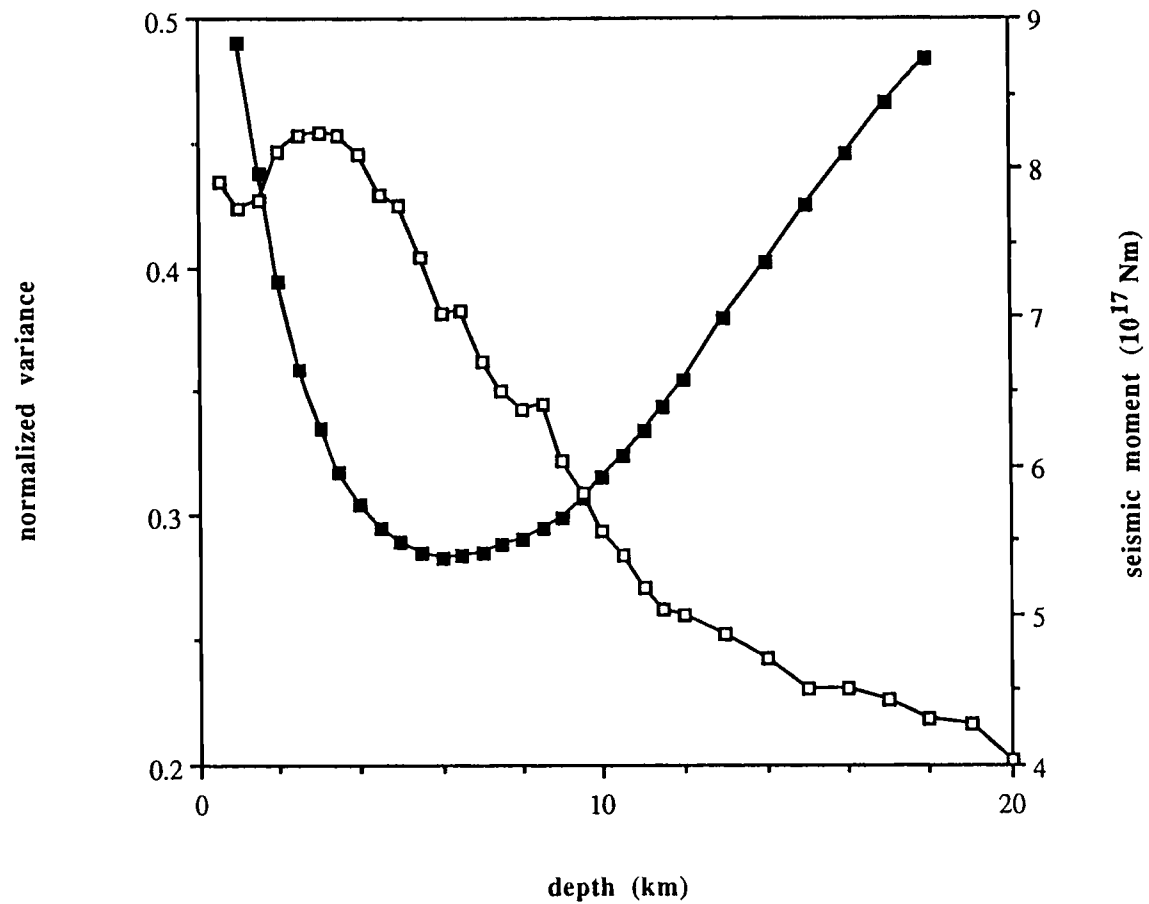
Figure 6.4.5   Residual variance (filled squares) and seismic moment (open squares) as a function of centroid depth.
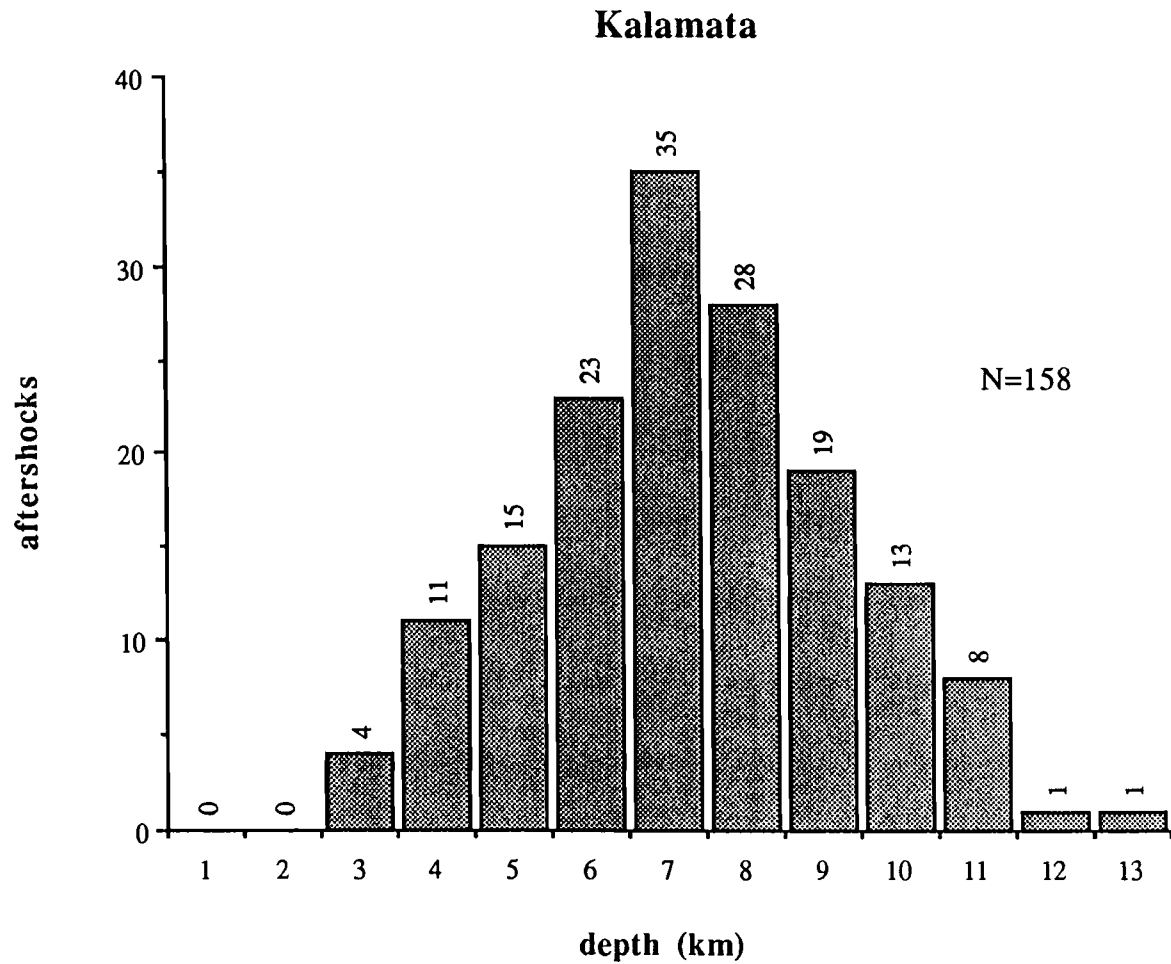
Kalamata

Figure 6.4.6 Aftershock depth distribution. Data are from Lyon-Caen et al. (1988) and Papazachos et al. (1988). Only a few aftershocks occurred below 11 km depth. N: total number of aftershocks included in histogram.

Kalamata - moment vs. depth

Legend:
- □ 15.3
- ◆ 15.75
- ▣ 16.2
- ◇ 16.65
- ■ 17.1
- ▢ 17.55
- ▲ 18.0
- ▲ 18.45
- ■ 18.9
- + 19.35
- ▣ 19.8
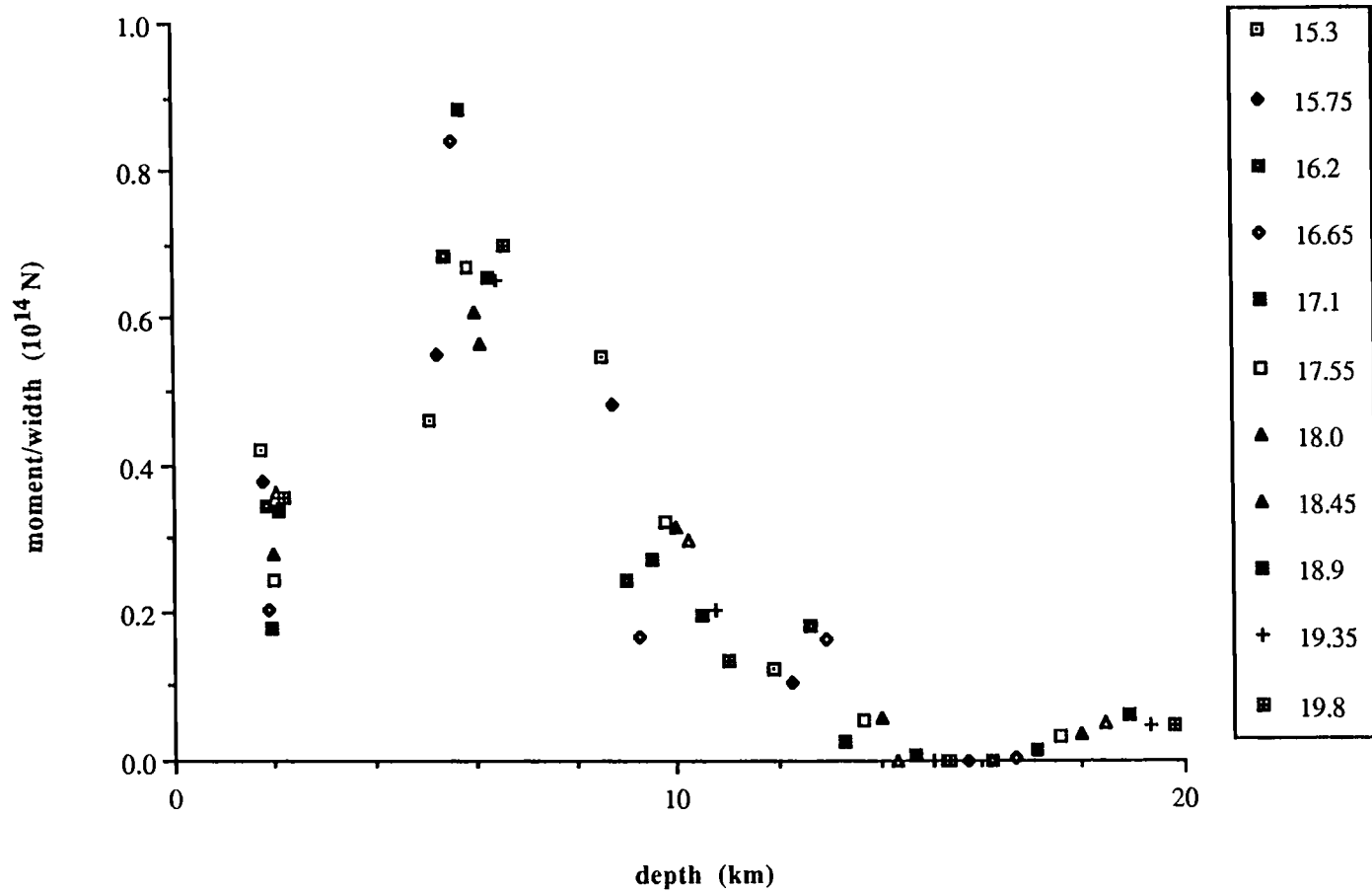
Figure 6.4.7   Seismic moment release vs. depth for the 09/13/1986 Kalamata earthquake. The figure is a compilation of 11 inversions in which 5 equally spaced sources were used. Numbers in legend correspond to deepest source of each model. Only minor moment release below 12-13 km depth.

7. Summary and Conclusions

Three main questions have been addressed in this thesis: 1) are the fault surfaces of large normal faulting earthquakes planar or curved. 2) is there evidence for detachment faulting in form of coseismic slip during large earthquakes at the base of the seismogenic upper crust, and 3) to what depths do ruptures of large normal faulting earthquakes extend in relation to their aftershock distribution.

Thirteen normal faulting earthquakes ($5.5 \leq M_w \leq 7.1$) from the Aegean region have been investigated in this study using long-period and broadband teleseismic waveforms. The source parameters were obtained by simultaneous inversion of P and SH waves, using the inversion routine of Nábĕlek (1984). The centroidal solutions are summarized in Table 7.1 and Figure 7.1 shows the fault plane solutions.

Synthetic Modeling

Numerical modeling for planar and listric fault geometries was performed in order to investigate the ability of the far-field body wave inversion method to recover correct estimates of the centroidal source parameters and the geometry of finite fault models.

It was found that the curvature effects are small, azimuthally dependent, and more pronounced for SH than for P waves. The centroidal parameters of the planar fault model and its curvature (or in this case the lack of one) were recovered correctly. Centroidal solutions for listric fault geometries at shallow depths showed an interesting result: interference of direct and reflected phases causes an underestimation of the expected fault dip by 10° for my models, a dip corresponding to sub centroid depths. The correct centroidal fault dip was found when the model was placed at greater depths such that the direct and reflected phases were separated. This result points to the limitations of teleseismic body wave analysis for shallow complicated earthquakes.

Distributed source models based on the biased centroidal solution and with fixed geometry are not able to retrieve fault curvature and fault dips correctly. However, a planar fault description is statistically significantly inferior to listric models and therefore it is still possible to distinguish between planar and listric geometries. Distributed source models where the dips of the individual sources can freely vary during the inversion provide a better estimate of the true fault dips with depth.

Fault Geometry

I concentrated on the largest normal faulting earthquakes (Alasehir, Gediz and Thessaloniki mainshocks, and the Corinth sequence), which were powerful enough to rupture the entire seismogenic width of the crust and therefore carry the information about the down-dip geometry.

A three step procedure was used to investigate the fault geometry. Source parameters and locations of a detachment source (step 2) and of distributed source models (step 3) were derived from the point source solution (step 1).

Detachment Faulting

Low-angle detachment faulting at the base of the seismogenic crust has been proposed for some of the investigated earthquakes (Eyidogan and Jackson, 1985; King et at., 1985). Inverting for the seismic moment of the detachment source showed that only a small amount of moment release (usually at most 10% of the moment release associated with the main rupture) was allowed by the data and the waveform fit did not significantly improve for any of the events.

Later arrivals observed in the P waves for the Alasehir and Gediz events were modelled with detachment faults by Eyidogan and Jackson (1985). Inclusion of the SH waves and of the amplitude information (Eyidogan and Jackson normalized their synthetics with respect to the observed seismograms), however, shows that the observed waveforms are incompatible with their results. Formal inversion for the seismic moment of the detachment source for the Alasehir event allows a relatively large possible moment release ($\approx$ 40% of the main rupture), however, the moment is distributed evenly over about 40 s duration without changing the synthetic waveforms significantly and still fails to generate the large P arrivals. Clear evidence for path or crustal structure related causes of these arrivals comes from the Gediz earthquakes, where a large late arrival at exactly the same time for the aftershocks and the main event is seen (Figure 6.1.24).

A possible explanation for the late arrivals in form of a low-velocity zone was put forward by Nábělek (1986) for the Corinth earthquakes. However, different crustal structures tested for the Alasehir event did not generate the correct amplitudes or arrivals for all stations simultaneously.

The results of this study do not indicate significant seismogenic slip along detachment surfaces at depth. Decoupling of the brittle upper from the lower ductile crust probably occurs aseismically in a ductile fashion.

Down-Dip Fault Geometry

Distributed source models were used to investigate the down-dip geometry of large normal faults (for details see section 3.2). Results of these models in conjunction with constraints provided by short period first motion data and centroidal solutions suggest that planar faulting is the dominant style of faulting. Fault curvature is not required for any of the studied large earthquakes; however, some allow or even suggest a small curvature.

Planar: the Gediz main shock and the 02/24/1981 Corinth earthquake ruptured along essentially planar faults. Distributed source models with fixed geometry allow only a very small curvature (<10° and <20° for the Gediz and Corinth event, respectively) and models where the dips are allowed to vary result in essentially planar geometries. The fault dip of the centroid does not indicate any flattening. The short period first motion data for the Gediz event are consistent with the centroid and the planar fault geometry. These two events had the widest faults and thus the fault geometry could be well resolved.

Planar, but curvature possible: the Thessaloniki main shock, and the 02/25/1981 and 03/04/1981 Corinth earthquakes do not exclude fault curvature. For fixed fault geometries the planar model provides a better fit than any listric model, however, the range allowed from the statistical test is broader (Thessaloniki: -30° - +40°, 02/25: -60° - +40°, 03/04: ±40°, where +: fault dip increases with depth, - fault dip decreases with depth). Allowing the dips of the subsources to vary indicates a small amount of flattening along the width of the fault for the Thessaloniki earthquake (maximum 10°-20° flattening), the short period first motion data, which are consistent with the centroidal solution, allow only minor flattening (<10 °). The short period first motion data of the two Corinth earthquakes do not constrain the fault dip at depth well, however, very steep (>60°) and very shallow (<30°) dipping nodal planes are excluded. Changes in fault dip with depth from the inversions where the dips are allowed to vary are smaller than for the Thessaloniki earthquake and are probably close to the resolution uncertainties, indicating essentially planar faulting.

Curvature suggested, but not required: results for the Alasehir earthquake and the 04/19/1970 Gediz aftershock suggest faulting along curved faults.

A slight increase of fault dip with depth is indicated for the Alasehir earthquake. A fault geometry with a 20° convex upward curvature fits slightly, but insignificantly better than the planar model. Allowing the dips of the subsources to vary resulted in the deeper

source being more steeply dipping than the intermediate depth source (by 8°-16°). The dip of the centroidal solution (41°) is also slightly steeper than the dip of the intermediate depth source (32°-39°). Assuming that the centroid dip represents an estimate of the fault at sub centroid depths, as suggested by the synthetic modelling, this would imply a small amount of curvature. The short period first motion polarities indicate that the fault dip at the nucleation point is about 40°. From these results a small convex curvature seems to be possible, but planar faulting is not excluded. Flattening of the fault, however, is not supported by the data.

The short period first motion data of the 04/19/1970 Gediz aftershock are not compatible with the centroidal solution. Moment release in two distinct pulses suggested a two source model, which improved the fit significantly. The first subevent has a steep northward dipping nodal plane consistent with the short period data, whereas the second event has a nodal plane more shallowly dipping towards north. No surface ruptures accompanied this small event and the fault plane ambiguity is not resolved. The exact spatial relation between the first subevent and the second subevent could not be resolved; however, the first was probably shallower than or at the same depth as the second subevent. Assuming that the two subevents ruptured along the same fault, the change in dip of the subevents implies fault curvature, either convex or concave. However, complicated internal deformation along two different fault planes in the highly strained region of aftershock concentration in the vicinity of the southeastern terminus of the main shock surface rupture is also possible.

Depth Extent of Rupture - Implications for Brittle-Ductile Transition

The depth extent of the main shock rupture was compared with the depth distribution of the locally recorded aftershocks for the Thessaloniki and Kalamata earthquakes and the three major earthquakes of the Corinth sequence. It was found that the larger shocks (Thessaloniki, 02/24/1981 and 03/04/1981 Corinth) penetrated below the depth where the main aftershock activity terminates.

The aftershock locations and the synthetic seismograms are sensitive to the crustal velocity model. Differences between depth extent of aftershock activity and main shock rupture observed for some events are probably not biased, since very similar velocity models have been used to locate the aftershocks and to calculate the synthetic seismograms.

The aftershock activity for the Thessaloniki earthquake was concentrated between 3 and 12 km depth, whereas the main shock rupture extended from the free surface to about 16-18 km depth.

Most of the aftershocks of the Corinth sequence are shallower than 13 km. Shallow aftershock activity (≤ 3 km) is quite abundant. However, King et al. (1985) mentioned that the depth of these shallow aftershocks is not well resolved (± 4 km) and the shallowest aftershock recorded with a precision of ± 2 km is 3.6 km deep. The first major event of 02/24/1981 had significant moment release to a depth of at least 15 km. The moment release of the 02/25/1981 earthquake drops sharply between 10 and 12 km depth, and no deeper moment release was detected. The third event of 03/04/1981, however, showed a moment release down to a depth of 15-16 km.

No significant moment release was observed below 12 km for the Kalamata earthquake, and the aftershock activity is confined to depths between 2 and 11 km.

The results can be interpreted in terms of a friction-rate model of a fault zone in which earthquakes can only nucleate in a region of unstable, velocity weakening friction (Scholz, 1988). The lack of shallow aftershock activity can be explained by stable frictional behaviour in the uppermost crust due to the presence of hydrous minerals, and the relatively sharp cut-off at depth marks the onset of plastic flow for some rock constituents due to an increase in temperature.

According to the model, only large earthquakes are able to penetrate into the semi-brittle region at the base of the brittle crust, which flows during interseismic periods. How do the depth extents of the studied events fit into this model? The smaller Kalamata event was not powerful enough to rupture (far) into the semi-brittle field, whereas the larger Thessaloniki earthquake penetrated into this stable frictional zone. Both results are in agreement with the model. The first and third event of the Corinth sequence apparently penetrated a few km into the semi-brittle zone, whereas the second event, which was actually larger than the third, did not. This shows that the situation for the Corinth sequence is more complicated. Furthermore, the 03/04/1981 shock occurred on an antithetic fault, which should terminate at about 10 km depth (assuming a graben width of 20 km and a fault dip of 45°) without any moment release at greater depth. However, this could also indicate that the major fault at the eastern end of the Gulf of Corinth dips towards south and not towards north.

The depth extent of the main shock ruptures roughly correlates with the predictions of fault zone models based on friction-rate behaviour of rocks (Scholz, 1988). However, sequences of large earthquakes, as suggested by the Corinth sequence, may not always

follow the model in a simple way. Changes in the stress distribution caused by preceding large shocks may influence the rupture behaviour of immediately following large shocks.

Implications for Models of Continental Extension

Two models of normal fault geometries were presented in Chapter 2.1.1: one involving sets of listric faults (e.g., Davis et al., 1980) and the second involving arrays of coeval planar high-angle faults (e.g., Morton and Black, 1975; Wernicke and Burchfiel, 1982; Jackson and McKenzie, 1983; Gans et al., 1985). The results of this study strongly support the second model.

Many different interpretations for the origin of detachment surfaces exist (see Chapter 2.1.2). The two most popular models, the 'simple shear' (e.g., Wernicke, 1981, 1985; Davis, 1983; Lister et al., 1986; LePichon and Barbier, 1987) and the 'pure shear' model (e.g., McKenzie, 1978b; Gans, 1987), predict a completely different seismic behaviour. In the 'simple shear' model the crust is cut by a shallow dipping seismogenic detachment fault, whereas in the 'pure shear' model the detachment represents an aseismic ancient brittle-ductile transition. No evidence for detachment faulting in the upper crust was found; the nodal planes of the point source and the first motion fault plane solutions for all studied events dip steeply. A significant amount of slip on a basal detachment during or immediately after the main moment release is not supported by the data of the large events which presumably ruptured through the entire upper crust. Furthermore, the planar geometry of the large, deeply biting seismogenic normal faults does not allow simultaneous operation of upper crustal shallow dipping detachment faults of large areal extent. The predictions of the 'simple shear' model are not matched by the observations, whereas the 'pure shear' model (Figure 2.1.2) describes the observations adequately. 'Simple shear' within the ductile layer, however, cannot be excluded by the data.

One may speculate what happens to the lowermost part of a fault between two major earthquakes. It was shown that large earthquakes can dynamically rupture into the frictional stable semi-brittle field along presumably planar faults (no indication for detachment faulting or significant shallowing of faults was found). Ductile flow during interseismic periods probably deforms the fault plane within the semi-brittle field. And the next large earthquake that penetrates into the semi-brittle field, therefore, has to generate a new planar lower part.

Table 7.1 Summary of Centroid Source Parameters for all Studied Earthquakes

	#	strike deg	dip deg	rake deg	moment 10^{17}Nm	Mw	depth km	duration s	curvature deg
Demirci	1	113 (296)	36 (54)	267 (272)	6.8	5.8	8.4	3	
	2	119 (308)	46 (44)	264 (276)	8.9	5.9	9.9	5	
Alasehir	3	300	41	263	128.5	6.7	3.3	15	<20
Gediz	4	304	41	263	505.2	7.1	7.7	21	<10
	5	283	38	282	2.6	5.5	7.8	3	
	6	278	50	267	7.1	5.8	9.6	6	
	7	297	51	282	6.5	5.8	6.6	3	
Thessaloniki	8	261	42	270	4.4	5.7	5.3	4	
	9	257	41	264	35.4	6.3	7.0	10	<30
Corinth	10	268	39	284	105.2	6.6	8.6	18	<20
	11	246	44	276	35.2	6.3	6.7	15	<60
	12	50 (238)	45 (45)	264 (276)	23.1	6.2	5.6	12	<40
Kalamata	13	201	45	284	7.0	5.8	6.2	4	

- event number corresponing to Figure 7.1. depth - centroid depth. duration - length of source time function. curvature - maximum decrease of fault dip with depth, indicated by the t-value corresponding to the 95% level of confidence that more curvature is significantly worse. Fault orientations in parantheses are for the auxilliary plane (#12) or for the second nodal plane (#1, #2), where the fault plane is not known. Note: orientations of Gediz aftershocks and Thessaloniki foreshock are given s.t. they share the same fault plane as the main event , which is not necessarily true.
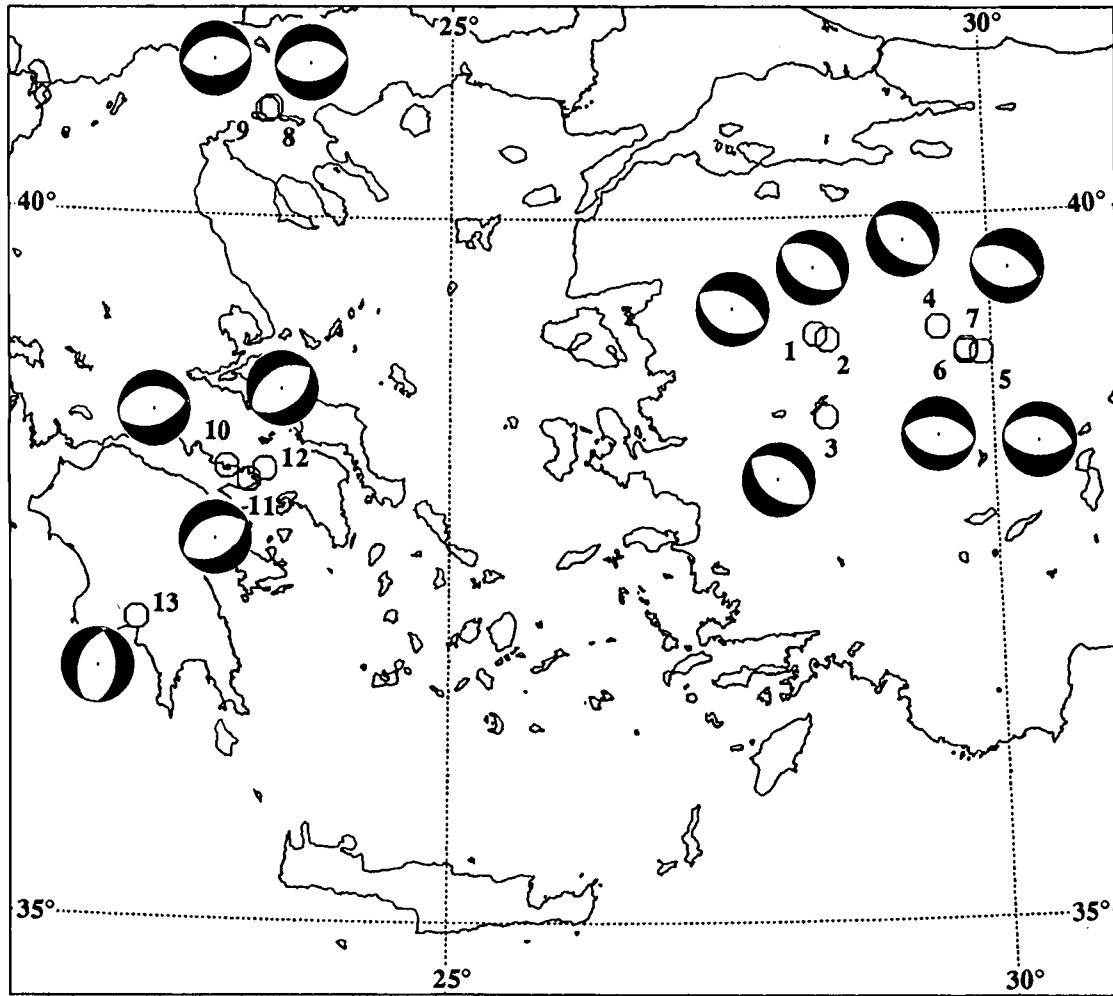
Figure 7.1 Map of the Aegean region. Fault plane solutions shown are point source descriptions of all events studied. Numbers next to the octagons and the fault plane solutions correspond to numbers in Table 7.1.

Bibliography

Aki, K., and P. G. Richards, *Quantitative seismology: theory and methods*, W. H. Freeman, San Francisco, 1980.

Allen, C. R., Geological criteria for evaluating seismicity, *Geol. Soc. Am. Bull.*, 86, 1041-1057, 1975.

Allmendinger, R. W., J. W. Sharp, D. Von Tish, L. Sherpa, L. Brown, S. Kaufman, J. Oliver, and R. B. Smith, Cenozoic and Mesozoic structure of the eastern Basin and Range province, Utah, from COCORP seismic reflection data, *Geology*, 11, 532-537, 1983.

Ambraseys, N. N., and J. S. Tchalenko, Seismotectonic aspects of the Gediz, Turkey, earthquake of March 1970, *Geophys. J. R. Astr. Soc.*, 30, 229-252, 1972.

Ambraseys, N. N., and J. A. Jackson, Earthquake hazard and vulnerability in the northeastern Mediterranean: the Corinth earthquake sequence of February-March 1981, *Disasters*, 5, 355-368, 1981.

Ambraseys, N. N., and J. A. Jackson, Seismicity and associated strain of central Greece between 1890 and 1988, *Geophys. J. Int.*, 101, 663-708, 1990.

Anagnostopolous, S. A., D. Rinaldis, V. A. Lekidis, V. N. Margaris, and N. P. Theodulidis, The Kalamata, Greece, earthquake of September 13, 1986, *Earthquake Spectra*, 3, 365-402, 1987.

Armijo, R., H. Lyon-Caen, and D. Papanastassiou, A possible normal-fault rupture for the 464BC Sparta earthquake, *Nature*, 351, 137-139, 1991.

Arpat E., and E. Bingöl, The rift system of western Turkey: thoughts on its development, *Bull. Min. Res. Explor. Inst. Turkey*, 73, 1-9, 1969.

Bally, A. W., D. Bernoulli, G. A. Davis, and L. Montadert, Listric normal faults, *Oceanologica Acta, Proc. 26. Int. Geol. Congress*, 87-101, 1981.

Barker, J. A., and C. A. Langston, Inversion of teleseismic body waves for the moment tensor of the 1978 Thessaloniki, Greece, earthquake, *Bull. Seis. Soc. Am.*, 71, 1423-1444, 1981.

Barrientos, S. E., R. S. Stein, and S. N. Ward, Comparison of the 1959 Hebgen Lake, Montana and the 1983 Borah Peak, Idaho, earthquakes from geodetic observations, *Bull. Seis. Soc. Am.*, 77, 784-808, 1987.

Bezzeghoud, M., A. Deschamps, and R. Madariaga, Broad-band modelling of the Corinth, Greece earthquakes of February and March 1981, *Ann. Geophys.*, 4, 295-304, 1986.

Bouchon, Teleseismic body wave radiation from a seismic source in a layered medium, *Geophys. J. R. Astr. Soc.*, 47, 515-530, 1976.

Brace, W. F., and D. L. Kohlstedt, Limits on lithospheric stress imposed by laboratory experiments, *J. Geophys. Res.*, 85, 6248-6252, 1980.

Brooks, M., and G. Ferentinos, Tectonics and sedimentation in the Gulf of Corinth and the Zakynthos and Kefallinia channels, western Greece, *Tectonophysics*, 101, 25-54, 1984.

Brune, J. N., Tectonic stress and spectra of seismic shear waves from earthquakes, *J. Geophys. Res.*, 75, 4997-5009, 1970.

Brune, J. N., Corrections to: tectonic stress and spectra of seismic shear waves from earthquakes, *J. Geophys. Res.*, 76, 5002, 1971.

Buck, W. R., Flexural rotation of normal faults, *Tectonics*, 7, 959-973, 1988.

Buck, W. R., F. Martinez, M. S. Steckler, and J. R. Cochran, Thermal consequences of lithospheric extension: Pure and simple, *Tectonics*, 7, 213-234, 1988.

Bürstle, W., and G. Müller, Moment and duration of shallow earthquakes from Love-wave modelling for regional distances, *Phys. Earth Planet. Int.*, 32, 312-324, 1983.

Byerlee, J. D., Brittle-ductile transition in rocks, *J. Geophys. Res.*, 73, 4741-4750, 1968.

Canitez, N., S. Büyükasikoglu, and U. Güclü, Seismicity of the Sinop and Trakya (Thrace) nuclear power plant sites and their vicinity, *Prog. Report 2 Trakya (Thrace) area*, 442 pp., Technical University of Istanbul, Istanbul, 1982.

Carver, D., and G. A. Bollinger, Aftershocks of the June 20, 1978, Greece earthquake: a multimode faulting sequence, *Tectonophysics*, 73, 343-363, 1981.

Chen, W.-P., and P. Molnar, The depth distribution of intracontinental and intraplate earthquakes and its implications for the thermal and mechanical properties of the lithosphere, *J. Geophys. Res.*, 88, 4183-4214, 1983.

Crittenden, M. D., Jr., P.J. Coney, and G. H. Davis (Eds.), *Cordilleran metamorphic core complexes*, 490 pp., Geol. Soc. Amer., Mem., 153, 1980.

Das, S., Appropriate boundary conditions for modeling very long earthquakes and physical consequences, *Bull. Seis. Soc. Am.*, 72, 1911-1926, 1982.

Das, S., and C. Scholz, Why large earthquakes do not nucleate at shallow depths, *Nature*, 305, 621-623, 1983.

Davis, G. A., J. L. Anderson, E. G. Frost, and T. J. Shackelford, Mylonitization and detachment faulting in the Whipple-Buckskin-Rawhide Mountains terrane, southeastern California, and western Arizona, in *Cordilleran metamorphic core complexes*, edited by M. D. Crittenden, Jr., P. J. Coney, and G. H. Davis, pp. 79-130, Geol. Soc. Amer., Mem., 153, 1980.

Davis, G. H., Shear-zone model for the origin of metamorphic core complexes, *Geology*, 11, 342-347, 1983.

Delibasis, N., J. Drakopoulos, and G. N. Stavrakakis, The Kalamata (southern Greece) earthquake of 13 September 1986, *Ann. Geophys.*, 5, 731-733, 1987.

Dewey J. W., Seismicity of northern Anatolia, *Bull. Seis. Soc. Am.*, 66, 843-868, 1976.

Doser, D. I., Earthquake processes in the Rainbow Mountain-Fairview Peak-Dixie Valley, Nevada, region 1954-1959, *J. Geophys. Res.*, 91, 12572-12586, 1986.

Doser, D. I., The Ancash, Peru, earthquake of 1946 November 10: evidence for low-angle normal faulting in the high Andes of northern Peru, *Geophys. J. R. Astr. Soc.*, 91, 57-71, 1987.

Doser, D. I., and R. B. Smith, An assessment of source parameters of earthquakes in the Cordillera of the western United States, *Bull. Seis. Soc. Am.*, 79, 1383-1409, 1989.

Dziewonski, A. M., and J. H. Woodhouse, An experiment in systematic study of global seismicity: centroid-moment tensor solutions for 201 moderate and large earthquakes in 1981, *J. Geophys. Res.*, 88, 3247-3271, 1983.

Dziewonski, A. M., G. Ekström, J. E. Franzen, and J. H. Woodhouse, Global seismicity of 1978: centroid-moment tensor solutions for 512 earthquakes, *Phys. Earth Planet. Sci.*, 46, 316-342, 1987a.

Dziewonski, A. M., G. Ekström, J. E. Franzen, and J. H. Woodhouse, Centroid-moment tensor solutions for July-September 1986, *Phys. Earth Planet. Sci.*, 46, 305-315, 1987b.

Dziewonski, A. M., G. A. Ekström, J. E. Franzen, and J. H. Woodhouse, Global seismicity of 1981: centroid moment tensor solutions for 542 earthquakes, *Phys. Earth Planet. Int.*, 50,155-182, 1988.

Ekström, G. A., A broad band method of earthquake analysis, *Ph. D. thesis*, 216 pp., Harvard University, Cambridge, Massachusetts, 1987.

Ekström, G. A., and P. England, Seismic strain rates in regions of distributed continental deformation, *J. Geophys. Res.*, 94, 10231-10257, 1989.

Eyidogan, H., and J. Jackson, A seismological study of normal faulting in the Demirci, Alasehir and Gediz earthquakes of 1969-1970 in western Turkey: Implications for the nature and geometry of deformation in the continental crust, *Geophys. J. R. Astr. Soc.*, 81, 569-607, 1985.

Gans, P. B., An open-system, two-layer crustal stretching model for the eastern Great Basin, *Tectonics*, 6, 1-12, 1987.

Gans, P. B., E. L. Miller, J. McCharty, and M. L. Ouldcott, Tertiary extensional faulting and evolving ductile-brittle transition zones in the northern Snake Range and vicinity: New insights from seismic data, *Geology*, 13, 189-193, 1985.

Gariel, J.-C., P.-Y. Bard, and K. Pitilakis, A theoretical investigation of source, path and site effects during the 1986 Kalamata earthquake (Greece), *Geophys. J. Int.*, 104, 165-177, 1991.

Gupta, I. N., Body wave radiation patterns from force applied within a half space, *Bull. Seis. Soc. Am.*, 56, 173-183, 1967.

Hamblin, W. K., Origin of 'reverse drag' on the downthrown side of normal faults, *Bull. Geol. Soc. Amer.*, 76, 1145-1164, 1965.

Hanks, T. H., and M Wyss, The use of body-wave spectra in the determination of seismic source parameters, *Bull. Seis. Soc. Am.*, 62, 561-589, 1972.

Harvey, D., and G. L. Choy, Broad-band deconvolution of GDSN data, *Geophys. J. R. Astr. Soc.*, 69, 659-668, 1982.

Huang, P. Y., S. C. Solomon, E. A. Bergman, and J. L. Nábĕlek, Focal depths and mechanisms of Mid-Atlantic ridge earthquakes from body wave inversion, *J. Geophys. Res.*, 91, 579-598, 1986.

International symposium on the Hellenic arc and trench (H. E. A. T.), (abstracts), *Natl. Tech. Uni. Athens*, 138 pp., 1981.

Jackson, J. A., Active normal faulting and crustal extension, in *Continental extensional tectonics*, edited by M. P. Coward, J. F. Dewey, and P. L. Hancock, pp. 3-17, Geol. Soc. London Spec. Publ., 28, 1987.

Jackson J. A., and T. J. Fitch, Seismotectonic implications of relocated aftershock sequences in Iran and Turkey, *Geophys. J. R. Astr. Soc*, 57, 209-229, 1979.

Jackson, J. A., J. Gagnepain, G. Houseman, G. C. P. King, P. Papadimitriou, C. Soufleris, and J. Virieux, Seismicity, normal faulting, and geomorphological development of the Gulf of Corinth (Greece): the Corinth earthquakes of February and March 1981, *Earth Plan. Sci. Lett.*, 57, 377-397, 1982.

Jackson, J. A., and D. McKenzie, The geometrical evolution of normal fault systems, *J. Struct. Geol.*, 5, 471-482, 1983.

Jackson, J. A., and D. McKenzie, The relationship between plate motions and seismic moment tensors, and the rate of active deformation in the Mediterranean and the Middle East, *Geophys. J.*, 93, 45-73, 1988.

Jackson, J. A., N. J. White, Z. Garfunkel, and H. Anderson, Relations between normal-fault geometry, tilting and vertical motions in extensional terrains: an example from the southern Gulf of Suez, *J. Struct. Geol.*, 10, 155-170, 1988.

Jackson, J. A., and N. J. White, Normal faulting in the upper continental crust: observations from regions of active extension, *J. Struct. Geol.*, 11, 15-36, 1989.

Kikuchi, M., and H. Kanamori, Inversion of complex body waves, *Bull. Seis. Soc. Am.*, 72, 491-506, 1982.

Kim, W.-Y., O. Kulhánek, and K. Meyer, Source processes of the 1981 Gulf of Corinth earthquake sequence from body-wave analysis, *Bull. Seis. Soc. Am.*, 74, 459-477, 1984.

King, G. C. P. , Z. Ouyang, P. Papadimitriou, A. Deschamps, J. Gagnepain, G. Houseman, J. A. Jackson, C. Soufleris, and J. Virieux, The evolution of the Gulf of

Corinth (Greece): an aftershock study of the 1981 earthquake, *Geophys. J. R. Astr. Soc.*, 80, 677-693, 1984.

King, G. C. P., and J.L. Nábĕlek, The role of bends in faults in the initiation and termination of earthquake rupture, *Science*, 228, 984-987, 1985.

Klemperer, S. L., T. A. Hauge, E. C. Hauser, J. E. Oliver, and C. J. Potter, The Moho in the northern Basin and Range province, Nevada, along the COCORP 40°N seismic-reflection transect, *Geol. Soc. Am. Bull.*, 97, 603-618, 1986.

Kulhánek, O., and K. Meyer, Source parameters of the Volvi-Langadhás earthquake of June 20, 1978 deduced from body-wave spectra at stations Uppsala and Kiruna, *Bull. Seis. Soc. Am.*, 69, 1289-1294, 1979.

Kusznir, N. J., G. Marsden, and S. S. Egan, A flexural-cantilever simple-shear/pure-shear model of the continental lithosphere extension: application to the Jeanne d'Arc, Grand Banks and Viking Graben, North Sea, in *The geometry of normal faults*, edited by A. M. Roberts, G. Yielding, and B. Freeman, pp 41-60, Geol. Soc. London Spec. Publ., 56, 1991.

Langston C. A., A body wave inversion of the Koyna, India, earthquake of December 10, 1967, and some implications for body wave focal mechanisms, *J. Geophys. Res.*, 81, 2517-2529, 1976.

Langston, C. A., and D. V. Helmberger, A procedure for modelling shallow dislocation sources, *Geophys. J. R. Astr. Soc.*, 42, 117-130, 1975.

Latin, D., and N. J. White, Generating melt during lithospheric extension: Pure shear vs. simple shear, *Geology*, 18, 327-331, 1990.

LePichon, X., and F. Barbier, Passive margin formation by low-angle faulting within the upper crust: the northern Bay of Biscay margin, *Tectonics*, 6, 133-150, 1987.

Lister, G. S., G. Banga, and A. Feenstra, Metamorphic core complexes of Cordilleran type in the Cyclades, Aegean Sea, Greece, *Geology*, 12, 221-225, 1984.

Lister, G. S., M. A. Etheridge, and P. A. Symonds, Application of the detachment fault model to the formation of passive continental margins, *Geology*, 14, 246-250, 1986.

Lister, G. S., and G. A. Davis, The origin of metamorphic core complexes and detachment faults formed during Tertiary continental extension in the northern Colorado River region, USA, *J. Struct. Geol.*, 11, 65-94, 1989.

Lyon-Caen, H., R. Armijo, J. Drakopoulos, J. Baskoutass, N. Delibassis, R. Gaulon, V. Kouskouna, J. Latoussakis, K. Makropoulos, P. Papadimitriou, D. Papanastassiou, and G. Pedotti, The 1986 Kalamata (south Peloponnesus) earthquake: detailed study of a normal fault, evidence for east-west extension in the Hellenic Arc, *J. Geophys. Res.*, 93, 14967-15000, 1988.

Mariolakos, I., I. Fountoulis, E. Logos, and S. Lozios, Surface faulting caused by the Kalamata (Greece) earthquake (13.9.86), *Tectonophysics*, 163, 197-203, 1989.

McKenzie, D. P., Active tectonics of the Mediterranean region, *Geophys. J. R. Astr. Soc.*, 30, 109-185, 1972.

McKenzie, D., Some remarks on the development of sedimentary basins, *Earth Planet. Sci. Lett.*, 40, 25-32, 1978a.

McKenzie, D. P., Active tectonics of the Alpine-Himalayan belt: the Aegean Sea and surrounding regions, *Geophys. J. R. Astr. Soc.*, 55, 217-254, 1978b.

Meissner, R., and J. Strehlau, Limits of stresses in continental crusts and their relation to the depth-frequency distribution of shallow earthquakes, *Tectonics*, 1, 73-89, 1982.

Mercier, J. L., N. Mouyaris, C. Simeakis, T. Roundoyannis, C. Angelidhis, Intra-plate deformation: a quantitative study of the faults activated by the 1978 Thessaloniki earthquakes, *Nature*, 278, 45-48, 1979.

Mercier, J. L., E. Carey-Gailhardis, N. Mouyaris, C. Simeakis, T. Roundoyannis, C. Angelidhis, Structural analysis of recent and active faults and regional state of stress in the epicentral area of the 1978 Thessaloniki earthquakes (northern Greece), *Tectonics*, 2, 577-600, 1983.

Morton, W. H., and R. Black, Crustal attenuation in Afar, in: *Afar Depression of Ethiopia*, vol. 1, edited by A. Pilger and A. Rösler, pp. 55-65, Schweizerbartsche Verlagsbuchhandlung, Stuttgart, 1975.

Myrianthis, M. L., Graben formation and associated seismicity in the Gulf of Korinth (central Greece), in *The geological evolution of the eastern Mediterranean*, edited by J. E. Dixon, and A. H. F. Robertson, pp.701-707, Geol. Soc. London Spec. Publ., 17, 1984.

Nábĕlek, J. L., Determination of earthquake source parameters from inversion of body waves, *Ph. D. thesis*, 361 pp., M. I. T., Cambridge, Massachusetts, 1984.

Nábĕlek, J. L., Evidence for crustal low-velocity zone in regions of continental extension (abstract), *Eos Trans. AGU*, 67, 1212, 1986.

Nábĕlek, J. L., Planar vs listric faulting: The rupture process and fault geometry of the 1983 Borah Peak, Idaho earthquake from inversion of teleseismic body waves, *J. Geophys. Res.*, in press.

North R. G., Seismic moment, source dimensions, and stresses associated with earthquakes in the Mediterranean and Middle East, *Geophys. J. R. Astr. Soc.*, 48, 137-161, 1977.

Okaya, D. A., and G. A. Thompson, Geometry of Cenozoic extensional faulting: Dixie Valley, Nevada, *Tectonics*, 4, 107-125, 1985.

Papazachos, B., D. Mountrakis, A. Psilovikos, and G. Leventakis, Surface fault traces and fault plane solutions of the May-June 1978 major shocks in the Thessaloniki area, Greece, *Tectonophysics*, 53, 171-183, 1979a.

Papazachos, B., D. Mountrakis, A. Psilovikos, and G. Leventakis, Focal properties of the 1978 earthquakes in the Thessaloniki area, *Bulg. Geophys. J.*, 6, 72-80, 1979b.

Papazachos, B. C., P. E. Comninakis, E. E. Papadimitriou, and E. M. Scordilis, Properties of the February-March 1981 seismic sequence in the Alkyonides gulf of central Greece, *Ann. Geophys.*, 2, 537-544, 1984.

Papazachos, B., A. Kiratzi, B. Karacostas, D. Panagiotopoulos, E. Scordilis, and D. M. Mountrakis, Surface fault traces, fault plane solution and spatial distribution of the aftershocks of the September 13, 1986 earthquake of Kalamata (southern Greece), *Pure Appl. Geophys.*, 126, 55-68, 1988.

Perissoratis, C., D. Mitropoulos, and I. Angelopoulos, The role of earthquakes in inducing sediment mass movements in the eastern Korinthiakos Gulf. An example from the February 24 - March 4, 1981 activity, *Marine Geol.*, 55, 35-45, 1984.

Planke, S., and R. B. Smith, Cenozoic extension and evolution of the Sevier Desert Basin, Utah, from seismic reflection, gravity and well data, *Tectonics*, 10, 345-365, 1991.

Ritsema, A. R., Catastrophic earthquakes in the European area, *Tectonophysics*, 53, 155-158, 1979.

Roberts, A. M., and G. Yielding, Deformation around basin-margin faults in the North Sea/mid-Norway rift, in *The geometry of normal faults*, edited by Roberts, A. M., G. Yielding, and B. Freeman, pp 61-78, Geol. Soc. London Spec. Publ., 56, 1991.

Roberts, A. M., G. Yielding, and B. Freeman (Eds.), *The geometry of normal faults*, 264 pp., Geol. Soc. Spec. Pub., 56, 1991.

Scholz, C. H., The brittle-plastic transition and the depth of seismic faulting, *Geologische Rundschau*, 77, 319-328, 1988.

Sibson, R. H., Fault zone models, heat flow, and the depth distribution of earthquakes in the continental crust of the United States, *Bull. Seis. Soc. Am.*, 72, 151-163, 1982.

Sibson, R. H., Roughness at the base of the seismogenic zone: contributing factors, *J. Geophys. Res.*, 89, 5791-5799, 1984.

Sibson, R. H., A note on fault reactivation, *J. Struct. Geol.*, 7, 751-754, 1985.

Sipkin, S. A., and R. E. Needham, Moment-tensor solutions estimated using optimal filter theory: global seismicity, 1984-1987, *Phys. Earth Planet. Sci.*, 57, 233-259, 1989.

Smith, R. B., and R. L. Bruhn, Intraplate extensional tectonics of the eastern Basin-Range: inferences on structural style from seismic reflection data, regional tectonics, and thermal-mechanical models of brittle-ductile deformation, *J. Geophys. Res.*, 89, 5733-5762, 1984.

Sorel, D., G. Gars, J. L. Mercier, K. Simeakis, and T. Rondoyannis, The 1981 Gulf of Korinthos earthquakes: field evidences (abstract), in *International symposium on the Hellenic arc and trench (H. E. A. T.)*, 132-133, 1981.

Soufleris, C., and G. S. Stewart, A source study of the Thessaloniki (northern Greece) 1978 earthquake sequence, *Geophys. J. R. Astr. Soc.*, 67, 343-358, 1981.

Soufleris, C., J. A. Jackson, G. C. P. King, C. P. Spencer, and C. H. Scholz, The 1978 earthquake sequence near Thessaloniki (northern Greece), *Geophys. J. R. Astr. Soc.*, 68, 429-458, 1982.

Spencer, J. E., and C. G. Chase, Role of crustal flexure in initiation of low-angle normal faults and implications for structural evolution of the Basin and Range province, *J. Geophys. Res.*, 94, 1765-1775, 1989.

Stavrakakis, G. N., A.-G. Tselentis, and J. Drakopoulos, Iterative deconvolution of teleseismic P waves from the Thessaloniki (N. Greece) earthquake of June 20, 1978, *Pure Appl. Geophys.*, 124, 1039-1050, 1987.

Stavrakakis, G. N., J. Drakopoulos, J. Latoussakis, D. Papanastassiou, and G. Drakatos, Spectral characteristics of the 1986 September 13 Kalamata (southern Greece) earthquake, *Geophys. J. Int.*, 98, 149-157, 1989.

Stavrakakis, G. N., S. V. Blionas, and C. E. Goutis, Dynamic source parameters of the 1981 Gulf of Corinth (central Greece) earthquake sequence based on FFT and iterative maximum entropy techniques, *Tectonophysics*, 1985, 261-276, 1991.

Stein, R. S., and S. E. Barrientos, Planar high-angle faulting in the Basin and Range: geodetic analysis of the 1983 Borah Peak, Idaho, earthquake, *J. Geophys. Res.*, 90, 11355-11366, 1985.

Stesky, R. M., Mechanisms of high temperature frictional sliding in Westerly granite, *Can. J. Earth Sci.*, 15, 361-375, 1978.

Strehlau, J., A discussion of the depth extent of rupture in large continental earthquakes, in: *Earthquake source mechanics*, edited by S. Das, J. Boatwright, and C. Scholz, pp. 131-146, AGU Geophys. Mono., 37, Washington D. C., 1986.

Tasdemiroglu, M., The 1970 Gediz earthquake in western Anatolia, Turkey, *Bull. Seis. Soc. Am.*, 61, 1507-1527, 1971.

Taymaz, T., J. A. Jackson, and D. McKenzie, Active tectonics of the north and central Aegean Sea, submitted to *Geophys. J. Int.*, 1991.

Tse, S., and J. Rice, Crustal earthquake instability in relation to the depth variation of frictional slip properties, *J. Geophys. Res.*, 91, 9452-9472, 1986.

Vita-Finzi C., and G. C. P. King, The seismicity, geomorphology and structural evolution of the Corinth area of Greece, *Phil. Trans. R. Soc. London*, A 314, 379-407, 1985.

Ward S. N., Body wave calculations using moment tensor sources in spherically symmetric, inhomogeneous media, *Geophys. J. R. Astr. Soc.*, 60, 53-66, 1980.

Wernicke, B., Low-angle normal faults in the Basin and Range province: Nappe tectonics in an extending orogen, *Nature*, 291, 645-648, 1981.

Wernicke, B., Uniform-sense normal simple shear of the continental lithosphere, *Can. J. Earth. Sci.*, 22, 108-126, 1985.

Wernicke, B., and B. C. Burchfiel, Modes of extensional tectonics, *J. Struct. Geol.*, 4, 105-115, 1982.

Wernicke, B., J. D. Walker, and M. S. Beaufait, Structural discordance between Neogene detachments and frontal Sevier thrusts, central Mormon Mountains, southern Nevada, *Tectonics*, 4, 213-246, 1985.

Wernicke, B., and G. J. Axen, On the role of isostasy in the evolution of normal fault systems, *Geology*, 16, 848-851, 1988.

Westaway, R., Block rotation in western Turkey 1. Observational evidence, *J. Geophys. Res.*, 95, 19857-19884, 1990.